© Copyright 2026

Youngshang Han

Printing and Recycling of Liquid Metal Composites for 3D Architected Thermoelectric Wearables

Youngshang Han

A dissertation submitted in partial fulfillment of the requirements for the degree of

Doctor of Philosophy

University of Washington

2026

Committee Members:

Mohammad H. Malakooti, Chair

Junlan Wang

Jie Xiao

Karl F. Böhringer

Program Authorized to Offer Degree:

Mechanical Engineering

Abstract

Printing and Recycling of Liquid Metal Composites for 3D Architected Thermoelectric Wearables

Youngshang Han

Chair of the Supervisory Committee:
Mohammad H. Malakooti
Department of Mechanical Engineering

Wearable thermoelectric devices (TEDs) enable the conversion between thermal and electrical energy as on-skin electronics by harvesting electricity from body heat or actively modulating skin temperature. However, their deployment has been challenged by insufficient energy conversion, limited conformability, impermeable interfaces, and a lack of recyclability. To address these bottlenecks, four studies are presented here to address the following research objectives: (1) Tailoring composites' material properties in each device layer through filler types and sizes and controlling device geometry via 3D printing enhance thermoelectric performance; (2) Engineering 3D device architecture improves thermal management while maintaining stretchability in wearable TEDs; (3) Electrohydrodynamic printing enables fabrication of permeable and thermally conductive skin–device interfaces; and (4) Thermally stable and recyclable liquid metal composites can be achieved by utilizing thermoset polymer matrix with dynamic covalent bonds. The studies presented in this dissertation collectively investigate materials, manufacturing processes, and device design to overcome the challenges associated with wearable TEDs.

In the first study, material properties and printability of multifunctional elastomer composites that comprise flexible TEDs are characterized. Liquid metal elastomer composites (LMECs) with high thermal conductivity function as compliant thermal interfaces or stretchable conductors depending on the size of liquid metal (LM) inclusions. Different synthesis strategies enable control of LM particle size, producing particles below 8 μm or above 100 μm for use in thermal interfaces or interconnects, respectively. Due to the passivating gallium oxide layer on the LM surface, the thermal interface LMEC is electrically insulating to prevent short circuits. In contrast,

LMEC interconnects can be electrically activated through mechanical sintering as the oxide shell on larger LM particles has a reduced effect. In the device core layer, hollow microsphere elastomer composite (HMEC) serves as a lightweight thermal insulator that minimizes thermal bypasses. These composite inks show shear-thinning behavior, allowing direct-ink-writing (DIW) of every layer with precisely controlled device geometry in 3D printed TEDs. The devices with functional layers successfully guide heat flux onto embedded thermoelectric (TE) pellets and deliver a great power density of 650 $\mu W \cdot cm^{-2}$ at a temperature gradient of 60 °C. Additionally, their tensile specimens withstand more than 15,000 stretching cycles at 30% strain due to soft composite encapsulations. Furthermore, the benefits of DIW are demonstrated via seamless integration on textiles and direct printing of stretchable heatsinks on TEDs, which also allowed further understanding of the importance of heat transfer in thermoelectric performance.

The printable composites are utilized in the second study to build 3D thermoelectric architectures, tailored for thermoelectric energy conversion. The resulting TEDs, featuring a novel air pocket structure in the core layer and a stretchable LMEC heatsink, achieved a power density of 115.4 $\mu W \cdot cm^{-2}$ at thermal equilibrium with an initial temperature gradient of 10 °C. Especially, the 3D printed HMEC air pocket separates the top and bottom thermal interfaces and allows TE pellets to be surrounded by air to maintain the temperature gradient across the thermoelectric semiconductors. This 3D structure results in higher output voltages and improved heating and cooling performance. In addition, the 2D lattice core layer structure with 12% infill density pattern also offers low stiffness and structural support to prevent early failure from deformation. The 3D-architectured device exhibits exceptional stretchability, minimal resistance variation, mechanical resilience, and electrical self-healing, which are favorable in active working scenarios. This series of work overcomes key limitations in wearable TEDs, demonstrated through powering wearable sensors, charging batteries, and illuminating LEDs by scavenging body heat at room temperature.

The third study addresses long-term wearing comfort and breathability at skin-device interfaces. Electrohydrodynamic (EHD) printing is employed to deposit a liquid metal-boron nitride-thermoplastic polyurethane (LM–BN–TPU) hybrid filler composite as a high-resolution fiber mat with lattice patterns designed to avoid occluding sweat pores. Despite the presence of air and moisture transport pathways, the EHD-printed interface achieves a through-plane thermal conductivity of 0.37 $W \cdot m^{-1} \cdot K^{-1}$. This layer also functions as a micropatterned heatsink when

integrated on the cold side of the devices. Skin compatibility is validated through water vapor transmission rates and a week-long attachment test on a forearm. The breathable TED generates 5.32 μW at equilibrium under an initial temperature gradient of 10 °C. Furthermore, a comprehensive recycling process recovers LM and BN fillers from the permeable interfaces, and LM fillers and TE pellets from the core layer, respectively. These components are reused to fabricate new TEDs, which exhibit thermoelectric performance comparable to the originals.

The fourth study develops recyclable liquid metal–vitrimer composites to address sustainability in flexible electronics. Vitrimer, a thermoset polymer with dynamic covalent bonds, combines the mechanical robustness of thermosets with the reprocessability of thermoplastics. At 50% LM volume fraction, the composite achieves a 6.53-fold increase in thermal conductivity while maintaining 137% failure strain, thermal stability above 360 °C, and electrical activation through mechanical sintering. Two distinct recycling strategies are demonstrated: (1) thermomechanical reprocessing, which enables circuit reconfiguration through consecutive fragmentation and reassembly; (2) chemical recycling, which recovers 94% of the LM filler to reuse it in new composites. Change in material properties during consecutive reprocessing and chemical interactions between the metallic filler and the polymer matrix are investigated to better understand the composites under repeated use. Collectively, by progressing from composite formulation and 3D device architecture to skin-compatible interfaces and sustainable end-of-life strategies, these four studies establish a body of knowledge for liquid metal composites and wearable thermoelectric devices.

Acknowledgements

I would like to begin by expressing my wholehearted gratitude to my thesis advisor, Prof. Mohammad H. Malakooti, for the opportunity to join the iMatter Lab at the University of Washington as a graduate student. His guidance and support throughout the journey have been invaluable. His attentive mentorship and clear direction ensured that I was never without guidance, and his influence has shaped my professional development. I am deeply thankful for all the thoughtful advice and encouragement.

I am also grateful to the members of my thesis committee, including Prof. Junlan Wang, Prof. Jie Xiao, and Prof. Karl F. Böhringer, for their time and insightful feedback. I would like to extend my appreciation to Dr. Christopher C. Bowland for his mentorship during my time at the Oak Ridge National Laboratory, where I received invaluable training and support.

I would like to thank collaborators and colleagues, especially Lijun Zhou and Ren-Mian Chin, for their academic and emotional support throughout the thesis process. Their friendship have been a lasting source of motivation.

Finally, I offer my deepest gratitude to my family. I am profoundly thankful to my wife, Sujung Kim, for her devoted support through both challenging and joyful times; to my mother, Sook-hee Choi, for her endless encouragement; and to my father, Heui-soo Han, for guiding me toward higher education. I am also thankful to Noah K. Han, whose presence has brought great joy to our family.

Table of contents

Table of Figures

List of Tables

Some sections or verbatim in this dissertation are reproduced with permission from the following published journal articles listed below.

- Y. Han, L.-E. Simonsen, M. H. Malakooti, Printing Liquid Metal Elastomer Composites for High-Performance Stretchable Thermoelectric Generators. *Adv. Energy Mater.* 12, 2201413 (2022).
- Y. Han, H. Tetik, M. H. Malakooti, 3D Soft Architectures for Stretchable Thermoelectric Wearables with Electrical Self-Healing and Damage Tolerance. *Adv. Mater.* 36, 2407073 (2024).
- Y. Han, S. S. Rohewal, S. Gupta, S. Paul, C. C. Bowland, and M. H. Malakooti, "Conductive Liquid Metal Vitrimer Composites for Reconfigurable and Recyclable Flexible Electronics." *Adv. Funct. Mater.* 35**,** e11119 (2025).
- Y. Han, C. S. Fernandes, E. Davis, and M. H. Malakooti, Electrohydrodynamic Printing of Liquid Metal Composites for Breathable Interfaces in Recyclable Thermoelectric Wearables. *ACS Appl. Mater. Interfaces.* Under Review.

Chapter 1: Introduction

1.1. Material for Wearable Devices

1.1.1 Intrinsically Soft Materials for On-Skin Electronics

Wearable devices refer to electronics that are designed to be worn on the human body,[1,2] including exoskeletons,[3] smart garments,[4,5] and skin-interfaced systems built on soft, stretchable substrates.[6–8] These electronics enable a wide range of applications, including continuous physiological monitoring, health assessment, and human–machine interfacing, by establishing direct or indirect interfaces with various body parts. Especially, on-skin electronics provide direct contact with the body that minimizes noise and motion artifacts.

In recent years, various stretchable electronics have been developed to meet the needs for on-skin wearable electronics such as compactness, flexibility, and skin-conformal form factors.[9] These electronics offer a promising solution that addresses the mechanical mismatch between traditional rigid electronics and soft curvilinear surfaces like human skin, because materials in those electronics (e.g., metals and inorganic semiconductors) cannot be conformally deformed. There are two main strategies to achieve stretchable electronics: stretchable structures and intrinsically stretchable materials.[10] Stretchable structures, such as serpentine, helical, or kirigami designs, employ geometric engineering that make originally rigid components stretchable. However, electronics based on these structural approaches often exhibit limitations, including stretchability that is constrained to predefined deformation modes or directions and the formation of microcracks under repeated mechanical loading. Furthermore, these structures often require encapsulation within soft substrates or elastomers to achieve a balance between flexibility and mechanical robustness. Consequently, the development of intrinsically soft materials is essential for enabling reliable, durable, and conformable wearable electronics.

1.1.2 Gallium-based Liquid Metal

Gallium-based liquid metals (LMs) are metal alloys that remain in a liquid state at room temperature (Figure 1.1a). Because of their fluidic nature, LM-based electronic systems can deform compliantly with soft substrates while maintaining metallic properties, including high thermal and electrical conductivities. In contrast, other conductive materials that are being studied for stretchable electronics either suffer from severe changes in conductivity under strain (e.g., particles and nanowires of copper, silver, and gold) or exhibit relatively low electrical and thermal conductivities (e.g., conductive polymers and ionic liquids).[11] Furthermore, unlike other

liquid metals such as mercury, rubidium, cesium, and francium, gallium-based LMs are non-toxic and exhibit excellent biocompatibility.[12,13] These attributes make them highly attractive for the development of stretchable and soft electronics.

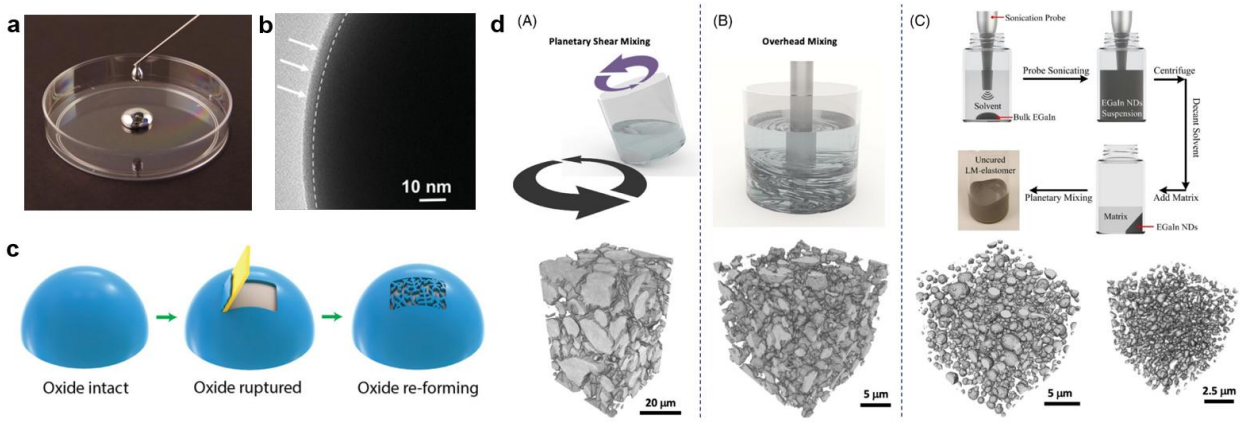

Figure 1.1 Gallium-based liquid metal and liquid metal composites: (a) A photograph of eutectic gallium-indium (EGaIn). (b) Transmission electron microscopy (TEM) of LM and its oxide surface.[14] Reproduced with permission from Wiley-VCH. © 2023 Wiley-VCH GmbH. (c) Instantaneous forming of oxide layer.[15] Reproduced with permission from Wiley-VCH. © 2024 Wiley-VCH GmbH. (d) Schematic of LM processing methods including planetary shear mixing (left), overhead emulsion mixing (center), and probe sonication (right).[16] Reproduced with permission from Wiley-VCH. © 2022 Wiley-VCH GmbH.

1.1.3 Liquid Metal Elastomer Composites

Dispersing functional fillers within the elastomer matrix is an effective strategy for synthesizing soft polymer composites for fabricating interconnects, thermal interfaces, substrates, or packaging materials in wearable electronics. Through appropriate filler selection and loading, these composites can be engineered to exhibit tailored thermal, electrical, and mechanical properties.[17–22] Among various fillers, eutectic-gallium-indium (EGaIn) is particularly attractive because of its high thermal conductivity (26.4 $W \cdot m^{-1} \cdot K^{-1}$), electrical conductivity (3.4×10^6 $S \cdot m^{-1}$),[23–28] and adjustable mechanical properties governed by particle size and morphology.[16,29,30] Additionally, its liquid state at room temperature minimizes the stiffening effect that is commonly associated with solid inclusions.[31] Typical solid inclusions, including graphene, silver, or nickel, adversely affect the mechanical properties of polymer composites by increasing the effective stiffness and reducing the elongation at break.[19] This embrittlement makes composites in previous studies that employed solid fillers unsuitable for wearable applications.[32,33]

Another unique feature of gallium-based LM is a passivating gallium oxide layer (1 – 5 nm in thickness) that surrounds the LM droplets (Figure 1.1b).[34,35] As shown in Figure 1.1c, the oxide

layer on bulk liquid metal can be ruptured by mechanical stress. The exposed liquid metal rapidly reoxidizes, stabilizing newly formed droplets and enabling progressive fragmentation into micro- and nanoscale LM particles.[15] As the particle size decreases, the surface-to-volume ratio increases, generating a larger fraction of oxide interface that enhances particle stability and makes further fragmentation more difficult. Because the oxide shell contributes significantly to the overall mechanical response of the inclusions, particle size strongly influences the resulting composite properties, including elastic modulus, thermal conductivity, and electrical conductivity.[36–40] Therefore, both particle size and filler volume fraction serve as key design parameters for liquid metal elastomer composites (LMECs).

Various mixing strategies can be utilized to break bulk LM and control the particle size (Figure 1.1d). Among them, shear-based processes, including planetary mixing and overhead emulsion mixing, are advantageous for their simplicity, scalability, and rapid processing, producing LM particles ranging from hundreds of nanometers to hundreds of micrometers. On the other hand, ultrasonication provides higher mechanical energy via acoustic cavitation, enabling both rapid downsizing and simultaneous surface functionalization with organic or inorganic materials.[41–43]

The mechanical properties of LMECs can be estimated by accounting for particle size and core-shell structure of gallium-based LM.[31,44] Figure 1.2a depicts predicted effective elastic moduli of LMECs with respect to the ratio of shell thickness to inclusion diameter. The result shows that as the ratio increases (i.e., LM particle size is reduced), the composites become stiffer due to greater influence of solid oxide layers. Thermal conductivity is another property that is being engineered.[45–47] As shown in Figure 1.2b, increasing the liquid metal volume fraction enhances the effective thermal conductivity because heat is transferred more efficiently through the conductive fillers than through the surrounding polymer matrix.[47] The increase in thermal conductivity becomes much larger when the LM concentration in the composites exceeds the percolation threshold, where densely packed LM fillers are no longer separated from each other in the polymer matrix. Figure 1.2c illustrates the trade-off between stretchability and thermal conductivity in polydimethylsiloxane (PDMS)-based LMECs, providing a design guideline for soft thermal interface materials (TIMs). At 50% filler volume fraction, the thermal conductivity exceeds that of the base polymer by more than six times. Furthermore, thermal conductivity can increase by as much as fifty-fold (9.8 ± 0.8 $W \cdot m^{-1} \cdot K^{-1}$hen the liquid metal inclusions are aligned or elongated along the direction of heat flow (Figure 1.2d and e).[23] Under mechanical strain, the

liquid inclusions deform together with the elastomer matrix, creating elongated conductive pathways that facilitate heat transport. This effect has also been demonstrated through infrared thermography, where composites containing rod-shaped liquid metal inclusions exhibited superior heat transfer compared with those containing spherical inclusions (Figure 1.2f).[48]

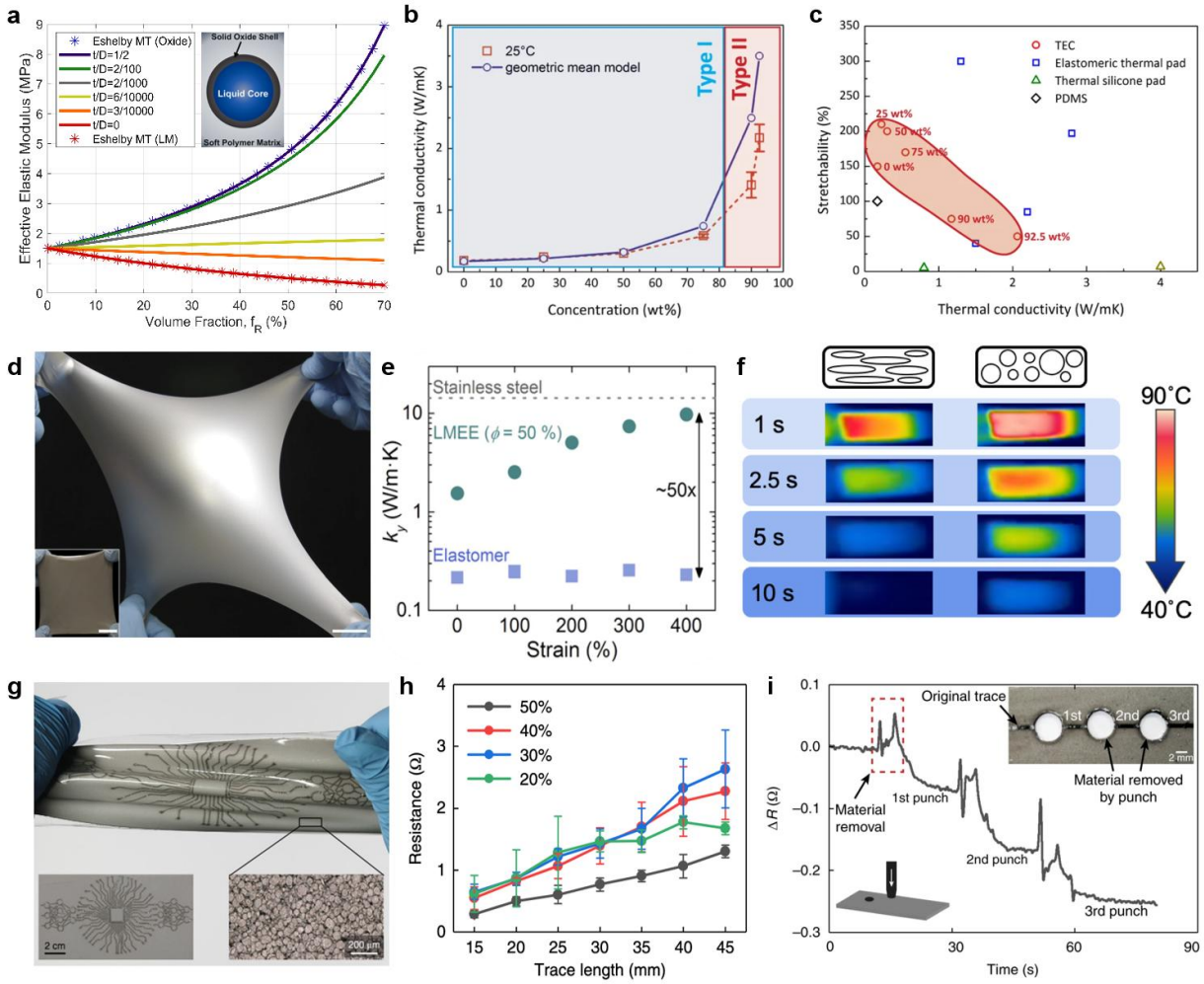

Figure 1.2. Multifunctionality of LMECs: (a) Effective elastic modulus of LMEC predicted by double inclusion model for different LM volume fractions and oxide shell to diameter ratio.[31] Reproduced with permission from Elsevier. © 2021 Elsevier Ltd. (b) LMEC thermal conductivity with varying LM concentration. Percolation threshold resides between Type I and Type II region.[47] Reproduced with permission from Springer Nature. © 2015 Springer Nature. (c) Stretchability of thermal elastomer composites (TEC) which is comprised of liquid metal fillers and PDMS with respect to thermal conductivity compared to off-the-shelf products.[47] Reproduced with permission from Springer Nature. © 2015 Springer Nature. (d) Photographs of LMECs under strain.[23] (e) Measured thermal conductivity of liquid metal embedded elastomer under strain.[23] © 2017 National Academy of Sciences. (f) Infrared thermography of LMECs with elongated LM and spherical LM.[48] Reproduced with permission from the American Chemical Society. © 2025 American Chemical Society. (g) Photographs of LMEC circuit activated by embossing.[27] (h) Measured electrical resistance of LMEC conductor during punching the trace.[27] Reproduced with permission from Springer Nature. © 2018 Springer Nature. (i) Electrical self-healing of LMEC electrical circuit.[27] Reproduced with permission from Springer Nature. © 2018 Springer Nature.

The electrical conductivity of LMECs can also be engineered through an activation process and tailored LM particle sizes.[49–51] As-prepared LMECs with an LM volume fraction below percolating threshold (~65%) are typically insulating because the passivating oxide shells surrounding the particles prevent electron transport between neighboring inclusions. However, with electrical activation methods, including mechanical sintering or laser welding, can rupture the oxide layers and establish conductive percolating networks throughout the polymer matrix. This activation process enables the selective patterning of conductive pathways within LMECs, allowing their use as stretchable interconnects and electronic circuits. One study studied the electrical conductivity of stretchable LMEC circuits activated through embossing (Figure 1.2g).[27] Similar to thermal conductivity, electrical conductivity increases with an increase in filler concentration as the conductive pathways within the composite increases (Figure 1.2h). Moreover, the activated LM circuits show self-healing behavior (Figure 1.2i), maintaining electrical conductivity even after being damaged. This is because gallium oxide forms instantaneously after the damage, and the LM network reconfigures to form alternative conductive pathways. In contrast, electrical activation can be prevented with substantially small LM inclusions.[38] When the particle diameter is reduced to a few micrometers or below, the influence of the oxide shell becomes dominant because of the increased surface-to-volume ratio. Consequently, substantially greater mechanical stress is required to rupture the particles and establish conductive pathways, causing the composite to remain electrically insulating. Therefore, LM particle size is the critical parameter for controlling the transition between electrically conductive and insulating LMECs.

As discussed above, the processing conditions used to fabricate LMECs are intimately linked to their resulting material properties. By controlling liquid metal particle size, alignment, morphology, and percolation behavior, the thermal, mechanical, and electrical characteristics of the composites can be systematically engineered. This combination of tunability, multifunctionality, and mechanical compliance has driven growing interest in liquid metal composites for soft and wearable electronics, as evidenced by the increasing number of related journal publications shown in Figure 1.3.

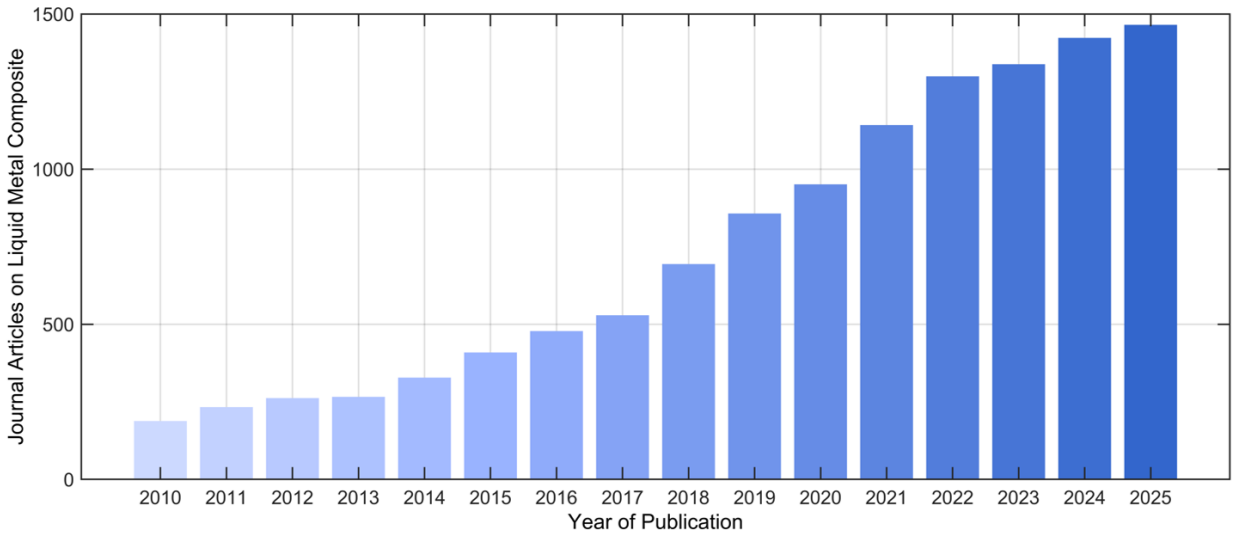

Figure 1.3. Published journal articles related to liquid metal composite between 2010 and 2025. Data collected from Web of Science.

1.2. Energy Demands for Wearable Electronics

1.2.1 Approaches in Wearable Energy Harvesting

Conventional portable devices rely predominantly on rechargeable batteries powered via wired charging ports or inductive charging. However, such approaches are not well-suited for conformable on-skin wearables as rigid charging interfaces and bulky batteries compromise mechanical compliance, while frequent recharging cycles pose inconvenience. To address the bottleneck in power sources, research efforts are directed toward self-sustainable energy harvesting strategies that can continuously scavenge ambient energy around the human body. Several mechanisms have been explored for wearable energy harvesting, each offering unique advantages and constraints. Radio frequency (RF) energy harvesting utilizes antennas to capture ambient RF signals and rectification circuits to convert them into usable direct current (Figure 1.4a).[52,53] However, RF signals inherently exhibit low power density, and maintaining antenna resonance under mechanical deformation remains a major challenge for flexible circuits. Photovoltaic energy harvesting, particularly through organic photovoltaics or thin-film solar cells, enables the utilization of abundant solar energy (Figure 1.4b).[54] Nevertheless, its operation depends strongly on environmental conditions, with performance restricted during nighttime or indoor use, while long-term reliability may be affected by sweat, abrasion, and environmental exposure. On the other hand, piezoelectric materials convert periodic mechanical deformation into electrical energy through changes in the materials' internal arrangement, as demonstrated in

footwear for energy harvesting during walking (Figure 1.4c).[55,56] Yet, their output is strongly dependent on the frequency and amplitude of external stimuli, limiting stable and continuous operation. Similarly, triboelectric nanogenerators rely on periodic mechanical contact and separation between dissimilar materials to generate pulsed alternating current (Figure 1.4d).[57–59] Although triboelectric systems provide high output voltages, they are susceptible to mechanical wear at contact interfaces and exhibit high output impedance, complicating energy storage and conversion. The presented mechanisms suffer from intrinsic challenges that restrict them from being reliable and continuous power sources in wearable applications.

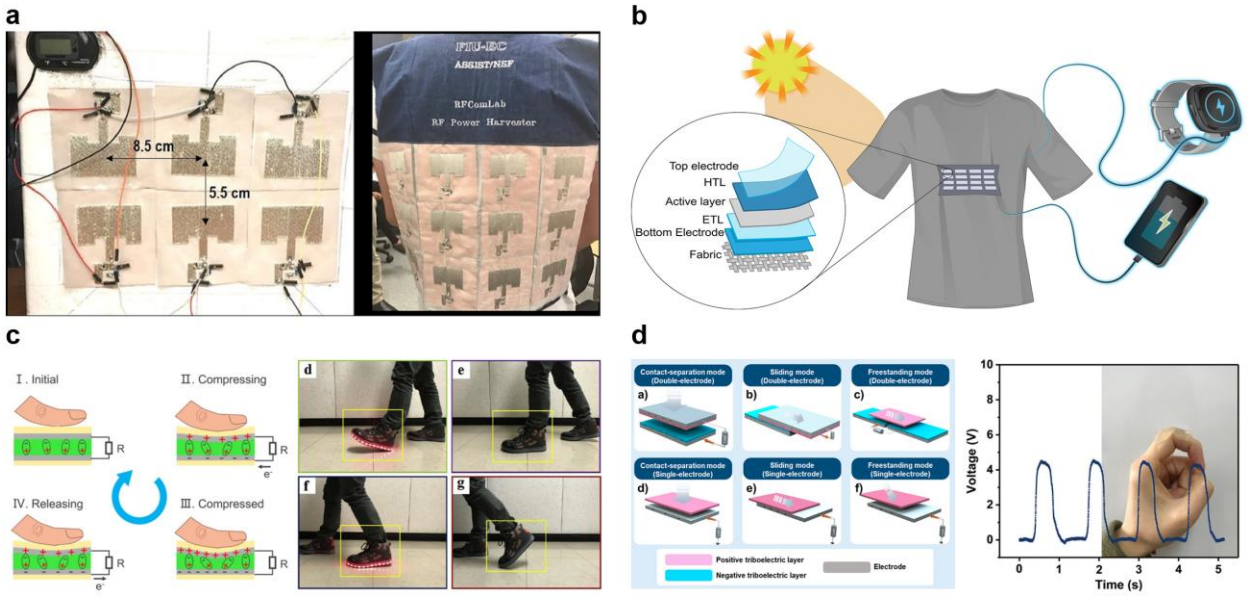

Figure 1.4. Various energy harvesting strategies: (a) Rectenna system on cloth for wireless energy harvesting.[53] Reproduced with permission from IEEE. © 2023 IEEE. (b) Schematic of textile solar cells on cloth.[54] Reproduced with license under CC BY 4.0. (c) Piezoelectric energy harvesting system.[55,56] Reproduced with license under CC BY 4.0. and permission from Elsevier. © 2019 Elsevier Ltd. (d) Triboelectric energy harvesting system.[57,59] Reproduced with permission from the American Chemical Society. © 2021 American Chemical Society and Elsevier. © 2020 Elsevier Ltd.

1.2.2 Thermoelectric Devices

Thermoelectric devices (TEDs) reversibly convert heat and electricity, enabling both power generation and thermal modulation in noise-free, vibration-free, and prolonged operations.[60,61] This energy conversion makes them favorable in wearable electronics where they can harvest body heat to power skin-interfaced electronics[62,63] or induce thermal sensation for personalized thermoregulation.[64–66] Especially in energy harvesting, TEDs operate continuously by utilizing a temperature gradient across thermoelectric (TE) materials via the Seebeck effect.[67] The heat flow

and harvested power of the thermoelectric semiconductors within a TED can be expressed by the following equations.[68]

$$Q_{TE} = \frac{k_{TE} \cdot A_{TE}}{l_{TE}} \Delta T_{TE} = \frac{\Delta T_{TE}}{R_{TE}} \quad (1)$$

$$P = \eta \cdot Q_{TE} \approx \frac{\eta_0(zT) \cdot \Delta T_{TE}}{T_H} \cdot Q_{TE} = \frac{\eta_0(zT)}{T_H \cdot R_{TE}} \cdot \Delta T_{TE}^2 \quad (2)$$

As in Equation (1), the total heat flow through TE semiconductor (Q_{TE}) is defined as the temperature difference across the semiconductor (ΔT_{TE}) multiplied by thermal conductivity (k_{TE}) and area (A_{TE}) of TE pellets and divided by the pellet length (l_{TE}) according to Fourier's law of heat conduction, which can be simplified by introducing the thermal resistance of the TE material (R_{TE}). From this one-dimensional heat transfer, TE semiconductors generate power (P), which is the product of energy conversion efficiency (η) and Q_{TE}. The efficiency η can be expressed in terms of the intrinsic conversion efficiency (η_0) that depends on the semiconductor's figure of merit (zT),[69] the hot side temperature (T_H), and ΔT_{TE}. The Equation (2) shows that increasing ΔT_{TE} is the critical factor that determines the power generation, whereas other factors are predetermined by the working conditions or material choice.

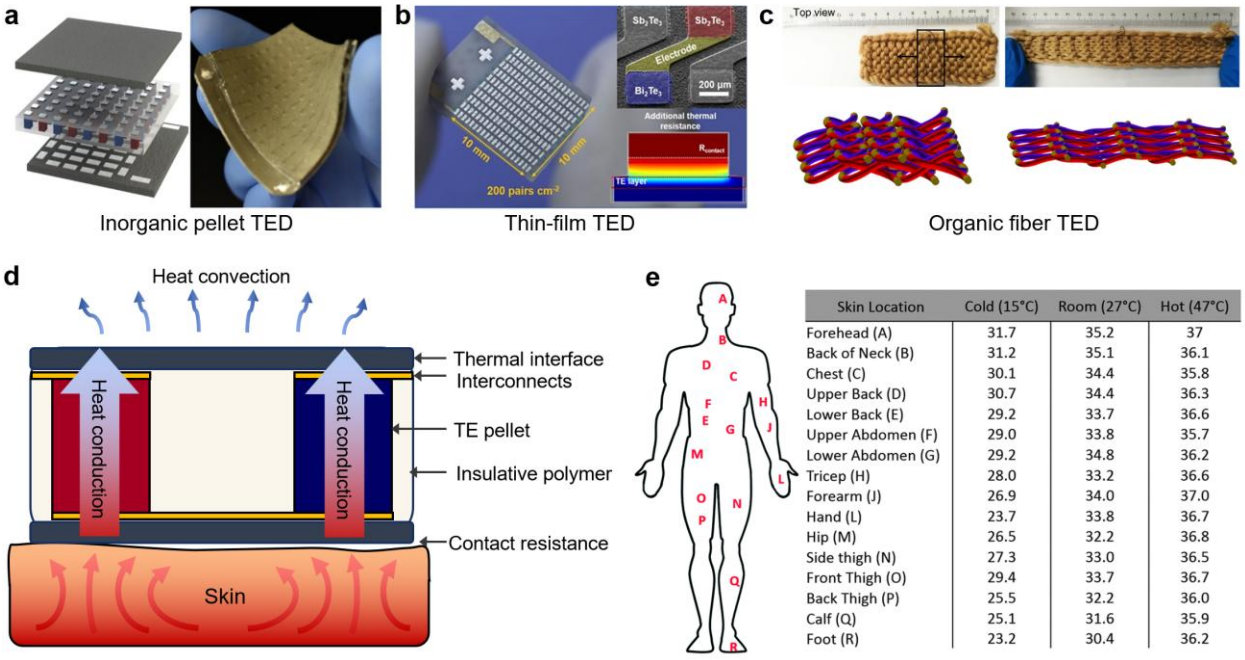

Skin Location	Cold (15°C)	Room (27°C)	Hot (47°C)
Forehead (A)	31.7	35.2	37
Back of Neck (B)	31.2	35.1	36.1
Chest (C)	30.1	34.4	35.8
Upper Back (D)	30.7	34.4	36.3
Lower Back (E)	29.2	33.7	36.6
Upper Abdomen (F)	29.0	33.8	35.7
Lower Abdomen (G)	29.2	34.8	36.2
Tricep (H)	28.0	33.2	36.6
Forearm (J)	26.9	34.0	37.0
Hand (L)	23.7	33.8	36.7
Hip (M)	26.5	32.2	36.8
Side thigh (N)	27.3	33.0	36.5
Front Thigh (O)	29.4	33.7	36.7
Back Thigh (P)	25.5	32.2	36.0
Calf (Q)	25.1	31.6	35.9
Foot (R)	23.2	30.4	36.2

Figure 1.5. Different thermoelectric device types for on-skin thermoelectric energy harvesting: (a) TED with inorganic TE pellets arranged in π-shaped configuration.[70] Reproduced with permission from the American Chemical Society. © 2020 American Chemical Society. (b) Thin-film-based TED.[71] Reproduced with permission from Elsevier. © 2020 Elsevier Ltd. (c) Organic fiber-based TED.[72] Reproduced with permission from Springer Nature. © 2020 Springer Nature. (d) Schematic of heat transfer in TED with embedded inorganic TE pellets attached to the skin. (e) Reported human skin temperatures for different points on the body at varying ambient temperatures.[73] Reproduced with permission from the Royal Society of Chemistry.

Embedding inorganic TE semiconductors into silicon elastomer is an effective strategy for fabricating stretchable TEDs (Figure 1.5a).[74–78] By serially arranging p-type and n-type TE pellets in a π-shaped configuration within the encapsulating elastomer and thermal interface materials, such devices achieve mechanical flexibility for low contact resistances while embodying high energy conversion efficiency of inorganic TE materials. Moreover, this structure facilitates a larger ΔT_{TE} for thermoelectric performance than other types of thermoelectric devices such as thin-film[79,80] or fiber-based[81,82] devices (Figure 1.5b and c). Three device layers exist in this design as shown in Figure 1.5d: (1) a hot side thermal interface that is in contact with the heat source; (2) a core layer that has TE pellets and the insulating elastomer; (3) a cold side thermal interface that dissipate heat to the ambient. Assuming the device is in contact with the human body as the heat source (Figure 1.5e), TED's thermal resistance can be expressed as follows.[83,84]

$$R_{TED} = R_{Contact} + R_{TIM,H} + R_{Core} + R_{TIM,C} \quad (3)$$

$$R_{Core} = \frac{R_{TE} \cdot R_{insulant}}{R_{TE} + R_{insulant}} \quad (4)$$

While thermal resistance is inversely proportional to thermal conductance, the thermal resistance of the TED (R_{TED}) is the sum of the thermal contact resistance ($R_{Contact}$), thermal resistance of hot side TIM ($R_{TIM,\ H}$), thermal resistance of core layer (R_{Core}), and thermal resistance of cold side TIM ($R_{TIM,\ C}$). In the core layer, the TE pellets are embedded in the insulating materials, so R_{Core} can be expressed as the parallel combination of the thermal resistances of the TE components (R_{TE}) and the insulating matrix ($R_{insulant}$).

Conformal contact with heat sources for conductive heat transfer is essential to minimize $R_{Contact}$, especially in wearable applications.[85,86] Poor contact at the skin–device interface increases $R_{Contact}$ that significantly suppresses ΔT_{TE} and thermoelectric power generation. This is shown in previous studies that stiff thermal interfaces could not harvest body heat effectively, even when highly conductive metallic or carbon-based materials were employed as fillers in composites.[73,87] This limitation underscores the need for soft, conformal thermal interface materials that can accommodate skin topography and maintain efficient heat transfer. With this design strategy, an early study embedded bismuth telluride (Bi_2Te_3) pellets within PDMS and serially connected the TE pellets with LM.[76] The combination of the soft encapsulation and the LM interconnects enabled the thermoelectric generator to remain flexible despite the rigidity of the TE pellets, allowing for conformal contact with the skin. However, the harvested power output was insufficient for practical use, primarily due to the limited heat transfer capability of PDMS interfaces. Their thermal interface was over 1 mm thick and had a low thermal conductivity (0.19 $W \cdot m^{-1} \cdot K^{-1}$), leading to a significant thermal resistance. To successfully transfer heat to the TE semiconductors, the interface must be not only compliant but also thermally conductive. This inefficiency is demonstrated in another study that used Ecoflex 00-30 as TIM in their stretchable TED.[77] Their encapsulating polymer shows a stiffness of 70 kPa, which is in the same range with the human skin, and has an excellent failure strain of ~900%. Although the authors ensured low contact resistance from the extremely soft interface, its low thermal conductivity limited the output voltage below 30 mV from the body heat harvesting. The temperature gradient across TE pellets within the device, combined with the heat source temperature (T_{hs}) and the ambient temperature ($T_{ambient}$), reveals the importance of thermal resistance in each layer:

$$\Delta T_{TE} = (T_{hs} - T_{ambient}) \cdot \frac{R_{Core}}{R_{TED}} = \frac{(T_{hs} - T_{ambient})}{\left(R_{Contact} + R_{TIM,H} + R_{TIM,C}\right) \cdot \left(\frac{1}{R_{TE}} + \frac{1}{R_{insulant}}\right) + 1} \quad (5)$$

The Equation (5) shows that minimizing $R_{Contact}$, $R_{TIM,\,H}$, and $R_{TIM,\,C}$, and maintaining high R_{TE}, and $R_{insulant}$ increases ΔT_{TE}, thereby improving thermoelectric power generation, as expressed in Equation (2). Especially, modifying $R_{TIM,\,H}$, and $R_{TIM,\,C}$, or $R_{insulant}$ is achievable through synthesizing thermally conductive elastomer composites.

1.2.3 Thermoelectric Devices with Liquid Metal Elastomer Composite Interfaces

The multifunctionality of LMECs is advantageous in inorganic TE pellet-based thermoelectric devices. A pioneering study that used LMEC as a thermal interface to encapsulate off-the-shelf TEDs (Figure 1.6a).[29] It is revealed that having LMEC interface minimally affects thermoelectric performance compared with the device without any interface due to conformal contact and high thermal conductivity (Figure 1.6b). Later, another study demonstrated a synthesis of liquid metal embedded elastomer, in which liquid metal particles were dispersed within a PDMS matrix to increase the composite's thermal conductivity to 1.6 $W \cdot m^{-1} \cdot K^{-1}$ (Figure 1.6c).[70] When integrated into stretchable TEDs, it could achieve a power density of 86.6 $\mu W \cdot cm^{-2}$ under a temperature gradient of 60 °C. The inherent stretchability of the polymer matrix allowed the device to be conformally wrapped around the wrist (Figure 1.6d). Although the highly conductive elastomer composite enhanced thermoelectric power generation, energy conversion efficiency at low temperature gradients was insufficient. Also, their manufacturing technique was based on labor-intensive manual fabrication, limiting the scalability and advanced device architecture while increasing the chance of defects. Furthermore, the use of large liquid metal particles in the interface layer introduces the risk of unintended electrical activation due to mechanical damage such as scratching during operation. To mitigate this issue, a different study employed nanoscale LM particles, which suppressed unwanted electrical percolation while maintaining comparable thermal conductivity (Figure 1.6e).[38] However, the trade-off was a poor flexibility due to increased stiffness and the absence of structural support. Incorporating a secondary conductive filler into the LMECs can further improve the composites' thermal conductivity.[19,21] One study embedded graphene nanoparticles in LMEC that increased thermal conductivity by 50% as shown in Figure 1.6f.[88] The device incorporating this thermal interface material generated 0.1

$\mu W \cdot cm^{-2} \cdot K^{-2}$ of normalized power density (Figure 1.6g). However, even with the improved thermal conductivity at the interface and higher aspect-ratio TE legs, the harvested power was still insufficient to be implemented as a standalone wearable power source.

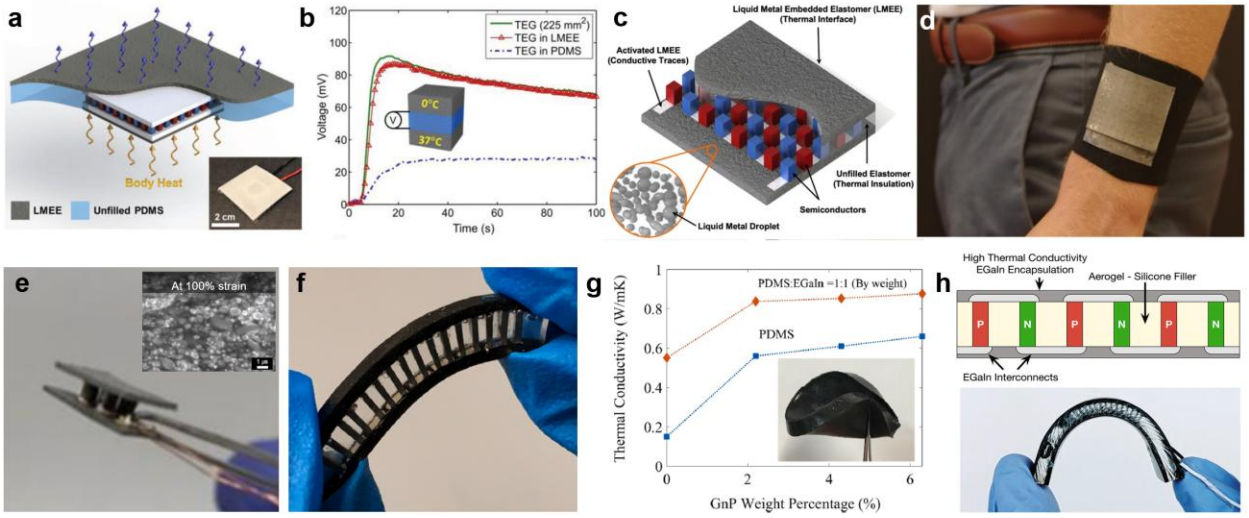

Figure 1.6. Soft TEDs with LMEC interfaces: (a) Images of commercial TED being encapsulated with liquid metal embedded elastomer interfaces.[29] Reproduced with permission from Wiley-VCH. © 2019 Wiley-VCH GmbH. (b) Output voltage from commercial TEDs without polymer interface, or with PDMS or liquid metal embedded elastomer interfaces.[29] Reproduced with permission from Wiley-VCH. © 2019 Wiley-VCH GmbH. (c) A schematic of soft TED with LMEC layers for both electrical circuit and heat transfer.[70] Reproduced with permission from the American Chemical Society. © 2020 American Chemical Society. (d) A photograph soft TED worn on wrist.[70] Reproduced with permission from the American Chemical Society. © 2020 American Chemical Society. (e) A thermoelectric unit with LMEC interfaces with nanosized particles.[38] Reproduced with permission from Wiley-VCH. © 2021 Wiley-VCH GmbH. (f) A photograph of flexible TED with LM–graphene polymer composite interfaces.[88] Reproduced with permission from Elsevier. © 2020 Elsevier Ltd. (g) Thermal conductivity of PDMS and LM–PDMS composite with varying graphene nanoparticle contents.[88] permission from Elsevier. © 2020 Elsevier Ltd. (h) Flexible TED with LMEC interfaces and aerogel–PDMS insulation composites.[84] Reproduced with license under CC BY 4.0.

Alternatively, embedding low thermal conductivity fillers or introducing porosity in the insulation layer increase $R_{insulant}$ for thermal insulation layer. One study mixed aerogel particulate with PDMS matrix to reduce the thermal conductivity of the core layer polymer by up to 50%, resulting in a two-fold increase in power density (Figure 1.6h).[84] Another study used granule-sized sugar as a sacrificial template in PDMS to create a porous insulation layer with a thermal conductivity of 0.08 $W \cdot m^{-1} \cdot K^{-1}$ and achieving a 23% increase in power density.[89] However, these approaches have limitations, including significantly compromised strain at failure below 40% from the solid fillers, as well as the fabrication complexity in template-based phase separation processes.

While the challenges in wearable TEDs must be addressed from interconnected aspects, including materials, manufacturing processes, and device architecture, previous studies have focused on only a narrow subset of these. This fragmented approach has limited comprehensive understanding and improvement of the field. Importantly, computational modeling and simulation have been largely absent in guiding device design, even though key performance metrics, including heat transfer, thermoelectric output, and mechanical compliance are strongly governed by design parameters. Therefore, analytical modeling and simulation must precede fabrication to inform device design, which is coupled with material processability and manufacturing techniques. As a result of these compounded challenges, highly efficient stretchable TEDs have yet to be realized.

1.3. Challenges and Breakthroughs

1.3.1 3D-Printed Device Structures and Additive Manufacturing

Insufficient power generation is the critical challenge in wearable TEDs. Although improving energy conversion efficiency of TE semiconductors is the most straightforward breakthrough, structural design and advanced packaging are also effective ways to enhance device performance.[90] Most flexible TEDs have been made with simple structures with traditional fabrication techniques such as casting,[91,92] but there have been few efforts to employ 3D device structures that enhance device performance.[93–95] One study fabricated a string of thermoelectric semiconductors with helical structures, improving structural robustness under strain (Figure 1.7a).[93] Another study implemented a Lego-like architecture that exposes long thermoelectric legs to maintain a large temperature gradient from the skin (Figure 1.7b).[95] These efforts demonstrated three-dimensional architectures that enhanced device performance, but their design flexibility remains limited as the underlying fabrication processes rely on conventional manufacturing methods.

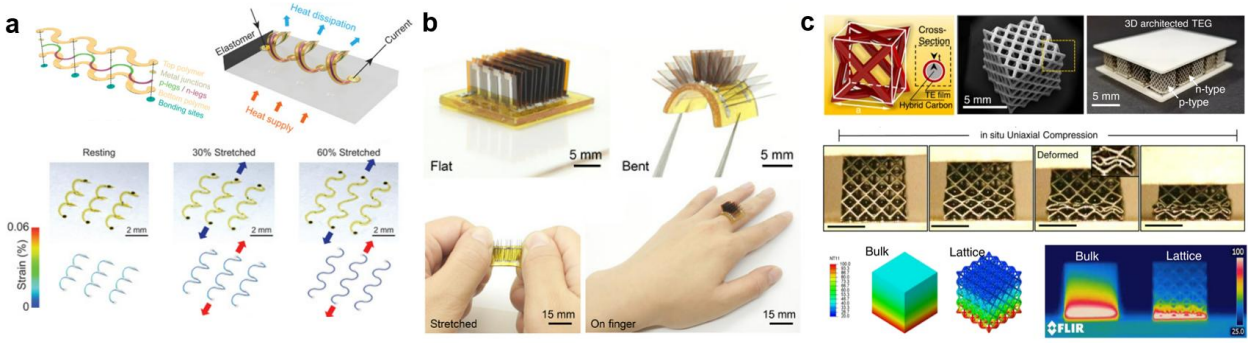

Figure 1.7. 3D Thermoelectric device structures: (a) Schematics and strain simulations of helical thermoelectric coils.[93] Licensed under CC BY-NC 4.0. (b) Photographs of thermoelectric devices with exposed TE pairs.[95] Licensed under CC BY-NC 4.0 (c) 3D structured thermoelectric legs and a device.[96] Reproduced with license under CC BY 4.0.

Additive manufacturing, commonly referred to as 3D printing, is a fabrication technology in which objects are constructed layer by layer.[97,98] In contrast to conventional subtractive manufacturing methods, additive manufacturing enables customizable and complex geometries with high spatial precision for device fabrication.[99] One study showed printed cellular lattice structures using a digital light projection method and deposited thermoelectric materials onto the prepared polymer lattices (Figure 1.7c).[96] Although their bulky device was not stretchable and incompatible for wearable applications, this work demonstrated the potential of additive manufacturing in stretchable thermoelectric devices.

Soft matter 3D printing enables exploration of novel 3D device structures that are intrinsically compliant and mechanically adaptive.[100] Direct ink writing (DIW), one of the 3D printing techniques that extrudes viscoelastic inks through nozzles under controlled pressure, is a simple and effective way to print liquid metal composites (Figure 1.8a and b).[101–103] Embedding LM droplets into a polymer matrix modifies the rheology, including surface tension and viscosity, thereby allowing the additive manufacturing (Figure 1.8c).[28] In contrast, extruding pure LM is challenging due to the high surface tension of LM (624 $mN \cdot m^{-1}$ for EGaIn at room temperature) and water-like viscosity (1.99 $mPa \cdot s$).[104–106] Moreover, the shear stresses experienced during extrusion through a narrow nozzle can deform and elongate liquid metal droplets, leading to anisotropic particle morphologies. This structural anisotropy can introduce directional properties, such as enhanced thermal and electrical conductivity along the alignment direction,[107] which is also demonstrated in elongated fillers in stretched LMECs.

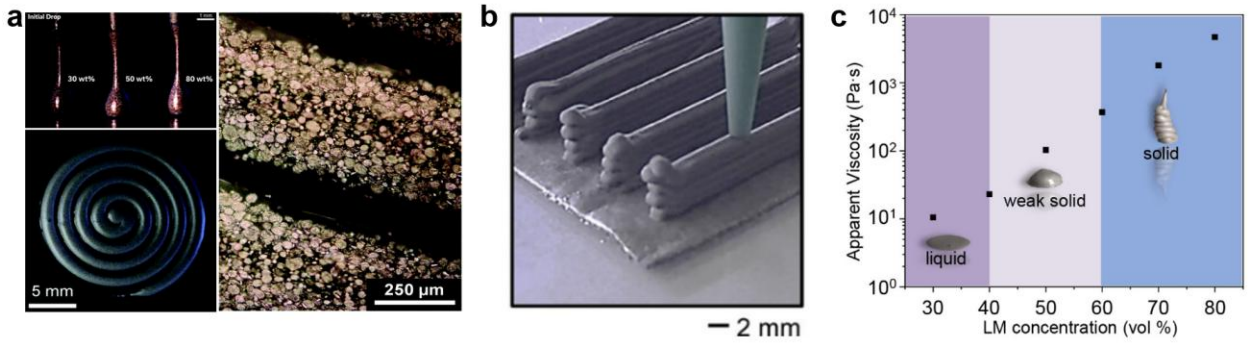

Figure 1.8. DIW printing of LMECs. (a) Images of LMECs extruded from the nozzle.[108] Reproduced with permission from the Royal Society of Chemistry. (b) DIW printed LMECs with vertically stacked lines.[109] Reproduced with license under CC BY 4.0. (c) Increase in viscosity depending on the volume fraction of LM.[103] Reproduced with permission from the American Chemical Society. © 2022 American Chemical Society.

Electrohydrodynamic (EHD) printing is another 3D printing technique capable of achieving higher resolution patterning than DIW. This technique applies voltage at the printing nozzle to drive ink jetting onto a grounded substrate, resulting in the formation of a Taylor cone (Figure 1.9a). This process is highly sensitive to processing parameters, including nozzle-to-substrate standoff distance, applied electric potential, nozzle diameter, and ink properties such as dielectric constant and surface tension. Jet stability strongly depends on the nozzle-to-substrate spacing. When the distance is large (>1 mm), the electric field becomes insufficiently focused, leading to jet instabilities such as whipping or dripping (Figure 1.9b). In contrast, when the nozzle is positioned too close to the substrate, the electric field intensity may exceed the dielectric breakdown strength of air or the surrounding medium, resulting in electrical discharge and arc formation instead of stable jetting. Applied voltage is another critical parameter. Insufficient voltage produces weak electrostatic forces and unstable jetting modes such as dripping or pulsation (Figure 1.9c), whereas excessive voltage can lead to multi-jet formation with poor directionality. Given the interdependence of these parameters, systematic optimization is essential for each material and application. Various functional materials, including silver nanowires,[110] conducting polymers,[111,112] and LM–polymer composites,[113] have been employed in EHD printing. One study demonstrated high-resolution patterning of LMEC conductors, overcoming limitations in patterning precision inherent to other 3D printing methods (Figure 1.9d).[113] Using a composite ink consisting of thermoplastic polyurethane (TPU) and EGaIn particles, the authors optimized processing conditions to achieve high-resolution LMEC interconnects with widths ranging from 4 to 70 μm. One remaining challenge in EHD printing of

LMECs is achieving sufficient thermal conductivity while avoiding unintended electrical conduction. During jetting, the conductive LM fillers are confined within a narrow polymer matrix, promoting inter-filler contact. This facilitates electrical conduction at high filler volume fractions, while the thermal conductivity at low volume fractions remains insufficient for use in thermal interface applications.

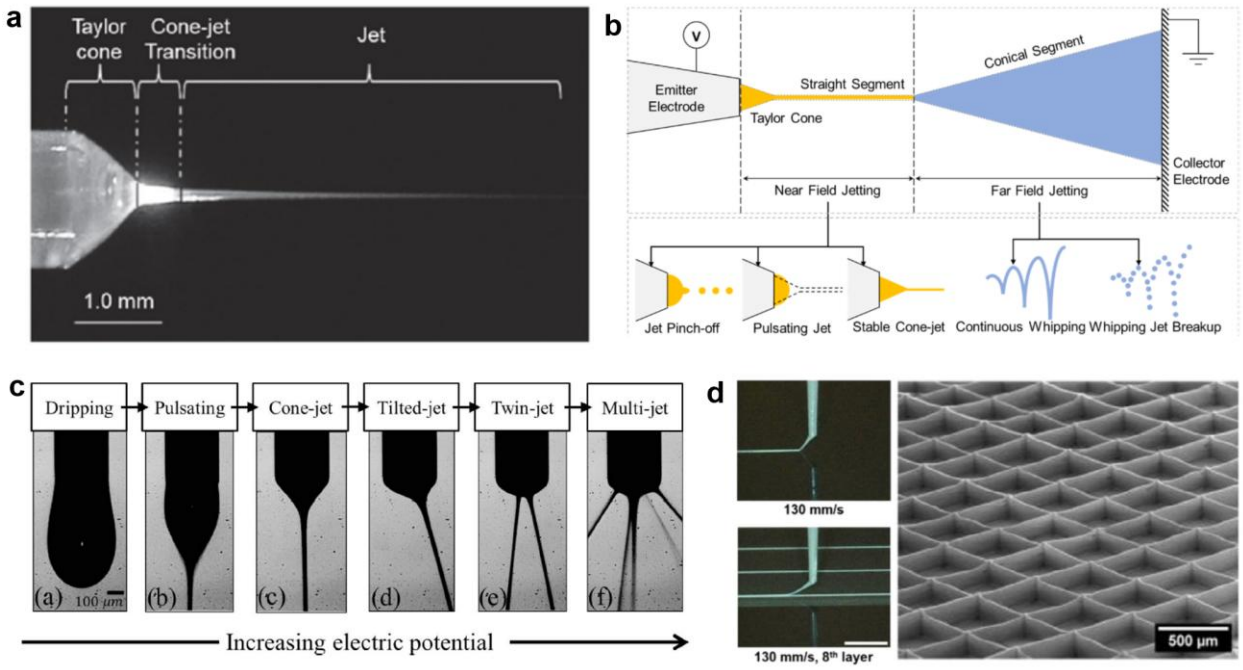

Figure 1.9. EHD printing of polymer composites. (a) An image of Taylor cone, the cone-jet transition zone, and the electrically driven jet.[114] Licensed under CC BY-NC-ND 4.0. (b) Schematics of electrified jet development and electrohydrodynamic behavior.[115] Reproduced with permission from Elsevier. © 2013 Elsevier Ltd. (c) jetting modes with respect to electric potentials.[116] Reproduced with permission from the American Chemical Society. © 2013 American Chemical Society. (d) Images showing EHD printing of LM–polymer microfibers.[113] Reproduced with permission from Wiley-VCH. © 2025 Wiley-VCH GmbH.

1.3.2 Permeable and Thermally Conductive Interfaces

The skin–electronics interface is a subsystem of wearable electronics, serving as the contact surface between electronic components and the human body. This interface mediates both electrical-mechanical-thermal coupling and user comfort.[117,118] A challenge that lies at this interface is the obstruction of sweat pores. Human skin contains approximately 2–4 million eccrine sweat glands with pore diameters ranging from 88 μm to over 220 μm (Figure 1.10a). Especially, the chest, shoulder, and arm have 91–104 eccrine glands per cm^2, where their sweat secretion regulates core body temperature through perspiration.[119,120] When wearable devices occlude these pores, sweat accumulates beneath the device, elevating local skin temperature,

promoting bacterial growth, and causing irritation or dermatitis that disturbs wearing comfort (Figure 1.10b).[121,122] As wearable devices trend toward continuous and long-term applications, it is essential to resolve this occlusion problem. A permeable skin–electronics interface that allows air and sweat to pass through the device is therefore a prerequisite for ergonomic, skin-compatible wearable systems. To achieve this, each contact region must be smaller than sweat pores (<80 μm), and the water vapor transmission rate must be higher than the skin respiration rate (>5–10 $g \cdot m^{-2} \cdot h^{-1}$).[123]

Heat transfer efficiency is another major consideration in skin-interfacing electronics.[124,125] In wearable devices, conventional thermal management approaches used in industrial hardware, such as metallic heatsinks, are impractical. As a result, thermal interfaces become the primary pathway for heat conduction. Designing a compliant thermal interface is therefore important to prevent heat accumulation and maintain user comfort. Despite these dual requirements, previously reported skin–electronics interfaces have struggled to address both simultaneously: thermally conductive designs tend to be rigid or impermeable, whereas breathable interfaces typically suffer from low thermal conductivity or high thermal contact resistance.

This challenge of simultaneously achieving breathability and efficient heat transfer becomes particularly significant in wearable thermoelectric devices. Unlike conventional TEDs, on-skin TEDs must be breathable to avoid discomfort during continuous use while being conformally attached to human skin. However, having air pathways in thermal interfaces inevitably results in decreased thermal conductivity due to the low thermal conductivity of the air and increased contact resistance from multiple contact locations. This is detrimental in thermoelectric performance as verified in Equation (5). Therefore, achieving a thermal interface that is both permeable and thermally conductive is critical in on-skin TEDs.

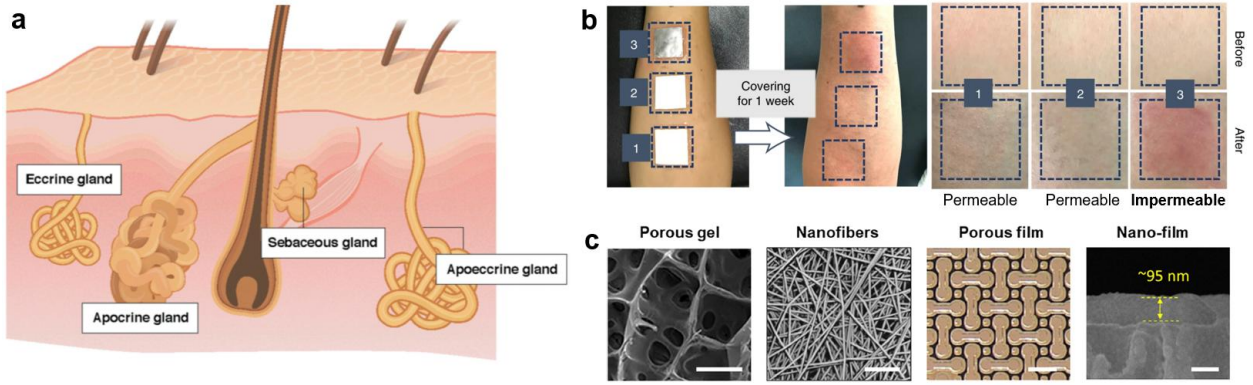

Figure 1.10 Importance of permeability in skin-electronics interfaces: (a) Different sweat glands on human skin.[119] Reproduced with permission from Taylor & Francis. © 2019 Taylor & Francis. (b) Images showing skin irritation tests of different polymer composites with and without permeability.[122] Reproduced with permission from Springer Nature. © 2021 Springer Nature. (c) Different approaches to realize permeable skin interfaces.[118] Reproduced with permission from the American Chemical Society. © 2024 American Chemical Society.

Several strategies have been reported to fabricate permeable interfaces for bio-integrated systems (Figure 1.10c),[118,126] but each approach brings its own challenges. For example, template-assisted porous structures (e.g., sugar,[127,128] salt,[129] or oil[130]) have inherently high porosity (>70%) which reduces bulk thermal conductivity, as the air-filled pores act as thermal insulators. Additionally, incomplete removal of templates may compromise biocompatibility and structural stability. Phase separation is another method for fabricating porous structures that utilizes a polymer blend with two or more distinct phases where one of the phases will be removed to yield a porous polymer network.[131–136] But challenges remain in controlling uniformity and reproducibility. Electrospinning, which shares the same physics as EHD printing, is an effective technique for fabricating permeable fiber mats by applying a high-voltage electric field to a polymer solution. The electric field applied to the ink induces a solution jetting that undergoes elongation, solvent evaporation, and solidification to form ultrafine fibers with diameters ranging from tens of nanometers to a few micrometers.[137–140] When collected into mats, these fibers create a nonwoven network with high porosity, large surface-to-volume ratio, and interconnected pores, allowing vapor and air permeability. However, electrospun mats have poor contact between fibers, which results in high contact resistance for heat conduction.[141] One study reported a TED with electrospun graphene nanoplatelet–PDMS and boron nitride–PDMS composite interfaces that generated a reduced power density of 1.026 $mW \cdot cm^{-2}$ at ΔT of 40 °C, while the same device architecture with a bulk PDMS interface could generate 1.683 $mW \cdot cm^{-2}$ at the same temperature gradient.[66] This is because of the inevitably low through-plane thermal conductivity (0.1 $W \cdot m^{-}$

$^{1}\cdot K^{-1}$) of electrospun fiber mat interfaces even with highly conductive fillers, compared to flat PDMS film with a thermal conductivity of 0.2 $W\cdot m^{-1}\cdot K^{-1}$. A two-dimensional micro-patterning, such as soft lithography, has been demonstrated to create patterned pores or channels.[142–144] This method provides better control over geometric features and can enable localized permeability while maintaining continuous solid regions for thermal conduction. However, fabrication complexity and lack of scalability are limitations of this process. Nano-films are polymer films at thicknesses below a few hundred nanometers, allowing partial vapor permeability and minimized thermal resistance.[145,146] Yet, their mechanical robustness is limited for dynamic wearable conditions. The series of strategies highlights the fundamental challenge of simultaneously achieving breathability and efficient heat transfer in thermal interfaces for wearable thermoelectric devices without compromising comfort or performance.

1.3.3 Recycling Liquid Metal Composites

The rapid growth of flexible electronics, including wearable TEDs, has driven demand for multifunctional materials that combine mechanical compliance, thermal stability, and electrical conductivity. However, this technological progress introduces environmental and supply chain challenges unless future devices are designed with end-of-life solutions for reuse or material recovery in mind.[147] The increasing volume of electronic waste (e-waste) not only threatens environmental sustainability but also results in the loss of valuable resources and the release of hazardous substances.[148] In stretchable electronic systems,[149] elastomer composites comprising thermoset polymer matrices (e.g., PDMS or Ecoflex 00-30) and conductive fillers commonly serve as key building blocks. Despite their thermal and mechanical stability, these functional composites are rarely designed for recycling or recovery of the conductive fillers due to the irreversible crosslinking of the thermoset, highlighting the need for sustainable alternatives that support both material reuse and device reconfiguration.

LM composites with conventional thermoset polymer matrices, which have been widely studied for interconnects or thermal interfaces in wearable electronics, are not recyclable. This limitation has driven growing interest in alternative polymers that facilitate recycling and recovery of valuable metallic fillers. One pioneering study recovered LM from thermoplastic composites by acid treatment, where the LM nanoparticles were grafted by polymers such as poly(methyl methacrylate) (PMMA).[42] Other efforts in recycling liquid metal from composites involve employing degradable polymer matrices such as thermoplastics,[150,151] thermoplastic block

copolymers,[152,153] or hybrid-crosslinked polyurethane with Diels–Alder reaction.[154] While these alternatives offer partial recyclability, they often suffer from complex synthesis processes, insufficient conductivity, and drawbacks such as low thermal stability, reduced mechanical performance, and limited chemical resistance. Therefore, a polymer matrix combining the benefits of thermosets and thermoplastics is in demand for soft and recyclable thermal interfaces.

Vitrimer, a class of polymers with covalent adaptive networks (CANs),[155–159] is a recyclable thermoset with a strong potential to address challenges in reprocessing thermoset composites and recovering embedded conductive fillers (Figure 1.11a). Its unique network structure provides mechanical and thermal robustness of thermosets, while enabling reprocessing through dynamic covalent bonds. Under external stimuli such as heat or light,[160,161] the crosslinked network can undergo bond exchange reactions, allowing reshaping and recycling. Building on these polymer properties, various recycling strategies have been developed for vitrimer composites,[162–167] including matrix dissolution and repolymerization in ethylene glycol (EG) solution to recover both the polymer matrix and solid carbon fibers.[162] For example, there has been an effort to recycle vitrimer-based triboelectric nanogenerator utilizing silver nanowire electrodes (Figure 1.11b).[168] This vitrimer composite sustained its energy harvesting performance after multiple cutting and healing cycles. However, recycling vitrimer composites with solid fillers relies on mechanical separation and are not suitable for systems incorporating liquid-phase conductors or a strong interaction between filler and matrix, such as LM. One study utilized surface-modified LM particles as a crosslinker in the vitrimer network.[169] But the chemical bonding between the LM and vitrimer hindered the recovery of both components, emphasizing the underlying challenge in recycling LM–vitrimer composites. Another study reported the synthesis of a vitrimer using epoxy-modified lignin, polyethylene glycol diacid, and ethylene glycol, together with incorporated LM nanoparticles.[170] Despite achieving high-resolution circuit printing (7.6 μm), the composite's flexibility was limited by the inherent brittleness of the lignin-based matrix, with a strain at failure of only 20%. Additionally, LM filler sedimentation in these composites prevents their implementation as soft TIMs. Sedimented LM particles create a thermal barrier at the LM-depleted top surface while simultaneously inducing short-circuiting at the LM-rich bottom surface. To deploy LM–vitrimer composites as soft TIMs with uniform filler distribution, the manufacturing process must be carefully investigated. Furthermore, this study didn't study reprocessing under elevated heat and compression, which can straightforwardly heal the

composite. Collectively, previous works have not achieved a stretchable, thermally stable, chemically robust, and recyclable LMEC.

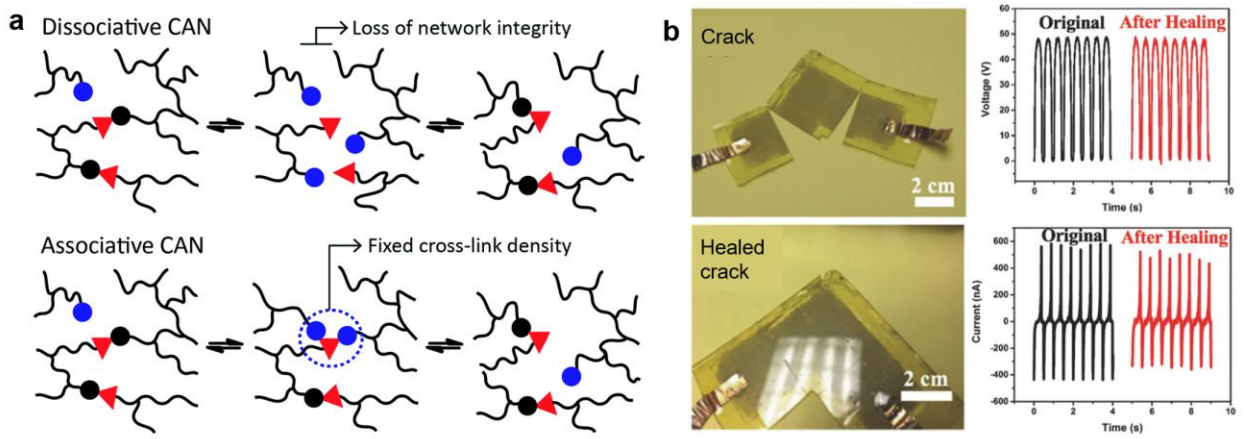

Figure 1.11. Covalent adaptive networks of vitrimers and recyclable electronics using vtirimer. (a) Crosslinking mechanisms of vitrimers.[159] Reproduced with license under CC BY 4.0. (b) Photographs and measured energy harvesting performance of vitrimer-based triboelectric nanogenerators.[168] Reproduced with permission from Wiley-VCH. © 2018 Wiley-VCH GmbH.

1.4. Objectives and Overview

Chapter 1 introduced the potential of wearable TEDs to serve as reliable power supply units for on-skin electronics. Nevertheless, several technical bottlenecks remain such as insufficient energy conversion efficiency, the lack of advanced manufacturing methods, the need for permeable and thermally conductive skin interfaces, and recyclable composites. From these, four research objectives are determined to address the challenges: (1) Tailoring composites' material properties in each device layer through filler types and sizes and controlling device geometry via 3D printing enhance thermoelectric performance; (2) Engineering 3D device architecture improves thermal management while maintaining stretchability in wearable TEDs; (3) Electrohydrodynamic printing enables fabrication of permeable and thermally conductive skin–device interface; and (4) Thermally stable and recyclable liquid metal composite can be achieved by utilizing thermoset polymer matrix with dynamic covalent bonds. The following chapters demonstrate how these objectives are achieved using LM composites.

Chapter 2 focuses on investigating the material properties and printability of elastomer composites, including thermally conductive yet electrically insulative liquid metal–elastomer LMEC, thermally and electrically conductive LMEC, and thermally/electrically insulative hollow microsphere elastomer composite (HMEC). These PDMS-based composites can be

extruded from a syringe for direct ink writing process, allowing automated fabrication and design flexibility. The thermoelectric generator developed in this chapter demonstrates excellent electromechanical robustness, effortlessly stretched over 15,000 cycles of 30% strain with minimal resistance change. The soft and stretchable TEDs achieve a power density of 650 $\mu W \cdot cm^{-2}$ under a temperature gradient of 60 °C. The versatility of DIW is demonstrated by printing stretchable heatsinks on top of the device. Furthermore, TED layers are printed directly onto fabrics for seamless integration. This also highlights the importance of the thermal interface where a permeable interface with low thermal conductivity hinders heat transfer, reducing the amount of energy harvested from the same heat source. The additive manufacturing process also allows printing of stretchable heatsinks directly on the device, facilitating a convective heat transfer that improves temperature gradient across the TE pellets.

From the insights gained in the previous chapter, Chapter 3 presents systematic device design with computational simulations and experimental validation to optimize both thermoelectric performance and mechanical stretchability. Based on the simulation, TEDs with three infill ratios (0%, 12%, and 100%) were fabricated to study the effects of core layer architecture on thermoelectric energy conversion and structural integrity. An air pocket structure, comprised of 12% infill of 50%V_f HMEC in the core layer, generates a higher voltage by surrounding embedded TE pellets with air compared to densely filled core layers. From a structural perspective, the 3D-printed core layer does not compromise stretchability because it provides support between the top and bottom interfaces, mitigating stress concentration under stretching. The use of soft composites and fine-tuned fabrication processes enabled devices that combine exceptional stretchability (electrical strain at failure of 230% and mechanical strain at failure of 600%), electromechanical durability (12% resistance change at 100% strain), damage tolerance, and electrical self-healing. TEDs with the novel air pocket core layer structure were expanded to a macro-TEDs with 48 pairs of high-aspect-ratio TE semiconductors and stretchable heatsinks, which achieved a record-breaking power density of 115.4 $\mu W \cdot cm^{-2}$ at thermal equilibrium under an initial temperature gradient of 10 °C. These ultrasoft, highly efficient TEDs address the technical bottleneck regarding energy conversion at low temperature gradients at the human skin interface, demonstrated through battery charging, and powering of LEDs and sensors directly from body heat. Furthermore, the potential of wearable TEDs in personalized thermoregulation is also demonstrated.

Chapter 4 addresses the development of permeable thermal interfaces for wearable TEDs by presenting EHD printed liquid metal–boron nitride–thermoplastic polyurethane (LM–BN–TPU) composites. LM is employed as the primary filler due to its high intrinsic thermal conductivity, mechanical deformability, and compatibility with polymer solution processing. Electrically insulating yet thermally conductive BN is incorporated as a secondary filler to complement LM. BN offers high thermal conductivity, wide bandgap, stable dielectric constant, and high dielectric strength, making it well-suited for electrically isolating applications that demand efficient thermal transport. EHD printing enables the deposition of high-resolution square lattice patterns specifically designed to avoid occlusion of sweat pores and maintain heat conduction capability. Skin compatibility is validated through water vapor transmission rate (WVTR) measurements and a week-long patch test. This fiber mat with a through-plane thermal conductivity of 0.37 $W \cdot m^{-1} \cdot K^{-1}$ is integrated as thermal interface layers in wearable TEDs. Systematic device design, supported by multiphysics simulation, reveals that the permeable interface also functions as a micro-patterned heatsink when positioned on the top of the device. The optimized device generates 0.43 $\mu W \cdot cm^{-2}$ at thermal equilibrium under an initial temperature gradient of 10 °C and exhibits stable performance under mechanical deformation and on-body operation. Furthermore, device recycling enables recovery and reuse of hybrid fillers and thermoelectric semiconductors, allowing device refabrication without performance degradation. This work overcomes the conflicting requirements of breathability and thermal conductivity in skin-electronics interfaces, on-skin energy harvesting, and personalized thermoregulation.

Chapter 5 addresses the sustainability bottleneck in liquid metal composites by employing vitrimer as a polymer matrix. The covalent adaptive network within the vitrimer enables both composite reprocessing and chemical recycling with 94% LM recovery, while maintaining high stretchability and thermal stability. These soft and reconfigurable composites feature uniformly distributed LM inclusions that enhance thermal conductivity up to 6.53-fold. Additionally, electrical circuit patterning, thermomechanical reprocessing through consecutive fragmentation and rejoining of the composites, and chemical interaction between the oxide, polymer matrix, and solvents during chemical recycling are investigated. The properties of LM–vitrimer composites, including thermal conductivity, thermal stability, stretchability, and recyclability, address the fourth research objective related to sustainable electronics and LM composites.

- Chapter 2: Printing Liquid Metal Elastomer Composites for Thermoelectric Generators
- Chapter 3**:** 3D Architectures for High-Performance Stretchable Thermoelectric Devices
- Chapter 4: Permeable Interfaces in Recyclable Thermoelectric Wearables
- Chapter 5: Reconfigurable Soft Liquid Metal–Vitrimer Composites

Chapter 2: Printing Liquid Metal Elastomer Composites for Thermoelectric Generators

Y. Han, L.-E. Simonsen, M. H. Malakooti, Printing Liquid Metal Elastomer Composites for High-Performance Stretchable Thermoelectric Generators. *Adv. Energy Mater*. 12, 2201413 (2022).

2.1. Introduction

In this chapter, a printed wearable thermoelectric generator with high stretchability and efficiency is presented to answer the first research objective: "Tailoring composites' material properties in each device layer through filler types and sizes and controlling device geometry via 3D printing enhance thermoelectric performance." This is achieved by 3D printing elastomer composites with engineered functional and structural properties at each layer. As illustrated in Figure 2.1a, the printed thermoelectric device consists of three different layers: two thermal interface elastomer layers and one insulation layer which separates the two and encapsulates inorganic thermoelectric semiconductors. In this design, the printed LMEC with high thermal conductivity serves as the thermal interface material. The insulation layer is printed with hollow microspheres embedded in elastomer to reduce both the density and the thermal bypass around the TE semiconductors. Moreover, a different LMEC with large LM droplets is printed to function as a stretchable electrical interconnect between the semiconductors (Figure 2.1b). Every device layer is 3D printed with multifunctional composites to fabricate stretchable TEDs with precise control of device geometry.

The wearable TEDs remain functional after more than 15,000 stretching cycles at 30% strain while undergoing a minuscule change of resistance. This proves the device's stability in long-term use and its capability of bearing deformations such as stretching, twisting, and bending. These stretchable thermoelectric wearables show an excellent performance by generating an open-circuit voltage of 392 mV and a power density of 650 $\mu W \cdot cm^{-2}$ at temperature gradient (ΔT) of 60 °C, which is more than 6.5 times increase in power density compared to previous stretchable TED with LMEC interfaces.[70] With the additive fabrication technique of thermoelectric wearables here, novel applications are explored such as printing the thermoelectric device on stretchable textile fabric as shown in Figure 2.1c. Moreover, customizable, and stretchable 3D heatsinks can be directly printed on the TED so that the whole device, including the heatsink, can be bent, stretched, and conformed to the target surface (Figure

2.1d). This stretchable heatsink enables maintaining a large temperature gradient across the device for higher output voltage. Figure 2.1e illustrates the effect of integrating a stretchable heatsink by comparing the open-circuit voltages of different devices. The steady-state voltage of the printed TED with the heatsink is significantly higher due to the increased surface area and thus enhanced heat dissipation on the cold side, while the peak voltage of this TED is slightly lower than that of the device without a heatsink because of a minor deviation in the fabrication process.

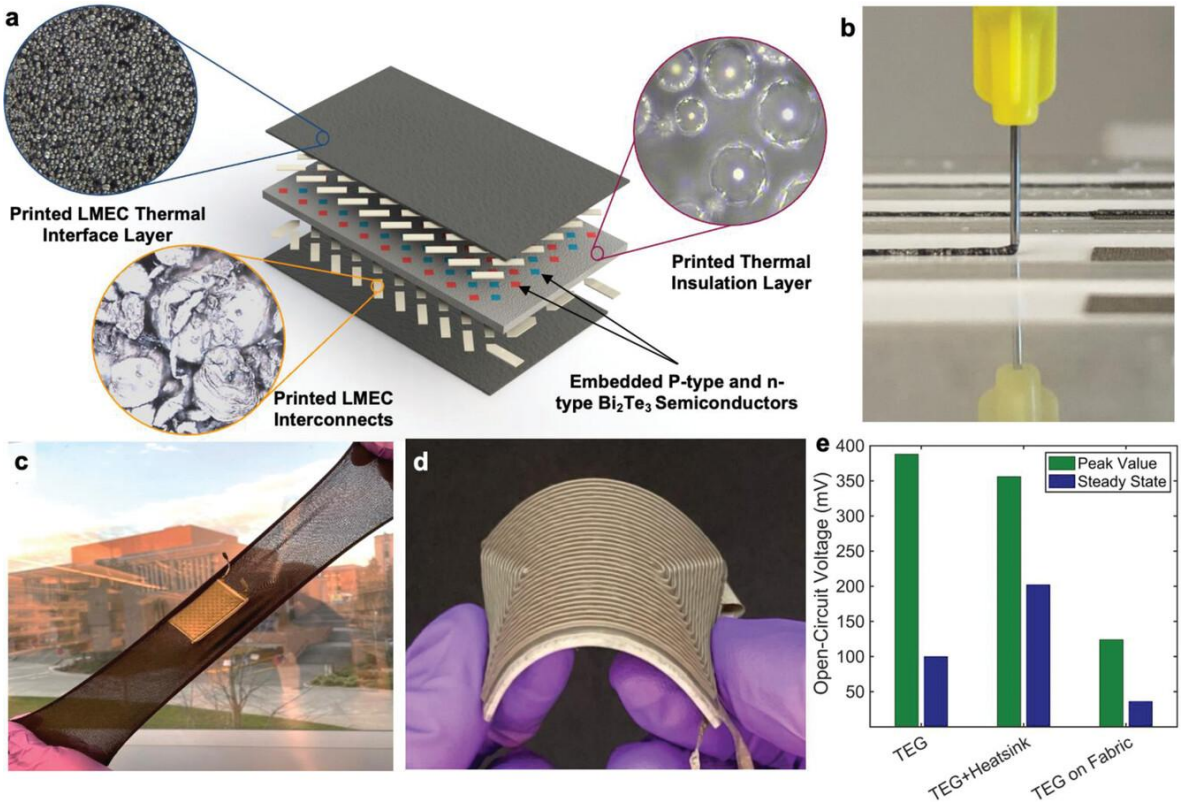

Figure 2.1. Wearable thermoelectric devices via 3D printing of multifunctional elastomer composites: (a) Schematic of a stretchable TED and micrographs of printed materials consisting of top and bottom thermal interface liquid metal elastomer composites (LMEC), thermal insulation layer with printed hollow microsphere elastomer composite (HMEC), encapsulated rigid semiconductors in the middle, and top and bottom LMEC interconnects. (b) Photograph of an LMEC interconnect in the printing process. (c) Photograph of a TED printed on a stretchable textile. (d) A TED with stretchable heatsink under bending deformation. (e) Measured voltage output of different stretchable TEDs at an initial temperature gradient of 60 °C: a reference device, a device with a printed stretchable heatsink in forced air convection condition, and a printed TED on fabric.

2.2. Printing Multifunctional Composites

Three different functional elastomer composites are formulated to print components of the TEDs. This includes 50% volume fraction (V_f) LMEC with sub-5 µm LM inclusions, 30%V_f LMEC with larger LM droplets (D > 100 µm), and 50%V_f hollow microsphere elastomer composite

(HMEC). PDMS was used as the matrix phase while its fillers and processing parameters were adjusted to fabricate these three composites with specific properties such as tailored particle size and distribution.

The 50%V_f LMEC, which is used as the thermal interface layer, requires effective heat conduction while remaining electrically insulating. To achieve these objectives, the size of liquid metal inclusions is engineered to be in the range of several microns, where the embedded LM droplets show resilience from external forces and can be uniformly dispersed in PDMS as shown in Figure 2.2a. Since thin and uniform printing is desirable for this layer, a 5% weight fraction of hexane (C_6H_{14}) was added into the ink to decrease the viscosity and further improve the print quality. Micrographs of the top and bottom regions of the LMEC cross-section in Figure 2.2b and c indicate the uniform distribution of LM microdroplets without sedimentation. This consistency throughout the thickness of printed LM-elastomer composites allows uniform thermal conductivity in this layer which is essential for effective heat transfer. To further increase the conductivity of the thermal interface layers, secondary filler materials such as copper, [171] tungsten,[172] graphene,[88] or chrome-coated diamond[173] can be added to the LM-elastomer composite. However, the increase in thermal conductivity via additional solid inclusions might be limited due to the increased number of interfaces in the elastomer matrix, which might cause unfavorable electrical connectivity and short circuit.[171] Moreover, the embedded solid particles will also affect the rheology (i.e., printability) and stretchability of the thermal interface materials.

In stretchable interconnects, the 30%V_f LM-elastomer composite has a much larger droplet size ($D > 100$ μm) compared to the size of LM droplets in the printed thermal interface LMEC ($D < 8$μm) as shown in Figure 2.2d. The ink with large EGaIn droplets and uncured PDMS facilitates direct writing of the short interconnects when TE pellets are packed densely. Moreover, this particle size enables rapid sedimentation and mechanical activation of the LM inclusions to form a percolating network inside the elastomer matrix.[174,175] Figure 2.2e shows the bottom view of a printed trace of LMEC with 100–200 μm EGaIn droplets and their sedimentation. The LMEC interconnects show high stretchability and great electrical conductivity (5.16×10^5 $S\cdot m^{-1}$) which makes them excellent electrical conductors for wearable thermoelectric generators. It should be mentioned that printing bulk EGaIn as an interconnect is extremely challenging due to the high

surface tension of EGaIn and the immediate formation of Ga-oxide layer on its surface.[176] Unlike bulk liquid metals, a mixture of LM and elastomer can be readily dispensed and printed after adjusting the rheology of the ink.[108,177–180]

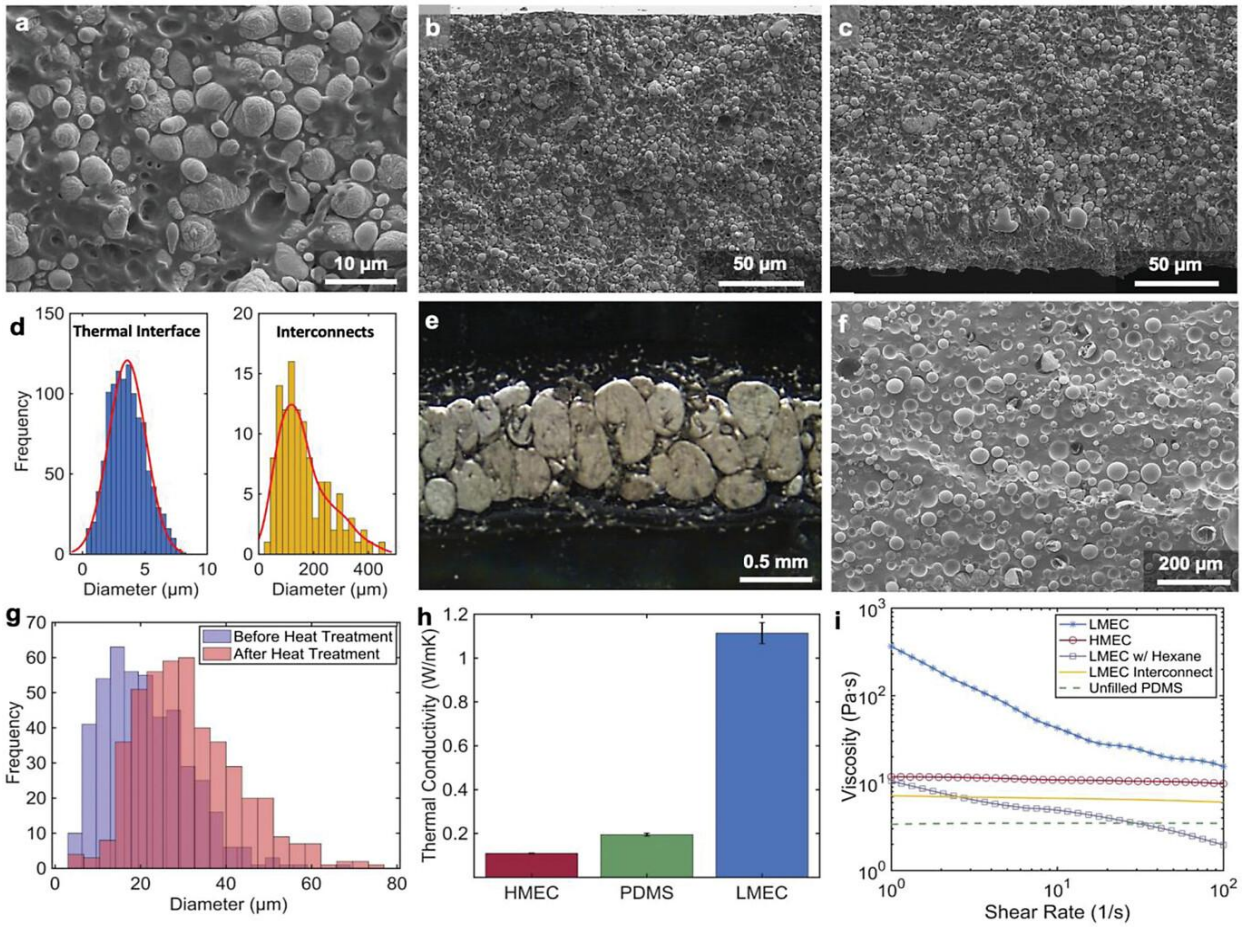

Figure 2.2. Multifunctional soft matter for printing stretchable TEDs: (a) Scanning electron microscopy (SEM) images of 50% volume fraction LMEC for printing thermal interface layers. (b and c) Top and bottom region of the thermal interface layer with uniformly dispersed LM inclusions. (d) Size distributions of EGaIn particles in LMEC in thermal interface layer (left) and electrical interconnects (right). (e) A microscopic image of a printed trace of LMEC interconnects with LM large droplets. (f) A SEM image of hollow microsphere elastomer composite (HMEC) for printing thermal insulation layer. (g) The size distribution of the microspheres before and after curing of the composite. (h) Thermal conductivities of the lightweight thermal insulation layer (HMEC), Sylgard 184 (PDMS), and LM-incorporated thermal interface layer (LMEC). (i) Viscosity of printing inks as a function of shear rate.

Lastly, HMEC with 50%V_f thermoplastic microsphere is engineered to act as the thermal insulation material between the cold and hot sides of the TED (Figure 2.2f). The microspheres embedded in the HMEC increase in diameter when the composite is cured at an elevated temperature (Figure 2.2g). Since the embedded microspheres are extremely lightweight and expand by heat, they essentially decrease the density of the ink to 0.6367 $g \cdot cm^{-3}$ which indicates

a 35.2% weight reduction compared to unfilled PDMS. Another positive effect of the microspheres is the reduction in thermal conductivity as shown in Figure 2.2h. Increasing the volume fraction of the hollow microspheres will further decrease the conductivity of the thermal insulation layer. However, the tradeoff will be reduced elongation at the break of the composites in addition to processing challenges such as inconsistent print quality. Combined with reduced weight and low thermal conductivity, this soft thermal insulation layer enhances the energy harvesting performance as it offers conformal contact to dynamic heat sources such as human body.

Thermal conductivity of the soft-matter composites was measured to determine the heat conduction performance of the thermal interface and insulating materials in TEDs. Using the transient hot-wire method, the measured thermal conductivity of LMEC with 50%V_f and average particle size of 4 μm was 1.1 $W \cdot m^{-1} \cdot K^{-1}$. The embedded LM microparticles increase the thermal conductivity of the unfilled PDMS (0.19 $W \cdot m^{-1} \cdot K^{-1}$) by 480%. While increasing the size of LM inclusions further improves the thermal conductivity of the LM-PDMS composite, a larger size will result in a non-uniform dispersion of LM droplets and make them prone to being damaged and leaking out. The measured thermal conductivity of HMEC was 0.11 $W \cdot m^{-1} \cdot K^{-1}$, which is one-tenth of that of the LMEC. The tailored properties of each layer will ensure effective heat transfer to TE legs and maintaining the temperature gradient across the device, improving the energy harvesting performance. Tailored thermal properties of these materials can be expressed as thermal conductance or heat transfer coefficients for numerical comparison. The thermal conductance, quantity of heat that can pass through the cross-sectional area and thickness, can be obtained by multiplying the thermal conductivity of the material and the cross-sectional area divided by the thickness.[181] Given the previously reported thermal conductivity of Bi_2Te_3 (1.37 $W \cdot m^{-1} \cdot K^{-1}$ at 300 K),[182] the thermal conductance of TE pellets, HMEC core layer, and LMEC thermal interface layer can be calculated as 2.014×10^{-1} $W \cdot K^{-1}$, 9.713×10^{-2} $W \cdot K^{-1}$, and 4.532 $W \cdot K^{-1}$, respectively. This result reveals the absorbed heat in the thermal interface will be concentrated on the TE legs to successfully harvest the energy.

It is necessary to understand the viscosity of each ink to confirm its printability. As illustrated in Figure 2.2i, mixing LM droplets or hollow microspheres in PDMS increases its viscosity. The rheology of LMEC shows it has a comparable viscosity and thixotropic behavior to previously reported liquid metal composites,[37,108] but a smaller LM particle size results in a small increment

in the viscosity. To mitigate this effect, a 5 wt% hexane was added to the thermal interface LMEC ink, decreasing the viscosity which allows printing a thin and uniform layer of LMEC at low dispensing pressure. The thermal interface printing was conducted at 7 kPa and 5 $mm \cdot s^{-1}$ with an 18-gauge needle. In contrast, the LMEC interconnect ink that has larger LM particles shows a slight increase in viscosity when compared to unfilled PDMS, allowing effortless direct ink writing of stretchable conductors. The printing pressure and speed for interconnection ink were 60 kPa and 1.5 $mm \cdot s^{-1}$ with a 32-gauge needle, respectively. The rheology test of the HMEC ink for the insulation layer also shows a small increase from the base elastomer in the viscosity as microspheres are added to the PDMS. Because of the shape of the microspheres (i.e., 0D filler materials) and the flexibility of the PDMS molecular chains, it is not expected to observe a difference in viscosity within this range of shear rates, making it suitable for 3D printing porous elastomeric structures. Therefore, these rheology results indicate that all the multifunctional elastomer composites here can be 3D printed for the fabrication of stretchable electronics.

2.3. Device Design and Fabrication

To fabricate TEDs, five printing steps are conducted on an array of TE pellets as illustrated in Figure 2.3a. First, inorganic p/n-type thermoelectric semiconductors are paired and arranged diagonally inside a mold. Bismuth telluride (Bi_2Te_3) is chosen as the TE material due to its advantageous combination of low thermal conductivity (1.2–1.6 $W \cdot m^{-1} \cdot K^{-1}$), high electrical conductivity (850–1250 $S \cdot cm^{-1}$), and excellent Seebeck coefficient (200–235 $\mu V \cdot K^{-1}$), resulting in exceptional figures of merit (zT) and conversion efficiency at ambient temperatures, making it suitable for the wearable application.[182,183] They are assembled in alternating order so that a complete circuit is formed after printing the electrical interconnects. After the arrangement of the Bi_2Te_3 semiconductors, the HMEC core layer is printed to fill up the gap between the pellets.

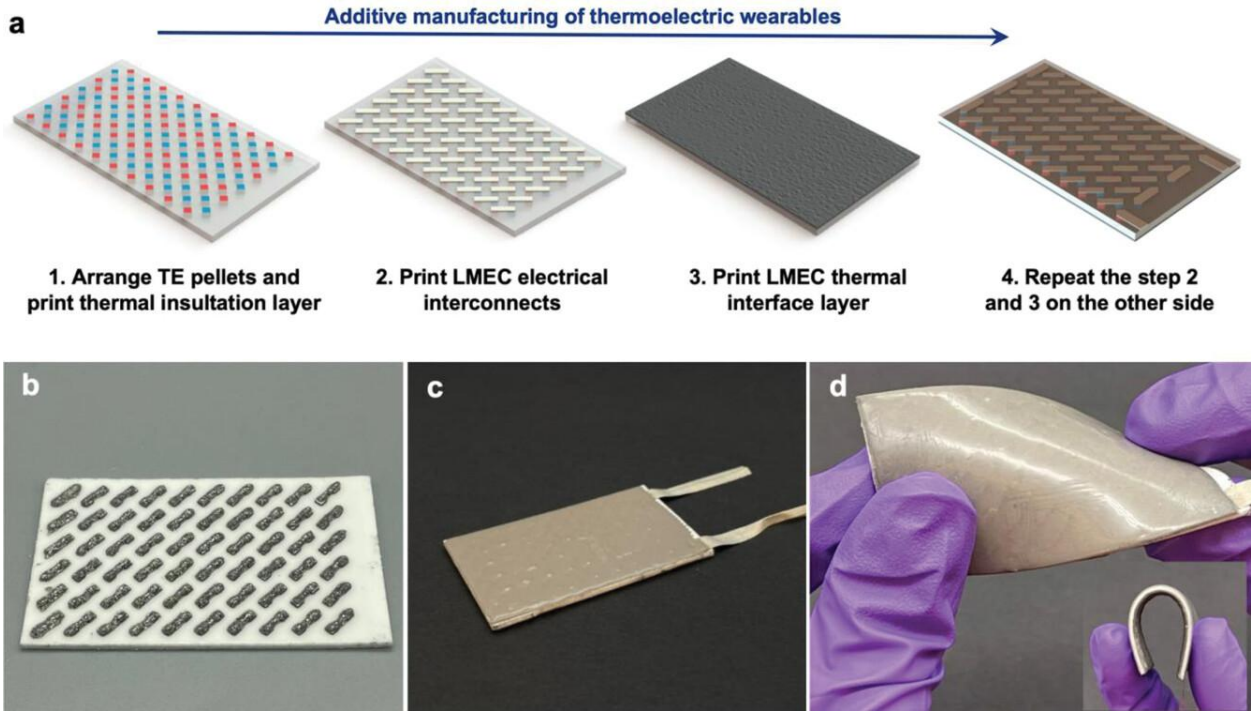

Figure 2.3. Design and fabrication of stretchable TEDs: (a) Schematic of the layer-by-layer fabrication process. (b) Photograph of printed liquid metal elastomer composites for interconnects. (c) A TED with 120 Bi_2Te_3 thermoelectric semiconductors with a dimension of 51.5×32×2.4 mm^3. (d) A printed TED is being deformed to demonstrate its high flexibility.

After curing the HMEC in oven at 90 °C for 3 hours, liquid metal is sprayed on top of the TE pellets using an airbrush and stencil to mitigate the contact resistance between the pellets and the electrical interconnects that are later printed. Next, an uncured LMEC with large liquid metal droplets is directly printed to connect the TE pellets and serve as stretchable interconnects on one side of the device (Figure 2.3b). Because of their high density and large particle size (D > 100 μm), the LM droplets rapidly sediment on the TE pellets and the core layer. Then the LM inclusions are "mechanically sintered" or "activated" by applying mechanical pressure on the cured traces.[27,184] In this process, the gallium oxide interphase ruptures and forms a percolating network that connects the p-type and n-type TE legs to complete one side of the circuit. After the activation, an electrically insulating LM-elastomer composite with high thermal conductivity is printed on top of the device to serve as a stretchable thermal interface layer. The embedded LM inclusions in this layer are significantly smaller (D < 8 μm) to ensure electrical insulation and eliminate the possibility of LM leakage. The same steps are applied to the other side to complete the fabrication of a stretchable thermoelectric generator.

Figure 2.3c shows a printed thermoelectric generator with 120 TE pellets (60 pairs) and a final dimension of 51.5×32×2.4 mm^3. A fill factor of this device, an area fraction filled by the TE materials, is calculated to be 14.27% which is chosen to have high energy harvesting performance and structural integrity without a significant trade-off. As depicted in Figure 2.3d, this TED with rigid TE pellets shows excellent flexibility to be worn on the body or placed over curved surfaces. The introduced additive manufacturing method significantly increases the design freedom for thermoelectric wearables and paves the road for creating customized device architectures.

2.4. Energy Harvesting and Structural Integrity

The open-circuit voltage and power output were measured to evaluate the printable TED's energy harvesting performance. In the context of wearable applications, human skin acts as a deformable heat source, with heat primarily dissipating to the ambient environment through natural convection. Given these conditions, "One Side Heat Conduction" method is chosen to characterize the energy harvesting performance, where the device is placed on a heat source so that heat is applied from one side and dissipates on the opposite side through convection (Appendix A.1.2). In this measurement, the output voltage peaks initially and then gradually reduces until it stabilizes at thermal equilibrium. As shown in Figure 2.4a, the peak open-circuit voltage (V_{OC}) of the device increases linearly with the temperature gradient between the hot plate and the room temperature (ΔT). The peak voltage output reaches up to 392 mV at ΔT = 60 °C with negligible deviations in measurements. At lower ΔT, the delivered heat flux to the TE semiconductors is reduced, resulting in smaller V_{OC}. For instance, the peak voltage of 74 mV is harvested when the temperature difference between ΔT is set to 10 °C. It should be mentioned that the V_{OC} in this study was achieved without using a metallic heatsink or cooling device, which is used in some previous studies to report the performance. The V_{OC} produced by the temperature difference within the device can be expressed as following.[73]

$$V_{OC} = N(\alpha_p + \alpha_n) * \Delta T_{TE} \quad (6)$$

Where N indicates number of pairs of TE pellets. α_p and α_n represent the Seebeck coefficients of p and n-type Bi_2Te_3 that are -161 $mV \cdot K^{-1}$ and 176 $mV \cdot K^{-1}$ at room temperature, respectively.[182,185] Based on experimental results and the simplified modeling with Equation (5)

and (6), it is calculated that ΔT_{TE} = 19.4 °C and dimensionless thermal resistance ratio acted on the device ($\frac{R_{Core}}{R_{TED}}$) = 0.34 at the peak response of ΔT = 60 °C.

TED's low internal resistance (R_{int} = 3.9 Ω) is also contributing to excellent energy harvesting performance. The total resistance of the device can be calculated by adding up three factors: resistance from the interconnects, the TE pellets, and the contact resistance. 70 mm interconnects with large LM inclusions showed 0.24 Ω average resistance and the total length of interconnects in the device is 423.01 mm. The resistance from the interconnects is therefore 1.450 Ω. For TE semiconductors, a 1.4×1.4×1.6 mm^3 Bi_2Te_3 has 7 mΩ that accounts for 0.84 mΩ in TED with 120 pellets.[70,77] According to these results, the contact resistance for 240 interfaces is expected to be as low as 1.01–1.61 Ω due to sprayed EGaIn on the head of TE pellets that successfully mitigate the contact resistance.

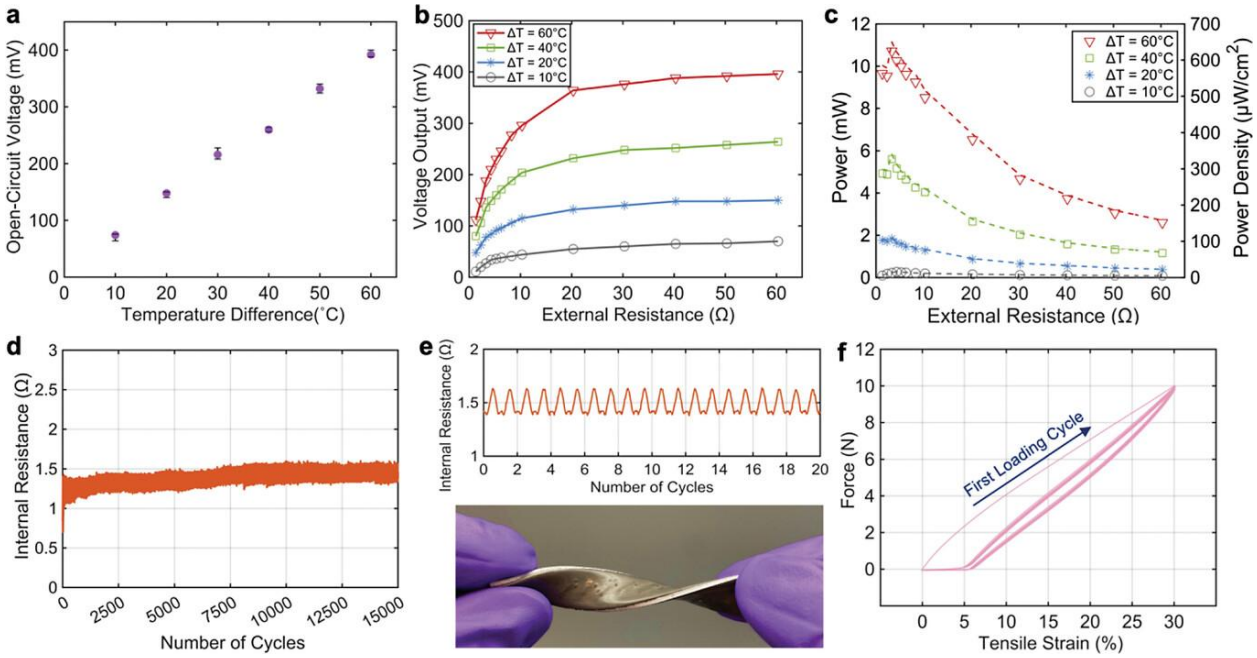

Figure 2.4. Thermoelectric energy harvesting performance and structural integrity: (a) Open-circuit voltage as a function of the temperature difference on the top and bottom layer. (b) Measured output voltage versus external resistor load at different temperature gradients. (c) Estimated power and power density of the printed TED showing the same optimal load resistance at three different temperature gradients. (d) Internal resistance of a TED tensile sample under 15,000 cycles of uniaxial tensile loading with 30% maximum strain. (e) Endurance of TED after being stretched by 30% for 15,000 cycles. Steady electrical resistance (top) and photograph of the TED under torsion without any damage or failure (bottom). (f) Hysteresis of TED tensile sample under uniaxial load up to 30% strain.

To quantify the power generation capability, the device was connected to an external load resistor (R_{ex}) and the output voltage (V) was measured across the resistor. Figure 2.4b shows the

measured voltage for four different temperature gradients (ΔT = 10, 20, 40, and 60 °C) across the external load resistors changing from 1 to 60 Ω. This response indicates that output voltage is highly dependent on the heat flux while a similar trend is observed at each temperature gradient. The measured voltage ramps up sharply at the beginning and then converges to the open-circuit voltage as the external resistance increases. At R_{ex} = 60 Ω or higher, the changes in the voltage output are negligible and it behaves like an open circuit. With the output voltage as a function of external resistance load, the generated power that has been delivered to the external resistor can be estimated as below.[29,186]

$$P_{delivered} = V^2/R_{ex} \quad (7)$$

Figure 2.4c illustrates the power and the corresponding power density, estimated power normalized by the device area. At all the four different temperature gradients, the maximum power appears at R_{ex} of ≈3 Ω. As predicted, the optimal load resistor is close to the internal resistance of the device of 3.9 Ω. At ΔT = 60 °C, the maximum power of 10.7 mW and the maximum power density of 649.9 μW·cm^{-2} was measured. This excellent energy harvesting performance holds true even at lower temperature gradients. For instance, a power density of 16.3 μW·cm^{-2} is measured at ΔT = 10 °C. There are several key factors that influenced the improvement of the performance and eliminated the need for bulky and solid heatsinks. First, the highly conductive thermal interface with the uniformly dispersed LM particles in the PDMS matrix efficiently delivers the heat to TE pellets from the hot side and releases the heat faster on the cold side of the device. Also, the printing method gives control over the thickness of the thermal interface layer. Printing LMEC with a thickness of 0.4 mm allows full contact on both sides and a fast response to the heat without any delamination which can further boost the heat flux through the device. Moreover, the low thermal conductivity of the insulation layer reduces heat dissipation in the in-plane (i.e., lateral) direction and concentrates the thermal energy in the TE legs by minimizing the thermal bypass through the surrounding materials. Furthermore, the thin LMEC layer and higher conformability of the insulation layer give better contact between the device and the heat source. Thus, the combination of tailored material properties at each layer and improved form factor enhances the thermal management within the device for the energy harvesting performance.

Robustness under deformation is a critical factor for stretchable electronics. Electromechanical stability and structural integrity of 3D printed TEDs under uniaxial tension were investigated. Rectangular-shaped tensile specimens with the same design architecture and characteristics were prepared for this purpose. This tensile specimen with 16 TE pellets and a total dimension of $70\times11\times2.4$ mm^3 had an average initial resistance of 1.10 Ω. After applying 15,000 cycles of tensile strain (0–30%) at the rate of 20 mm·min^{-1}, the final resistance was measured to be 1.28 Ω under the stress-free condition. A maximum strain of 30% was chosen for this test because that is the maximum tolerable strain for human skin and a common design criterion for electronic tattoos and wearables.[187,188] As shown in Figure 2.4d, the electrical resistance of the wearable TED sample increases slowly until the interconnections in the sample are fully adjusted and seemingly began to plateau afterward. During this test, the LMEC thermal interface layer remains electrically insulative due to the small size of the LM inclusions. After completing 15,000 cycles, the device remains fully functional without any electrical or mechanical failure. A zoomed-in view of the captured signal after the cyclic test indicates that the resistance proportionally increases as the sample stretches to the maximum strain and it decreases as the sample comes back to its original length (Figure 2.4e). The small peaks at every 0% strain indicate the bending of the sample at zero displacements that are caused by the viscoelastic response of the elastomer composites. The photograph of the twisted specimen in Figure 2.4e shows that the tensile sample is fully intact after 15000 loading cycles. Comparing generated voltage before and after the cyclic loading further ensures the robustness of TED, which is measured to be 29.6 mV and 31 mV at $\Delta T = 40$ °C, respectively. To further characterize the elastic behavior, mechanical force as a function of applied strain at the same rate is measured, as depicted in Figure 2.4f. The device shows strain-softening after the first cycle (i.e., Mullins effect) while there is negligible hysteresis behavior between loading and unloading in the consecutive cycles.[189] From the uniaxial cyclic loading, the device stiffness is estimated to be 1.26 MPa, while the softened specimen does not experience tensile stress up to 5% strain. As the tensile strain increases up to the range of 50–70%, the devices experience mechanical failure because of the stress concentration caused by the rigid and inextensible TE pellets inside the device.[70] The mechanical robustness and electrical stability of the printed thermoelectric generators under continuous deformation along with their high energy harvesting performance make them excellent candidates to realize self-powered wearable electronics.

2.5. Functionalities Enabled by 3D Printing

Additive manufacturing technique and printable elastomer composites enable creative device architectures and integrations. To demonstrate this unique compatibility, a layer of thermal interface LMEC is printed on a textile (95% polyester, 5% spandex) and then the rest of the TED is assembled on the uncured LMEC to complete the device fabrication. As demonstrated in Figure 2.5a, this wearable thermoelectric generator can be easily wrapped around the arm and be conformally deformed due to the high stretchability of both the device and the textile. This shows that the printed LMEC bonds strongly to both the fabric and the TED which allows seamless integration of thermoelectric into garments and sportswear. Most importantly, the presence of the textile layer provides permeability to moisture and air for the skin to be healthy.

The open-circuit voltage was measured to investigate the effect of introducing the fabric as another layer (i.e., thermal barrier) on thermoelectric energy harvesting. The fabricated TED with the textile layer has the same dimensions and shows a slightly lower resistance by 0.6 Ω compared to the previously presented TED, while the major difference is the presence of the fabric layer on the hot side. Figure 2.5b shows that the V_{OC} is, again, linearly proportional to the temperature difference while the overall performance is decreased since the fabric is working as a thermal barrier. The median was measured to be V_{OC} = 120 mV at ΔT = 60 °C which is 70% lower than that of the device without the extra fabric layer. This result confirms the crucial role of TIMs in thermoelectric systems and their impact on thermal management in wearable electronics.

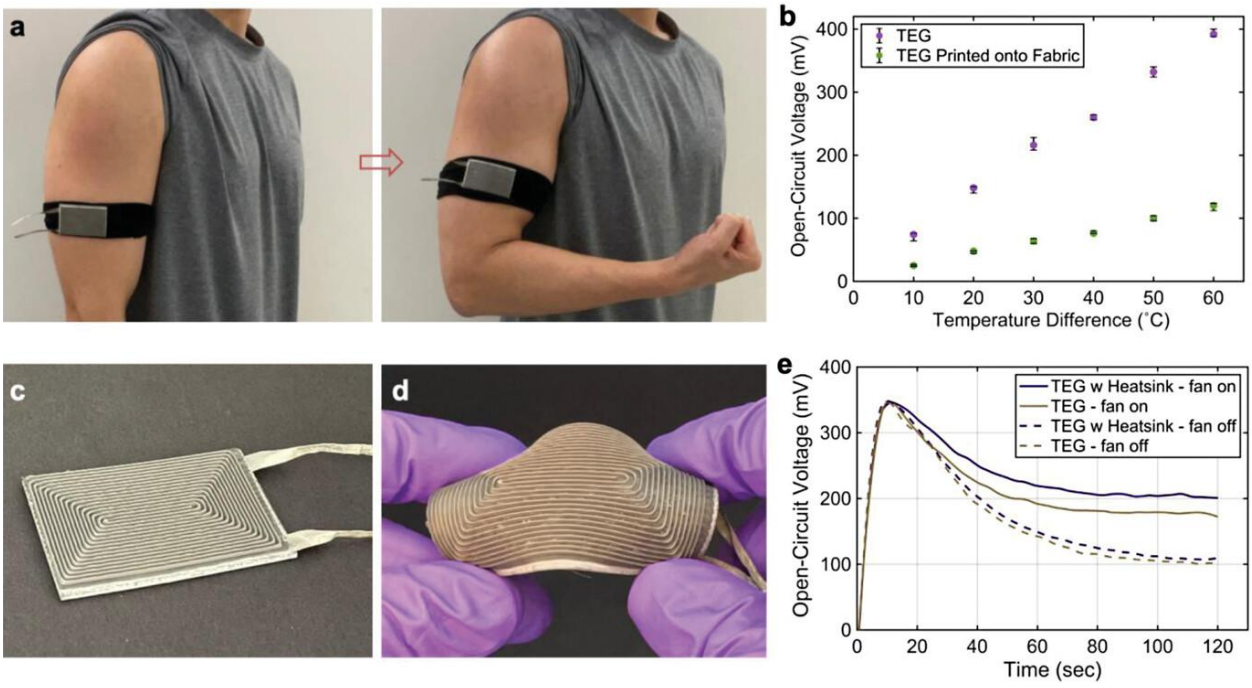

Figure 2.5. 3D printed liquid metal composites for thermoelectric wearables: (a) A wearable TED printed on a stretchable fabric, tied around the biceps at rest (left) and at maximum voluntary contraction (right). (b) Open-circuit voltage of the TED and TED directly printed onto fabric as a function of the temperature difference. (c) A stretchable heatsink printed on TED. (d) Deformed TED with the stretchable heatsink. (e) Open-circuit voltage of the TED with/without the heatsink as a function of time (t) at ΔT = 60 °C and under forced air convection (fan on) conditions.

Printing stretchable heatsinks with controlled geometry is another unique advantage of the additive manufacturing. While the existence of a heatsink on a thermoelectric energy harvester promises performance improvement, previous studies on the heatsink for this application rather focused on the structure optimization of the device or the use of flexible materials.[190–192] For the first time, a 3D printing of the heatsink on top of the thermoelectric generator is demonstrated which is not only flexible but also stretchable (Figure 2.5c). Similar to the printing of the thermal interface layer, a 50%Vf LMEC ink with the same thermal conductivity of 1.1 $W \cdot m^{-1} \cdot K^{-1}$ is used to print the heatsink. This stretchable heatsink is composed of concentric rectangles that are printed layer by layer and have a 1 mm gap. The final height of the rectangles is also 1 mm. Since the same material is used for printing the heatsink and the thermal interface layer on the cold side of the TED, these two layers become one part after curing and show uniform elastic and thermal properties. This ensures structural integrity while improving the heat dissipation ability of the device. As illustrated in Figure 2.5d, this passive heat dissipator deforms and stretches with the device which indicates its high conformability.

The ability to fabricate thermoelectric modules with 3D printed heatsink allows studying the effect of the heatsink and convective heat transfer on thermoelectric energy harvesting. The open-circuit voltage with and without the LMEC heatsink are compared, where a fan was used to blow air on the device and study its effect on voltage generation over time. Figure 2.5e shows V_{OC} in four different conditions until the temperature gradient within the device plateau at ΔT = 60 °C. Under all four conditions, the TEDs reach the same peak voltage, but the steady-state voltage outputs are different. Without forced air convection (fan off), the device with the heatsink generates a V_{OC} of 109.4 mV at the steady-state condition which is higher than that of the device without the heatsink by 7.7 mV. However, the difference in voltage generation between the two devices is quite distinct when they are subjected to forced convection as air is blown by the fan. The TED with 3D printed heatsink produces a voltage of 201 mV while the voltage of the reference TED is measured to be 172.5 mV under forced heat transfer from air convection. This corresponds to ≈16.5% increase in steady-state voltage because of the heatsink and an 83.7% increase due to the airflow. As expected, the airflow induces enhancement of the heat dissipation at ΔT = 60 °C and the output voltages hit the plateau faster in this working condition. Owing to the 3D printing technique and novel properties of LMEC, a wide range of flexible and stretchable heatsinks with arbitrary design and geometry can be 3D printed to further enhance thermal management and energy harvesting in thermoelectric systems.

2.6. Conclusion

This work introduces a versatile approach to print multifunctional elastomer composites for high-performance thermoelectric generators with mechanical and electrical robustness. Inks of elastomer composites are formulated to print thermal interface layers, a thermal insulation layer, and electrical conductors that connect an array of 120 Bi_2Te_3 semiconductors in TEDs. By adjusting the size of embedded LM droplets in PDMS matrix, stretchable liquid metal elastomer composites are engineered to be either electrically conductive or insulating while maintaining high thermal conductivity. In addition, hollow thermoplastic microspheres are dispersed in PDMS to create printable inks for the thermal insulation layer. This additive fabrication of elastomer-based TEDs creates stretchable energy harvesting units capable of generating an average open-circuit voltage of 392 mV and a power density of 650 $\mu W \cdot cm^{-2}$ at ΔT = 60 °C. If the temperature gradient across the TED is set to only 10 °C for wearable applications, the open-circuit voltage, and power density reduce to 74 mV and 16.3 $\mu W \cdot cm^{-2}$, respectively. Moreover,

this thermoelectric generator shows high flexibility and excellent durability as it remains intact even after 15,000 cycles of 30% tensile strain without any change in device functionality. These unique characteristics are achieved by leveraging 3D printing and tuning the material properties of each device layer, addressing the fabrication bottleneck of subtractive fabrication processes in previous works. Also, other advantages of additive manufacturing are demonstrated by directly printing thermoelectric modules on a textile substrate for wearable applications and 3D printing of a stretchable heatsink for improved thermal management at elevated temperatures.

The first study demonstrated tailored material properties of multifunctional composites along with their printability. However, the energy harvested at thermal equilibrium was not yet sufficient to supply power to onboard electronics, especially under the small temperature gradients. The effect of three-dimensional device architecture on thermoelectric performance was also minimally explored, despite DIW's capability to build customizable 3D structures. Furthermore, active heating and cooling performance, an area not yet examined, is expected to benefit from advanced device architectures alongside energy harvesting. Additionally, failure strain was limited to 50 to 70% due to the PDMS elastomer matrix, which is inadequate for body parts such as the elbow or shoulder that undergo larger deformations. The device stiffness of 1.26 MPa also mismatches with soft human skin, potentially causing poor interfacial contact and unexpected failure under dynamic conditions. Achieving higher stretchability and damage tolerance without compromising thermoelectric performance thus remains a critical bottleneck for on-skin electronics. These limitations motivate Chapter 3, where ultrasoft, 3D-printed thermoelectric architectures with damage tolerance are developed to realize highly efficient TEDs.

Chapter 3: 3D Architectures for High-Performance Stretchable Thermoelectric Devices

Y. Han, H. Tetik, M. H. Malakooti, 3D Soft Architectures for Stretchable Thermoelectric Wearables with Electrical Self-Healing and Damage Tolerance. *Adv. Mater.* 36, 2407073 (2024).

3.1. Introduction

This chapter introduces 3D soft thermoelectric architectures that are designed for maximizing thermal management to answer the second research objective: "Engineering 3D device architecture improves thermal management while maintaining stretchability in wearable TEDs." This is achieved with the successful integration of stretchable functional composites through 3D printing, the use of self-healing liquid metal interconnects, the incorporation of inorganic TE materials, and a deliberately designed device architecture for optimal thermoelectric energy conversion and preserved structural integrity (Figure 3.1a). The stretchable TEDs show damage-tolerance, while setting new performance records for energy harvesting and achieving exceptional conformability.

To investigate the effect of the thermal insulation layer structure, the printed TEDs feature three distinct infill ratios (0%, 12%, and 100%) in the core layer, representing thermoelectrics with an interlayer gap, air pockets, and a densely filled layer, respectively. The designed structure is first determined through multiphysics simulations, then the 3D printing of multifunctional LMEC and HMEC with ultra-stretchable silicone elastomer matrix (Ecoflex 00-30) is subsequently employed to fabricate highly deformable TEDs for wearable applications with unique features, such as a stretchable heatsink (Figure 3.1b). While the low conductivity of the HMEC in the thermal insulation layer is effective in concentrating heat flux in the TE legs, the presence of air pockets demonstrates higher voltage generation and does not compromise the device stretchability, as shown in Figure 3.1c. The results indicate that the soft-matter-engineered TEDs, featuring stretchable multifunctional materials and lightweight thermal insulation interlayers, can withstand up to 600% uniaxial strain before mechanical failure, with electrical interconnects maintaining connectivity up to 230% strain. Importantly, TEDs stretched close to 600% without experiencing mechanical failure and regained their electrical conductivity when returned to their unstrained condition. Additionally, these TEDs can restore their energy harvesting and active heating/cooling after being punctured multiple times with a sharp object. This is attributed to the use of liquid metal and its ability to recreate conductive pathways upon contact. Furthermore, the

punctured devices can fully function after undergoing 2,000 stretching cycles from 0% to 50% strain, enabled by the combined effect of the ultrasoft composites with enhanced toughness and self-healing interconnects.

These thermoelectric generators, featuring stretchable 3D structures, achieve a considerable power density of 115.4 $\mu W \cdot cm^{-2}$ at a low-temperature difference of 10 °C. Once the device reaches thermal equilibrium after an initial ΔT of 10 °C, the power density decreases to 16.1 $\mu W \cdot cm^{-2}$. When considering normalized power density relative to the temperature gradient across the device and strain limit, thermoelectric generator in this study significantly outperform recent stretchable TEDs including the previous work as depicted in Figure 3.1d.[33,46,70,72,77,82,84,193–205] Due to the use of various test setups in the literature to report the performance of stretchable TEDs, a detailed comparison of reported works is provided in Table A.1. Regardless of these differences, a series of innovations in this study improve energy harvesting performance by 70% and incorporate robustness, thus addressing previous challenges. Engineered soft architecture also allows efficient temperature modulation for active heating or cooling, showing more than 45% increase in Peltier cooling performance with mitigated parasitic heating after. This level of energy conversion can immediately be implemented as a power source in wireless electronics as it demonstrates battery charging and powering wearable sensors. Furthermore, powering an LED upon contact with the body at ambient temperature is demonstrated for the first time, which unlocks the potential of Macro-TEDs as a reliable power source for wearable electronics (Figure 3.1e).

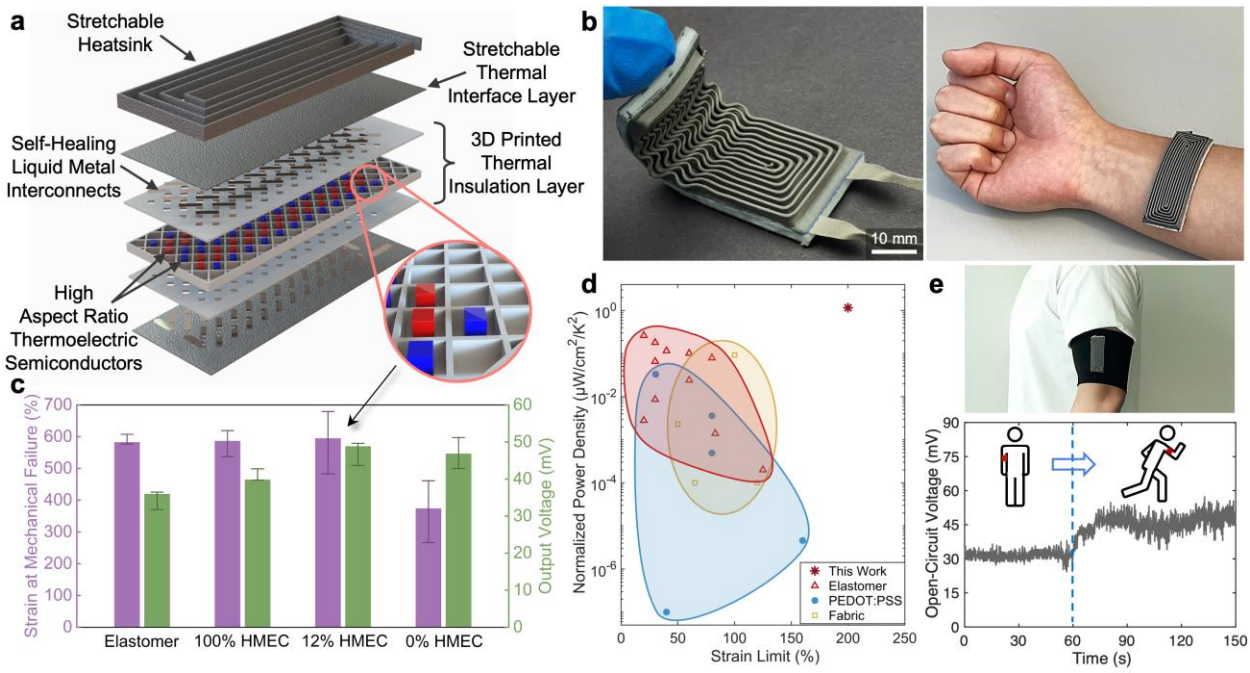

Figure 3.1. High-performance, stretchable TED with 3D soft architectures. (a) Schematic illustration of the device design and its multifunctional layers. (b) Images of the TED when it is bent by a finger (left) and worn on the wrist (right). (c) Comparison of stretchable TED tensile test specimens with respect to strain at mechanical failure and output voltage at equilibrium. (d) Scattered plot for comparison of soft and stretchable TEDs. (e) A wearable thermoelectric generator is worn on the upper arm with enhanced energy harvesting during running.

3.2. Functional Soft Matter Composites for Printing

To create 3D-structured stretchable thermoelectrics, two elastomer inks are formulated for printing the thermal interface and thermal insulation layers. The thermal interface material utilizes a composite of EGaIn droplets and an ultra-stretchable silicone elastomer, with proven biocompatibility.[206] The thermal interface LMEC, with a 50% volume fraction of EGaIn and an average particle size of 13.7 μm (Figure A.1), shows a relatively high thermal conductivity of ~1.3 $W \cdot m^{-1} \cdot K^{-1}$ (Figure 3.2a) without electrical conductivity.

For the thermal barrier, the same base polymer was used to ensure robust layer bonding. The thermally insulating HMEC separates the top and bottom layers in the device and provides structural support for the TE legs. Although the hollow microspheres have a low density of 0.0309 $g \cdot cm^{-3}$, they can be uniformly distributed in the elastomer at 50% volume fraction. The thermal conductivity of the Ecoflex-based HMEC is measured to be ~ 0.1 $W \cdot m^{-1} \cdot K^{-1}$ and its density is calculated to be 0.723 $g \cdot cm^{-3}$ which corresponds to a 32.4% reduction from the unfilled elastomer ($\rho_{Ecoflex}$ = 1.07 $g \cdot cm^{-3}$). This indicates the encapsulating composites in this study have similar functional properties to that of the previous study, as they enhance heat management

within the device, but the stretchability is expected to be improved by far. Additionally, the hybrid-structured device leverages Bi_2Te_3 thermoelectric semiconductors to show distinct enhancement in thermoelectric performance from the 3D printed architecture compared to the previous work.

3.3. Enhanced Efficiency via Device Architecture

To maximize the energy conversion in stretchable thermoelectrics, the heat management within the TED must be optimized. Certain design principles are applied to study device performance through simulations and experiments. Increasing the height of TE legs is an effective strategy to increase the temperature gradient across the device as the distance between the hot and cold sides has increased. Figure 3.2b shows the experimental and simulated V_{OC} at thermal equilibrium for a pair of TE legs with LMEC thermal interfaces and densely filled HMEC core layer featuring two distinct aspect ratios: 1.4×1.4×1.6 mm^3 and 1.4×1.4×3.0 mm^3. The simulation result is validated experimentally with a normalized output voltage of TED samples, demonstrating excellent agreement in V_{OC} of various temperature gradients. For the same cross-sectional area, the Bi_2Te_3 pair with 3.0 mm in height represents the high aspect ratio TE legs, which in turn produces a higher output voltage. Moreover, while both cases show a linear increase in output voltage with increasing the hot side temperature with respect to the ambient temperature, the high aspect ratio TE legs show a more rapid increase. Therefore, the high aspect ratio pellets are utilized in device fabrication due to their enhanced energy conversion, and study other structural facets of the device.

Other factors that significantly affect heat management and energy conversion in TEDs are the thermal and geometrical properties of the insulation layer as well as the area fraction of the TE legs. 3D printing of soft functional matter allows design freedom with the possibility of improved performance and integration of unique features such as 3D stretchable heatsinks, as demonstrated in the first study. This capability is extended by leveraging 3D printing to create 3D soft architectures with low heat conductance in the core layer. Four different core layer structures are investigated through simulation and experiment (Figure 3.2c). Based on the 3D printing infill percentage and print materials, four distinct designs have classified as follows: TED with interlayer gap (0% infill HMEC), featuring no material deposition between the top and bottom surfaces except for a shell around the device; TED with air pockets (12% infill HMEC), using a simple 12% infill density pattern to print HMEC between TE legs for structural support;

the third design involves densely filled HMEC (100% infill HMEC), HMEC fully covers the space between thermal interface layers; and the fourth design comprises densely filled elastomer (100% infill Elastomer), with the base elastomer fully covering the space between thermal interface layers and serving as the common device structure for elastomer-based thermoelectric generators. The responses at equilibrium with One Side Heat Conduction are subjected for comparison because of its higher practical relevance. This approach indicates the device's ability to consistently generate power across a wider range of temperatures on the hot side without the need for active heating and cooling mechanisms on each side.

To study each of the four designs at thermal equilibrium, multiphysics finite element modeling was employed to evaluate the combined effects of the packing density of the rigid TE semiconductors, the TE fill factor, and the core layer's material and structure. The applied boundary conditions and input parameters used in the finite element model are detailed in Figure A.2 and Table A.2. The simulation results indicate a strong influence of both the TE fill factor and the core layer materials and design on ΔT_{TE} across a pair of TE legs, as depicted in Figure 3.2d. To maximize the temperature gradient across the embedded TE pellets, which directly increases the output voltage, it is essential to minimize the overall thermal conductivity of the core layer. This overall conductivity is influenced by several factors, including the design type, the thermal properties of the materials, and the TE fill factor. In addition, employing 3D structures (TEDs with air pockets) or eliminating this layer (TEDs with an interlayer gap) results in a greater ΔT_{TE}, which in turn produces higher voltage and power under the same heating conditions. This is because the low thermal conductivity of air prevents heat conduction, concentrating the heat flux onto the semiconductors. However, as the fill factor increases, the simulated ΔT_{TE} decreases and eventually converges for all different designs and materials used in the core layer. This occurs at high TE filler factors because the overall thermal conductivity of the core layer increases since it is mainly occupied by the TE material with higher conductivity compared to air, base elastomer, and HMEC.

It is important to highlight that a higher TE fill factor, which corresponds to a greater number of TE legs arranged in a unit area, leads to an increased normalized V_{OC}, as shown in Figure 3.2e. Despite a smaller temperature gradient across each TE material, the greater TE content within a given space allows for more efficient energy conversion, resulting in a continuous increase in normalized output voltage as the fill factor increases. Nonetheless, the simulation results suggest

that TEDs with interlayer gap (0% infill HMEC) and TEDs with air pockets (12% infill HMEC) show similar output voltage per area when reaching a steady-state condition, making these findings relevant for continuous power generation and practical applications.

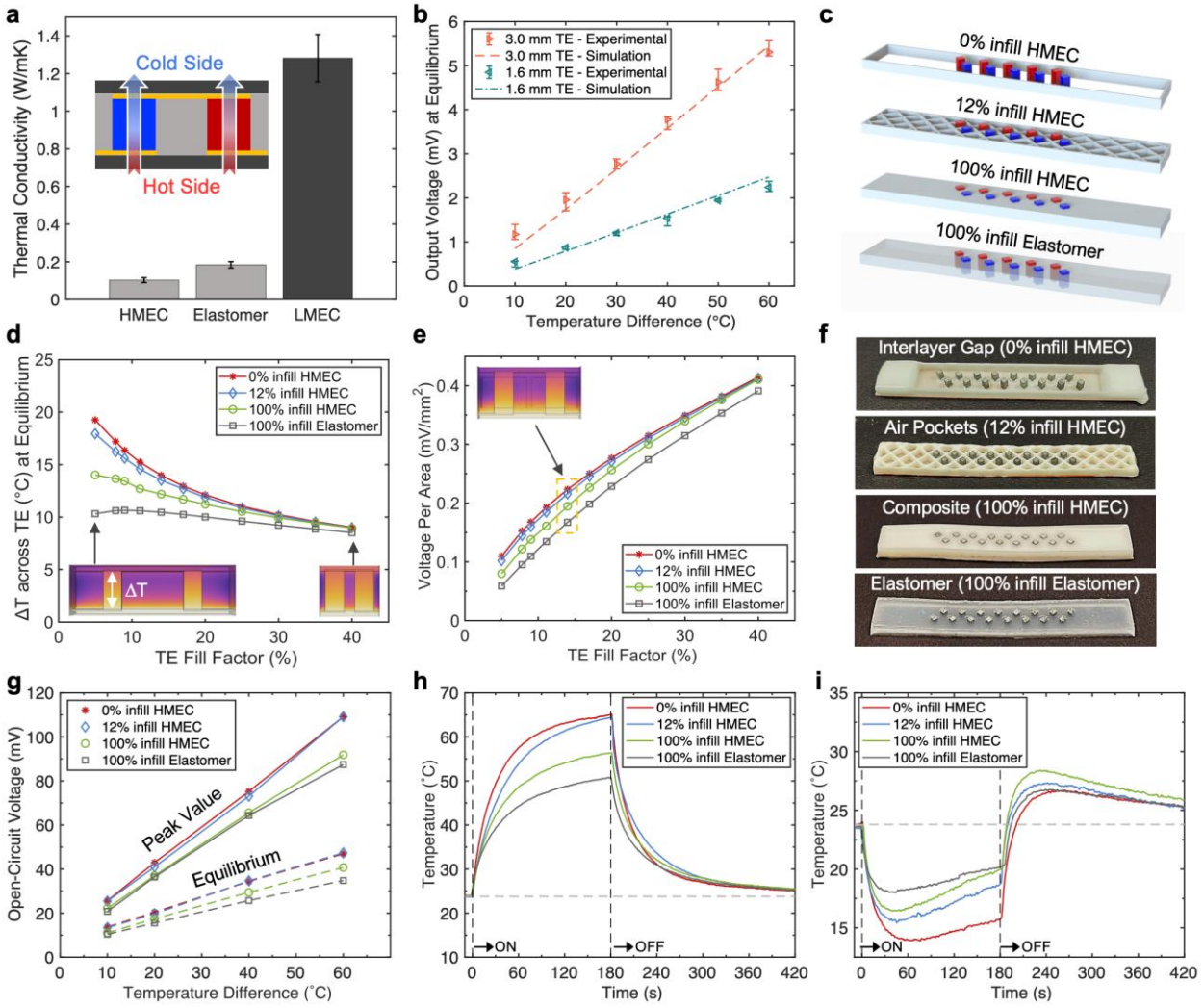

Figure 3.2. Enhanced energy conversion through soft-matter engineering: (a) Thermal conductivities of the materials in the core layer (HMEC and unmodified elastomer) and thermal interface layers (LMEC). (b) Simulation and experimental data for a pair of low and high-aspect ratio TE legs in a densely filled HMEC core layer. (c) Schematics of four different designs of the core layer. (d) The temperature gradient across TE pellets at thermal equilibrium from the simulation of a single pair of TE pellets with four different core layers at ΔT = 60 °C. Inset: Cross-section images of 5% and 40% TE fill factors with the simulated temperature profile. (e) Output voltage at thermal equilibrium normalized by area from the simulation of a single pair of TE pellets. Inset: A cross-section image of a 14.2% TE fill factor with the simulated temperature profile. (f) Photographs of the four different core layer architectures. (g) Measured peak and steady-state values of the open-circuit voltage with different initial temperature gradients. (h) Measured surface temperature of TEDs in active heating mode over time. The power was switched off after 3 minutes. (i) Measured surface temperature of TEDs in active cooling mode for 3 minutes. Parasitic heating is observed after the current is switched off.

For experimental validation and design comparison, TED samples (70×10×4 mm^3 with 16 TE pellets) with the four distinct core layers are fabricated as shown in Figure 3.2f and Figure A.3. An infill percentage of 12% was chosen first based on the print resolution achievable with direct-ink-writing, and a TE fill factor of 14.2% was selected due to its substantial output voltage while maintaining noticeable differences in the energy harvesting performance between different core layer structures. Also, the fluidity and capillary force of uncured ink prohibited higher packing of TE pellets. The chosen 14.2% TE fill factor, which is the same fill factor as the previous study, allows direct comparison for examining how much the 3D architecture in the core layer contributes to the thermoelectric performance.

The V_{OC} of four different TE specimens is measured at initial temperature gradients ranging from 10 °C to 60 °C for 150 s to comprehensively understand the voltage response upon contact with the heat source. The voltage generated from TEDs follows a similar trend: it initially exhibits a peak response, then it decreases over time until it stabilizes at equilibrium (Figure A.4). However, the V_{OC} from low infill cases (0% and 12% infill HMEC) exhibits significantly higher values than the other two TEDs with densely filled core layers, confirming the improved thermal management within the device and enhanced energy harvesting performance. Figure 3.2g provides a summary of V_{OC}, both peak and steady-state values, in relation to the temperature gradient. The results indicate an excellent alignment with the simulation data. TEDs with 0% and 12% infill HMEC show nearly identical responses. This similarity can be attributed to the structural differences between these TEDs. While TED with air pockets has extra material in the core layer that allows heat transfer, it has robust support to the top layer. However, TED without any support material in the core layer can easily bend under its own weight, resulting in a reduction of the distance between the hot and cold sides of the device. This structural contrast clarifies the similarity in their responses. Furthermore, Figure 3.2g illustrates the impact of core layer material and structure modifications. Replacing the base elastomer with a low thermal conductivity composite (HMEC) yields a substantial 13% increase in V_{OC} while an additional improvement of 14% is achieved by printing HMEC with a 2D lattice structure (i.e., air pockets).

In addition to their energy harvesting functionality, stretchable thermoelectric devices can be employed for active heating and cooling applications when supplied with electricity. Each of the four designs is anticipated to yield a unique temperature profile. Figure 3.2h-i show temperature changes in TED specimens for on-demand heat and cooling when placed on a polystyrene

substrate. Under the influence of an electric field, TE pellets create a temperature gradient, and the resulting heat flux is transferred to the thermal interface layers, causing the device's surface to either heat up or cool down. The combination of Joule heating and the Peltier effect is responsible for the heating function, while only the Peltier effect brings the temperature down on the cold side of the TED.[207] Figure 3.2h demonstrates the significantly enhanced active heating performance because of the 3D soft architecture in the core layer when comparing the four TEDs under a 1 A direct current. As expected, the TED with 100% infill Elastomer exhibits the least temperature increment with a slow response rate due to its less efficient thermal management. In contrast, the TEDs with 0% and 12% infill HMEC show similar and considerably improved responses, indicating their promising performance in active heating applications. Similarly for active cooling, Figure 3.2i highlights the effective reduction and control of temperature when there is less material in the core layer. This is because the supporting structure allows heat conduction between the thermal interface materials, decreasing the thermal management capability compared to the interlayer gap. Furthermore, the lower infill in the core layer suppresses parasitic thermal residue from spreading to the opposite side once the power is turned off. These thermoelectrical responses suggest the importance of TED's architecture to align with its intended purpose, whether it is energy harvesting or temperature modulation.

3.4. Electromechanical Robustness and Electrical Self-healing

Ensuring robustness against large deformation and external damage is essential for the practical applications of TEDs. Figure 3.3a shows the devices' flexibility, capable of simply bending at two points, even with embedded 3.0 mm rigid semiconductors. To systematically study the stretchability of the designed TEDs, uniaxial tensile test was conducted on the soft elastomer composites to characterize the mechanics of each layer within the device. Figure A.5 shows the tensile specimens comprising HMEC, LMEC, and printed HMEC with 12% infill, along with the obtained stress-strain plots that show the material's elasticity. The results show that the thermal interface material, LMEC, is highly stretchable with an average failure strain of 979% while the thermal insulation material, HMEC, is slightly stiffer with a reduced failure strain of 768%. This difference comes from embedding liquid inclusions versus solid, yet hollow microspheres. When testing specimens with 12% infill HMEC in the reduced section, the failure strain remains reasonably high at 710%. These material properties imply that the TEDs are expected to show a high level of stretchability regardless of the embedded TE pellets and layered structure.

Tensile tests on the four types of TEDs made of functional composites demonstrate remarkable mechanical strain at failure of nearly 600%, except for the device with interlayer gap (Figure 3.3b). This level of extensibility comes from the intrinsic properties of the base elastomer and the seamless fabrication process, while the TE pellets in the core layer cause stress concentration in the soft structure, restricting its stretchability. Since the TED with interlayer gap lacks materials in the core layer to provide structural support for the thermal interface layers and TE pellets, this design tends to experience premature failure under tension. In Figure 3.3c, a comparison of device stiffness reveals that the TED with 100% Elastomer shows the lowest stiffness, while the device with 100% HMEC exhibits the highest average stiffness due to HMEC's greater stiffness compared to unmodified elastomer and thermal interface layers. However, reducing the infill percentage mitigates the stiffening effect of the HMEC on the device. This result indicates that TEDs with air pockets are mechanically robust and capable of achieving conformal contact with non-planar surfaces for effective thermoelectric energy conversion.

Room-temperature liquid metal electrodes and the elastomer encapsulation provide TED with a stable electrical response under large deformations. Cyclic loading tests for each TE tensile specimen are conducted to study electromechanical robustness over an extended period, as shown in Figure 3.3d. A 50% strain was chosen, which is the strain that the TED in the first study failed and exceeds the commonly used design criterion for wearable electronics.[187,208] The excellent electrical conductivity and fluidity of liquid metal interconnects result in a negligible change in the internal resistance of the TEDs over 2,000 cycles. Examining the resistance changes when the TED with air pockets is stretched to twice its original length reveals that the electrical connections in TED remain intact at 100% strain, with only a minor increase in resistance by 0.14 Ω (Figure A.6). This stable electrical response, combined with the thermoelectric performance and mechanical strength of the four different device architectures, leads to the conclusion that the design featuring high aspect ratio TE legs with air pockets in the core layer is suitable for wearables.

Besides stable electromechanical response, the energy harvesting performance of the TED with air pockets is studied under tensile strain to ensure its capability to generate power when stretched. Figure 3.3e shows the measured V_{OC} at ΔT = 20 °C as a function of applied uniaxial strain, varying from 0% to 50%. Although the peak value slightly decreases with higher strain,

there are negligible variations in output voltage when the device reaches thermal equilibrium. This is because initially, the thermal interface deforms nonuniformly due to the embedded rigid TE legs, resulting in less conformal contact with the hot surface (Figure 3.3e-inset) and reduced heat flux in the TE. However, the LMEC thermal interface effectively transfers heat over time, resulting in a constant voltage across the strain range from 0% to 50%.

The excellent stretchability of thermoelectric devices with a 3D soft architecture is also evident from their stable internal resistance up to a strain level of 230%, as shown in Figure 3.3f. This indicates that the device remains fully operational until it experiences exceptionally high tensile strain. Under such large deformations, the rigid TE pellets can disrupt the connection between the liquid phase conductive traces, causing sudden electrical failure. Since these devices do not mechanically fail up to 600% strain, the once electrically failed TE specimens recover their functionality when returned to their initial state at 0% strain. This is because of the elastic deformation and resilience of the stretchable 3D architecture, which realigns the LM interconnects when the strain is removed, and the fluidity of the LM, which allows it to reconnect and regain electrical conductivity upon contact with other segments of the LM traces.

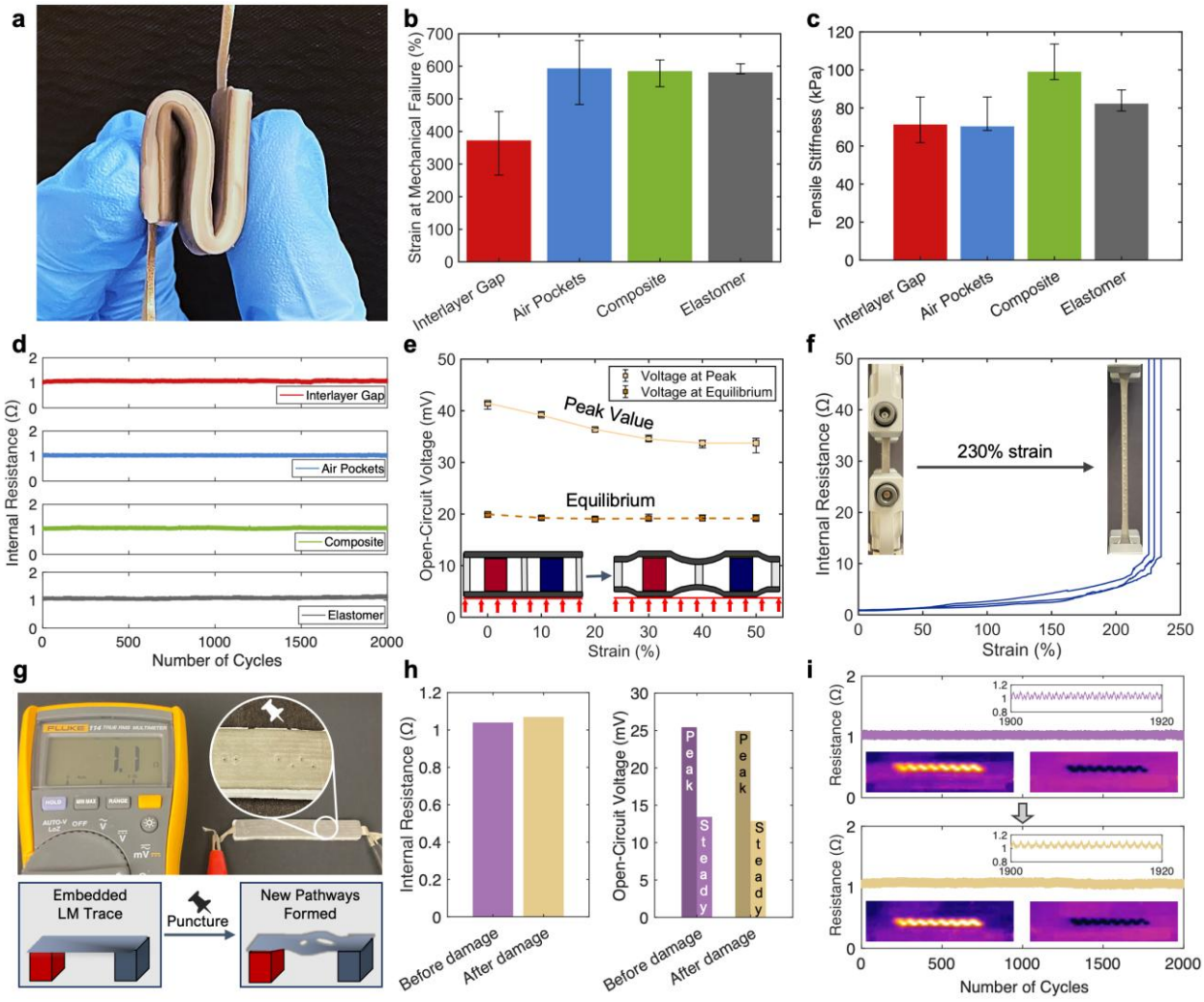

Figure 3.3. Electromechanical response and self-healing: (a) Photograph of folded TED with air pockets. (b) Maximum strain at mechanical failure and (c) Measured stiffness of four different designs under uniaxial tension. (d) Measured internal resistances of four different TE tensile specimens over 2,000 cycles of 0 to 50% uniaxial strain. (e) Measured open circuit voltages of air pocket TE tensile specimen under 0 to 50% uniaxial strain at the temperature gradient of 20 °C. Inset: schematics of TED cross-section when uniaxially strained. (f) Measured internal resistances of air pocket TE tensile specimen with electrical disconnection at 230% strain on average. (g) A photograph of the TE specimen after being punctured by a pushpin (top) and the schematic of electrical self-healing (bottom). (h) Measured internal resistance and open-circuit voltage responses at peak and thermal equilibrium of the TED tensile specimen before and after being pierced by a push pin. (i) Measured internal resistances before and after being punctured for over 2,000 stretching cycles of 50% uniaxial strain. Inset: IR images of active heating (left) and cooling (right) before and after damage.

Alongside extreme stretchability, LM interconnects equip the TEDs with electrical self-healing during operation. Figure 3.3g illustrates the device's ability to self-repair and maintain its functionality, even after being punctured multiple times with a sharp object. This autonomous self-healing feature is demonstrated by comparing the internal resistance and open-circuit voltage of the TED before and after damage. As depicted in Figure 3.3h, the resistance and V_{OC}

show negligible change in both peak and steady-state response after the device is punctured with a push pin. The self-healing behavior of the LM circuitry is attributed to the formation of new conductive pathways in the EGaIn interconnects and the immediate formation of the gallium oxide layer upon each piercing or cut.[27,209–211] Furthermore, the soft elastomer composites in TED keep the device physically intact, preventing premature mechanical failure. To further highlight this unique capability, the electromechanical response of the TED is examined with air pockets before and after damage. Figure 3.3i shows the measured device resistance during cyclic mechanical loading from 0 to 50% strain for 2,000 cycles. The damaged device exhibits virtually identical electrical responses with no apparent signs of mechanical or electrical failure. The demonstrated high level of damage tolerance and stable electromechanical behavior suggests not only consistent thermoelectric energy conversion but also robust temperature modulation even after the piercing. To illustrate this, TED's heating and cooling performance are analyzed by comparing the IR photos before and after damage in Figure 3.3h-inset. This self-repair behavior is due to the reconfigured LM pathways connecting the TE legs, confirming that these thermoelectrics can also maintain their functionality as a temperature modulator when damaged. The mechanical robustness and consistent high performance, even under severe conditions, lay a foundation for their macro-scale implementation and practical applications.

3.5. Macro-TED with Practical Wearable Applications

TEDs must cover an optimal area to harvest considerable amounts of energy at low temperature gradients or effectively heat up or cool down surfaces on demand, enabling applications such as powering sensors or providing localized thermal comfort. To address this need, the insights from the systematic study are leveraged to fabricate Macro-TEDs with air pockets in the core layer and 48 pairs of high aspect ratio TE semiconductors (Figure 3.4a). The maximum output voltage is measured in the range of 115.7 mV to 648.5 mV which reduces to ~30% of its peak value after reaching thermal equilibrium, as temperature across the thermoelectric generator varies from 10 to 60 °C (Figure 3.4b). Similarly, the generated power decreases to ~8.3% of its peak value and stabilizes at 0.12 mW and 3.19 mW for the initial temperature gradients of 10 and 60 °C as shown in Figure 3.4c. For all different temperature ranges, the optimal power is obtained when the external load resistor is 2 Ω, which is relatively close to the TED's internal resistance at 2.7 Ω. With the One Side Heat Conduction method, power densities are measured up to 3 $mW \cdot cm^{-2}$ at ΔT = 60 °C when considering the peak value. However, for practical purposes, the

power density at equilibrium is considered, which ranges from 9.3 $\mu W \cdot cm^{-2}$ to 241.8 $\mu W \cdot cm^{-2}$ based on the initial temperature difference. This great power-harvesting capability, especially at low temperature gradients, makes the stretchable thermoelectric generator an ideal candidate for emerging applications, such as self-powered wearable electronics.

To further enhance thermoelectric energy conversion under steady-state conditions, a soft and stretchable heatsink is 3D printed using the same liquid metal composite on one side of the Macro-TED. As illustrated in Figure 3.4d, the heatsink effortlessly bends and stretches along with the device due to its inherent compliance. This innovative heatsink, featuring 3D soft architecture, is anticipated to improve heat management within the device, particularly in the context of convection boundary conditions. As shown in Figure 3.4e, the power density at thermal equilibrium is dramatically increased from 9.3 $\mu W \cdot cm^{-2}$ to 16.1 $\mu W \cdot cm^{-2}$ at the low-temperature gradient of 10 °C, and from 241.8 $\mu W \cdot cm^{-2}$ to 358.5 $\mu W \cdot cm^{-2}$ at ΔT = 60 °C, respectively, by printing the soft 3D structured heatsink. Alongside power measurements, we studied changes in V_{OC} over time, as shown in Figure 3.4f. The integrated heatsink increases TED's output voltage at equilibrium from 190.7 mV to 231.5 mV at ΔT = 60 °C. However, the heatsink is expected to be more effective under airflow conditions. Under simulated "light breeze" condition (i.e., wind speed of 2.5 m/s), the TED exhibits a higher harvested voltage with faster convergency, while maintaining similar peak values. Under this forced air convection, V_{OC} at steady-state condition increases from 341.9 to 388.5 mV with the stretchable heat dissipator. Similar trends are observed for V_{OC} under different temperature gradients, as shown in Figure 3.4g. This data indicates the effectiveness of the 3D heatsink, resulting in a 32.2% increase in V_{OC} without any airflow and an additional 17.5% increase after enhancing the output voltage through forced air convection.

Excluding the performance enhancements achieved under light breeze conditions, which may not be applicable in certain working environments, this soft-matter-engineered thermoelectric generator demonstrates an overall 70% increase in output voltage. This improvement is attributed to the thermal insulation material (13%), core layer architecture (14%), and deformable heatsink (32%). To showcase the collective impact of employing 3D soft architecture in TEDs, the generated power is utilized to charge a coin cell battery, comparing it with a flexible TED in the first study as the control specimen. Figure 3.4h shows the measured voltages

of the battery during charging with an initial ΔT of 60 °C. The TED with 3D soft architectures exhibits a faster charging rate compared to the reference device which has an unfilled elastomer and low aspect ratio TE legs in the core layer and lacks the 3D heatsink. This result indicates the promising application of high-performance stretchable thermoelectrics in self-sustainable electronics.

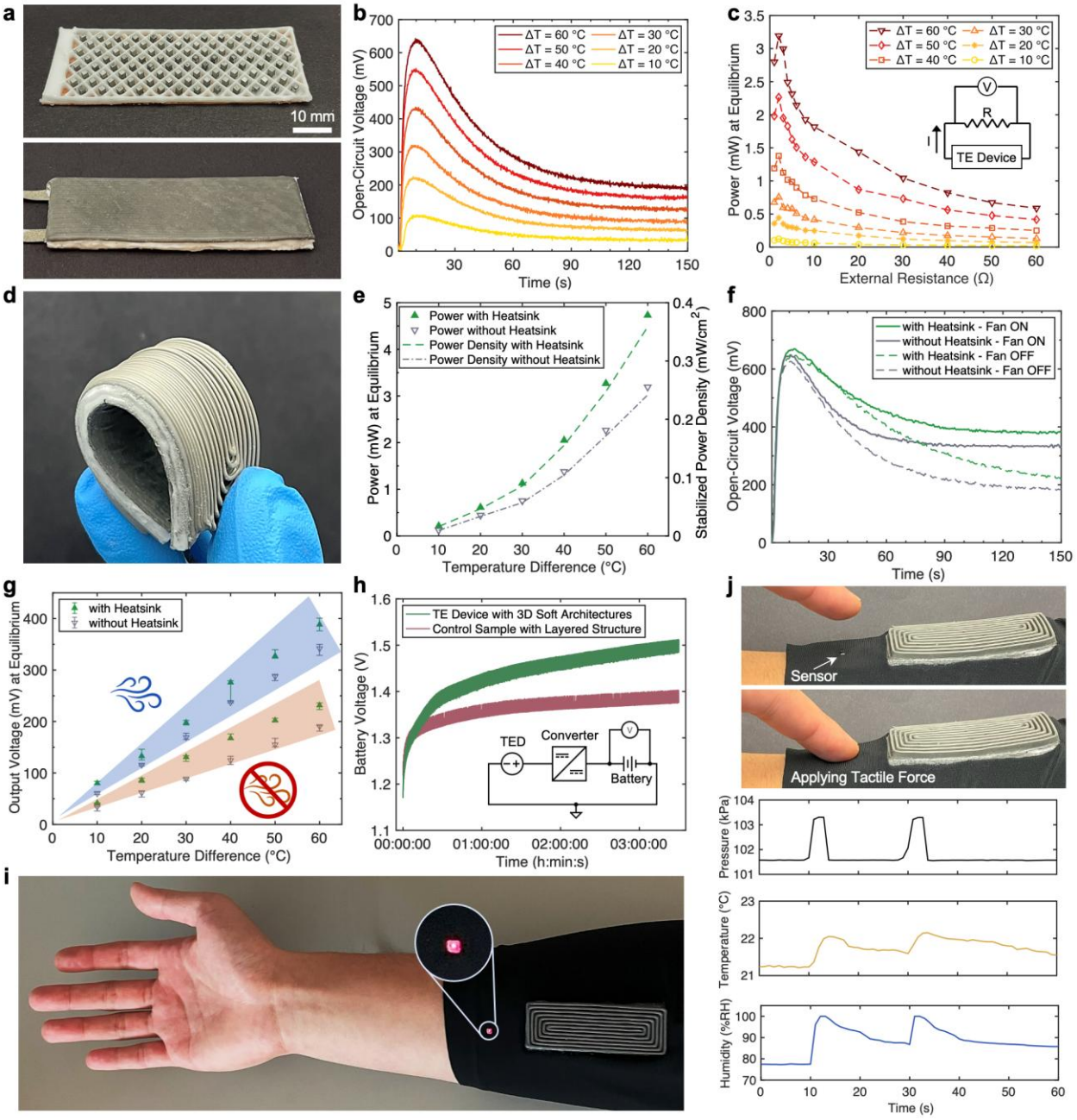

Figure 3.4. Macro-TED with 3D soft architecture for higher energy harvesting performance and applications. (a) Photographs of Macro-TED with 12% infill core layer and a dimension of 60×22×4 mm^3. (b) Measured open-circuit voltage of Macro-TED at ΔT = 10–60 °C with respect to time. (c) Measured power delivered from TED to load

resistor at thermal equilibrium at ΔT = 10–60 °C with respect to the resistance. (d) A photograph of Macro-TED with a stretchable heatsink being bent, showing its superior flexibility. (e) Measured power and power density of the Macro-TED at thermal equilibrium with and without the stretchable heatsink with respect to the temperature gradient. (f) Measured open-circuit voltage of Macro-TED with and without the heatsink and forced air convection as a function of time at ΔT = 60 °C. (g) Open-circuit voltage at thermal equilibrium with and without the heatsink and forced air convection as a function of the temperature gradient. (h) Measured battery voltage charged by TEDs with and without the 3D soft architecture at ΔT = 60 °C. An inset schematic shows the battery charging circuit with a boost converter. (i) A photograph of an LED powered by harvested energy from body heat at room temperature (24 °C). (j) Photographs that show sensors powered by TED being touched with a finger for wearable applications (top). Measured pressure, temperature, and humidity from the sensors powered by TED with respect to time (bottom).

The most enabling features of stretchable TEDs are their ability to conformally contact non-planar surfaces and effective energy conversion at low temperature gradients for realizing their full potential in wearable technology. Having addressed these two major bottlenecks, these TEDs can be worn on the body to directly power LEDs and sensors. Figure 3.4i shows that the TED illuminates an LED the moment it is placed on the forearm at room temperature. The temperature gradient between the forearm (34 °C) and the ambient temperature (24 °C) is only 10°C, yet it is sufficient to power the LED due to the TED's enhanced performance. This stretchable TED exhibits remarkable performance, efficiently harnessing body heat for immediate LED activation, indicating their potential as a viable power source for wearables.

Moreover, wearable thermoelectric generator can power off-the-shelf sensors, facilitating dual sensing capabilities – one for pressure and temperature sensing and another for temperature and humidity sensing (Figure 3.4j). Both the thermoelectric device and the sensors are seamlessly integrated into a textile and worn on the forearm. The data indicates an instantaneous response of measured pressure and humidity to applied tactile force on the respective sensors and consistent values are measured upon repeated touches. The recorded high humidity and low temperature are due to the cold and rainy weather conditions during the experiment. This outcome demonstrates the advancements towards self-powered electronics, as TED eliminates the need for batteries and the associated inconvenience of replacement or recharging.

3.6. Conclusion

Soft and stretchable thermoelectric devices are reported in Chapter 3, distinguished by their unprecedented energy density and physical robustness which make it well-suited for emerging applications such as wearables and self-sustainable electronics. Employing multiphysics simulation, various device architectures are analyzed with the aim of sustaining a prolonged temperature gradient across the embedded TE semiconductors. Experimental validations

confirmed the effectiveness of the TED with air pockets and a supporting structure made from insulating elastomer composites at the core layer. This specific device architecture with tailored multifunctional composites not only showed high thermoelectric energy conversion but also exhibited significant structural integrity, withstanding stretching up to 230% strain before experiencing electrical failure. Extending the analysis to the damage tolerance of these stretchable TEDs, the findings revealed no perceptible changes in electrical resistance, electromechanical response, energy harvesting performance, and active heating and cooling functionalities before and after being punctured with a sharp object. The electrical self-healing and stability demonstrated in the damaged device, even under 50% strain for over 2,000 cycles, can be attributed to the incorporation of liquid metal conductors and the utilization of ultra-soft elastomer composites in these TEDs.

The scalability of the design and additive manufacturing process was showcased through the fabrication of a "Macro-TED" composed of 96 rigid TE pellets. Additionally, directly integrated soft 3D structure on the TED served as a stretchable heatsink to enhance the device's internal heat flux management. This Macro-TED, equipped with the heatsink, exhibited a power density peaking at 115.4 $\mu W \cdot cm^{-2}$, which stabilized at 16.1 $\mu W \cdot cm^{-2}$ under a low temperature gradient of 10 °C. While the data confirmed the further improvement of thermoelectric energy conversion under forced air convection, TED's capability as a power supply unit was demonstrated through powering electronics when worn on the body at an ambient temperature of 24 °C, eliminating the need for additional energy storage devices. These results and demonstrations highlight the potential of the high-performance, damage-tolerant, and stretchable thermoelectric devices in emerging applications such as wearable electronics, soft robotics, and self-sustainable intelligent systems.

This study showed how material properties and device structure affect thermoelectric performance. Through systematic design, multiphysics simulation, and 3D printed layers, the device achieved excellent thermoelectric performance and stretchability to be used as a wearable energy harvesting application. Up to this chapter, I have shown how 3D printed thermoelectric device architectures with soft composites address the impending bottleneck in wearable thermoelectrics from coupled material, architecture, and manufacturing aspects. However, the devices' interface which directly contacts skin is not designed considering the long-term wearing comfort. Current impermeable skin-electronics interfaces will obstruct sweat pores, causing skin

irritations and discomfort. As wearable devices trend toward continuous and long-term applications, it is essential to resolve this occlusion problem. However, introducing breathability to the interfaces will significantly reduce effective thermal conductivity and increase contact resistance. As discussed in introduction, these trade-offs are detrimental in thermoelectric performance. This conflict leads to Chapter 4, where permeable thermal interface layers in thermoelectric wearables are fabricated via EHD printing.

Chapter 4: Permeable Interfaces in Recyclable Thermoelectric Wearables

Y. Han, C. S. Fernandes, E. Davis, and M. H. Malakooti, Electrohydrodynamic Printing of Liquid Metal Composites for Breathable Interfaces in Recyclable Thermoelectric Wearables. *ACS Appl. Mater. Interfaces.* Under Review.

4.1. Introduction

In this chapter, wearable thermoelectric generators with breathable and thermally conductive interfaces are presented to address the third research objective: "Electrohydrodynamic printing enables fabrication of permeable and thermally conductive skin–device interfaces." This is achieved by sweat pore considered interface design and micropatterning of liquid metal–boron nitride–thermoplastic polyurethane (LM–BN–TPU) composites through electrohydrodynamic printing (Figure 4.1a). The ink is synthesized by dispersing LM and BN particles in TPU polymer matrix to enhance thermal conductivity and suppress electrical conduction while maintaining processability for EHD printing. The printed mat with lattice geometry is specifically designed to avoid blocking sweat pores while maximizing heat transfer through its layer (Figure 4.1b). This approach helps mitigate the trade-off between thermal conductivity and permeability in skin-electronics interfaces, achieving a through-plane thermal conductivity of 0.37 $W \cdot m^{-1} \cdot K^{-1}$ and maintaining a water vapor transmission rate comparable to that of textiles used in sports garments (Figure 4.1c).

The EHD-printed LM–BN–TPU composites are employed as thermal interfaces in breathable TEDs (Figure 4.1d). The device has two EHD-printed layers on top and bottom. The bottom side acts as a permeable thermal interface between the skin and TED, while the top side behaves as a micropatterned composite heatsink that enhances heat dissipation. In the device's core, bismuth telluride (Bi_2Te_3) thermoelectric pellets are embedded in laser-patterned TPU layers. The patterned TPU layer holds TE pellets under deformation while allowing air and sweat to traverse the device. The TE pellets are electrically connected using sprayed LM and encapsulated with a composite of LM and styrene-ethylene-butadiene-styrene (SEBS), which prevents LM leakage and mechanically interlocks the thermal interfaces and the core layer. The thermoelectric energy harvesting performance was systematically investigated through both computational simulations and experimental characterization, spanning device design optimization to performance validation. As a result, this TED generated 5.32 μW at thermal equilibrium under an initial temperature gradient of 10 °C. Furthermore, when the device is mounted on the biceps at room

temperature, it generated a power density of 1.38 $nW \cdot cm^{-2}$ under quasi-static conditions while the subject stood still. Recyclability was also investigated for sustainable use of breathable TEDs, especially to recover the conductive fillers and TE pellets. The retrieved components were subsequently used to reconstruct TEDs that show uninterrupted energy harvesting performance. Table A.3 highlights the novelty of this work, which combines permeability, wearing comfort, high power density, and recyclability. The proposed approach mitigates the compromise between breathability and heat transfer efficiency in permeable thermal interfaces, addressing the long-standing design constraint.

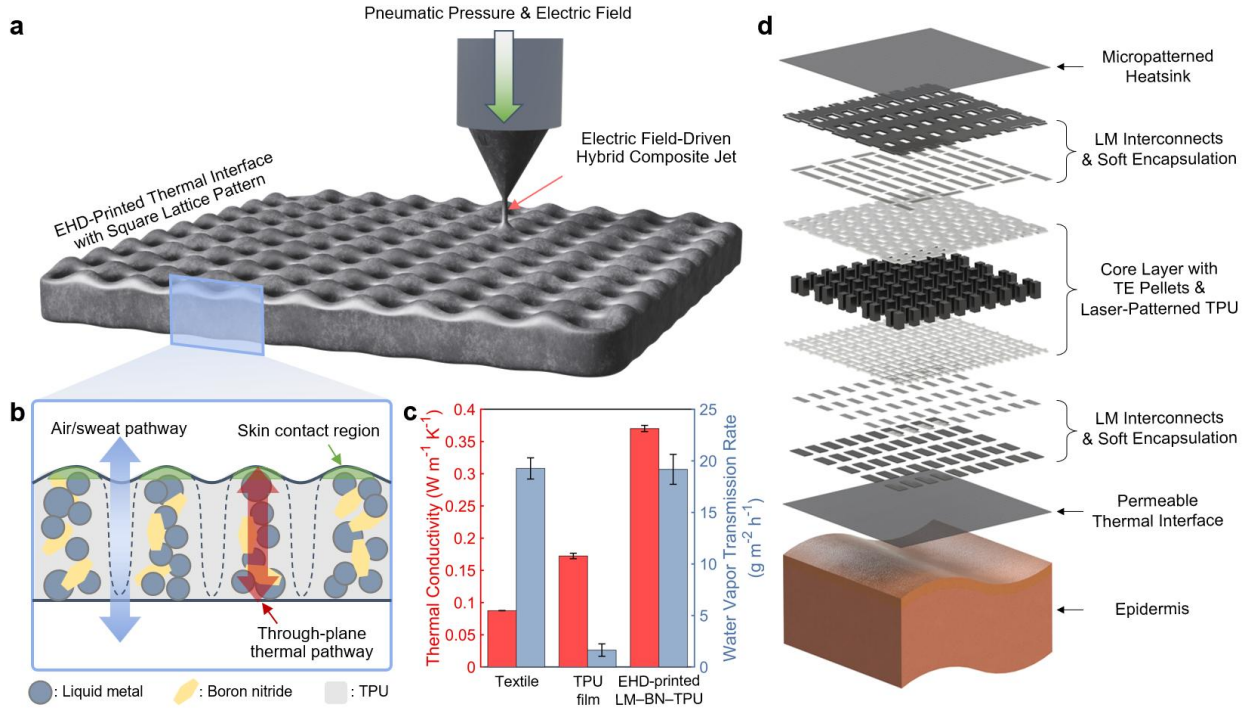

Figure 4.1. EHD-printed permeable thermal interfaces and thermoelectric device application: (a) A schematic of EHD printing with a square lattice pattern. (b) An illustration of EHD printed LM–BN–TPU composites. (c) Comparison of thermal conductivity and water vapor transmission rate between textile, TPU film, and EHD-printed LM–BN–TPU composites. (d) An exploded view of breathable thermoelectric device with multifunctional device layers.

4.2. Materials and Design for Skin–Electronics Interfaces

Skin–electronics interfaces intended for continuous wear should be designed with attention to skin compatibility, target body site, and sweat pore distribution. Liquid metal (eutectic gallium–indium, EGaIn) serves as the primary filler owing to its high thermal conductivity (26.4 $W \cdot m^{-1} \cdot K^{-1}$), deformability, skin compatibility, and processability in polymer solutions.[23,24] However, EGaIn also has high electrical conductivity (3.4×10^6 $S \cdot m^{-1}$), so a high loading can make the

composite electrically conductive. To keep the composite electrically insulating, BN platelets, which are electrically insulating yet thermally conductive, were introduced as a secondary filler.[212–215] BN has a high in-plane thermal conductivity (~400 $W \cdot m^{-1} \cdot K^{-1}$), a wide band gap (5.95 eV), a dielectric constant of 3−7, and a high dielectric strength (80–147 $kV \cdot mm^{-1}$), which complement the properties of EGaIn for EHD printing. These fillers were dispersed by probe sonication following TPU dissolution to prepare the LM–BN–TPU ink (Figure A.7).

To provide both breathability and heat conduction, the area of the skin-contact regions was controlled to be small enough to leave sweat pores unobstructed while remaining large enough to support heat conduction from skin. The upper chest, shoulder, and arm were selected as regions of interest, as these sites are commonly targeted for on-skin health-monitoring devices.[120] The sweat pore distribution in these regions was modeled conservatively to inform the design of the interface layer with a sweat pore diameter of 80 μm and a distance between the sweat pores of 400 μm (Figure A.8).[143]

The skin contact regions are circular as the undulating topography of EHD-printed structures arises from node accumulation in additive manufacturing. When inks are deposited repeatedly from multiple directions, material builds up at the intersections of printed lines. Consequently, EHD printing produces dome-like protrusions at the nodes, which yield discrete and circular skin-contact points (Figure A.9). To print permeable patterns, a square lattice is selected because it can densely fill a confined area while requiring only two depositions per node when printed in an Eulerian path (i.e., single-stroke drawing). Alternative two-dimensional geometries, including triangular or honeycomb grids, require three or more depositions per node per layer, leading to excessive node accumulation that hinders reliable multilayer stacking. This undulating geometry also preserves permeability when electronic components are mounted on the planar side of the interface. In EHD-printed interfaces, however, the lateral gaps between contact points from the wavy profile provide pathways for air and moisture transport, thereby preventing sweat pore occlusion.

4.3. Electrohydrodynamic Printing of Hybrid Filler Composites

EHD printing is an electric-field driven additive manufacturing process (Figure 4.2a). By applying high voltage at the emitter or nozzle, dielectric polymer inks become charged and are drawn into a Taylor cone geometry. When the Coulombic force within the Taylor cone exceeds

the surface tension of the ink, a continuous jet or discrete droplets are dispensed from the emitter, enabling additive ink deposition. Figure 4.2b shows EHD printing using the LM–BN–TPU composite ink. The fabricated mat is optically translucent due to square airways, confirming the mat's permeability (Figure 4.2c). It is observed that the printed line width decreases with successive layer stacking, such that lines deposited in the first layer are wider than those in subsequent layers as shown in Figure 4.2d. This height change is due to the line-by-line deposition followed by layer stacking. As a result, the bottom side of the EHD-printed interfaces always has a flat surface and wider traces, making it well-suited for attaching other layers or mounting electronic components.

EHD printing is highly sensitive to various processing parameters, including ink properties, nozzle diameter, solvent ratio, nozzle-to-substrate standoff distance, and applied electric field. Given the interdependence of these parameters, systematic optimization is crucial for successful printing. Figure 4.2e shows the experimentally determined EHD printability with respect to LM–BN–TPU ink composition. Increasing the LM volume fraction (V_f) enhances thermal conductivity, but an excessive LM V_f above 60% promotes electrical conduction through the composite. Moreover, at LM V_f exceeding 65% of the total ink, arcing was observed between the metallic nozzle and the substrate during printing at voltages as low as 150 V, causing print defects and interrupting continuous deposition. Increasing the BN content similarly improves thermal conductivity and dielectric stability, but the solid particulate filler is prone to clogging narrow nozzle tips. Based on compositional screening, a 55:5:40 composite (i.e., LM:BN:TPU volume ratio of 55:5:40) was selected as the optimal ink formulation.

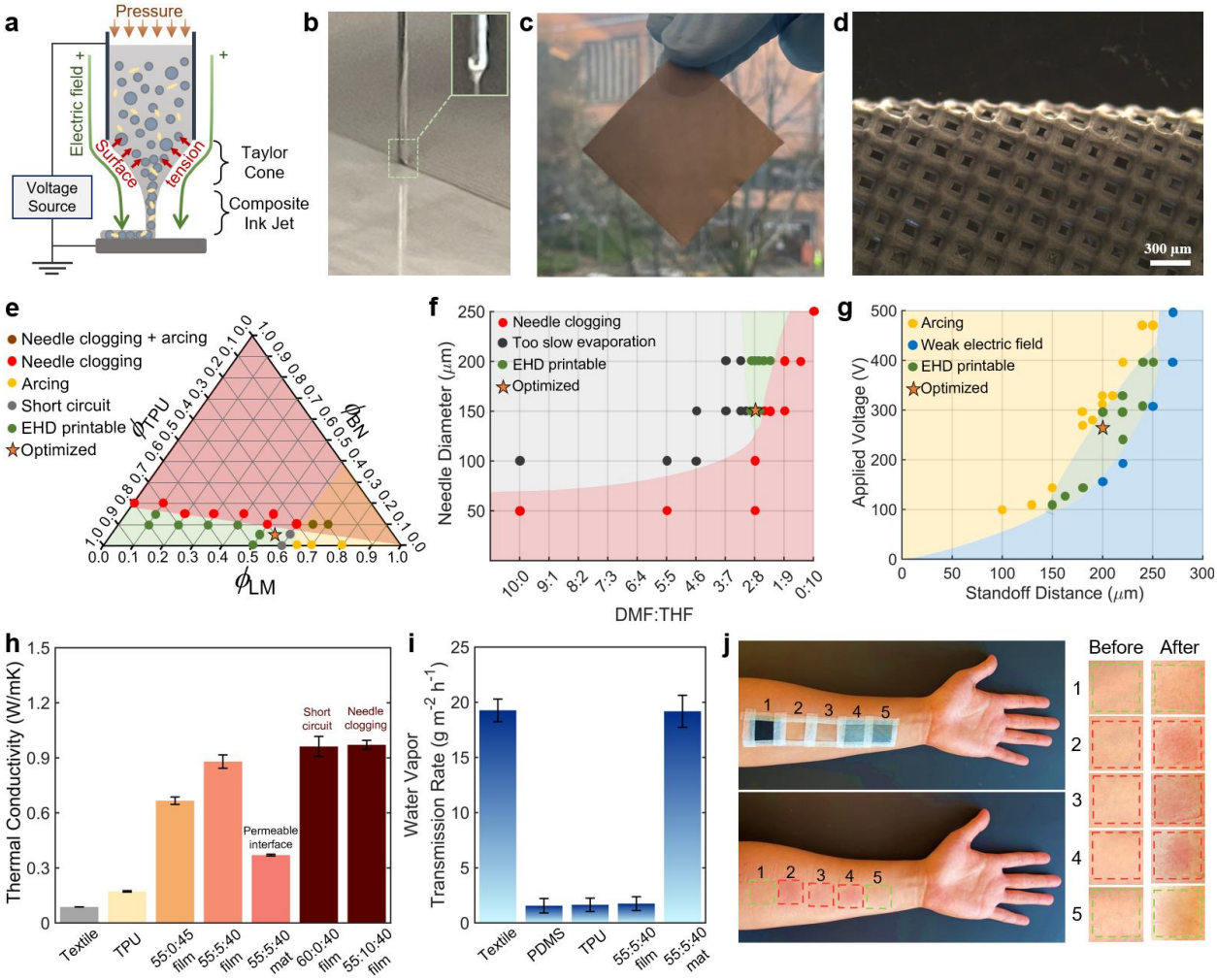

Figure 4.2. EHD printing of permeable thermal interfaces using LM–BN–TPU composites: (a) EHD printing mechanism. (b) Photograph showing LM–BN–TPU composite ink EHD printing. Inset: Zoomed-in image during EHD printing. (c) Photograph of translucent permeable interface. (d) Microscopic image of permeable interface. (e) Ternary plot for LM:BN:TPU ratios and EHD printability. (f) EHD printability as a function of needle diameter and solvent ratio. (g) EHD printability as a function of applied voltage and standoff distance. (h) Thermal conductivities of textile and LM–BN–TPU composite). (i) Water vapor transmission rate of textile, PDMS, and LM–BN–TPU composites. j) one-week skin allergy test for: (1) textile, (2) PDMS, (3) TPU film, (4) 55:5:40 LM–BN–TPU film, and (5) EHD-printed 55:5:40 LM–BN–TPU mat.

Needle diameter and solvent composition are additional determinants of EHD printability and print resolution (Figure 4.2f). A 30-gauge stainless steel needle with an inner diameter of 150 μm was selected as it enables deposition at the resolution required by the interface design, while not being too small to cause clogging. Using the selected needle diameter, the solvent composition was investigated, which determines ink evaporation rate and printed trace fidelity. Two solvents were evaluated: dimethylformamide (DMF), which has high polarity and a relatively low evaporation rate that promotes stable jetting and prolongs the liquid state of the ink; and

tetrahydrofuran (THF), which evaporates rapidly and facilitates the formation of sharper, well-defined traces. Balancing these solvents is critical because excessively slow drying from a high ratio of DMF causes printed lines to lose shape and re-dissolve previously deposited structures, while a high ratio of THF leads to excessively fast drying, premature solidification at the nozzle tip, and clogging. For the selected ink composition and needle diameter, a DMF:THF volume ratio of 2:8 produced stable jetting and precise patterning without nozzle clogging.

Standoff distance is another parameter that must be optimized (Figure 4.2g). When the standoff distance, defined as the needle-to-substrate distance, is large (>1 mm), jet instability arises, resulting in unpredictable whipping or dripping.[216] These behaviors are used in other techniques, such as electrospinning or electrospraying, for fabricating bulk fibrous or particulate structures, but they lack patterning capability. Conversely, when the needle is positioned too close to the substrate, the electric field may exceed the dielectric breakdown strength of the working medium. This leads to electrical discharge and generates an arc rather than stable Taylor cone jetting.[113] The applied voltage is also a critical parameter governing EHD printing behavior. Insufficient voltage fails to generate the electrostatic force required to sustain stable jetting, resulting in behavior resembling direct ink writing where the deposited ink forms discrete droplets rather than continuous lines (Figure A.10). In contrast, excessive voltage induces multi-jet formations with unstable trajectories or arcing. With the optimized ink composition, needle diameter, and solvent ratio, the standoff distance and applied voltage were chosen to be 200 μm and 268 V, respectively, for fabricating permeable thermal interface, corresponding to an electric field strength of 1.34 $V \cdot \mu m^{-1}$.

Ten layers of square lattice patterns were stacked with the selected EHD parameters. The number of layers was selected to balance mechanical stability and thermal performance as fewer layers make the interfaces susceptible to tearing, while excessive layers reduce heat transfer efficiency. With the resulting structure, the skin-contact region diameter was ~60 μm at each node and the height of the node was ~175 μm. For line spacing, 230 μm is identified as the optimal spacing that densely packs printed lines for through-plane heat transfer, while maintaining open square grids for permeability. These selected parameters enable EHD printing of permeable and thermally conductive layers that overcome challenges in skin-compatible soft thermal interfaces.

4.4. Permeable Skin–Electronics Thermal Interfaces

The EHD-printed mat maintains sufficient heat transfer capability, demonstrating its potential for thermal management. Figure 4.2h compares the thermal conductivity of textile, TPU film, and LM–BN–TPU composites with varying filler ratios and forms. The textile, which is commonly used in sports garments, shows the lowest thermal conductivity due to its intertwined fibrous structure, intrinsically low thermal conductivity, and high inter-fiber contact resistance. The TPU film shows slightly higher thermal conductivity of 0.17 $W \cdot m^{-1} \cdot K^{-1}$ although its film shape sacrifices the breathability. Incorporating nanosized LM particles at 55%V_f in the TPU film increases the thermal conductivity to 0.66 $W \cdot m^{-1} \cdot K^{-1}$, while the addition of 5%V_f of BN further increases it by 0.22 $W \cdot m^{-1} \cdot K^{-1}$. However, when LM content exceeds 60% or BN exceeds 10%, the composite becomes electrically conductive or experiences nozzle clogging during printing, respectively. With the optimized filler ratio and structural design, EHD-printed mat shows the average through-plane thermal conductivity of 0.37 $W \cdot m^{-1} \cdot K^{-1}$, confirming its efficient heat transfer even with the micropatterned air pathways.

The effectiveness of this permeable thermal interface is validated through computational simulation (Figure A.11 and Table A.4). The simulated temperature and thermal resistance of the TPU film, the 55:5:40 EHD-printed mat, and the 55:5:40 film show that the EHD-printed thermal interface transfers heat effectively despite its permeability. The EHD-printed mat reaches thermal equilibrium the fastest while maintaining heat dissipation comparable to that of the 55:5:40 composite film, making it suitable for breathable TED designs.

The lattice-patterned interface's permeability is comparable to that of textiles, as experimentally validated through water vapor transmission rate measurements (Figure 4.2i). Unlike polymer films with water vapor transmission rates below 2 $g \cdot m^{-2} \cdot h^{-1}$ (i.e., PDMS, TPU, and 55:5:40 composite film), the EHD-printed mat exhibits a high permeability of 19.18 $g \cdot m^{-2} \cdot h^{-1}$, exceeding the typical transepidermal water loss of human skin (5–10 $g \cdot m^{-2} \cdot h^{-1}$).[123] To evaluate long-term skin compatibility, the interface samples were attached to the forearm of a single volunteer for one week (Figure 4.2j). Polymer film samples caused redness and itchiness after approximately two days of continuous attachment, whereas the textile and EHD-printed mat samples caused no noticeable skin irritation. To further validate long-term biocompatibility of the interfaces, future investigations involving multiple volunteers and standardized skin compatibility testing methods can be conducted. The measured properties of EHD-printed 55:5:40 mat demonstrate a favorable

balance between thermal conductivity, permeability, and skin compatibility for on-skin thermal interfaces.

4.5. Breathable Thermoelectric Device Design

Soft and permeable thermal interfaces offer a promising strategy to resolve the trade-off between energy conversion efficiency and breathability in wearable thermoelectric devices. To improve thermoelectric energy harvesting while maintaining breathability, five device architectures were evaluated and compared with a reference design. The five designs shared an EHD-printed permeable interface on the hot side and differed in the TPU layer design, TE pellet spacing, and cold-side interface. The reference design used impermeable 55:5:40 composite films as thermal interfaces on both sides to provide a baseline which is made of the same materials (Figure 4.3a and Figure A.12). In Design 1, only a single thermal interface layer is present at the bottom, and the rest of the device is exposed to the ambient air, letting heat be dissipated primarily via convection. This configuration with copper interconnects not only lacks a protective layer and is therefore vulnerable to external damage but also produces the lowest output voltage as shown in Figure 4.3b. The detailed relationship between thermoelectric power generation, the temperature gradient across the TE pellets, and device structure is further illustrated in Figure A.13. The simulation results indicate that thermoelectric power generation depends on both the TE fill factor (i.e., the area packing density of thermoelectric semiconductors) and the device architecture. The energy harvesting performance is primarily governed by the temperature gradient across the TE pellets (Figure 4.3c), highlighting the importance of structural designs that enhance heat transfer along the thermoelectric elements. Design 2 incorporates encapsulated LM interconnects and laser-patterned TPU layers attached to both ends of the TE pellets, constituting the device core layer. The two TPU layers provide structural integrity by holding the TE legs in place under deformation while enabling heat conduction through the upper layer, thereby increasing the temperature gradient across the semiconductors. In Design 3, the temperature gradient is further enhanced by introducing a 55:5:40 composite film thermal interface on top of the TPU layer. However, this configuration exhibits lower energy harvesting performance than the reference design, primarily due to reduced contact with the heat source and a smaller cold side thermal interface area resulting from the suspended TPU layer.

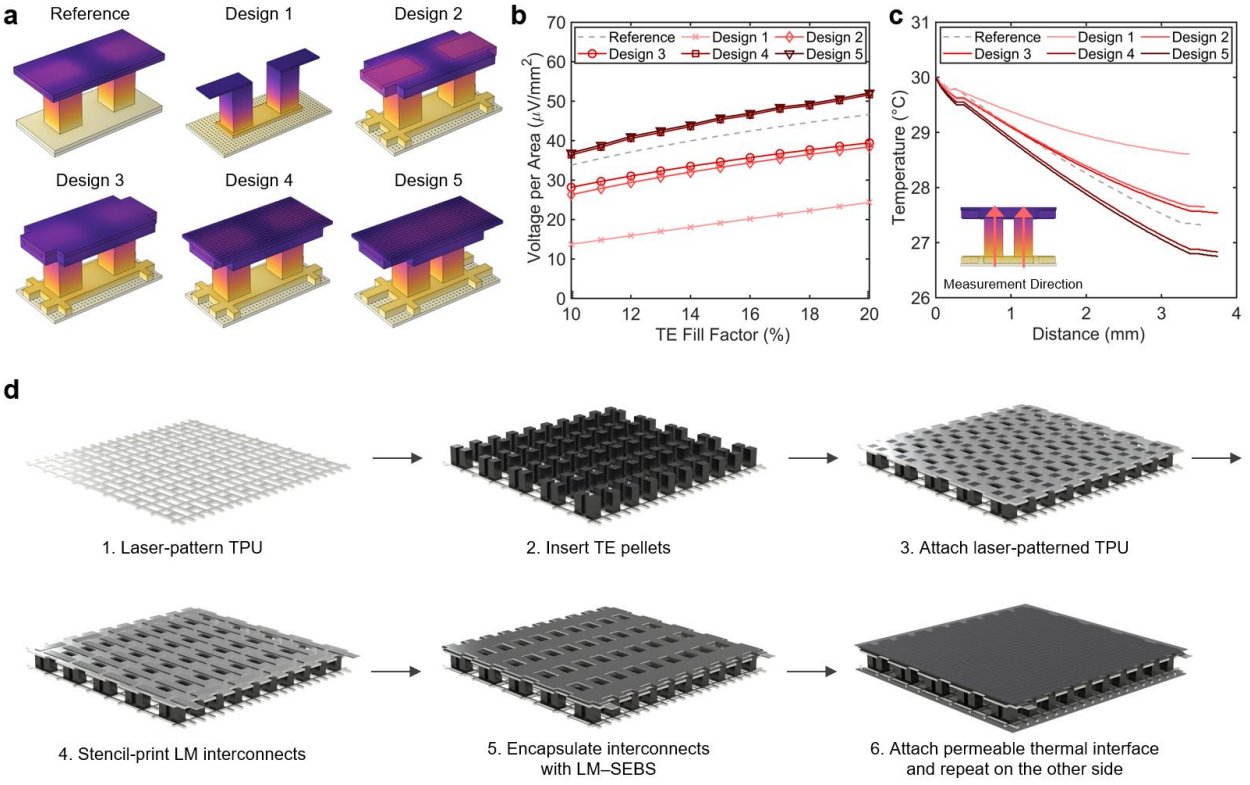

Figure 4.3. Design and fabrication of breathable thermoelectric devices: (a) Different TED designs. (b) Simulated voltage per area with respect to device design and TE fill factor. (c) Simulated temperature within the device at 16% TE fill factor with respect to device design and distance from the heat source. (d) Fabrication process for breathable thermoelectric devices.

Integrating heatsink is an effective way to enhance heat dissipation in electronic systems. In Designs 4 and 5, the EHD-printed interface is also placed on top of the device to function as a micropatterned heatsink. With this approach, the simulated output voltage and temperature gradient exceed those of the reference design. The heatsink efficiency can be evaluated through a heat transfer coefficient (Figure A.14). The heat transfer coefficient per area is estimated to be 9.25 $W \cdot m^{-2} \cdot K^{-1}$ at 16% TE fill factor in Design 5. The integrated heatsink reduces thermal resistance per area to 7.71×10^{-3} $m^2 \cdot K \cdot W^{-1}$ with the same design, facilitating heat conduction through the device.

In all designs except Design 5, the TE pellets are arranged in exactly the same pattern. However, in Design 5, the pellets in each pair are closer together, leaving larger gaps between neighboring pairs while keeping the fill factor constant. As a result, the ratio of the distance within each pair to the distance between pairs becomes 2:8. This configuration increases the open space within the TPU layers, facilitating airflow through the device. In addition, as the pellets within each pair

are positioned closer together, the pair behaves like a single mechanical unit under bending or twisting, rather than as two independent rigid elements. Reducing the spacing below this ratio leads to fabrication challenges and increases the risk of short-circuiting under mechanical deformation. The 2:8 distance ratio allows the interconnects to better accommodate deformation, improving device reliability under mechanical strain.[217] Even with these structural advantages, the thermoelectric performance remains unchanged, highlighting the benefits of closer spacing within TE pairs and larger separation between neighboring pairs. Therefore, Design 5 was chosen to further investigate the effectiveness of the permeable thermal interface through device fabrication.

With the optimized design from computational simulations, wearable TEDs are fabricated using permeable thermal interfaces (Figure 4.3d). A TE fill factor of 16% was selected as it provides substantial thermoelectric output while avoiding excessive packing of rigid semiconductor elements, which would otherwise compromise device flexibility. Additionally, beyond this fill factor, further increases in packing density do not yield proportional gains in harvested power.[45] A TPU film was first laser-patterned to create openings for inserting TE pellets and to provide air and gas pathways. P- and n-type TE pellets were then inserted into the patterned TPU layer in an alternating order. Prior to insertion, the TE pellets were dipped in a THF solvent to partially dissolve the TPU surface upon contact. After the THF solvent evaporates, the TPU resolidifies, securely anchoring the TE legs within the patterned TPU. A second TPU layer was subsequently attached to the opposite ends of the TE pellets to provide structural integrity and to serve as a substrate for the interconnects and thermal interface. Then, LM was stencil-printed to serially connect the arranged TE pellets. An LM-SEBS composite solution prepared in toluene was then deposited on top of the LM and TPU layer to prevent the liquid-state interconnects from smudging or leaking. The strategic use of the LM–SEBS composite in this layer prevents dissolution of the TPU-based layers and the permeable interface during the subsequent interlocking process (Figure A.15). The permeable interface layer was then wetted with toluene and attached to the LM–SEBS layer to partially dissolve the SEBS through the structured pores. The softened SEBS infiltrates the lattice structure, creating mechanical interlocking between the two layers through the resolidification. After repeating steps 4–6 on the opposite side to complete the fabrication, the device maintains breathability even after stacking all functional layers due to the presence of patterned TPU layers and the EHD-printed interfaces.

4.6. Device Characterization

A fabricated TED comprising 50 pairs of TE pellets with a dimension of 35×35×3.8 mm^3 is shown in Figure 4.4a. When the device contacts a hot surface, the resulting temperature difference across the semiconductors drives charge carriers from the hot to the cold region, harvesting thermal energy. Figure 4.4b shows the measured open-circuit voltage (V_{oc}) of the devices placed on a hot plate with varying initial temperatures relative to room temperature (*Initial* ΔT). Within the first 15 s, V_{oc} reaches its peak, reflecting maximum thermal transport within the TE pellets. Following this peak, the response enters a transient regime before reaching thermal equilibrium. At equilibrium, the temperature gradient across the TED (ΔT_{TED}) is significantly lower than the *Initial* ΔT, as heat transfer from the source to the device plateaus. Although the response at peak shows higher output, energy harvesting performance at equilibrium is more relevant for long-term energy harvesting under open-air wearable conditions. The measured ΔT_{TED} at equilibrium was 2.7 °C and 9.2 °C for an *Initial* ΔT of 10 °C and 40 °C, respectively (Figure 4.4c). In this realistic test setup, increasing the hot-plate temperature also raises the ambient temperature, resulting in a slightly reduced ratio between the ΔT_{TED} and *Initial* ΔT at higher temperatures. Figure 4.4d presents voltage–current sweeps through the TED at thermal equilibrium. The maximum power at an *Initial* ΔT of 10 °C and 40 °C was measured to be 5.32 μW and 103.77 μW, corresponding to power densities of 0.43 $\mu W \cdot cm^{-2}$ and 8.47 $\mu W \cdot cm^{-2}$, respectively.

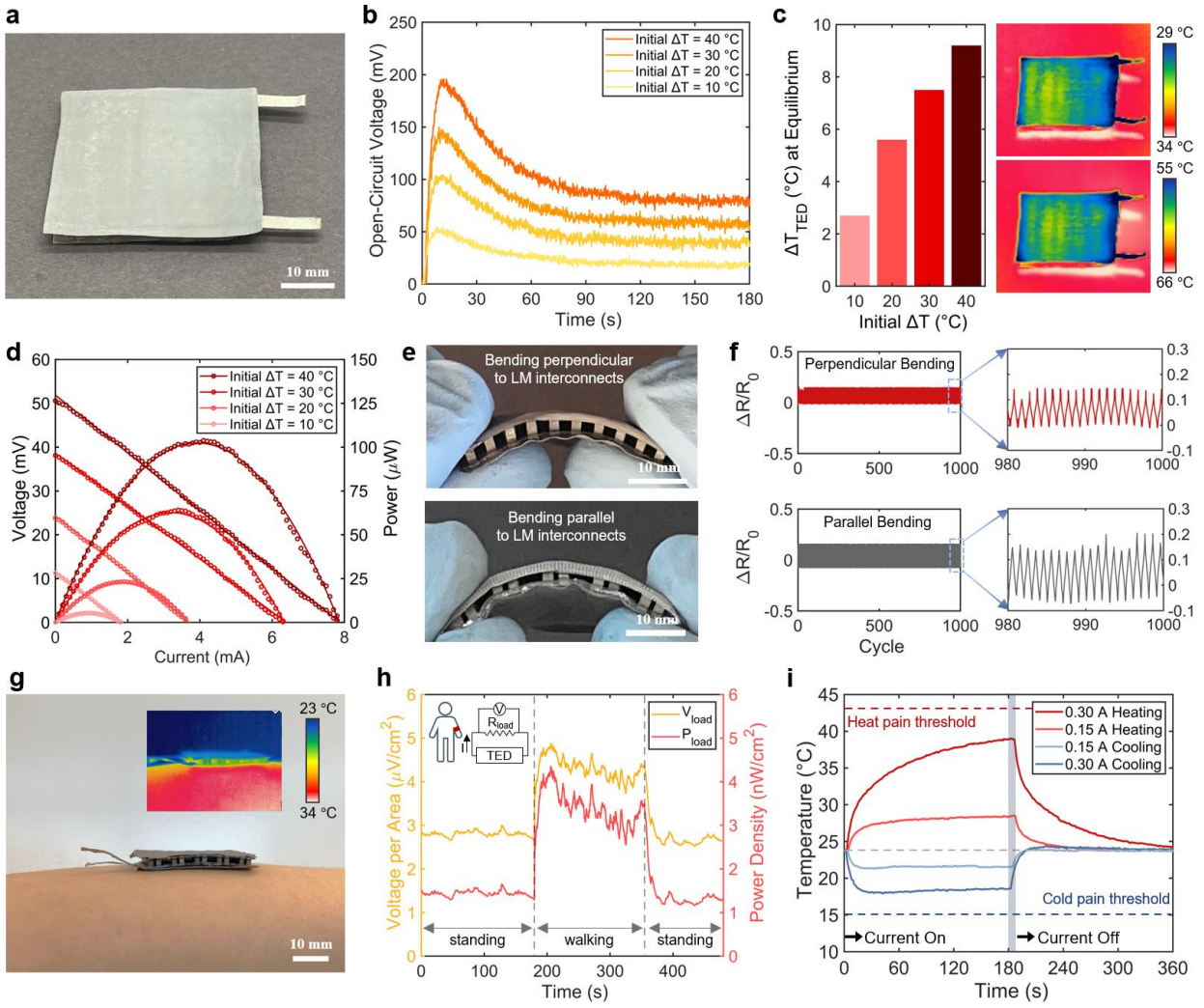

Figure 4.4. Breathable TED characterization: (a) A photograph of breathable TED. (b) Measured open-circuit voltage with different initial temperature gradients. (c) Temperature gradient across TED and IR images at thermal equilibrium. (d) Measured voltage and estimated power by sweeping through current at thermal equilibrium with different initial temperature gradients. (e) Breathable TEDs being bent in two orthogonal directions. (f) Change in resistance under cyclical bending with a bending radius of 15 mm. (g) A photograph of breathable TED on the biceps. Inset: IR image showing temperature profile of TED and the biceps. (h) Delivered voltage per area and power density when the TED was worn on biceps and a subject is standing or walking. (i) Thermoelectric heating and cooling performance with different applied currents.

Mechanical flexibility is essential for wearable devices to conform to curved body surfaces. To evaluate this, cyclic bending tests were conducted in two orthogonal directions with a bending radius of 15 mm, which reflects the curvature of target body parts (Figure 4.4e). Electrical resistance shows slightly different variations depending on the bending direction due to the different spacing ratios between TE pellets and the orientation of the LM interconnects. When bending parallel to the interconnect direction, 90 LM interconnects are stretched, whereas only 9 interconnects are stretched when the device is bent perpendicular to them. When the device is

bent perpendicular to the LM interconnects, the resistance cyclically fluctuated by 17% during repeated bending, while bending parallel to the LM interconnects results in a slightly larger fluctuation of about 20% (Figure 4.4f). These small resistance variations indicate that the wearable TEDs can conform to target body surfaces while maintaining stable electrical performance.

Actual wearable conditions often differ from the controlled environments for testing wearable electronics. Figure 4.4g shows the device placed on the biceps, with the inset infrared image illustrating the temperature distribution across the device when the biceps serve as the heat source. The delivered voltage and power under wearable conditions were characterized by using an external load resistor (R_{load}), in which the power delivered to the load resistor can be calculated as $P_{load} = {V_{load}}^2/R_{load}$ (Figure A.16).[45,46] Table A.5 summarizes the terms used to describe the output power of TEDs, providing a clear definition of each power-related term used in this study. As shown in Figure 4.4h, the device was wrapped around the biceps while a subject was either standing or walking. During walking, arm swinging and the slight increase in skin temperature caused by enhanced blood circulation increase heat transfer through the device, resulting in higher output voltage and generated power. When the subject stops walking, the output voltage returns to its baseline. These results allow us to estimate energy output under different wearable conditions and body movements.

Another function of the TEDs is active thermoelectric heating and cooling, which operates via reverse mechanism of energy harvesting.[218–220] When an electric current is applied, the TE pellets generate a temperature gradient that propagates to the thermal interfaces, producing hot or cold sensations. Figure 4.4i shows the active heating and cooling performance under varying source currents. The temperature on one side of the device was modulated by the applied current and remained within the upper and lower thresholds at which the skin begins to feel discomfort from hot or cold contact. When the current is turned off after 180 s, the temperature gradient gradually diminishes, and the device surface returns to ambient temperature. This demonstrates the successful fabrication of the device with EHD-printed permeable interfaces. It also indicates that the composite interfaces enable relatively uniform temperature modulation across the surface during both active heating and cooling, highlighting the potential of these devices to provide personalized thermal sensations in thermo-haptic applications.

4.7. Component Recycling

The rapid proliferation of electronic devices has led to an increase in electronic waste, raising environmental and sustainability concerns. As wearable electronics continue to expand, developing strategies for sustainable material recovery and reuse becomes important.[221] In particular, recycling high-value functional fillers is critical for sustainable electronic fabrication. To address this need, this study demonstrates a recycling process that enables recovery of both fillers from the LM–BN–TPU composites used in breathable thermoelectric devices (Figure 4.5a).

Upon application of toluene, the SEBS which previously interlocked the permeable thermal interfaces and the core device layer is selectively dissolved, allowing the layer separation. The recycling pathway for the permeable thermal interface is illustrated in the recycling cycle on the left side of Figure 4.5a and Figure A.17a. First, the TPU matrix within the interfaces was removed by dissolving the composite mat in THF and centrifuging the solution. After decanting the THF containing dissolved TPU, a sodium hydroxide (NaOH) solution was added to the centrifuge tube and the mixture was centrifuged. Under alkaline conditions, the liquid metal coalesced into a droplet and separated from the suspension. The NaOH solution was then decanted, and hydrochloric acid (HCl) solution was introduced to the tube to dissolve any residual gallium or indium oxide contaminants and clean the surfaces of the BN particles for reuse. Both basic and acidic solutions can be used to recycle LM by removing gallium oxide on the surface, but the NaOH solution was used first, because HCl can dissolve indium and gallium from the EGaIn core by forming metal chlorides,[222] resulting in a reduced amount of LM after recycling. After removing the HCl solution, the BN particles were sequentially washed by centrifugation in deionized water and ethanol to neutralize the BN and remove any remaining residues, respectively. The qualitative recovery of both LM and BN from the permeable interface is confirmed via energy-dispersive spectroscopy (EDS) peaks, as shown in Figure 4.5b and c.

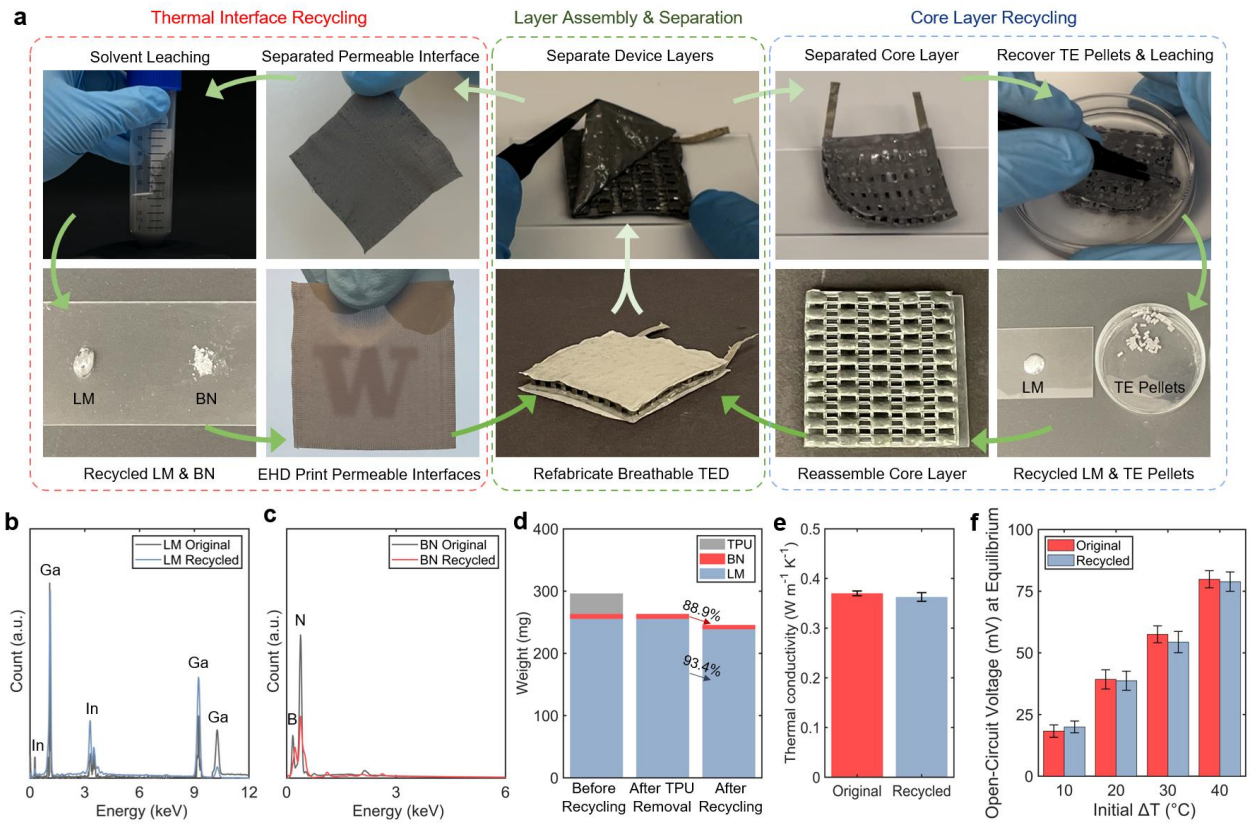

Figure 4.5. Recycling breathable thermoelectric devices. (a) Recycling process for permeable thermal interface (left), refabrication and layer separation (center), and device core layer (right). (b) EDS curves for original and recycled LM. (c) EDS curves for original and recycled BN. (d) Stacked bar plot showing the weights of LM, BN, and TPU in recycling process. (e) Measured open-circuit voltage at thermal equilibrium of TEDs before component recycling (original) and after refabrication (recycled).

The recycling efficiency is quantified by measuring the change in mass before and after the recovery process (Figure 4.5d). The permeable mat made of the 55:5:40 LM–BN–TPU composite weighed 296.60 mg after removal from the device. Following the recycling procedure, which involved sequential solvent treatment, centrifugation, and washing steps, an average of 238.71 mg of LM and 6.94 mg of BN were recovered, corresponding to recycling efficiencies of 93.4% and 88.9%, respectively. The reduced LM weight is attributed to the formation of gallium oxide or gallium oxide hydroxide during ultrasonication. These nanoparticles are detached from EGaIn droplets and are removed during multiple washing and decantation steps rather than being recovered as part of the LM droplets from the base or acid treatment. Similarly, the loss of BN is primarily attributed to the repeated centrifugation and decantation processes, during which a fraction of the nanoscale BN platelets can remain suspended in the supernatant and be inadvertently discarded. Despite these losses, the overall recycling efficiency remains high

considering that the process involves the simultaneous recovery of two different fillers with distinct physical and chemical properties. The recovered LM and BN were reused to prepare composite ink for EHD printing, demonstrating the feasibility of filler recycling. As demonstrated in Figure 4.5e, the through-plane thermal conductivity of the recycled permeable thermal interfaces remained unchanged compared with that of the original permeable interfaces.

In addition to the permeable interface, LM and TE pellets in the core layer can also be recycled (Figure 4.5a and Figure A.17b). The separated core layer was first treated with THF to dissolve the surrounding polymer matrix. The TE pellets were recovered from the dissolved solution and rinsed again with THF using planetary mixing to remove residual polymers. The remaining mixture that contained dissolved polymers and LM agglomerations was centrifuged in THF three times, allowing both SEBS and TPU to be dissolved and separated, after which an additional NaOH treatment was used to recover the LM from the core layer. The recycled components were then reused to fabricate a new breathable thermoelectric device. As shown in Figure 4.5f, the refabricated device exhibits thermoelectric performance comparable to that of the original device. These results demonstrate the recyclability of breathable TEDs and support their sustainable use.

4.8. Conclusion

EHD printing of LM–BN–TPU composites was developed to create permeable thermal interfaces for wearable thermoelectric devices. The processing parameters were tuned to achieve high-resolution features while enabling efficient heat transfer and maintaining electrical isolation between the conductive fillers. The printed composite mat was designed as a square lattice with a wavy surface profile that leaves skin sweat pores unobstructed, supporting wearing comfort over extended periods. Despite the air and vapor transport pathways through the mat, it exhibited a through-plane thermal conductivity of 0.37 $W \cdot m^{-1} \cdot K^{-1}$, indicating the effectiveness of the LM and BN dual filler system for heat conduction. The skin compatibility of the permeable interface was further evaluated through water vapor transmission rate measurements and a week-long on-skin attachment test, which gave results comparable to those of common sportswear textiles. Together, these measurements show that the EHD-printed thermal interfaces can provide both improved heat conduction and comfort during prolonged skin contact.

Building on these permeable interfaces, breathable TEDs were fabricated and characterized. The printed interface was found to act as a micropatterned heatsink when integrated on the cold side of the device, which improved thermoelectric performance. With a 16% TE fill factor, the device remained flexible while sustaining a sufficient temperature gradient across the TE semiconductors. At thermal equilibrium, it retained approximately one quarter of the initial temperature gradient, allowing continuous thermoelectric power generation. For an initial ΔT of 10 °C, the device preserved a gradient of 2.7 °C at equilibrium and produced a maximum power of 5.32 μW. On-skin tests further illustrated the potential of these devices for off-grid power generation and personalized thermoregulation in wearable applications.

Finally, the recyclability of the breathable TEDs was examined to support sustainable use of wearable electronics. Through a multi-step recycling process, the LM and BN fillers were recovered from the permeable interfaces and reused to formulate composite ink for EHD printing. The LM and TE pellets were likewise recovered from the device core layer. The refabricated devices showed thermoelectric performance comparable to that of the original devices, confirming the recyclability of both the permeable interfaces and the breathable TEDs. Collectively, these findings demonstrate a permeable and recyclable thermal interface that supports continuous TED operation during on-skin wear. The design strategy presented here may guide future development of wearable electronics.

Although the recyclable composite presented here is well suited in wearable applications, the TPU matrix has several limitations in extreme working conditions in industry settings. Under repeated thermal cycling at higher temperature, it's relatively high coefficient of thermal expansion and viscoelastic creep behavior will lead to progressive delamination and interfacial degradation, compromising long-term contact conductance at bonded surfaces. The relatively narrow temperature window of thermoplastics restricts deployment in applications where steep thermal gradients or Joule-heating can drive local temperatures beyond its typical operating range. Also, it is susceptible to hydrolytic and oxidative degradation, particularly in humid or elevated-temperature environments compared to silicone- or epoxy-based matrices. These limitations motivate the next chapter, where an alternative polymer matrix that equips chemical stability, thermomechanical robustness, and recyclability, is explored.

Chapter 5: Reconfigurable Soft Liquid Metal–Vitrimer Composites

Y. Han, S. S. Rohewal, S. Gupta, S. Paul, C. C. Bowland, and M. H. Malakooti, Conductive Liquid Metal Vitrimer Composites for Reconfigurable and Recyclable Flexible Electronics. *Adv. Funct. Mater.* 35, e11119 (2025).

5.1. Introduction

In this chapter, a recyclable and stretchable liquid metal–vitrimer (LM–Vit) composite and its two different reprocessing strategies are introduced. The thermoset-based recyclable vitrimer matrix enables both composite reconfiguration and LM recovery (Figure 5.1a). The soft vitrimer is synthesized through the covalent reaction between the epoxy groups of bisphenol A diglycidyl ether (DGEBA) and the carboxylic acid groups of catalyzed fatty acid. This reaction forms a β-hydroxy ester-based covalent adaptive network (CAN), which enables topological rearrangement of polymer chains. By incorporating EGaIn as a filler, the functional groups in the vitrimer matrix may also chemically interact with the LM particles through multiple bonding mechanisms. The LM inclusions enhance the composite's thermal conductivity by 6.53-fold at 50% volume fraction, which facilitates heat dissipation from flexible electronics (Figure 5.1b). This liquid-phase filler slightly reduces the composites' Young's modulus to 2.63 MPa while preserving its thermal stability and high failure strain (137.3% tensile strain). The embedded LM droplets provide additional functionalities such as selective electrical conductivity through mechanical sintering, which allows direct fabrication of flexible electronic circuits (Figure 5.1c).

The multifunctional solid-liquid composites exhibit can be recycled through two strategies: thermomechanical reprocessing and chemical recycling. The first method involves physically fragmenting the composite and rejoining the pieces at elevated temperatures and pressures using a hot press (Figure 5.1d). This reprocessing restores both mechanical integrity and electrical conductivity by repairing previously separated segments of the LM–Vit composite, as demonstrated by successive LED circuit reconfigurations with various geometries. During this process, the LM droplets are compressed and aligned in the in-plane direction, which results in anisotropic thermal and mechanical properties while restoring circuit functionality. The second strategy focuses on chemical retrieval of both the LM filler and the vitrimer matrix (Figure 5.1e). Due to interfacial interactions between the LM particles and the matrix, simple dissolution-based recycling is not sufficient to recover fillers. To overcome this, the LM–Vit composite is first treated with EG to dissolve the matrix that is not chemically bonded to the LM particles. The

remaining material is then treated with a mixture of EG and HCl solution, which breaks filler–matrix interactions and removes the oxide layer on the LM surface.[42,223] This approach achieves 94% recovery of the LM used in the synthesis of the composite, which is then reused to make a new circuit on the LM–Vit composite. This flexible, recyclable LM–vitrimer composite enables simple patterning of conductive traces and efficient heat dissipation, making it a truly multifunctional material platform for reconfigurable electronics and sustainable e-waste reduction.

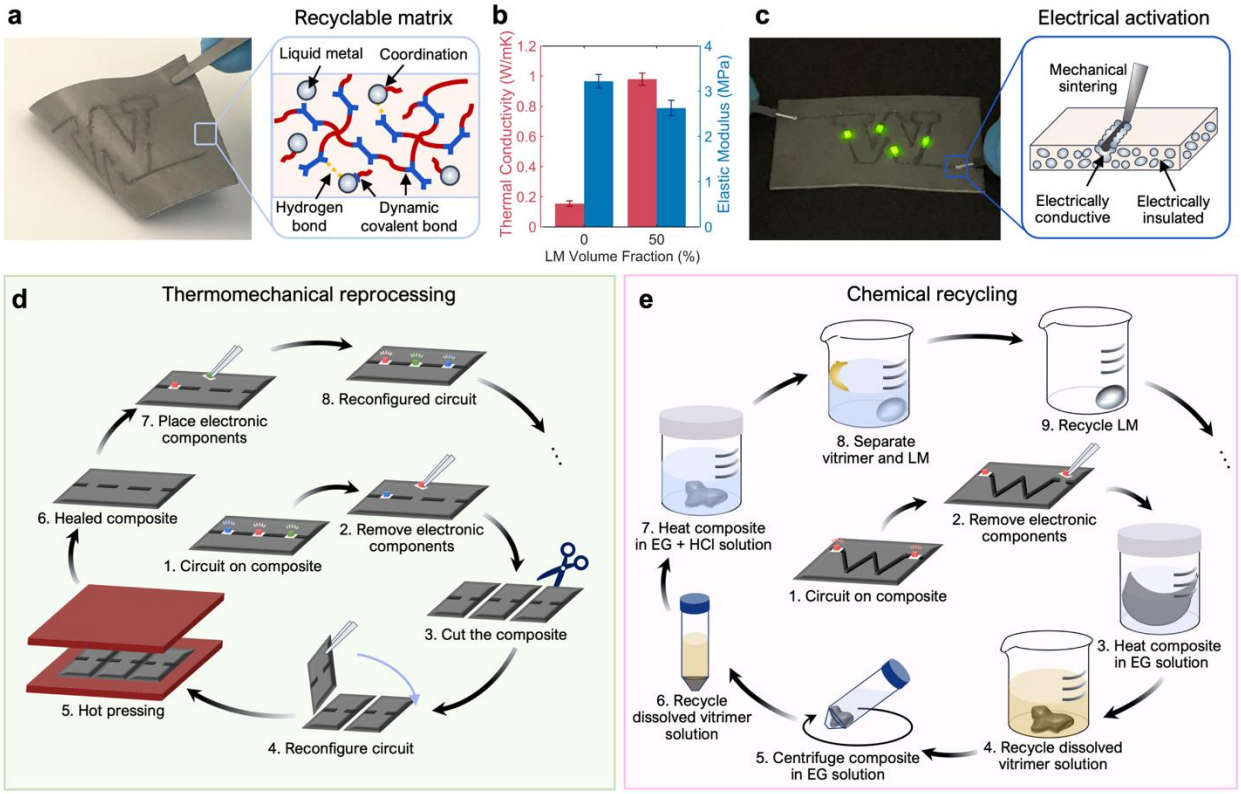

Figure 5.1. A liquid metal vitrimer (LM–Vit) composite and its recycling strategies: (a) Flexible LM–Vit composite and chemical interactions within the vitrimer matrix. (b) Improved thermal management and reduced mechanical stiffness enabled by LM incorporation. (c) Mechanically sintered conductive traces with LEDs on LM–Vit composite and the electrical activation mechanism. (d) Thermomechanical reprocessing of LM–Vit composite to reconfigure a flexible circuit. (e) Chemical recycling of LM–Vit composite to recover the LM.

5.2. Synthesis Mechanism of LM–Vitrimer Composites

Achieving small LM particle size is crucial for ensuring uniform filler dispersion within the vitrimer matrix because the viscosity of the polymer precursor significantly changes during the curing process. As crosslinking progresses, the precursor initially experiences a sharp drop in viscosity before the composite solidifies. During this low-viscosity window, large LM droplets

are prone to settling, which causes filler sedimentation and results in distinct layer separation within the composite. To prevent this issue and achieve uniform dispersion, EGaIn is first probe-sonicated in ethanol prior to mixing with the vitrimer precursor (Figure A.19), effectively reducing the average particle size to 3.85 ± 1.06 μm.[16,39] The filler volume fraction was varied from 0% to 50% with 10% increments to investigate the effect of filler content on the composite properties.

The inherent acidity of the carboxylic acid-based polymer is another factor influencing the size of LM inclusions. The acidic condition weakens the oxide interface, making it easier for LM particles to coalesce into larger particles.[42,187] The applied shear stress during polymer-filler mixing breaks the weakened oxide shell, promoting micro-sized LM droplets to merge into a larger particle. Meanwhile, nano-sized LM inclusions are less affected due to the higher stability of their oxide shells at smaller sizes.[39] As a result, synthesized LM–Vit composite with V_f of 50% (50% LM–Vit) contains polydisperse populations of LM inclusions – microscale droplets with an average particle size of 6.73 ± 3.80 μm and nanoscale particles – with both size ranges uniformly distributed throughout the matrix (Figure A.19).

To evaluate how LM inclusions affect the composite's curing behavior, isothermal differential scanning calorimetry (DSC) was conducted on uncured LM–Vit samples (Figure A.20). The results show that the total heat required for curing the composites and the peak of heat flow both decrease as LM content increases. This reduction occurs because LM inclusions occupy space that would otherwise be available for vitrimer network formation. Interestingly, at V_f of 10% and 20%, the presence of LM slightly accelerates the curing rate, likely due to enhanced thermal conductivity from LM particles. However, at higher volume fractions (V_f of 40% and 50%), the curing rate slows down as densely packed fillers interrupt polymer chains from interacting. With minor differences in curing rates, all formulations with different filler fractions reached complete crosslinking in approximately 150 minutes, which indicates that LM fillers have only a minor influence on the curing characteristics of vitrimer.

Cured composites are further analyzed using Fourier transform infrared (FTIR) spectroscopy confirm successful network formation. Figure A.21 reveals that all composites have FTIR peaks associated with synthesized fatty acid vitrimer, especially the carbonyl ester group (1735 – 1750 cm^{-1}),[157,162] confirming that CAN is successfully created regardless of embedded particles. These

findings demonstrate that LM particles can be effectively integrated into the vitrimer matrix without altering the synthesis mechanism, enabling facile synthesis of LM–Vit composites.

5.3. Multifunctional Properties of LM–Vitrimer Composites

The exceptional thermal stability of vitrimer composites distinguishes them from other recyclable polymer systems. As shown in Figure 5.2a and Figure A.22, LM–Vit composites retain nearly their entire mass up to 350 °C during thermogravimetric analysis (TGA), indicating high thermal stability. The composites' characteristic temperatures, including the temperature at 5% weight loss ($T_{5\%}$) and the onset of thermal degradation (T_o), reveal a wide range of operating windows for high-temperature applications (Table A.6). By adding LM inclusions, T_o slightly decreases and $T_{5\%}$ increases simultaneously, as metallic fillers facilitate heat transfer without decomposing. DSC results in Figure 5.2b further confirm the thermal stability of these composites as there are no signs of degradation observed for temperatures up to 260 °C. The DSC curves reveal three phase transitions: the melting peak of sub-4 μm LM particles (-23 °C),[29] the melting peak of larger LM particles (18 °C),[29] and the glass transition of the vitrimer matrix (5–15 °C).[157] Based on this result, the size of LM particles in the composites with lower V_f from 10% to 30% is mostly a few micrometers due to the heightened supercooling effect of LM microdroplets at this scale,[29] as observed by LM's sharp melting peak at -23 °C and smooth transitions around the vitrimer's glass transition temperature (T_g). However, for composites with LM V_f of 40% and 50%, it appears some of the particles coalesce during the mixing process, forming larger LM droplets with the melting peak at 18 °C. As previously described, the acidity of the fatty acid precursor weakens the oxide shells on LM droplets and mixing in a highly viscous colloid causes the particles to merge at high V_f, which is exhibited in SEM images (Figure A.23). Dynamic mechanical analysis (DMA) shows consistent storage moduli and tan δ peaks at approximately 32 °C across all formulations (Figure A.24). The results demonstrate that the incorporation of LM particles does not alter the vitrimer's viscoelastic behavior or glass transition temperature, ensuring the composites' thermal stability.

Unlike conventional polymers, vitrimers behave like thermosets below the topology freezing temperature (T_v), where bond exchange reactions (BERs) are inactive. Above T_v, activation of these dynamic BERs enables a transition to thermoplastic-like flow. This temperature serves as a critical parameter for vitrimer composites, as it defines the upper limit of thermosetting behavior

while also representing the lower threshold for reprocessing. To evaluate this transition, stress relaxation experiments were conducted using a rotational rheometer across a range of temperatures (Figure A.25). All synthesized LM–Vit composites show minimal stress relaxation below T_v, behaving like thermosets. In contrast, stress relaxation becomes pronounced above T_v, with a decrease in relaxation time (τ^*) as temperature increases, which reflects faster BERs at elevated temperatures. At 220 °C, the neat vitrimer exhibits a τ^* of 46 seconds. In comparison, the 50% LM–Vit composite shows a longer τ^* of 195 seconds. This extended relaxation time at higher LM loadings can be attributed to increased physical entanglement and stronger interfacial adhesion between the LM inclusions and the vitrimer network. The greater filler content also limits polymer chain mobility, thereby impeding BERs and resulting in the extended τ^*. Despite these changes, neither the activation energy (the minimum energy required for transesterification) nor the T_v is affected by LM incorporation, which is the desired outcome. As shown in Figure 5.2c, the activation energy and T_v across all the compositions remain within the range of 151–169 kJ/mol and 120–132 °C, respectively. These consistent thermal properties suggest that the outstanding thermal stability of LM–Vit composites is preserved, even at high LM volume fractions.

A major advantage of embedding LM inclusions in vitrimer is the substantial improvement in thermal conductivity, enabling better thermal management and heat dissipation in flexible circuits. Figure 5.2d demonstrates that the thermal conductivity of LM–Vit composite increases with increasing the LM V_f. In 50% LM-Vit composite, the average thermal conductivity was measured to be 0.98 $W \cdot m^{-1} \cdot K^{-1}$, which represents a 6.53-fold improvement compared to the neat vitrimer (0.15 $W \cdot m^{-1} \cdot K^{-1}$). This high thermal conductivity is comparable to that of LM–PDMS composites (~1.1 $W \cdot m^{-1} \cdot K^{-1}$) with the same filler volume fraction and similar particle morphology,[46] and can be further enhanced by incorporating hybrid fillers.[19,224] To demonstrate the effectiveness of LM–Vit composites in thermal management, a patterned sample containing 50% LM–Vit composite in the shape of a “W” and unfilled vitrimer was exposed to a 75 °C heat source (Figure 5.2d-inset). The lower surface temperature observed on the W pattern indicates improved heat dissipation, supporting the composite’s capability to manage heat generated in flexible and stretchable electronics.

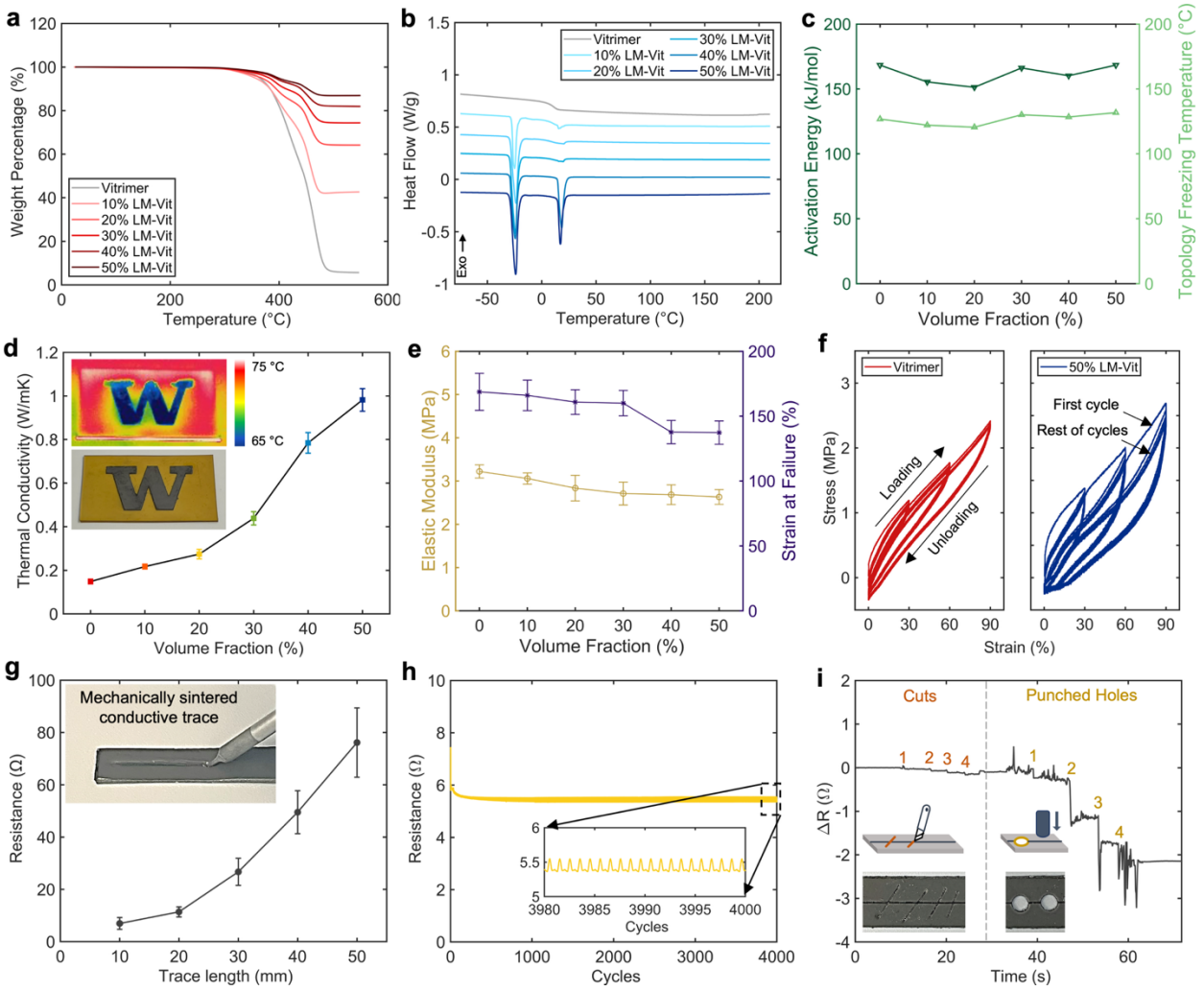

Figure 5.2. Soft and stretchable multifunctional LM–vitrimer composites: (a) Thermogravimetric analysis showing weight percentage as a function of temperature. (b) Measured heat flow from differential scanning calorimetry. (c) Estimated activation energy and topology freezing temperature as a function of LM volume fraction, calculated from rheological measurements. (d) Thermal conductivity as a function of LM volume fraction (n = 3). Inset: Photograph and IR image of neat vitrimer and 50% LM–Vit composite on a hotplate at 75 °C. (e) Elastic modulus at 100% strain and strain at failure of LM–Vit composites (n = 5). (f) Stress–strain behavior of neat vitrimer and 50% LM–Vit composite under uniaxial cyclic loading to 30%, 60%, and 90% tensile strain. (g) Electrical resistance of mechanically sintered conductive traces on 50% LM–Vit composite as a function of trace length (n = 5). Inset: Mechanical sintering demonstration. (h) Resistance of a 20 mm conductive trace over 4,000 cycles of uniaxial 50% strain. (i) Electrical self-healing of conductive traces after cuts and punched holes.

Alongside enhanced thermal conductivity, the LM–Vit composites maintain desirable mechanical properties for flexible electronics. As shown in Figure 5.2e, the elastic modulus of neat vitrimer (3.22 MPa) decreases with increasing LM content, which highlights the advantage of liquid-phase fillers that mitigate the stiffening effect. Strain at failure is also mildly affected by LM inclusion with a notable decrease observed at 40% LM–Vit due to the presence of large LM particles. At LM V_f of 50%, the composite preserves the soft and stretchable characteristics

with an average elastic modulus of 2.63 MPa and a failure strain of 137.3%. These properties are comparable to those of PDMS (Sylgard 184, Young's modulus of ~2 MPa and failure strain of ~120%), a widely used elastomer substrate for stretchable electronics.[225,226] LM–Vit composites were further subjected to uniaxial cyclic loadings at strains of 30%, 60%, and 90% (Figure A.26). The stress-strain curves reveal that hysteresis is induced by LM inclusion, evidenced in a difference in strain energy between loading and unloading, particularly in the first cycle (i.e., Mullins effect).[189] However, this strain-softening stabilizes after a few cycles even at the high LM V_f of 50%, as shown in Figure 5.2f. Despite minor variations in mechanical response, LM–Vit composites maintain excellent stretchability suitable for applications in flexible electronics.

Selective patterning for creating conductive traces is a unique functionality that LM filler provides to the composite. As shown in Figure 5.2g, electrical circuits can be directly inscribed on LM–Vit composite with a sharp object resulting in an average electrical conductivity of 1.017×10^{-3} S/m. Unlike common LM-embedded polymer conductors, the mechanical sintering can be performed on both sides of the composite because of uniformly dispersed fillers across the matrix. The 50% LM−Vit composite was used to measure electrical properties as it has the highest LM fraction for maximized functionalities compared to the base polymer. When localized mechanical force is applied, the passivating oxide layer on the LM particles ruptures, forming a percolating network between droplets that creates continuous conductive pathways within the vitrimer matrix.

Minimal resistance change under deformation and electrical self-healing are key advantages of conductive traces on LM–Vit composites for applications such as wearables and flexible electronics. Electromechanical coupling is investigated by measuring changes in resistance of a written conductive trace with a length of 20 mm under uniaxial strain of 0 to 50% over 4,000 cycles as shown in Figure 5.2h. The resistance decreases during the first thousand cycles as the activated LM droplets deform along the strain direction and expand the percolating network. After this period, the electromechanical response stabilizes, with only a 3.4% fluctuation in resistance during the remainder of the test. The trace also exhibits an exceptional electrical self-healing capability as demonstrated in Figure 5.2i. Even after several cuts and punctures, the circuit maintains uninterrupted connectivity. Interestingly, the electrical resistance of the traces decreases after damage. This is attributed to the liquid-state conductor creating new pathways

upon damage, coupled with rupturing nearby LM particles. This effect generates additional conductive networks and was initially shown in thermoset LM–PDMS composites.[27] These multifunctional LM–vitrimer composites combine thermal stability, mechanical flexibility and stretchability, enhanced heat dissipation, and LM-derived electrical conductivity, representing a promising new class of materials that is well-suited for stretchable electronics with recyclability and reconfigurability.

5.4. Thermomechanical Reprocessing

Thermomechanical reprocessing repairs separated vitrimer pieces back into a unified material to restore the original properties. At elevated temperature and pressure applied via a hot press, BERs within the vitrimer's CAN enable previously crosslinked active groups to reorganize.[161] However, the presence of a liquid-state secondary phase in the LM–Vit composite affects the vitrimer's reprocessing behavior and its ability to recover mechanical strength, while also exhibiting filler shape distortion when compressed. Figure 5.3a illustrates the reprocessing of LM–Vit composites. The illustrated sequence highlights healed regions where vitrimer matrices effectively reform crosslinks at the fractured interface, as well as unhealed regions where LM extrudes from the matrix and obstructs BERs. To analyze the change in filler morphology during reprocessing, aspect ratios of LM inclusions are measured. As shown in Figure 5.3b, increase in aspect ratio and broadened distribution are observed after each cycle of hot pressing. Cross-sectional SEM images of the 50% LM–Vit composite show spherical LM droplets in the original composites, and elongated inclusions formed under compressive stress after the second reprocessing.

Compressive reprocessing affects composites' material properties, as the fillers adapt their shapes and align in the in-plane direction. To investigate the corresponding changes in material properties from the compressed fillers, DSC and DMA analyses were performed on reprocessed LM–Vit composites (Figure A.27). DSC results indicate that the melting peak associated with the large LM droplets becomes noticeably smaller after reprocessing. The reduction in peak arises from the elongated droplets having higher surface-to-volume ratio compared to their original spherical shape. The increase in surface energy and liquid-core/solid-oxide interfaces of LM after reprocessing promotes LM supercooling,[29] suppressing the melting peak of large LM inclusions. Furthermore, DMA results show a higher loss modulus below T_g, which suggests that the composite stores less elastic energy in the in-plane direction. This is expected, as the liquid-

state fillers, which are incapable of storing elastic energy, become directionally aligned after compression, contributing to compromised mechanical properties. At temperatures above T_g, an increase in storage modulus and decrease in loss modulus are measured, indicating a stiffened composite. Stress-strain curves for the reprocessed samples confirm this influence of the elongated and oval LM inclusions (Figure A.28), as they display a higher elastic modulus and a lower failure strain. In addition, changes in filler shape and alignment also affect the material's thermal conductivity as shown in Figure 5.3c. The reduction in through-plane thermal conductivity is attributed to the anisotropic deformation of the conductive filler, which reduces heat transfer efficiency perpendicular to the surface. Nevertheless, this elongated LM is anticipated to enhance in-plane thermal conductivity as reported in earlier studies.[23,227] This directional trade-off lowers vertical conductivity of the LM–Vit composite yet sustains its overall thermal management capability because lateral heat dissipation becomes more efficient.

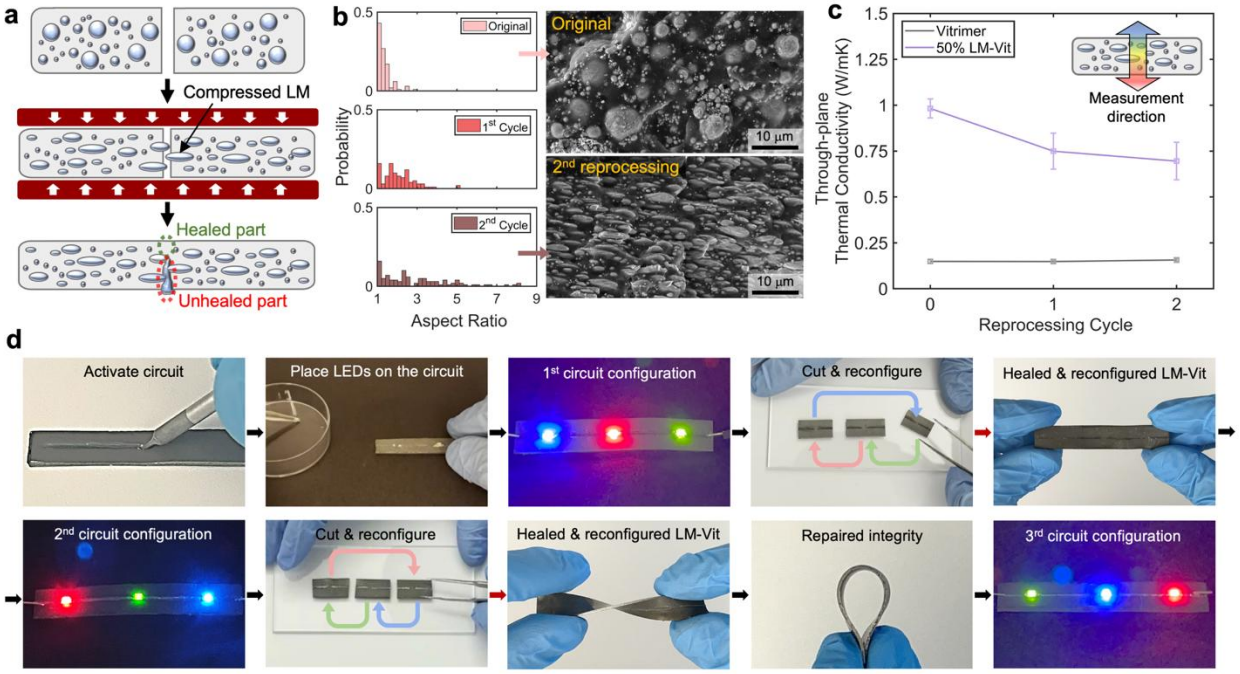

Figure 5.3. Thermomechanical reprocessing of LM–vitrimer composites for reconfigurable flexible circuits: (a) Schematic illustration of the thermomechanical reprocessing sequence. (b) Aspect ratios and cross-sectional SEM images of LM inclusions across reprocessing cycles (n = 100). (c) Through-plane thermal conductivity of reprocessed vitrimer and 50% LM–Vit (n = 3). Inset: Schematic showing the through-plane thermal conductivity measurement direction. (d) Fabrication of an initial LED circuit on the LM–Vit composite and its reconfiguration into two new circuits via thermomechanical reprocessing. The burgundy arrow indicates the hot-pressing step.

To demonstrate device-level circuit reconfiguration using thermomechanical reprocessing, an LM–Vit circuit with three serially connected LEDs is fabricated (Figure 5.3d). The electrical

circuit was first patterned on the surface of a 50% LM−Vit composite via mechanical sintering, followed by LED placement. The circuit was completely fragmented and subsequently healed – both mechanically and electrically – through thermomechanical reprocessing, as shown in Figure 5.3d. The separated pieces were rearranged and hot-pressed for 2 hours at 220 °C. During this reassembly, the vitrimer matrix undergoes BERs that reform the polymer network, while previously activated LM traces preserve their electrical continuity, allowing the LEDs to illuminate again. Compression during reprocessing helps merge the sectioned traces and align LM inclusions along the direction of the conductive paths, while subsequent sintering can further improve electrical connectivity in the reprocessed composite. Multiple cycles of cutting, repositioning, and reprocessing produced new circuit geometries, each of which operated reliably. This series of demonstrations confirms that LM–Vit composites can maintain the functionality from repeated reconfigurations.

5.5. Chemical Recycling

Featured with filler recycling efficiency of approximately 94%, the chemical recycling strategy involves the separation of LM particles from the vitrimer matrix. Interaction between the EGaIn inclusions and the vitrimer polymer matrix are investigated using X-ray photoelectron spectroscopy (XPS). As shown in Figure 5.4a, the survey spectra of the 50% LM–Vit composite reveal the presence of both the ultrasonicated EGaIn particles and the vitrimer. In particular, the Ga 3d core-level spectra show binding energies corresponding to metallic gallium (Ga^0) at 17.70 eV and oxidized gallium (Ga^{3+}) at 20.22 eV,[35,228] both of which are shifted to higher binding energies by 0.40 eV and 0.34 eV, respectively, in the LM–Vit composite (Figure 5.4b). These shifts indicate reduced electron density around gallium, which is attributed to electron-donating groups in the polymer matrix forming weak coordination interactions with the oxide surface of LM.[229–231] Additionally, in the C 1s core-level spectra, the carboxylate (O–C=O) peak shifts to a lower binding energy by 0.26 eV, suggesting interaction with gallium ions (Figure 5.4c).[170,232] Beyond coordination, hydroxyl groups on the LM oxide surface may also participate in reversible covalent transesterification reactions with ester linkages in the vitrimer matrix.[233] The ester and β-hydroxy moieties in the matrix may further contribute to interfacial adhesion through hydrogen bonding with the gallium oxide surface. While both reversible covalent bonding and hydrogen bonding are plausible, they do not appear to be dominant, as minimal shifts and negligible broadening are observed in hydroxyl-related peaks in the XPS C 1s spectra

(Figure A.29). These observations support a multi-modal interfacial interaction mechanism involving partial coordination, reversible covalent bonding, and hydrogen bonding. Further characterization is needed to clarify the relative contributions of each interaction type.

To disrupt the chemical interactions and enable component recycling, the vitrimer network, composed of a zinc acetylacetonate hydrate ($Zn(acac)_2$)-catalyzed fatty acid mixture and epoxy, was first depolymerized via transesterification in EG solution, as illustrated in Figure 5.4d and Figure A.30. However, this reaction leaves hydroxyl groups on both the fatty acid and epoxy segments,[162] which are expected to enhance hydrogen bonding with the oxide surface of LM particles. The increased polymer-matrix interaction makes recycling more difficult, resulting in recovering only 17% of vitrimer matrix by weight from 50% LM–Vit composite even after the centrifuge (Figure A.31). The synergistic effect of coordination, reversible covalent bonding, and hydrogen bonding between the LM oxide surface and vitrimer functional groups complicate the separation of the deformable metallic filler. To overcome this challenge, the composite was subsequently treated with a mixture of EG and HCl at 130 °C. This acid treatment successfully disrupted the filler–matrix interactions, enabling effective separation. As a result, the residual vitrimer separates from the LM, and the particles coalesce into a single large LM droplet (Figure 5.4e).

Using this two-step process, 6.05g of LM from a 50% LM−Vit sample is recovered, compared to the initially embedded 6.42 g, corresponding to 94.2% recovery rate by weight. Approximately 6% of the filler loss is primarily attributed to the dissolution of gallium oxide in the acidic solution.[234] Although the recovery efficiency is comparable with the previously reported recovery rates (Table A.7), it can potentially be improved through alkaline treatment, more advanced recycling strategies, and multiple washing and rinsing cycles. The acid treatment that enables LM reclamation also degrades the vitrimer network through functional group substitution. As observed in DSC curves after the dissolution and repolymerization (Figure A.31), the altered polymer matrix may disrupt subsequent transesterification after the recovery. It should be noted that, as the vitrimer comprises only 1.09 g out of a total 7.51 g of the 50% LM–Vit composite, recovering this small amount of bio-based polymer is unlikely to offer meaningful environmental or practical benefits.

Given the high filler recovery, the recycled LM was used to fabricate a new LM−Vit composite to build another circuit, as shown in Figure 5.4e. Unlike conventional thermoset-based LM composites, LM–Vit can be easily recycled with a simple two-step chemical treatment. The full recycling process involves dissolving the composite in EG, followed by centrifugation, and subsequent acid treatment in EG-HCl at 130 °C for 30 minutes. After fully drying, the recovered LM is reintegrated into a freshly prepared LM–Vit composite. The new LM–Vit composite is then patterned with conductive traces to form a new circuit with a different configuration of LEDs. The versatile recycling strategies, enabled by the CAN, offer a sustainable approach to utilizing this new class of liquid metal polymer composites to mitigate e-waste and promote responsible use of rare and critical metals.

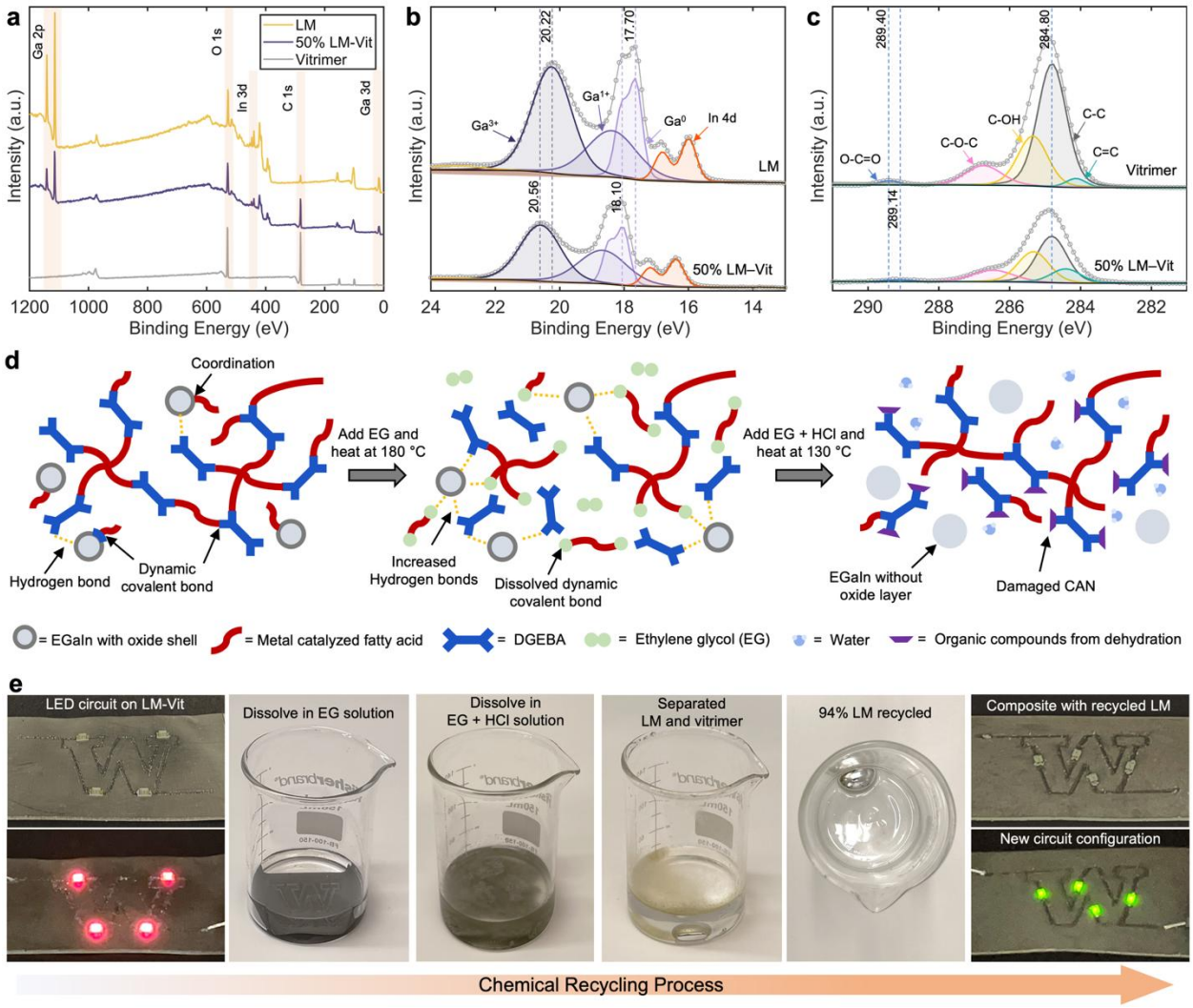

Figure 5.4. Filler–matrix interactions and chemical recycling of LM–vitrimer composites: (a) XPS spectra of EGaIn LM particles, 50% LM–Vit composite, and unfilled vitrimer. (b) XPS Ga 3d spectra of LM particles and 50% LM–Vit composite. (c) XPS C 1s spectra of vitrimer and 50% LM–Vit composite. (d) Chemical recycling sequence showing synthesized LM–Vit composite (left), dissolved LM–Vit composite in EG solution (center), and separated LM and vitrimer in EG and HCl solution (right). (e) Chemical recycling of LM–Vit composite and use of recycled LM to fabricate LED circuits.

5.6. Conclusion

This chapter presented a multifunctional LM–vitrimer composite with sustainable end-of-life strategies. The highly compatible LM filler significantly enhances the vitrimer's properties, including a 6.53-fold increase in thermal conductivity at a 50% filler volume fraction. The liquid-state filler also preserves the vitrimer's flexibility, resulting in a slightly reduced elastic modulus of 2.63 MPa and a failure strain of 137.3%, without compromising thermal stability. Electrically conductive traces were inscribed on this thermally conductive and stretchable

composite via mechanical sintering. The activated traces demonstrate stable electromechanical performance, exhibiting only a 3.4% change in resistance under 50% uniaxial strain, along with electrical self-healing capabilities crucial for flexible circuits and wearable applications. Selective electrical activation is achieved on both sides of the composite, enabled by the uniform dispersion of LM inclusions and consistent material properties throughout the LM–Vit composite.

Two distinct recycling methods, thermomechanical reprocessing and chemical recycling, allow simple circuit reconfiguration and effective LM recovery, respectively. Thermomechanical reprocessing demonstrates the composite's ability to heal both mechanically and electrically, enabling reconfiguration of flexible circuits. Using this approach, the 50% LM–Vit composites were successfully disassembled and reassembled multiple times. During this process, deformation of the liquid-phase fillers introduces anisotropic material properties, while maintaining electrical connectivity to power LEDs in the reconfigured circuits. Moreover, chemical recycling enables 94% recovery of the LM by dissociating the fillers from the matrix via EG and EG–HCl treatments. Further investigation into the chemical interactions between LM–Vit composites and the EG–HCl solution reveals that, while LM filler recovery is highly efficient, the vitrimer matrix undergoes acid-induced degradation. Nonetheless, the recovered LM is successfully reintegrated into a new LM–Vit composite and used to fabricate an LED circuit with a different configuration. The demonstrated multifunctional properties and recycling strategies offer a sustainable pathway to advancing flexible and wearable electronics.

Beyond environmental impact, LM–vitamer composites' recyclability and material recoverability translate into other benefits including reduced material consumption, lower manufacturing costs, and decreased dependency on supply chains. Each chapter built upon the last, the four chapters addressed the core challenges in wearable thermoelectric devices from three different perspectives: material design, device architecture, and manufacturing processes. However, the integration of LM-vitrimer composites into onboard electronics systems with thermal and chemical robustness has not been demonstrated, Also, the full recycling of every device component including thermoelectric elements, electronic components, interconnects, and encapsulating polymer matrix remains unachieved. These unmet research goals become one of the well-motivated future works.

Summary and Future Works

6.1. Summary

Wearable thermoelectric devices hold promise as self-sustaining power sources for on-skin electronics, yet their adoption has been limited by insufficient energy conversion under the low temperature gradient between the ambient and the human body, rigid device architectures that conflict with soft human tissue, impermeable interfaces that compromise wearing comfort, and single-use composite materials that contribute to electronic waste. This dissertation addressed these four interrelated challenges by developing 3D printed architectures with liquid metal composites for stretchable thermoelectric wearables. Throughout the studies, materials, device architecture, and manufacturing processes are treated as a coupled system, which yields compounding improvements in printability, thermoelectric performance, mechanical robustness, skin-compatibility, and recyclability. The contributions of this dissertation can be summarized as follows:

1. Printable multifunctional elastomer composites were developed for all device layers of flexible thermoelectric generators (Chapter 2). By controlling the size of embedded liquid metal inclusions in PDMS, the same composite was engineered to serve either as an electrically insulating thermal interface or as a stretchable electrical conductor. A hollow microsphere elastomer composite provided thermal insulation in the core layer. Shear-thinning rheology enabled direct ink writing of these composites to fabricate a flexible TED that achieved a power density of 650 $\mu W \cdot cm^{-2}$ at ΔT = 60 °C, while surviving over 15,000 cycles of 30% tensile strain with negligible resistance change.
2. Three-dimensional device architecture was shown to substantially improve thermoelectric performance and provide damage tolerance (Chapter 3). Multiphysics simulation guided the design of an air pocket core layer structure that preserved a large temperature gradient across embedded TE semiconductors by surrounding them with air rather than solid matrix. Combined with an ultrasoft composite and stretchable heatsinks, the resulting Macro-TED with 96 TE pellets achieved a record power density of 115.4 $\mu W \cdot cm^{-2}$ at thermal equilibrium under an *Initial* ΔT of 10 °C. The device demonstrated 230% electrical failure strain, damage tolerance with intact functionality after puncture, electrical self-healing from liquid metal conductors, and stable performance over 2,000 cycles at 50% strain.

3. Electrohydrodynamic printing was employed to fabricate permeable thermal interfaces that resolve the trade-off between breathability and thermal conductivity in wearable TEDs (Chapter 4). A liquid metal–boron nitride–TPU hybrid filler composite was deposited as a high-resolution fiber mat with lattice patterns designed to avoid occluding sweat pores. Despite the presence of air and moisture transport pathways, the EHD-printed interface achieved a through-plane thermal conductivity of 0.37 $W \cdot m^{-1} \cdot K^{-1}$. The mat also functioned as a micropatterned heatsink on the cold side of the device. Skin compatibility was demonstrated through the WVTR measurement and the week-long skin attachment test. The breathable TED generated 5.32 μW at equilibrium under an *Initial* ΔT of 10 °C.

4. Recyclable liquid metal–vitrimer composites were developed for sustainability in flexible electronics (Chapter 5). The vitrimer matrix, featuring dynamic covalent bonds, combined the robustness of thermosets with the reprocessability of thermoplastics. At 50% LM volume fraction, the composite achieved a 6.53-fold increase in thermal conductivity while maintaining 137% failure strain and thermal stability above 360 °C. Two distinct recycling strategies were demonstrated: thermomechanical reprocessing for circuit reconfiguration, and chemical recycling for 94% recovery of the liquid metal filler. The recovered LM was successfully reintegrated into new composites and reconfigured circuits.

These four studies establish a body of knowledge for wearable thermoelectric device development, progressing from composite formulation and device architecture to skin-compatible interfaces and sustainable materials. Each chapter addressed a specific research objective while building upon the insights and limitations identified in the preceding work.

6.2. Future Works

6.2.1 Printed Soft Thermoelectric Materials with High Figure of Merit

The thermoelectric devices in this dissertation relied on rigid inorganic Bi_2Te_3, while all surrounding layers, including thermal interfaces, electrical interconnects, insulation, and heatsinks, were fabricated from printable soft composites. In this hybrid architecture, the rigid TE pellets are a source of stress concentration under deformation. The 230% electrical failure strain reported in Chapter 3 was achieved not by eliminating this mismatch but by

accommodating it through ultrasoft encapsulation and liquid metal conductors that tolerate local displacement. As the number of TE elements increases or the device conforms to tighter curvatures, the cumulative effect of the rigid parts is expected to constrain overall device compliance and durability.

Future studies should explore printed thermoelectric materials that are inherently flexible to achieve fully stretchable TEDs. However, printed thermoelectric materials currently exhibit significantly lower figures of merit compared to bulk inorganic pellets, resulting in reduced power output. The figure of merit is defined as $zT = \frac{S^2 \sigma T}{\kappa}$, where S is the Seebeck coefficient, σ is the electrical conductivity, T is the absolute temperature, and κ is the thermal conductivity of a thermoelectric material. Therefore, the development of new 3D-printable soft thermoelectric materials requires a combination of a high Seebeck coefficient, high electrical conductivity, and low thermal conductivity. Achieving this combination is challenging because soft materials undergo structural changes when subjected to mechanical deformations, which can alter their thermoelectric properties and often lead to performance degradation.

The challenge is not simply substituting one material for another material. It is a co-designing of the printed TE material, the device geometry, and the composite architecture to compensate for lower intrinsic zT through material innovation, novel fabrication processes, and structural advantages. For example, the air pocket core layer developed in Chapter 3 could be adapted to accommodate a larger number of thin-film printed TE elements with higher packing density. Similarly, the EHD printing process demonstrated in Chapter 4 could potentially be extended to deposit thermoelectric composite fibers that are encapsulated in thermal interface materials, creating functionally graded structures that integrate energy conversion and thermal management at the microstructural level. Future work should investigate these integrated architectures, evaluating whether the gains offered by fully printed devices can offset the reduction in thermoelectric conversion efficiency relative to rigid pellet-based devices.

6.2.2 Long-Term Reliability and Temperature Modulation in Wearable Applications

While the durability of the devices was characterized through thousands of stretch cycles under controlled laboratory conditions, real-world deployment introduces combined loading of sweat exposure, UV radiation, abrasion from clothing, and variable ambient humidity over weeks to months. Chapter 4 showed permeable thermal interfaces with the week-long skin attachment test,

but the device-level robustness has not been demonstrated. Future studies can develop accelerated aging measurements that combine cyclic mechanical loading with controlled humidity and temperature profiles to predict the service life of LM-based composites. Additionally, demonstrating standalone energy generation and the powering of wireless sensors over a longer period would make wearable thermoelectric devices more practical.

Another promising avenue is the development of real-time, on-demand thermoregulation systems based on closed-loop control. By integrating temperature sensors, control algorithms, and thermoelectric devices, the system could continuously monitor and regulate the temperature of a target surface, such as human skin, batteries, or electronic components. Such a feedback-controlled approach would enable dynamic temperature modulation in response to a changing working condition. This could significantly expand the application of soft thermoelectric devices. For wearable applications, localized heating or cooling could improve thermal comfort and safety for individuals operating in extreme environments, such as scuba divers exposed to cold water or runners exercising in hot weather. Beyond wearable systems, thermoelectric devices could be integrated into battery packs and electronic systems to provide active thermal management. For example, batteries could be cooled during high-power operation to improve efficiency, performance, and cycle life. These thermoelectric modules can deliver localized heating or cooling to electronic components in areas that are difficult to access using conventional thermal management technologies. Future research should investigate the integration of sensing, control, and power-management architectures, as well as optimize the response time, energy efficiency, and long-term reliability of the thermoregulation system. Such advancements could enable intelligent thermal managements to address real-time thermal demands across a broad range of wearable and electronic applications.

6.2.3 Higher Thermal Conductivity in Breathable Interfaces

The EHD-printed permeable interface achieved a through-plane thermal conductivity of 0.37 $W \cdot m^{-1} \cdot K^{-1}$, which is significantly higher than that of an unmodified porous textile but still substantially below that of bulk LM–BN composites. Improving this value without sacrificing breathability would directly increase thermoelectric performance at equilibrium. Future work should explore material compositions and manufacturing processes that enable higher thermal conductivity while preserving skin compatibility. One emerging research field is machine

learning-assisted inverse design of composites[235] This approach can reveal composition–property relationships for improved thermal conductivity, elasticity, or density. Another approach is aligning conductive fillers vertically for improved thermal conductivity in the through-plane direction. As discussed in Section 1.1.3, fillers facilitate heat flux along the alignment direction. Therefore, positioning BN platelets or stretching LM fillers in vertical direction should increase through-plane conductivity.

6.2.4 Vitrimer Composites as Thermoelectric Device Layers

The LM-vitrimer composite developed in Chapter 5 was characterized as a flexible thermal interface but was not integrated into a complete thermoelectric device. Future work should investigate the use of vitrimer-based composites in TEDs and wearable electronics, replacing conventional PDMS or Ecoflex-based interfaces. The dynamic bond exchange in the vitrimer could enable device-level repair and reconfiguration if the vitrimer is implemented in TEDs. For instance, thermoelectric heating could heal a damaged TED and restore its function. However, the viscoelastic relaxation behavior of vitrimer at elevated temperatures may affect the stability of the interface contact, and these coupled thermomechanical effects must be characterized under thermoelectric operating conditions. Another future research direction is the 3D printing of LM–Vit without filler sedimentation. While pre-curing and low-density fillers can buffer the vitrimer's rapid drop in viscosity, additive manufacturing of LM–Vit with uniformly distributed inclusions has not been demonstrated, mainly because of EGaIn's high density and liquid state. The proposed future work will enable highly efficient and sustainable wearable TEDs.

Vita

7.1. Education

Doctor of Philosophy, Mechanical Engineering (June 2026)

University of Washington, Seattle, Washington

M.S. Mechanical Engineering (March 2022)

University of Washington, Seattle, Washington

B.S. Mechanical Engineering (February 2020)

Chung-Ang University, Seoul, South Korea

7.2. Publications

- **Y. Han**, C. S. Fernandes, E. Davis, and M. H. Malakooti. "Electrohydrodynamic Printing of Liquid Metal Composites for Breathable Interfaces in Recyclable Thermoelectric Wearables" *ACS Appl. Mater. Interfaces*. Submitted (2026).
- **Y. Han**, S. S. Rohewal, S. Gupta, S. Paul, C. C. Bowland, and M. H. Malakooti. "Conductive Liquid Metal Vitrimer Composites for Reconfigurable and Recyclable Flexible Electronics" *Adv. Funct. Mater.* 35, e11119 (2025).
- M. Zadan, A. Wertz, D. Shah, D. K. Patel, W. Zu, **Y. Han**, J. Gelorme, H. J. Mea, L. Yao, M. H. Malakooti, S. H. Ko, N. Kazem, C. Majidi, Stretchable Thermoelectric Generators for Self-Powered Wearable Health Monitoring. *Adv. Funct. Mater.* 34, 2404861 (2024).
- **Y. Han,** H. Tetik**,** and M. H. Malakooti. "3D Soft Architectures for Stretchable Thermoelectric Wearables with Electrical Self-Healing and Damage Tolerance", *Adv. Mater.* 36, 2407073 (2024).
- R. Chin, **Y. Han**, and M. H. Malakooti, "Surface-Engineered Liquid Metal Particles for Printing Stretchable Conductive Composites with Enhanced Stability Under Different Strain Rates", *Adv. Mater. Technol*. 9, 2301324 (2024).

- R. L. Creighton, M. Doan, C. I. Tobos, T. Guo, K. A. Faber, **Y. Han**, C. Chiew, I. Hull, M. H. Malakooti, K. A. Woodrow. "High-Resolution 3D Deposition of Electrospun Fibers on Patterned Dielectric Elastomers", *Adv. Eng. Mater.* 25, 2300670 (2023).
- **Y. Han**, L.-E. Simonsen, and M. H. Malakooti. "Printing Liquid Metal Elastomer Composites for High-Performance Stretchable Thermoelectric Generators", *Adv. Energy Mater.* 12, 2201413 (2022).

Appendix

A.1. Printing Liquid Metal Elastomer Composites for Thermoelectric Generators

A.1.1 Experimental Section

Thermal Interface LMEC Ink Formulation: The LMEC ink for the thermal interface layer was prepared by mixing eutectic gallium indium (EGaIn—75 wt.% Ga and 25 wt.% In) with a PDMS (Sylgard 184; Dow Chemicals). The PDMS base (part A) was placed into the immersion mixer (Caframo, BDC250) in a 20 mL plastic cup at 600 rpm for 30 min. Then EGaIn was added drop by drop using a syringe until the EGaIn made up 50% volume fraction of the total ink. After emulsion mixing the ink, the PDMS curing agent (part B) was added to the ink at 1/10 of the weight of the PDMS part A (10:1 mass ratio). Hexane was added to 5 wt.% of total ink to lower the viscosity. The ink was mixed again using a planetary shear mixer (FlackTek SpeedMixer, DAC 150.1 FVZ-K) for 1 min and 2500 rpm.

Conductive LMEC Ink Formulation: PDMS (Sylgard 184; Dow Chemicals) parts A and B were prepared at a 10:1 mass ratio in a 20 mL glass vial. Then EGaIn was added to create an ink with 30% EGaIn by volume. The vial was placed in the planetary shear mixer (FlackTek Inc, DAC 150.1 FVZ-K) for 5 min at 700 rpm until the shearing force broke EGaIn into smaller particles and the size of the EGaIn particles in the interconnection ink became ≈150 μm. This LMEC ink for interconnection was then transferred into a syringe for printing. The ink separated into a PDMS-rich zone and LM-rich zone after 15 min due to the density difference. The LM-rich portion of the interconnection ink was only used for better electrical conductivity.

Thermally insulative HMEC Ink Formulation: Expancel (551 DE 40 d42; Nouryon) and PDMS (Sylgard 184; Dow Chemicals) were added with the volume ratio of 1:1 in a plastic cup and hand mixed for one minute. Then PDMS part B was added to a tenth of the weight of part A, and they were shear mixed for 1 min at 2500 rpm.

Printing Process: A high-precision dispenser system (Musashi Engineering, ML 808GX) on a 3-axis robotic arm equipped with a heated vacuum plate was used for direct-ink-writing of three different types of inks. For thermal interface layer printing with LMEC ink, the printing was conducted at 7 kPa and 5 $mm \cdot s^{-1}$ with an 18-gauge needle. For printing conductive interconnect ink, the ink was placed in the syringe for 15 min before the printing. The printing pressure and speed for interconnection ink were 60 kPa and 1.5 $mm \cdot s^{-1}$ with a 32-gauge needle. The

interconnect printing was conducted twice to ensure high electrical conductivity. For printing the heat insulation layer, a syringe with a 32-gauge needle was used with a dispensing pressure of 190 kPa and a speed of 1.5 $mm \cdot s^{-1}$. Printing of the thermal insulation layer was also conducted in two passes to completely fill the gap between the TE pellets. After the printing of each layer, the samples were heated in the oven to fully polymerize the elastomer composites. The thermal interface layer was cured in an oven at 90 °C for 4 h while the thermal insulation layer and interconnects were heated in an oven at 90 °C for 3 h after printing.

Thermal Conductivity Measurement: A 25-μm-diameter platinum wire was soldered at each end to stranded copper wire to measure thermal conductivity using the transient hot-wire method. The platinum wire was cast within target elastomer composites inside of a 70×11×4 mm^3 acrylic mold to acquire thermal conductivities of the target materials. After curing the casted elastomer composites, the casted specimens were connected to a SourceMeter (Keithley 2450), and the voltage was measured while applying a consistent 100 mA current for 0.9 s. The thermal conductivity of each material was then calculated as a function of platinum wire length, the output voltage, and the current. During this calculation, a nonlinear fitting technique was applied to derive thermal conductivity, as used in previous studies.[23,37,38]

Rheology Measurement: The rheology experiments were done by using a modular compact rheometer (Anton Parr MCR 302) with a thermal chamber attached 25 mm parallel plate geometry. Inks were prepared as mentioned earlier and each specimen was mixed for 1 min at 2000 rpm before the rheology test. Then a 5 ml pipette was used to disperse the mixture on the 25 mm parallel plate. Each specimen was tested from 1 to 100 s and held at 22 °C for the duration of the test.[37]

Voltage and Power Measurement: The printed wearable TEG device was connected to an oscilloscope (Tektronix, TDS2004C) to measure the output voltage. A hotplate stirrer (Fisherbrand Isotemp) was used as a heat source. Before loading the device on the hot plate, the temperatures of the hotplate and the TEG were measured using a thermometer (Fluke, 62 MAX Infrared Thermometer) to achieve the exact temperature difference. The device was placed on the hot plate, and the output voltage was measured for 120 s at each test. To measure the generated power of the printed TEG, a resistance decade box (Extech, 380400) was connected to the device in parallel to be utilized as the external resistance (R_{ex}). The output voltage was

measured at each point and converted to the power and power density by estimating the current based on the known value of R_{ex}.

Electromechanical Characterization: A 70×11×2.4 mm^3 tensile TEG sample was fabricated to be stretched under a displacement-controlled test. A voltage divider and an external power supply (Electro Industries, DIGI 35A) were used to measure the resistance change of LM-elastomer conductors while a linear actuator was used to strain the specimens. Arduino, LabVIEW, and NI QAD were used to collect the change in voltage, control the linear actuator, and collect the data. The displacement rate for the cyclic electromechanical test was set to 20 $mm \cdot min^{-1}$. Moreover, a universal load frame (Instron 68SC-2) was used to acquire the force-displacement data at a displacement rate of 20 $mm \cdot min^{-1}$ for ten cycles.

Microscopy Imaging: Scanning electron microscopy (SEM) was conducted on an FEI Sirion XL30 operating at 5 kV for the LMEC, Expancel microspheres, and HMEC samples. The micrograph of the LM composites with large droplets was captured using an optical microscope (Leica DMi1).

A.1.2 Energy Harvesting Performance Characterization Methods

Method 1: One Side Heat Conduction

Here refer to “One side heat conduction” to describe a characterization technique wherein the device is placed on a heat source without mounting heatsinks on the opposite side. In this setup, high temperature is transmitted through heat conduction from the heat source and dissipated on the other side via heat convection to the ambient environment.

1. Response at thermal equilibrium with One Side Heat Conduction

This method reports a thermoelectric performance at the thermal equilibrium. It measures the most practical output for wearable applications and studies the effect of air convection. However, the actual temperature gradient across TE legs is different from the temperature gradient of the test setup as the heat transfer converges to reach thermal equilibrium, reporting mitigated voltage outputs compared to other methods.

2. Response at peak with One Side Heat Conduction

This method reports the maximum output acquired from the given test conditions. However, it has a drawback as the temperature difference within the TED decreases over time until it reaches a state of thermal equilibrium. The output voltage converges to a lower value than the peak value since the initial large temperature gradient cannot be maintained.

Method 2: Active Temperature Control on Both Sides

In this approach, the device is placed between a heat source and a heatsink, both equipped with closed-loop temperature control systems to maintain a precise temperature gradient during measurements. This ensures accurate control and monitoring of the temperature gradient, maintaining a constant temperature difference throughout the test. However, this method may not reflect practical working conditions, especially for wearables.

A.2. 3D Architectures for High-Performance Stretchable Thermoelectric Devices

A.2.1 Experimental Section

Thermal Interface LMEC Ink Formulation: Ecoflex 00-30 (Smooth-On) and EGaIn are used to make LMEC ink for thermal interface printing. Ecoflex part A was poured into a 20 ml plastic cup and EGaIn was added drop-by-drop into the cup with a 1:1 volume ratio. The composite was mixed for 30 minutes at 600 RPM with an immersion mixer (Caframo, BDC250). Similarly, Ecoflex part B was poured into another plastic cup and EGaIn was added and mixed in the same manner. In this composite with Ecoflex part B, Slo-jo (Smooth-On) was added with a weight fraction of 4% of the total Ecoflex to prolong the pot life of the final ink. The two LMEC inks with different Ecoflex parts were transferred to another cup and shear mixed for 1 minute at 2500 RPM using a planetary shear mixer (FlackTek SpeedMixer, DAC 150.1 FVZ-K) before being printed.

Heatsink LMEC Ink Formulation: Like the thermal interface LMEC ink, Ecoflex 00-30 (Smooth-On) and EGaIn are utilized for heatsink ink formulation. Ecoflex part A was poured into a 20 ml plastic cup and mixed for 30 minutes and 600 RPM by immersion mixer (Caframo, BDC250). At the start of the mixing, EGaIn was added drop-by-drop to the plastic cup using the syringe until the EGaIn took 50%V_f of the total volume of the mixture. In the same way, Ecoflex part B and EGaIn were immersion mixed in the different 20 ml plastic cup. Slo-jo (Smooth-On) was added to this cup with a weight fraction of 1% of the total Ecoflex. The two inks were transferred to another cup and shear mixed for 1 minute at 2500 RPM in a shear mixer (FlackTek SpeedMixer, DAC 150.1 FVZ-K) before transferring the heatsink ink to the syringe for printing.

Thermally Insulative HMEC Ink Formulation: In a 20 ml plastic cup filled with part A of Ecoflex 00-30 (Smooth-On), Expancel® (920 DE 80 d30; Nouryon) was added with the 50%V_f based on the volume of the Ecoflex in the cup. THI-VEX (Smooth-On) was also added by 2%wt of the Ecoflex part A in the cup to increase the viscosity while printing the ink. In a different 20 ml plastic cup, Ecoflex part B and Expancel were poured with the same amount and ratio. In this cup, Slo-jo (Smooth-On) was added 2%wt of the Ecoflex part B. The two separate plastic cups were shear mixed using a planetary shear mixer (FlackTek SpeedMixer, DAC 150.1 FVZ-K) for 1 minute and 2500 RPM. These two inks were transferred to another cup and shear mixed for 1 minute and 2500 RPM before printing the heat insulation layer architecture.

Thermal Imaging and Temperature Measurement: A thermal imaging camera (FLIR-T621xx) was used to take Forward Looking Infrared (FLIR) images for thermoelectric devices. A 1 ampere current was applied to the TED to induce a change in temperature on the surface for active heating and cooling. The real-time temperature was recorded via FLIR Tools software. The current was applied for 180 seconds to investigate the change in temperature and the thermal regulation performance in the four different samples. Then the current was cut off to see how the residual heat affects the thermal interface layer.

Wearable Electronics Applications: For battery charging, TEDs were placed on the heat plate with a temperature gradient of 60 °C with respect to the room temperature and connected to a boost converter (MCRY-EVALKIT, MATRIX). The converted voltage was supplied to the coin cell battery (TS920E, Seiko Instruments) for 3 hours and 30 minutes. The battery with a nominal voltage of 1.5 V was discharged to 1.2 V before the measurement to characterize the charging performance of the TEDs with and without the 3D soft architecture. To light up the LED, Macro-TED with the soft architecture and the boost converter were serially connected and attached to the fabric. The integrated device was then worn on the forearm to demonstrate that the body heat can power the LED at room temperature. Similarly, harvested energy from body heat supplied power to a low current temperature/humidity sensor (SPX-16618, Sparkfun), or pressure/temperature sensor (SEN-11084, Sparkfun). The conditions for these sensor demonstrations were an outside temperature of 6 °C and a relative humidity of 81%RH. The sensors were pressed using the index finger for 3 seconds twice, and the measured outcome was delivered to Arduino Uno. The sample rate was set to 1 second and the measured signals were combined after the measurements from two different sensors. A signed consent letter was obtained from the volunteer for wearing the stretchable thermoelectric generator.

A.2.2 TED Performance Comparison

Table A.1. Reported stretchable thermoelectric devices for a comprehensive comparison.

Reference #	Configuration	TE fill factor (%)	Normalized Power Density ($\mu W \cdot cm^{-2} \cdot K^{-2}$)	Performance Measurement Method	Strain limit (%)
2nd Study	π-shaped rigid TE	14.2	**0.161**	**Response at thermal equilibrium with One Side Heat Conduction**	**230**
84	π-shaped rigid TE	20	0.1157	Response at thermal equilibrium with One Side Heat Conduction	40
194	π-shaped rigid TE	4	0.0014	Response at thermal equilibrium with One Side Heat Conduction	83
2nd Study	π-shaped rigid TE	14.2	**1.154**	**Response at peak with One Side heat Conduction**	**230**
46 (1st Study)	π-shaped rigid TE	14.27	0.1806	Response at peak with One Side Heat Conduction	30
70	π-shaped rigid TE	10	0.0241	Response at peak with One Side Heat Conduction	60
194	π-shaped rigid TE	28	0.0656	Response at peak with One Side Heat Conduction	30
33	π-shaped rigid TE	26.2	0.26	Active Temperature Control on Both Sides	20
72	PEDOT:PSS and fabric	N/A	0.0036	Active Temperature Control on Both Sides	80
77	π-shaped rigid TE	9	0.0002	Active Temperature Control on Both Sides	125
82	Fabric and rigid TE	32.3	0.0023	Active Temperature Control on Both Sides	50
196	π-shaped rigid TE	62	0.1015	Active Temperature Control on Both Sides	60
197	π-shaped rigid TE	7	0.0086	Active Temperature Control on Both Sides	30
198	π-shaped rigid TE	10	0.0791	Active Temperature Control on Both Sides	80

199	π-shaped rigid TE	28.4	0.0028	Active Temperature Control on Both Sides	20
200	PEDOT:PSS	N/A	0.0004908	Active Temperature Control on Both Sides	80
201	PEDOT:PSS	N/A	4.58E-6	Active Temperature Control on Both Sides	160
202	PEDOT:PSS and fabric	N/A	1.00E-07	Active Temperature Control on Both Sides	40
203	PEDOT:PSS and fabric	N/A	0.033	Active Temperature Control on Both Sides	30.5
204	Fabric and rigid TE	N/A	0.0928	Active Temperature Control on Both Sides	100
205	Fabric	39	0.0001	Active Temperature Control on Both Sides	65
206	Fabric and elastomer	N/A	0.0001	Active Temperature Control on Both Sides	120

A.2.3 Filler Images and LM Size Distribution

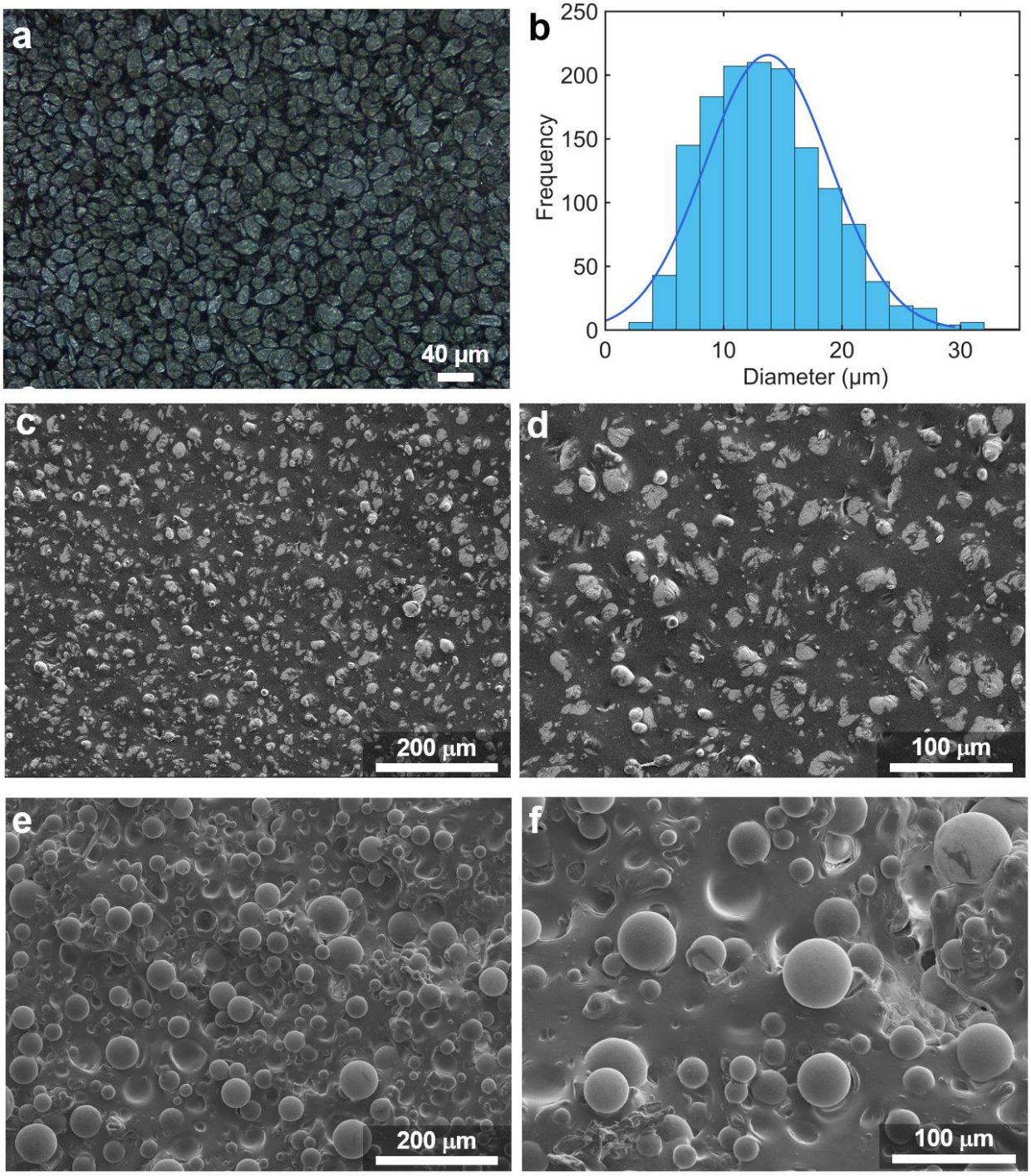

Figure A.1. Microscopic images of liquid metal particles in LMEC and their size distribution. (a) Microscopic images of LMEC, 20x magnification. (b) Size distribution of liquid metal particles in LMEC with an average size of 13.7 mm. SEM images and thermal conductivity of multifunctional elastomer composites. (c) SEM image of LMEC, 150x magnification. (d) SEM image of LMEC, 300x magnification. (e) SEM image of HMEC, 150x magnification. (f) SEM image of HMEC, 300x magnification.

A.2.4 Computational Simulation

COMSOL Multiphysics® was utilized for finite element analysis of thermoelectric simulation. The simulated result corresponds to the output voltage response of the actual TED at the thermal equilibrium, enabling the estimation of harvested voltage from different core layer structures. The ambient room temperature was set to 293.15 K and the convective heat transfer coefficient of the air was set to 12 $W \cdot m^{-2} \cdot K^{-1}$. The thermal conductivity of LMEC and HMEC were set to 1.28 $W \cdot m^{-1} \cdot K^{-1}$, and 0.11 $W \cdot m^{-1} \cdot K^{-1}$, respectively. The properties of the bismuth telluride were chosen according to the pre-defined data in the FEA software. Detailed parameters for the simulation are denoted in Table A.2. The boundary conditions were a heat conduction at the bottom thermal interface with a constant temperature of 353.15 K, and a heat convection from the air on the top thermal interface. Since a representative volume element (RVE) with a pair of p-type and n-type semiconductors is considered in the simulation, periodic boundary conditions were applied to the four sides of the element. For calculating the TE fill factor, an out-of-plane area taken by thermoelectric pellets was divided by an out-of-plane area of the RVE. The simulated TE fill factors were 5, 7.8, 9, 11.1, 14, 17, 20, 25, 30, 35, and 40% by changing the cross-sectional area of RVE while anchoring the area of TE pellets as 1.4×1.4 mm^2.

Table A.2. Parameters used in COMSOL simulation.

Parameter	Value	Unit
Ambient temperature	20	℃
Hot side temperature	80	℃
Thermoelectric leg thermal conductivity	2	$W \cdot m^{-1} \cdot K^{-1}$
Thermoelectric leg electrical conductivity	87000	$S \cdot m^{-1}$
Thermoelectric leg Seebeck coefficient	± 220	$\mu V \cdot K^{-1}$
EGaIn thermal conductivity	26.4	$W \cdot m^{-1} \cdot K^{-1}$
EGaIn electrical conductivity	3.4×10^6	$S \cdot m^{-1}$
EGaIn thickness	0.1	mm
Ecoflex 00-30 thermal conductivity	0.19	$W \cdot m^{-1} \cdot K^{-1}$
LMEC thermal conductivity	1.28	$W \cdot m^{-1} \cdot K^{-1}$
HMEC thermal conductivity	0.11	$W \cdot m^{-1} \cdot K^{-1}$
Air thermal conductivity	0.0242	$W \cdot m^{-1} \cdot K^{-1}$
Heat transfer coefficient	12	$W \cdot m^{-2} \cdot K^{-1}$

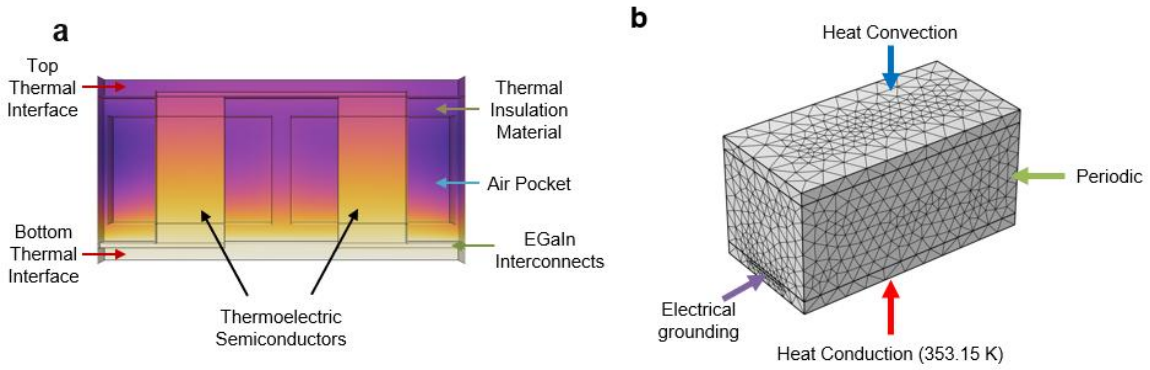

Figure A.2. Representative Volume Element (RVE) for computational simulation of TED with four different core layer structures. (a) A cross-section of RVE with the denoted components in TED. (b) Meshed RVE with the denoted boundary conditions for thermoelectric FEA simulation.

A.2.5 TED Fabrication Process

P and N-doped thermoelectric semiconductors were arranged in an alternating order on the acrylic mold to fabricate the TED. The orange-colored tape was used on the acrylic mold to locate the TE semiconductors. In the second step, HMEC ink was printed on the gap between the TE legs to create an elastic foundation and hold the TE pellets. Third, HMEC ink was printed to create a 3-dimensional HMEC structure for core layers. The prepared structure was then attached to a layer of uncured HMEC printed on another substrate to cover the other side. Next, EGaIn was stencil printed on the prepared core layer to create stretchable interconnects. After that, LMEC was printed to encapsulate the liquid phase interconnects and provide a thermal interface layer. The last two steps were repeated on the other side to finish the fabrication. The TED specimens for comparing core layer architectures have a dimension of 70×10×4 mm^3 with marginal spaces to clip the specimen for testing, and the Macro-TED with 12% infill HMEC core layer has a dimension of 60×22×4 mm^3. Additionally, the stretchable heatsink was 3D printed on top of the fabricated Macro-TED. Flexible wire or silver tape was attached to the two ends of the TED's electrical circuit to connect the TEDs with other electronics.

For the printing details, a high-precision dispenser system (ML 808GX; Musashi Engineering) with a 3-axis dispensing grip was used for direct-writing the multifunctional inks. All the elastomer composite inks were transferred to a syringe and shear mixed for 15 seconds and 2500 RPM before printing to remove trapped air. To print the thermal insulation HMEC ink, a blunt-tip 23 gauge and a pressure of 200 kPa were chosen to achieve a thin line of highly viscous ink. Printing speeds were set to 9 $mm \cdot s^{-1}$ for a single line and 20 $mm \cdot s^{-1}$ for a densely filled region. For thermal interface LMEC ink, printing parameters of 35 kPa and 15 $mm \cdot s^{-1}$ were used with a cone-shaped 18-gauge nozzle. The heatsink LMEC ink was printed with a speed of 5 $mm \cdot s^{-1}$ and a pressure of 35 kPa. The height of the heatsink wall was set to 2.5 mm and the gap between the walls was set to 1.2 mm. Each elastomer composite ink was cured in the oven at 50 °C for more than 4 hours after being printed.

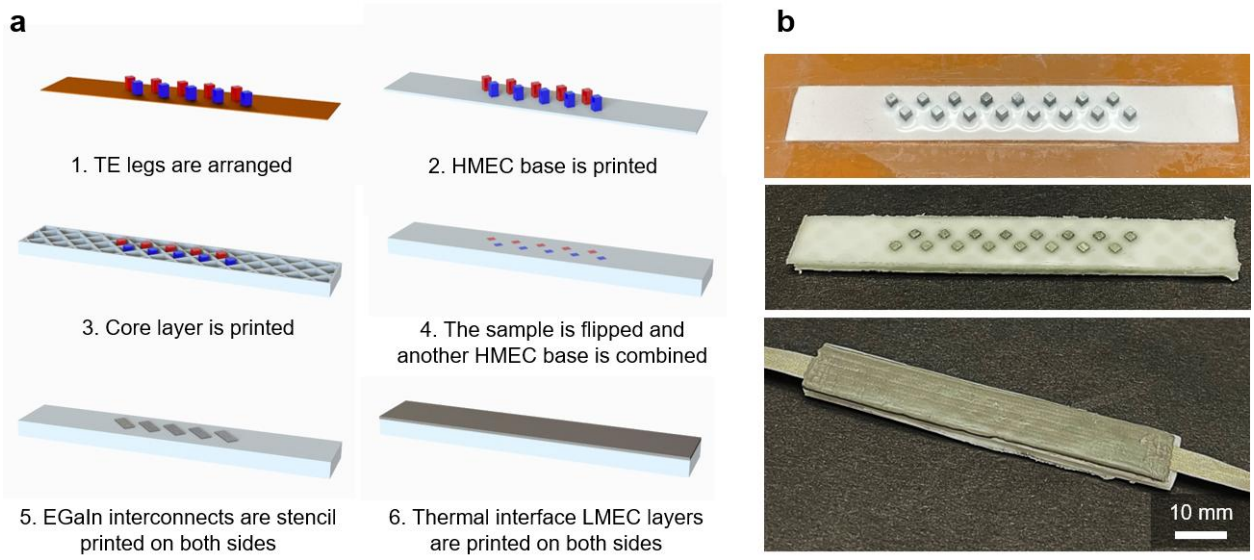

Figure A.3. An additive fabrication process of TE tensile specimen. (a) A schematic of layer-by-layer TED fabrication process with 3D printed core layer structure. (b) Photographs of 12% infill HMEC specimen with arranged TE legs, structured air pockets with visible regions indicating the air pockets with trapped air, and fabricated TE tensile specimen.

A.2.6 Open-Circuit Voltage Response of TEDs with Different Core Layers

To measure the open-circuit voltage, a hot plate stirrer (Fisherbrand™ Isotemp™) was used for the heat source. The temperature of the plate surface and TE specimens were measured by a thermometer (Fluke, 62 MAX Infrared Thermometer) to maintain exact temperature gradients with respect to the room temperature. Each test was conducted for more than 150 seconds to acquire voltages at peak and thermal equilibrium at every temperature gradient. The V_{OC} was measured by connecting the TED with an oscilloscope (Tektronix, TDS2004C) and placing the device on the hot plate.

The harvested voltage can be varied according to the material and the structure of the core layer. Employing HMEC enhances the overall voltage response compared to the base elastomer (Ecoflex 00-30). With the 100% infill HMEC core layer, the measured voltage at thermal equilibrium was increased by 13%. Moreover, the output voltage is further improved with the 3D printed core layer structures, which allow thermoelectric semiconductors to be surrounded by the air. As a result, unwanted heat transfer, such as heat conduction through the device without passing through the TE pellets, is constrained. It additionally increases the harvested voltage by 14% at the thermal equilibrium due to improved thermal management from the structural design.

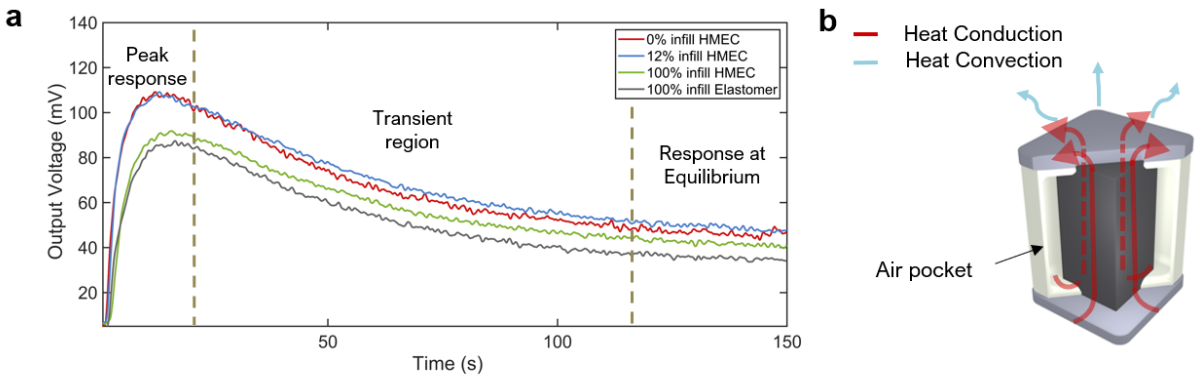

Figure A.4. Output voltage responses of four different core layer TE specimens. (a) Measured output voltage with respect to time at ΔT = 60 °C. (b) A schematic image of concentrated heat transfer in 12% infill HMEC thermoelectric architecture.

A.2.7 Uniaxial Strain Test of Functional Composites

To investigate the mechanical strain failure of the functional composites, a universal load frame (Instron 68SC-2) was used to obtain the stress-strain data. Following the ASTM D638-14 Standard Test Method, Type IV dog bone specimens with different elastomer composites and structures were fabricated. The displacement rate of every test was 20 mm·min^{-1}.

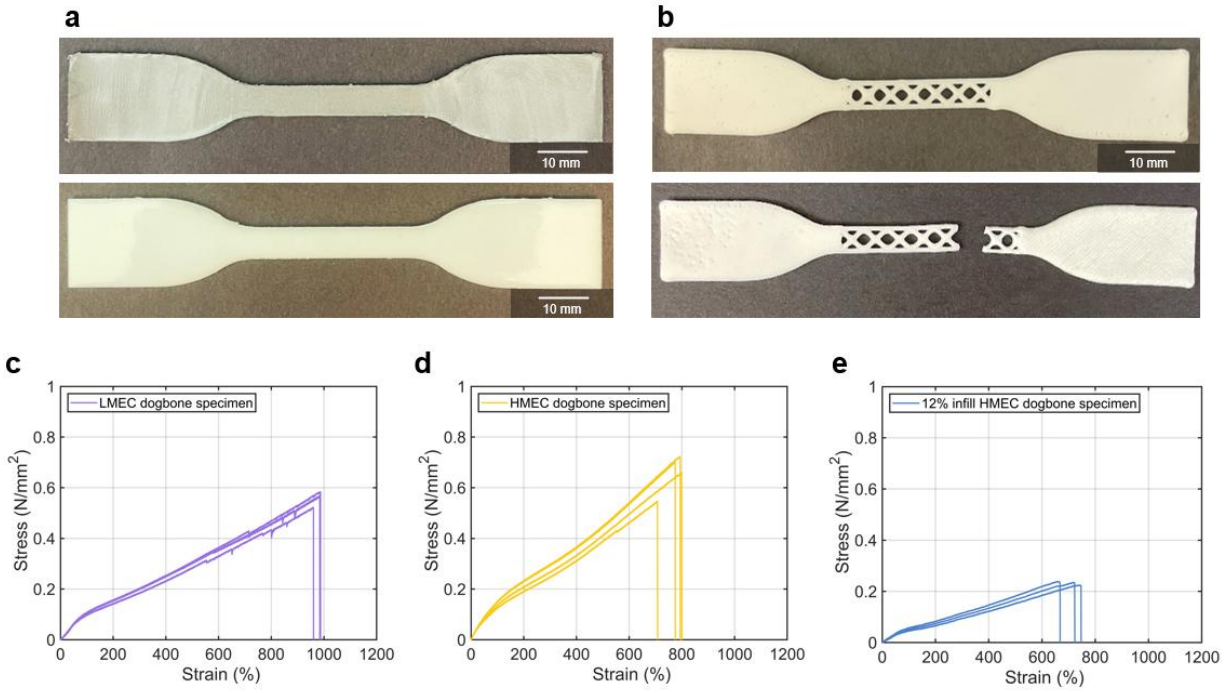

Figure A.5. Uniaxial tensile test of multifunctional elastomer composites. (a) Photograph of dog-bone shaped LMEC (top) and HMEC (bottom) tensile specimen according to ASTM D638-14 Type IV Standard Testing Method. (b) Photograph of dog-bone shaped HMEC tensile specimen representing 12% infill structure according to ASTM D638-14 Type IV Standard Testing Method. (c) A stress-strain plot of LMEC tensile specimens. (d) A stress-strain plot of HMEC tensile specimens. (e) A stress-strain plot of 12% infill HMEC tensile specimens.

A.2.8 Mechanical/Electromechanical Characterization under Uniaxial Strain

A universal load frame (Instron 68SC-2) was also utilized to investigate the mechanical strain failure. The TE tensile specimens with four different designs (Interlayer Gap, Air Pockets, Composite, and Elastomer) have a dimension of 70×10×4 mm^2 with 16 TE pellets. The displacement rate of every test was 20 $mm \cdot min^{-1}$, and the gauge length was 33 mm.

The same device architectures were utilized to study robustness under the cyclic loading. Devices were connected to a voltage divider electronic circuit to measure the internal resistance of the tensile samples. A power supply (Electro Industries, DIGI 35A) applied the voltage to the circuit while Arduino controlled linear actuator was stretching the specimen. The voltage of the TE specimen was measured and recorded using LabVIEW and NI QAD. All tensile samples were under 50% strain at a strain rate of 1 mm/s for 2,000 cycles. The measured voltage across the TE tensile specimens in the voltage divider circuit was later converted to resistance using MATLAB. To study the excellent robustness of the TE tensile specimen with air pockets, the 12% infill specimen was under uniaxial strain of 100%, or even higher strain until electrical failure.

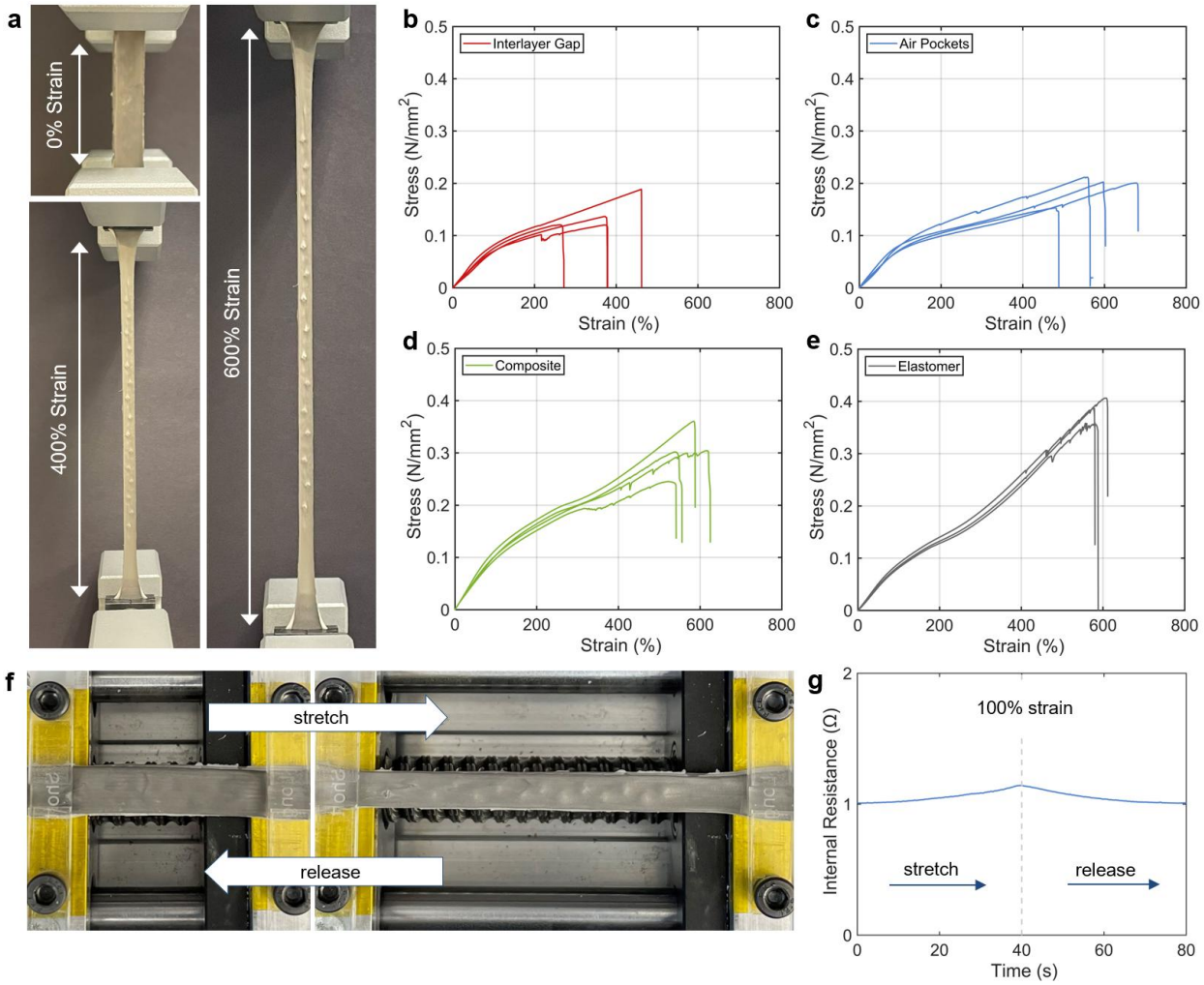

Figure A.6. Uniaxial tensile test of TE tensile specimens. (a) Photographs of TE tensile specimen with air pockets under 0%, 400%, and 600% strain without mechanical failure. (b) A stress-strain plot of Interlayer Gap TE tensile specimens. (c) A stress-strain plot of Air Pockets TE tensile specimens. (d) A stress-strain plot of Composite TE tensile specimens. (e) A stress-strain plot of Elastomer TE tensile specimens. (f) Photographs of TE specimen with 12% infill HMEC core layer at rest (left) and being stretched to 100% (right) (g) Measured internal resistance of 12% infill HMEC TE tensile specimen during the stretch and release.

A.3. Breathable Interfaces in Thermoelectric Wearables

A.3.1 Experimental Section

EGaIn Synthesis: Eutectic gallium-indium (EGaIn) was prepared by alloying gallium (99.99% purity, Luciteria) and indium (99.995% purity, RotoMetals) to serve as a liquid metal filler. Gallium was melted in the oven (Heratherm OGS60, Thermo Scientific) at 90 °C for 3 hours, and indium was added into the melted gallium in a glass jar with the ratio of 75 wt% Ga and 25 wt% In. The jar was placed on a hot plate (HP88850100, Thermo Scientific) at 200 °C overnight to complete the synthesis.

Composite Inks Formulation: LM, BN (Powder, 98% purity, MilliporeSigma), TPU (Texin® RxT85A, Covestro), and SEBS (H1522, Asahi Kasei) were used to formulate composite inks in 20ml vial. Sonifier (SFX 550, Brandson) and planetary mixer (DAC 150.1 FVZ-K, FlackTek SpeedMixer) were used for dispersing the particles. To prepare LM – SEBS encapsulation ink in 20 ml vial, SEBS was first dissolved in toluene overnight with weight ratio of 25%. LM was added to the vial with 1:1 volume ratio with respect to the dissolved SEBS and mixed at 3500 RPM for 3 minutes using the planetary mixer.

EHD printing: A high-precision dispenser system (ML 808GX, Musashi Engineering) and a 3-axis robotic arm were used to print the prepared composite inks. Before printing, the composite inks were transferred to a 5-cc syringe barrel (7366101, Nordson) with a 150 μm inner diameter needle (7018433, Nordson). The high voltage source (PS/EL30P01.5, Glassman High Voltage, Inc.) was connected to the stainless-steel part in the needle to supply the electric potential to the ink. The printing pressure was 80 kPa and the printing speed was 55 $mm \cdot s^{-1}$. The printing height was increased by 10 μm for each additional layer deposited on top.

Thermal Conductivity Measurement: Thermal conductivities were measured with the transient hot wire method with sample size of 3. A 25 μm-diameter platinum wire with a length of 20 – 25 mm was soldered at each end to a solid copper wire and two testing samples with 30×30 mm^2 were sandwiching the platinum wire. 50 g weight and acyclic sheet coated with PDMS was placed on top of the samples to ensure contact between samples and the platinum wire. The prepared samples were connected to a high-current source measure unit (Keithley 2460, Tektronix), and the voltage of the platinum wire was measured at 70 mA current for 0.9 seconds.

Using nonlinear fitting, the thermal conductivity of samples was calculated based on the input current, measured voltage, and the length of the platinum wire.

Skin Compatibility Tests: For water vapor transmission rate measurement, a modified wet-cup method based on ASTM E96 was used to measure the water vapor transmission rate of the interface samples with sample size of 3. A 50 mL centrifuge tube (SimPure) was filled with deionized water to half capacity (25 mL), and the sample was sealed over the tube opening with an exposed diameter of 24 mm. The assembly was maintained at a controlled temperature of 23–24 °C and relative humidity of 45–55%. The weight change was recorded over a period of 3 days using high-precision balance scale (MS105DU, Mettler Toledo), and water vapor transmission rate was calculated from the steady-state weight loss. For allergy test, five different samples were taped on a subject's forearm using breathable medical tape (Transpore™, 3M) for a week. The samples were re-secured immediately if they became detached during the test period

Laser patterning: TPU layers were designed through CorelDraw and patterned using high-precision CO_2 laser system with a wavelength of 10600 nm (Series 8000, Epilog Laser). Laser parameter was selected as 457.2 mm/s, 8W, and 2500 Hz. TPU was cast on a stainless-steel plate and laser treated to pattern holes for TE pellets and air pathways.

Field-emission scanning electron microscope (SEM): SEM was performed with a scanning electron microscope (Apreo 2S, Thermo Scientific). Gold was coated on the sample surfaces using a sputter coater (Cressington 108 Auto V2, Ted Pella) to see it under the scanning electron microscope.

Thermoelectric Energy Harvesting Performance Measurement: The temperature of the surface of the hot plate stirrer, biceps, and TED surfaces were measured with an IR thermometer (62 Max, Fluke) to ensure exact temperature gradients in experiments. TEDs were connected to an oscilloscope (TDS2004C, Tektronix) for open circuit voltage data collection, an oscilloscope and a resistance decade box (Extech, 380400) for delivered power measurement, or a high-current source measure unit (Keithley 2460, Tektronix) for voltage-current sweep.

Thermal Imaging and Thermoelectric Temperature Modulation: A thermal imaging camera (FLIR-T621xx, Flir) was used to take Forward Looking Infrared (FLIR) images. TEDs were placed on an aluminum plate, and currents were applied to the TED using power supply (DIGI 35A, Electro Industries) to induce a change in temperature on the surface for active heating and

cooling. The real-time temperature was recorded using FLIR Tools software. The current was applied for 180 seconds to investigate the change in temperature before cutting off the current.

Bending test: A linear actuator and acrylic sheets were used to bend the thermoelectric devices in two orthogonal directions with a bending radius of 10 mm. Arduino, LabVIEW, and NI QAD were used to control the actuator and collect the change in resistance during cyclic bending.

Recycling: Recycling efficiency was measured via EDS for qualitative estimation and change in weight with sample size of 3 for quantitative estimation, respectively. A field-emission scanning electron microscope with 25 kV (Apreo 2S, Thermo Scientific) was used for EDS, and high-precision balance scale (MS105DU, Mettler Toledo) was used for weighting. To centrifuge the solutions during the recycling process, a benchtop centrifuge (Centrifuge 5810 R, Eppendorf) was used with 1 minute acceleration and deceleration.

A.3.2 Breathable Thermoelectric Devices Comparison

Table A.3 compares previously reported breathable thermoelectric devices. The two primary comparison criteria are device architecture and normalized power density, as these determine the thermoelectric output. The use of additional rigid components, such as heatsinks or solid electrodes, is also considered, as it affects wearability through added weight, reduced softness, and discomfort during long-term wear. The final criterion is recyclability, which is important for the sustainability of flexible electronics but difficult to achieve in certain device architectures.

Table A.3. Reported breathable thermoelectric devices.

Reference	Device architecture	Use of additional rigid components	Normalized Power density ($nW \cdot cm^{-2} \cdot K^{-2}$)	Recyclability
This work	Inorganic TE materials and patterned composite interfaces	X	64.37	Yes (both fillers and TE material)
[236]	Inorganic TE materials and woven fabric interfaces	Aluminum heatsinks and copper wires	980.64	X
[66]	Inorganic TE materials and electrospun composite interfaces	Copper electrodes	0.64	X
[237]	Woven TE fabrics	X	1.35	X
[203]	Woven TE fabrics	X	0.15	X
[238]	Electrospun/Electrosprayed TE fabrics	X	0.13	X
[239]	Woven TE fabrics	X	4.46×10^{-2}	X
[240]	Electrospun TE fabrics	X	1.09×10^{-3}	X
[241]	Coated TE fabrics	X	6.74×10^{-6}	X

A.3.3 LM–BN–TPU Composite Ink Synthesis

The composite ink synthesis procedure is illustrated in Figure A.7a. A binary solvent system consisting of dimethylformamide (DMF) and tetrahydrofuran (THF) at a 2:8 volumetric ratio was prepared in a 20 mL vial. LM was first introduced into the solution and probe sonicated at 82.5 W for 10 minutes to achieve uniform dispersion. BN particles were subsequently added and subjected to identical sonication in the same vial. The resulting suspension exhibited well-dispersed LM with particle size below 4 μm and 2-dimensional BN platelets with a major axis length below 250 nm (Figure A.7b). Although reduced particle size generally diminishes the bulk thermal conductivity of composites, it is necessary to prevent nozzle clogging during EHD printing. Notably, nanoscale BN platelets (Figure A.7c) electrically isolate the LM to prevent short-circuiting, while bridging the adjacent particles for thermal transport. After the two successive sonication, TPU was introduced into the suspension and allowed to dissolve over 24 hours under ambient condition. The final ink was homogenized in a planetary mixer at 2,500 RPM for 1 minute, yielding a uniform composite ink ready for deposition (Figure A.7d).

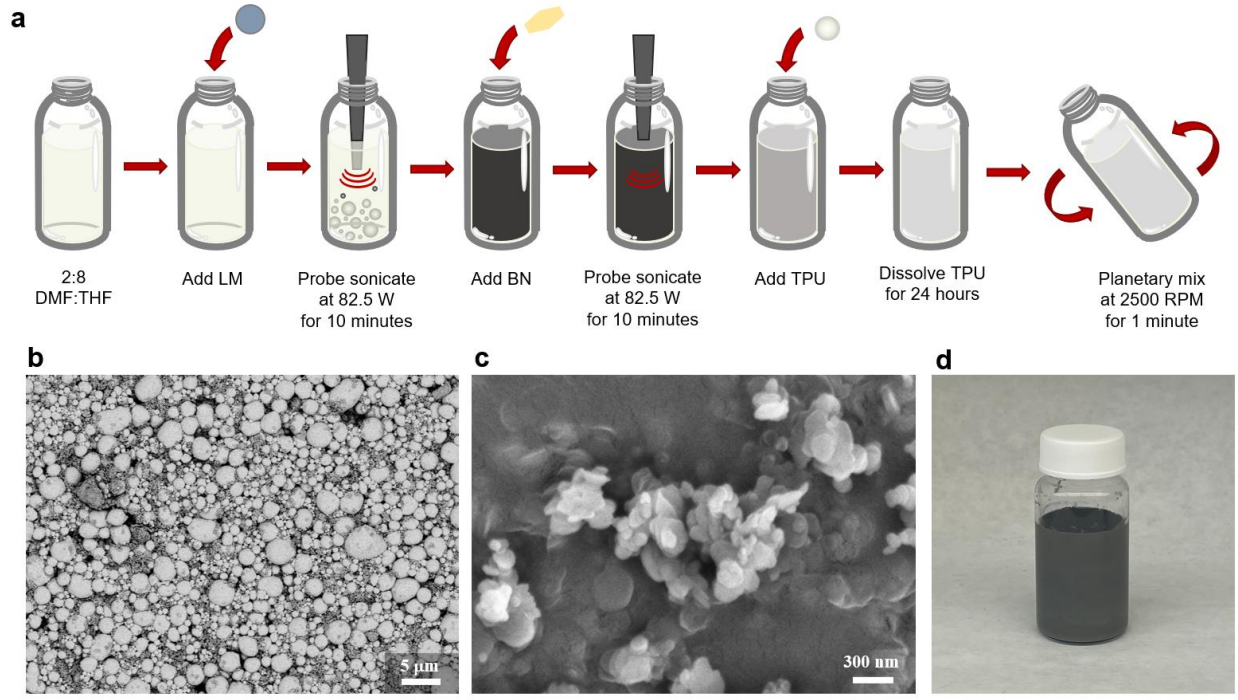

Figure A.7. LM–BN–TPU composite ink synthesis process: a) A schematic illustrating the synthesis process. b) SEM image of probe sonicated LM and BN. c) SEM image of BN. d) Synthesized LM–BN–TPU composite ink.

A.3.4 Sweat Pore and Permeable Interface Design

Sweat pore distributions were conservatively modeled to guide the design of the permeable thermal interface layer.[143] Figure A.8a illustrates the targeted body regions, the modeled sweat pore distribution, and the permeable interface layer positioned on the skin. The diameter of each sweat pore in the model is set to 100 μm, with 400 μm spacing between the pores (Figure A.8b). The printed thermal interface adopts a square lattice pattern with a line spacing of 230 μm. Circular skin-contact regions at the lattice nodes have a diameter of approximately 60 μm (Figure A.8c). This permeable interface is designed to avoid occluding sweat pores, thereby maintaining breathability while optimizing the structure for efficient heat conduction.

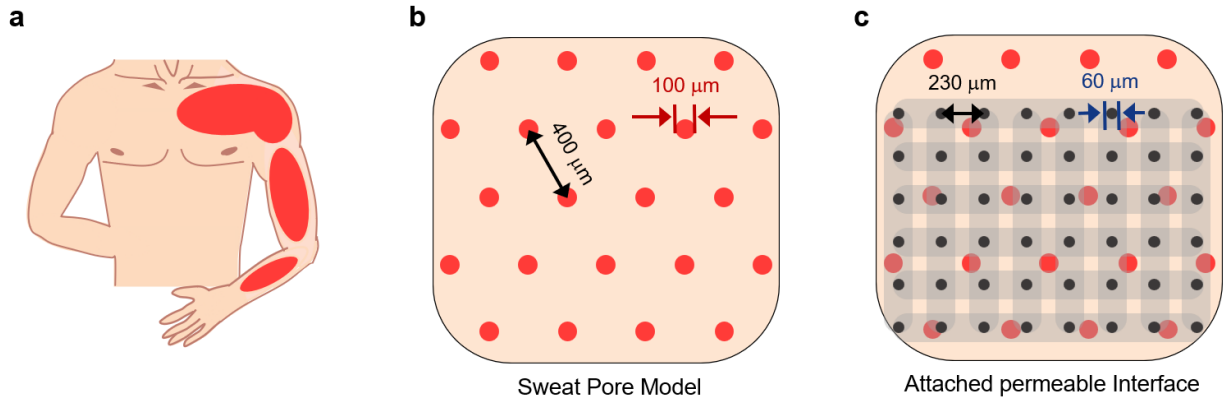

Figure A.8. Sweat pore and permeable interface design: a) Upper chest, shoulder, and arm as targeted body parts. b) Conservative sweat pore model. c) Permeable interface design with square lattice pattern.

A.3.5 EHD-Printed Mat with the Square Lattice Pattern

The structural characteristics of the EHD-printed permeable interfaces incorporate a sweat-pore-considered top surface and a flat bottom surface (Figure A.9a). The top surface shows a wavy profile consisting of discrete circular skin-contact regions (Figure A.9b). This geometry minimizes continuous surface coverage on the skin and helps preserve open pathways between the contact regions, thereby preventing blocking sweat pores. In contrast, the flat bottom surface provides a stable platform for attaching other layers or mounting electronic components (Figure A.9c).

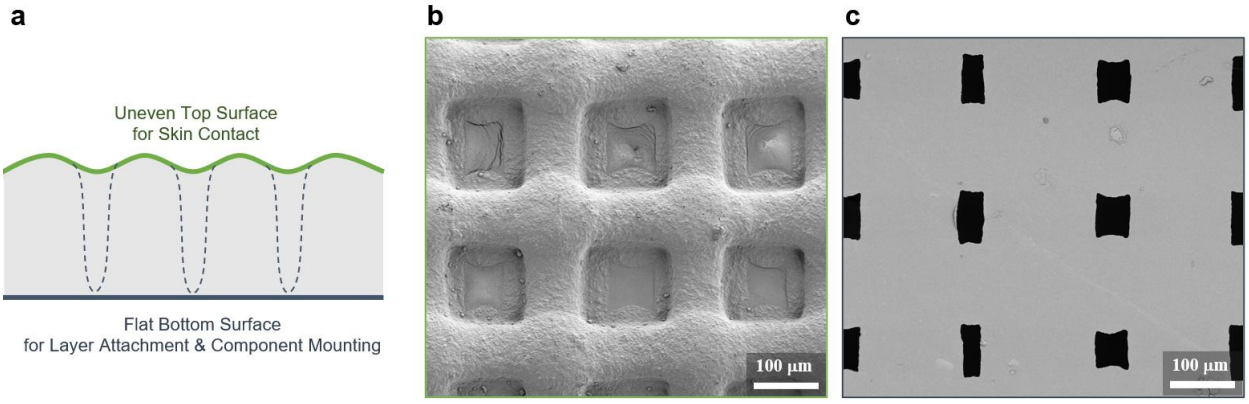

Figure A.9. Top and bottom surfaces of EHD-printed permeable interfaces: a) A schematic showing top and bottom surfaces. b) SEM image of the top surface. c) SEM image of the bottom surface.

A.3.6 Electric Field in EHD Printing

The electric field is a governing parameter in EHD printing, as the electric potential between the emitter and substrate drives composite ink jetting. When the electric field is insufficient, the electrostatic force cannot overcome the surface tension of the ink at the nozzle, preventing the formation of a stable jet. Furthermore, in the absence of an electric field, the process transitions to direct ink writing (DIW), where ink is deposited onto the substrate solely by mechanical pressure (Figure A.10a). This results in discrete droplets and poor printing resolution. In contrast, under an adequately applied electric field, EHD printing enables stable jetting and the formation of continuous, high-resolution lines (Figure A.10b).

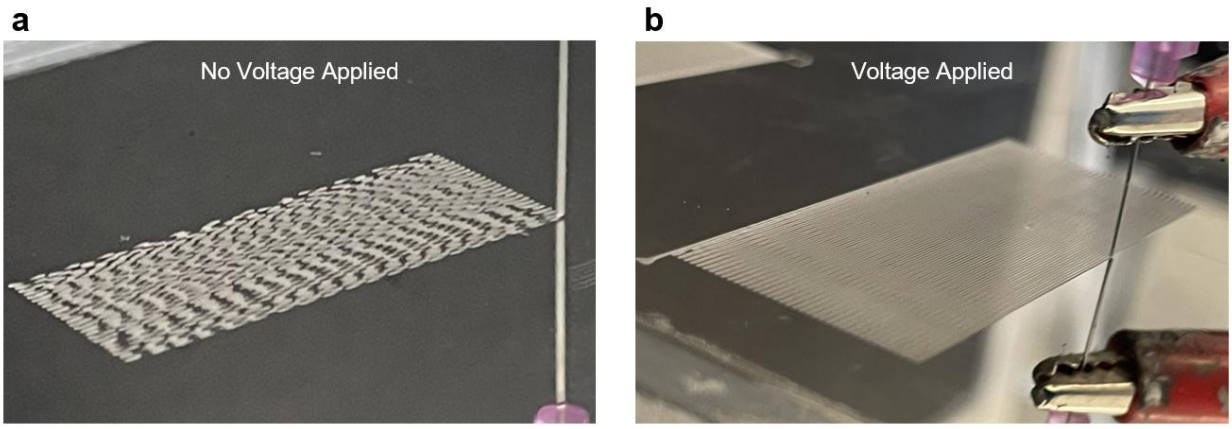

Figure A.10. DIW and EHD printing: a) DIW printing without electric field and composite ink jetting. b) EHD printing with electric field and composite ink jetting.

A.3.7 Multiphysics Simulation

Multiphysics simulations were performed to evaluate the thermoelectric performance of different device architectures as shown in Figure 4.3, Figure A.11**,** and Figure A.12. The simulation parameters are summarized in Table A.4**.** Before simulation, the thermal conductivities of the materials were experimentally measured. Thermal simulations were first conducted on different interfaces, including the 55:5:40 film, EHD-printed 55:5:40 mat, and TPU, to evaluate the effect of interface geometry (Figure A.11). After confirming their thermal properties, the EHD-printed permeable thermal interfaces were incorporated into the design of the breathable TEDs. A representative volume element was used to model TEDs, and periodic boundary conditions were applied to represent interactions with neighboring units.[45,63] A constant heat flux from the skin was applied to the bottom surface of the device. Because the structure is breathable, convective heat transfer was applied to the remaining exposed surfaces. TE semiconductors have a dimension of 1.4×1.4×3 mm^3. The thermal interface layers, TPU layers, LM interconnects, and LM–SEBS encapsulations have thicknesses of 0.175 mm, 0.25 mm, 0.1 mm, and 0.2 mm, respectively.

Table A.4. Simulation parameters

Parameter	Value	Unit
Bi_2Te_3 thermal conductivity	1.6	$W \cdot m^{-1} \cdot K^{-1}$
Bi_2Te_3 electrical conductivity	86957	$S \cdot m^{-1}$
Bi_2Te_3 Seebeck coefficient	±210	$\mu V \cdot K^{-1}$
LM–BN–TPU thermal conductivity	0.8795	$W \cdot m^{-1} \cdot K^{-1}$
LM–SEBS thermal conductivity	0.8655	$W \cdot m^{-1} \cdot K^{-1}$
LM Interconnect thermal conductivity	26.4	$W \cdot m^{-1} \cdot K^{-1}$
LM Interconnect electrical conductivity	3.4×10^6	$S \cdot m^{-1}$
TPU thermal conductivity	0.1724	$W \cdot m^{-1} \cdot K^{-1}$
Convective heat transfer coefficient	10	$W \cdot m^{-2} \cdot K^{-1}$
Skin temperature	303.15	K
Ambient temperature	293.15	K

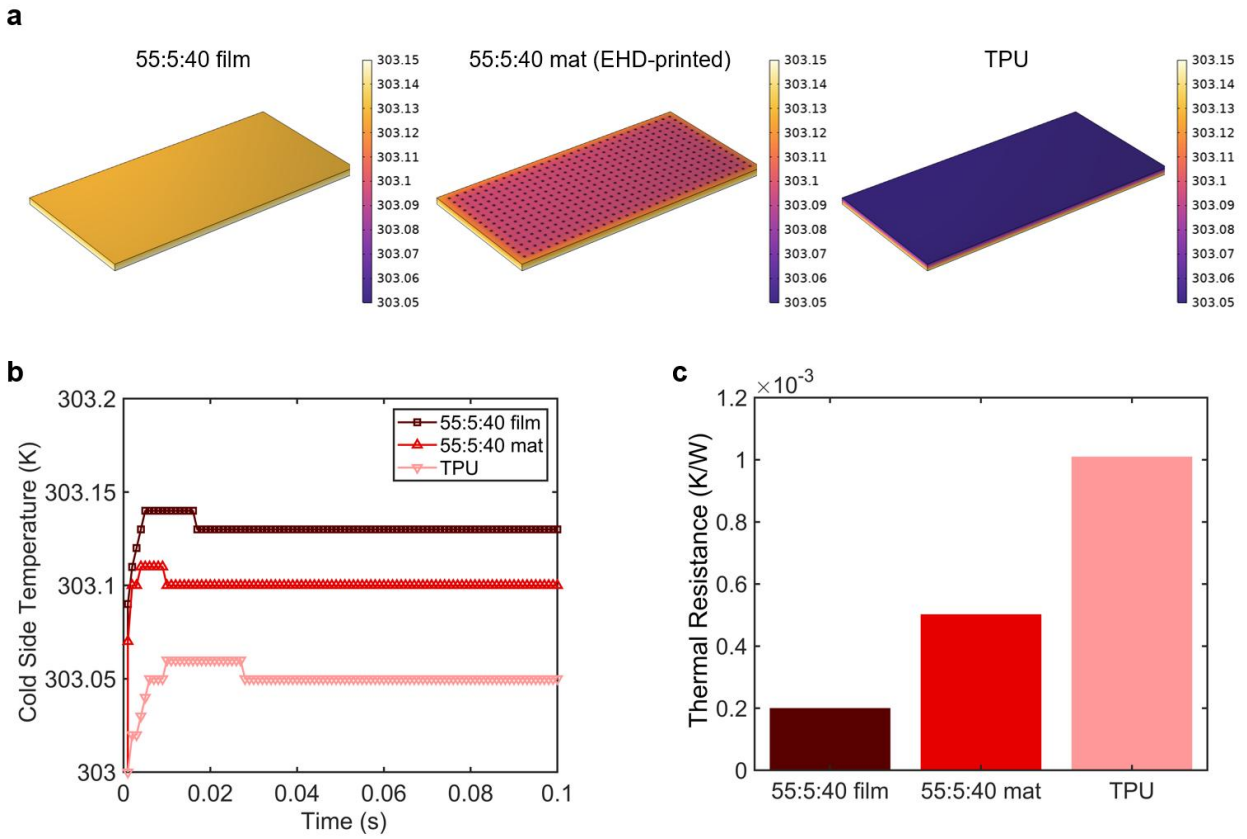

Figure A.11. Thermal interface comparisons: a) Temperature distributions in 55:5:40 film, EHD-printed 55:5:40 mat, and TPU film thermal interfaces with the same thickness. b) Simulated cold side temperature with respect to time when the interfaces are in contact with the skin at 0 second. c) Estimated thermal resistances of thermal interfaces.

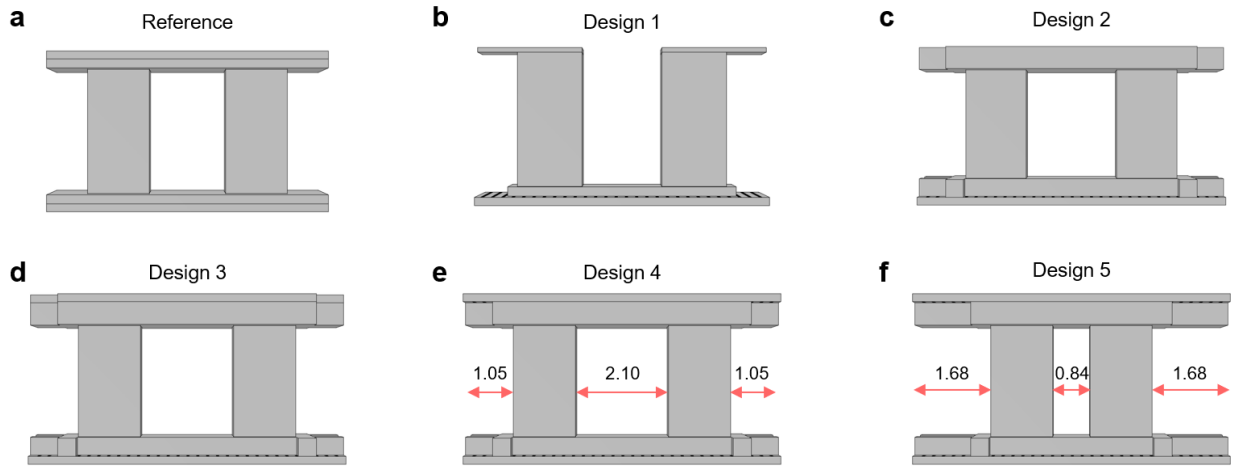

Figure A.12. Side view of TED designs: a) Impermeable reference design. b) Design 1 with copper interconnects. c) Design 2 with LM interconnects and upper TPU layer. d) Design 3 with LM interconnects, upper TPU layer, and composite interface on the cold side. e) Design 4 with LM interconnects, upper TPU layer, and micropatterned heatsink. f) Design 5 with LM interconnects, upper TPU layer, micropatterned heatsink, and 2:8 TE pair distance ratio.

A.3.8 Thermoelectric Energy Harvesting

Thermal circuit and heat transfer mechanisms of breathable TEDs are shown in Figure A.13. As validated through Equation (1) to (7), the harvested energy from thermoelectric devices is highly dependent on conjugated heat transfer through the device that maximizes the temperature gradient within the TE pellets.

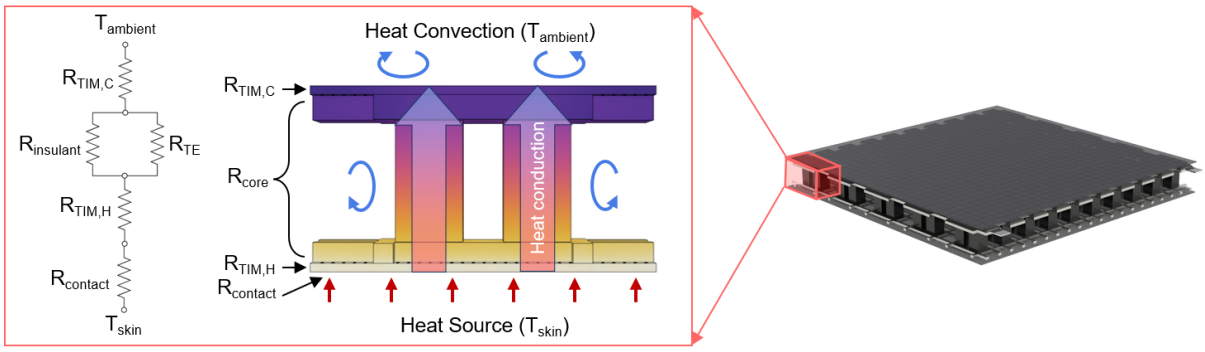

Figure A.13. Thermal circuit and heat transfer mechanisms of breathable TEDs.

A.3.9 Micropatterned Heatsink

EHD-printed thermal interface functions as a micropatterned heatsink when integrated on the hot side of TEDs (Figure A.14a), generating higher thermoelectric voltage as demonstrated in Design 4 and 5. The heat dissipation capability of the heatsink was evaluated using the normalized heat transfer coefficient (h) and the thermal resistance per area across the device (R_{th}):

$$h = \frac{Q_{\text{conv}}}{A(T_{\text{surface}} - T_{\text{ambient}})} \tag{A.1}$$

$$R_{th} = \frac{T_{\text{skin}} - T_{\text{ambient}}}{Q} \tag{A.2}$$

Q_{conv} is convective heat transfer from the heatsink, A is the surface area of the heatsink, $T_{surface}$ is the temperature of the heatsink surface, and $T_{ambient}$ is the ambient temperature. Figure A.14b and c present h and R_{th} as functions of TE fill factor and distance ratio, respectively. Design 4 corresponds to a 5:5 distance ratio, while Design 5 corresponds to a 2:8 ratio. The heat transfer coefficient remains nearly constant across device architectures, whereas the device thermal resistance decreases with increasing TE fill factor. This reduction in thermal resistance leads to the estimated increases in voltage output per unit area.

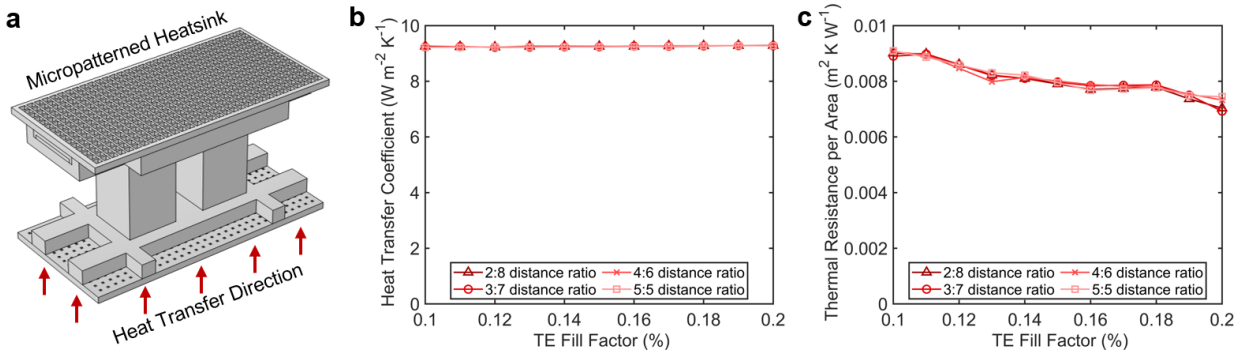

Figure A.14. EHD-printed thermal interfaces as a micropatterned heatsink: a) CAD model showing integrated micropatterned heatsink. b) Simulated normalized heat transfer coefficients as a function of distance ratio and TE fill factor. c) Simulated thermal resistance per area as a function of distance ratio and TE fill factor.

A.3.10 Permeable Interface Interlocking via Partial SEBS Resolidification

The permeable thermal interfaces and the LM–SEBS encapsulation layers are mechanically interlocked through partial dissolution and resolidification of SEBS, as illustrated in Figure A.15a. To achieve this interlocking structure, toluene is applied onto the EHD-printed LM–BN–TPU mat. The solvent readily wets the porous EHD-printed structure. While toluene does not dissolve the TPU in the mat, it partially dissolves the outer surface of the LM–SEBS encapsulation layer upon contact. During solvent evaporation, the softened SEBS phase becomes mobile and infiltrates the lattice-like pores of the permeable interface. As the residual toluene evaporates, the SEBS resolidifies within the porous network, producing a mechanically interlocked interface between the LM–SEBS layer and the permeable mat. This process enables strong adhesion without damaging the TPU-based fiber mat. Microscopic images further confirm the formation of the interlocked structure (Figure A.15b–d). This indicates the infiltration of SEBS into the porous structure of the EHD-printed mat to mechanically adhere the layers.

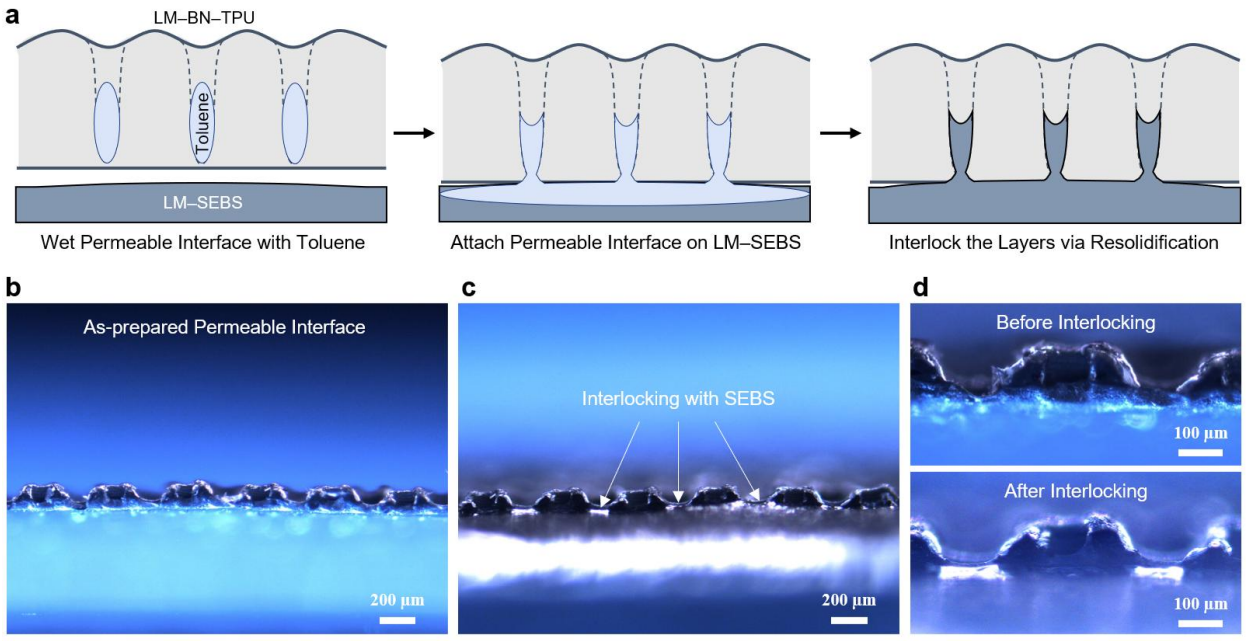

Figure A.15. Interface interlocking via SEBS resolidification: a) A schematic illustrating the interlocking process. b) A cross-section of permeable interface before interlocking. c) A cross-section of permeable interface after interlocking. d) Cross-sections of permeable interface before and after interlocking.

A.3.11 Delivered Power

The electrical power delivered from TED to an external load resistor was characterized.[45,46] Measurements were performed under *Initial ΔT* of 10 °C and 30 °C (Figure A.16a and b). In both temperature gradients, the measured power across the load resistor follows a trend similar to the open-circuit voltage response. The output power rapidly increases at the early stage, corresponding to the peak response, and then gradually approaches saturation as the device reaches thermal equilibrium.

The maximum power output occurs when the load resistance matches the internal resistance of the TED as shown in Figure A.16c. Experimentally, the peak power was obtained at R_{load} of 6.5 Ω, which closely matches the internal resistance of the device (~7 Ω). Under the initial temperature gradient of 10 °C, the maximum delivered power at equilibrium was measured to be 12.464 μW. This result is consistent with impedance matching behavior expected in thermoelectric power generation systems.

Table A.5 summarizes the power-related terminology used throughout this work to avoid ambiguity. Maximum power refers to the highest power output measured from a sourcemeter during a current sweep performed under thermal equilibrium conditions at different initial temperature gradients. Delivered power was measured using an external load resistor, and represents the electrical power transferred from the TEDs to the connected electronics. Delivered power at peak refers to the highest delivered power at the largest achievable temperature gradient across the thermoelectric pellets prior to reaching thermal equilibrium. Power density is defined as the delivered power normalized by the device area and is used to quantify power generation per unit area, enabling comparison with other thermoelectric devices.

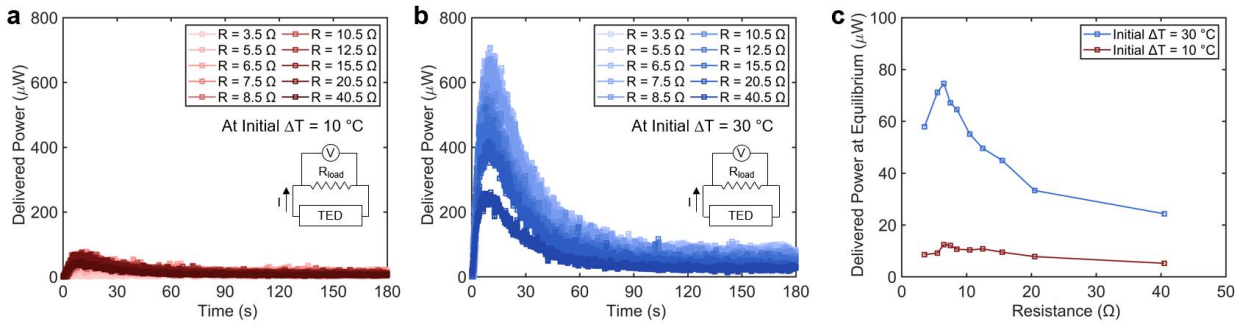

Figure A.16. Delivered power to the external load resistor from TED: a) Delivered power to the load resistor at the initial temperature gradient of 10 °C. b) Delivered power to the load resistor at the initial temperature gradient of 30 °C. c) Delivered power at equilibrium with respect to resistance of external load resistor.

Table A.5. Power-related term definitions

Term	Definition	Condition	Effective device area (A_{device})
Maximum power	Maximum $V \cdot I$ value measured from source measure unit at thermal equilibrium	After 150 s when ΔT_{TE} reaches equilibrium	35×35 mm^2
Delivered power	$V_{load}^2 \cdot R_{load}^{-1}$ with R_{load} of 6.5 Ω at thermal equilibrium	After 150s when ΔT_{TE} reaches equilibrium	35×35 mm^2
Delivered power at peak	$V_{load}^2 \cdot R_{load}^{-1}$ with R_{load} of 6.5 Ω at maximum ΔT_{TE}	Within first 15 s after TED is placed on the hot plate	35×35 mm^2
Power density	Delivered power normalized by the effective device area $V_{load}^2 \cdot R_{load}^{-1} \cdot A_{device}^{-1}$	After 150s when ΔT_{TE} reaches equilibrium	35×35 mm^2

A.3.12 Recycling of Permeable Interfaces and Core Layer

The permeable interfaces and the device core layer were subjected to recycling procedures to fabricate breathable TEDs with recovered materials. For the permeable interfaces, the primary objective was the reclamation of LM and BN (Figure A.17a). After removal from the device via toluene treatment, the interface was transferred to a centrifuge tube containing THF to dissolve the TPU matrix. The suspension was mixed and centrifuged at 10,000 rpm for 10 minutes, after which the supernatant containing dissolved TPU was decanted. An aqueous NaOH solution was then added to the tube to facilitate separation of LM from the remaining composite. The mixture was agitated and centrifuged again at 10,000 rpm for 10 minutes, allowing the LM to be recovered as a single droplet and separated from the solution. Subsequently after decanting NaOH, an HCl solution was added to remove residues. After decanting the acid solution, the remaining BN was collected and purified through sequential washing with deionized water and ethanol, each followed by centrifugation at 10,000 rpm for 10 minutes.

The device core layer went through a separate recycling process to recover TE pellets and LM (Figure A.17b). The core layer was first transferred to a glass container with THF, which dissolves both TPU and SEBS, thereby releasing the encapsulated TE pellets. The pellets were manually retrieved using tweezers and further cleaned by planetary mixing in THF. The remaining composite mixture, consisting of LM, TPU, and SEBS, was then transferred to a centrifuge tube for polymer removal. The suspension was mixed and centrifuged at 6,000 rpm for 10 minutes, and this process was repeated three times to ensure the removal of the polymeric components. After decanting the polymer-containing supernatant, a NaOH solution was added to the tube. The mixture was agitated and centrifuged at 10,000 rpm for 10 min to recover LM droplets from the residual composite. 50 p-type TE legs with a total weight of 2.025 g, 50 n-type TE legs with a total weight of 2.027 g, and LM droplet with a weight of 1.316 g are reclaimed from the core layer with a weight of 5.766 g.

The recycled LM remains as bulk liquid droplets, so no change in filler morphology or particle size distribution is expected. Boron nitride is a solid filler, so SEM images of BN and LM–BN after sonication were taken to determine whether the morphology or particle size distribution changed. No apparent change was observed in the BN platelets or the sonicated LM–BN particles, as shown in Figure A.18a and b. Over multiple recycling cycles, the recoverable material quantity and recycling efficiency are expected to decline slightly. In recycling LM–BN–

TPU composites, gallium oxide must be removed from the LM to recover the particles. Because repeated sonication increases the oxide fraction and reduces droplet size, recycling efficiency may decline over successive cycles.

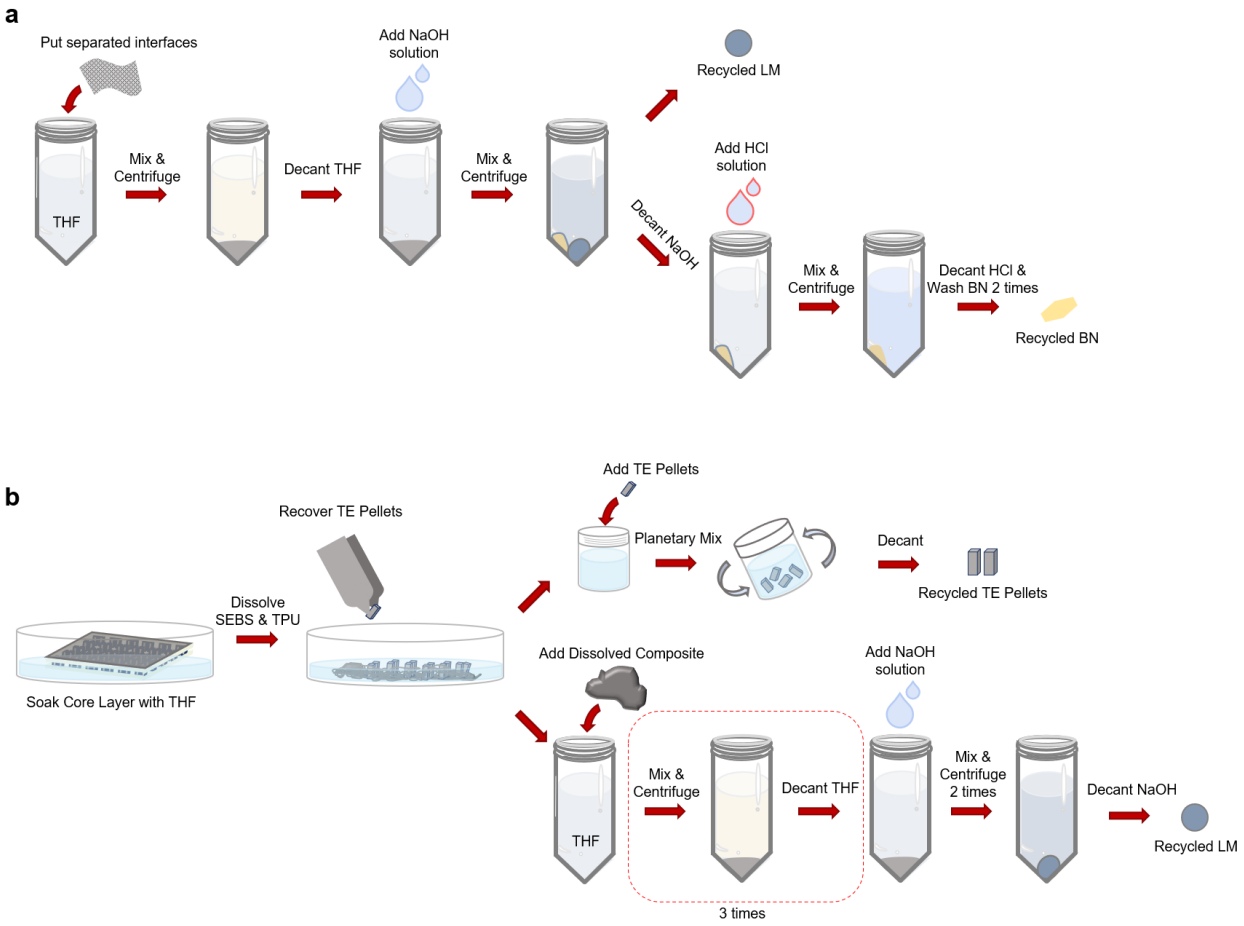

Figure A.17. Recycling of permeable interfaces and core layer in breathable TEDs: a) A schematic of permeable interface recycling process. b) a schematic of core layer recycling process.

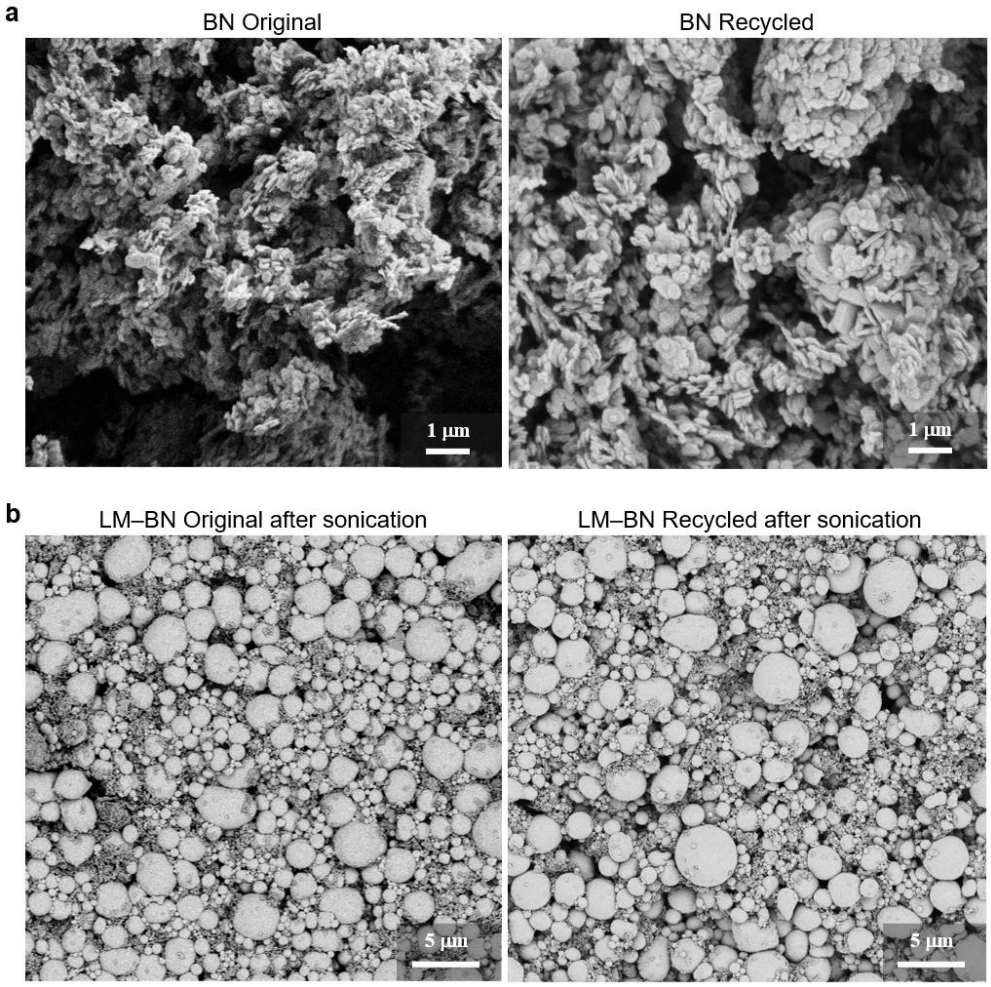

Figure A.18. SEM images of particles before and after recycling. a) BN platelets before and after recycling. b) Sonicated LM and BN particles before and after recycling.

A.4. Reconfigurable Soft Liquid Metal–Vitrimer Composites

A.4.1 Experimental Section

EGaIn Synthesis: Eutectic gallium-indium (EGaIn) was synthesized by alloying gallium (99.99% purity, Luciteria) and indium (99.995% purity, Luciteria), and incorporated as a liquid metal in this study. Liquid-state gallium was prepared by heating it in the oven at 90 °C for 3 hours. Indium was transferred to a glass jar and the melted gallium was poured into the jar at the ratio of 75 wt% Ga and 25 wt% In. The jar was placed on a hotplate at 200 °C overnight to make EGaIn.

Vitrimer Synthesis: The metal catalyst (Zinc acetylacetonate hydrate, Millipore Sigma) was mixed with fatty acids (Pripol 1040, Cargill).[157] In a glass beaker containing the fatty acids, the catalyst was added at 5 mol% to COOH groups of the fatty acids. The beaker was heated at 180 °C under vacuum for 3 hours until no gas evolution was observed, and the catalyst was fully dissolved. The fatty acid mixture and epoxy resin (Bisphenol A diglycidyl ether (DGEBA), Millipore Sigma) were poured into a 40 ml plastic cup with 1:1 stoichiometry ratio between COOH groups and epoxy. The cup with polymer precursor was mixed using a planetary mixer (DAC 515-200 pro, FlackTek) at 2500 RPM for 1 minute. The mixed polymer precursor was poured into a mold and cured in the oven at 100 °C for more than 6 hours.

LM−Vit Synthesis: Bulk EGaIn was dispersed in ethanol by ultrasonic processor with microtips (Q700, Qsonica). 10 g of EGaIn and 10 g of ethanol were added into a 20 ml glass vial and probe sonicated with the power of ~5 W and processing time of 15 minutes. The solution vial was cooled down with a water bath during the probe sonication. The sonication was performed using 10 seconds of pulse-on and 3 seconds of pulse-off to prevent overheating of the solution. The sonicated solution was transferred to a plastic cup and sat for an hour to allow the LM particles to settle. The ethanol in the solution was decanted after LM and ethanol separated, and the plastic cup was dried in the oven at 80 °C for an hour to completely evaporate the ethanol. The catalyzed fatty acid mixture and epoxy resin were added to the plastic cup with dried LM particles. The ingredients in the cup were thoroughly mixed using a planetary mixer at 2500 RPM for 5 minutes. The composite precursor was heated in the oven at 100 °C for 30 minutes and mixed once more at 2500 RPM for 1 minute. The precured mixture was poured into a metal mold with PTFE tapes and cured at 100 °C. The temperature was set to 100 °C as higher

temperature causes composite phase separation during curing. After 10 minutes, the mixture was doctor bladed to produce a flat top surface. The composite was then cured for more than 6 hours to ensure complete crosslinking.

Fatty Acid Acidity Measurement: The acidity of the vitrimer precursor was evaluated using pH test strips (HYDRION, pH range 2.0–10.0) and was found to be in the range of pH 3.5–4.5. Measurements were taken at four points: immediately after mixing the precursor before curing, after 15 minutes of curing at 100 °C, after 30 minutes of curing at 100 °C, and after 45 minutes of curing at 100 °C. After 60 minutes of curing, the precursor became highly viscous due to extensive crosslinking, making pH measurement no longer feasible.

Microscopic Imaging and Particle Size Measurement: A high-resolution digital microscope (VHX-7000 Digital Microscope, Keyence) was used to capture the size of the liquid metal particles. A 3-dimensional analysis to estimate the particle size was done with "Depth-up" integrated analysis tool. For scanning electron microscopy (Mira3, Tescan), the composites were cryofractured and sputter coated (208 HR, Cressington Sputter Coater) with 10 nm of gold. The LM particle size was measured through ImageJ software, and the long axis of each particle was reported as its diameter.

Density Measurement: Fatty acid vitrimer density was measured with a pycnometer (Ultrapyc 5000, Anton Paar and AccuPyc II 1340, Micromeritics). A 1.0–1.5 g solid piece and a 0.25–0.30 g pulverized vitrimer were tested to ensure accurate measurement. The average density of vitrimer was measured to be 1.06 g cm^{-3}.

Differential Scanning Calorimetry: Thermal behavior of cured and uncured composites was measured using a hermetic lid, aluminum pan, and DSC calorimeter (DSC 2500, TA Instruments). For cured composites, 5–10 mg samples were tested from -80 to 260 °C with the heating rate of 10 °C min^{-1}. For uncured composites, 5–10 mg samples were tested under 4 hours of isothermal conditions at 100 °C and 0–50% LM V_f.

Fourier Transform Infrared Spectroscopy: Components and functional groups within the LM–Vit composites were analyzed with Fourier Transform Infrared (FTIR) Spectrometers from PerkinElmer. Small sample pieces (~10 mg) and the test fixture were rinsed with isopropyl alcohol prior to clamping the samples.

X-ray Photoelectron Spectroscopy (XPS) Analysis: All XPS spectra were acquired using a Kratos Axis Ultra DLD spectrometer. This instrument has a monochromatized Al Kα X-ray source and a low-energy electron flood gun for charge neutralization. X-ray spot size for these acquisitions was approximately 700×300 μm^2. Pressure in the analytical chamber during spectral acquisition was less than 3×10^{-8} Torr. Pass energy for survey and detailed spectra (composition) was 80 eV. Pass energy for the high-resolution spectra was 20 eV. The take-off angle (the angle between the sample normal and the input axis of the energy analyzer) was 0° (0-degree take-off angle ~ 100 Å sampling depth). The Kratos Vision2 software program was used to determine peak areas and to calculate the elemental compositions from peak areas. CasaXPS was used to perform peak fitting the high-resolution spectra. For the high-resolution spectra, a Shirley background was used, and all binding energies were referenced to the C ls C–C bond peak at 284.8 eV.

Thermogravimetric Analysis: Thermal degradation and volume fraction of composites were investigated using thermogravimetric analyzer (Q500, TA Instruments). The sample mass varied between 20–50 mg. The temperature was ramped from 25 °C to 700 °C at a rate of 10 °C min^{-1} in a nitrogen environment.

Dynamic Mechanical Analysis: Dynamic mechanical analysis (Q800, TA Instruments) was conducted with sample sizes of 10×25×1.5 mm^3 at 1 Hz and 0.05% strain amplitude in a tension fixture. A preload of 0.01 N was applied, and the heating ramp was 3 °C min^{-1} from -50 °C to 150 °C.

Stress Relaxation Measurement: To calculate the activation energy and topology freezing temperature (T_v), stress relaxation experiments were performed on a DHR-3 rotational rheometer (TA Instruments). The rheometer was equipped with an 8 mm stainless steel parallel plate geometry, maintaining a sample thickness of ~1.5 mm. A constant normal force of 10 N was applied throughout the experiment to ensure optimal contact between the sample and the rheometer plates. Stress relaxation measurements were performed by applying a 5% shear strain while monitoring the shear modulus over a duration of one hour. Experiments were conducted over a temperature range of 70 °C to 220 °C. Prior to each measurement, the sample was equilibrated at the target temperature for 5 minutes.

Thermal Conductivity Measurement: Thermal conductivities of composites were measured by the hot disk method (Fox 50, TA Instruments). The upper temperature was 15 or 25 °C depending on the sample and the lower temperature was 5 °C. A chiller (ThermoCube, Solid State Cooling Systems) helped to control the temperature of the disks. The composites were cut into circular disks with a diameter of 5 cm and a thickness of 1–1.5 mm.

Mechanical Testing: Tensile and cyclic loading test specimens were prepared according to the ASTM D638 with Type IV specimen. An extensometer was attached to the tensile frame (Alliance RT/5, MTS Systems Corp.) to precisely measure the elongation of the samples. Pneumatic clamps were used to secure the soft composites and avoid damage or distortion. The strain rate was 20 mm min^{-1} for tensile and cyclic loading tests. In cyclic loading tests, 5 cycles were conducted for each strain step.

Electrical and Electromechanical Characterization: Four-probe electrical multimeter (Keithley 2000, Tektronix) and portable electrical multimeter (Fluke 114) were used to measure electrical resistance. For the electromechanical measurements, samples were mounted on a linear actuator which was connected to Arduino, LabVIEW, and NI DAQ for data acquisition. The strain rate of 20 mm min^{-1} with 50% uniaxial strain was used for 4,000 cycles.

Statistical Analysis: Experimental data from each test were analyzed using MATLAB for statistical processing. Assuming a normal distribution, results are presented as mean ± one standard deviation. Sample sizes (n) are specified in the figure captions or legends. Electrical conductivity measurements, tensile tests, and cyclic loading tests were conducted with five independent replicates per parameter setup. All other measurements were performed with a minimum of three independent replicates.

A.4.2 Synthesis process and LM particle size distribution

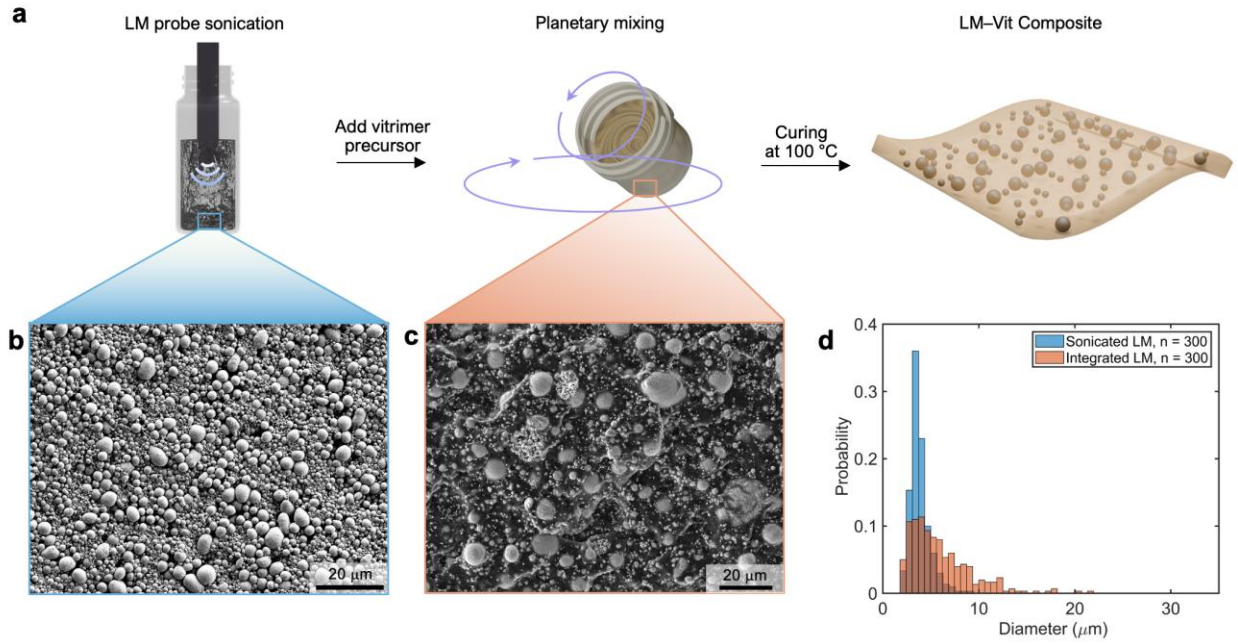

Figure A.19. Illustration of liquid metal vitrimer (LM–Vit) composite synthesis and LM particle size distributions: (a) Illustration of LM–Vit composite synthesis process with probe sonication, planetary mixing, and curing at 100 °C. (b) SEM image of probe sonicated LM. (c) SEM image of LM in the 50% LM–Vit composite after being cured. (d) Particle size distributions of sonicated LM and integrated LM after 50% LM–Vit has been cured (sample size of 300).

A.4.3 Isothermal Differential Scanning Calorimetry on Uncured LM–Vit

In differential scanning calorimetry (DSC) test, heat flow ($\frac{dH_t}{dt}$) and heat (H_t = time-dependent heat, ΔH_t = heat generated up to time t, ΔH_{tot} = total heat required to complete the reaction) can be measured.[242,243] From this measurement, degree of conversion (a), representing the extent to which the polymer is cured upon heating, and the conversion rate ($\frac{da}{dt}$), representing the speed of the composite's solidification due to CAN formation, can be derived as below:

$$a = \frac{\int_0^i dH_t}{\Delta H_{tot}} = \frac{\Delta H_t}{\Delta H_{tot}} \tag{A.3}$$

$$\frac{da}{dt} = \frac{1}{\Delta H_{tot}} \times \frac{dH_t}{dt} \tag{A.4}$$

In composites with low filler fractions (10% and 20%V_f), the conversion rate is slightly faster than that of the neat vitrimer. However, composites with higher filler fractions (40% and 50%V_f) show a slower conversion rate in the early stage. This can be explained by the conductive fillers improving heat distribution, which speeds up the curing process in low-fraction composites. In contrast, the excessive LM content in high-fraction composites occupies spaces and impedes CAN formation, slowing the curing rate.

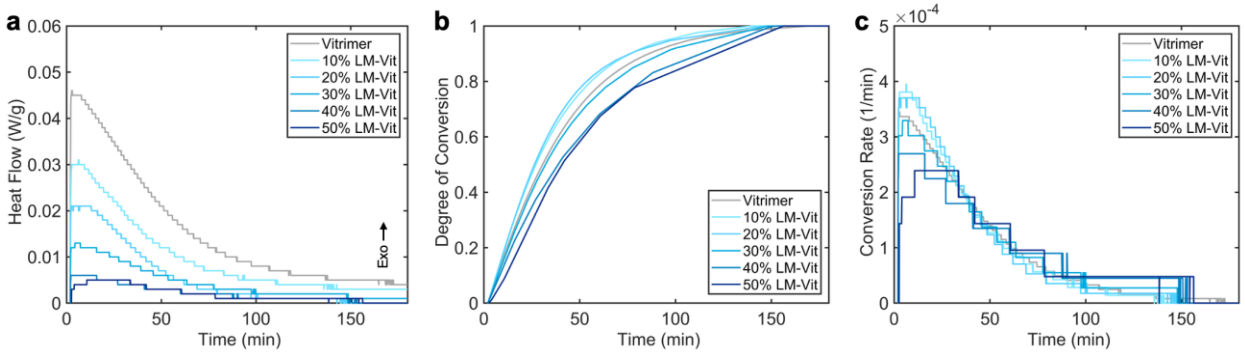

Figure A.20. Isothermal DSC results at 100 °C for uncured LM–Vit with different volume fractions: (a) Isothermal heat flow. (b) Degree of conversion. (c) Conversion rate.

A.4.4 Fourier Transform Infrared spectroscopy

In FTIR results, LM inclusions impede infrared signals, resulting in tilted absorbance slope and weak peaks with high loading of LM. Carbonyl ester group (1735–1750 cm^{-1}) and broad hydroxyl group (3100–3650 cm^{-1}) peaks imply that CAN is successfully created in LM–Vit composites, while decreasing with higher LM contents due to fewer sites for CAN.

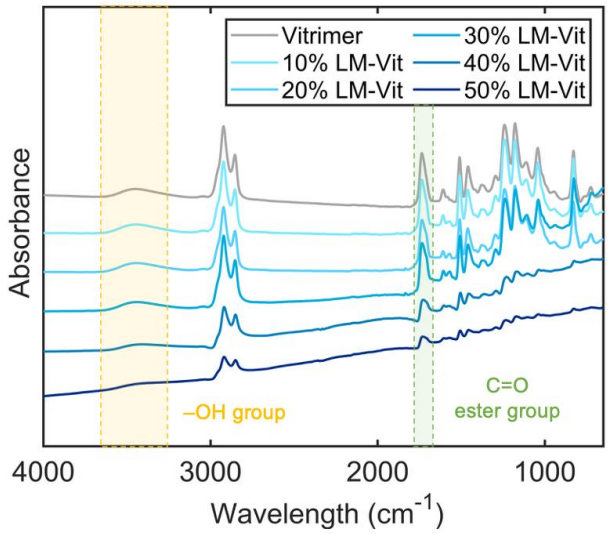

Figure A.21. FTIR spectroscopy analysis of LM–Vit composites.

A.4.5 Thermogravimetric analysis

Temperature corresponding to 5% mass loss ($T_{5\%}$) and the onset of thermal degradation (T_o) inform the thermal stability of LM–Vit composite. The remaining mass after the experiment was also utilized proportionally to infer the volume fraction of LM in the composite synthesis, which is 5.7% for carbonized vitrimer and 100% for LM as the boiling point of EGaIn is higher than 2000 °C.[244]

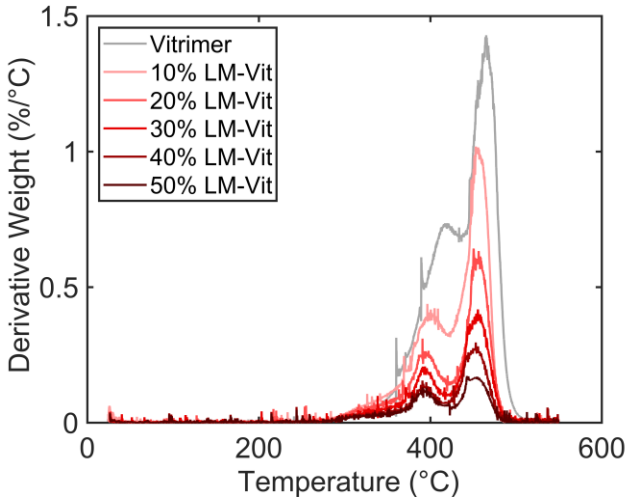

Figure A.22. Calculated derivative weight of LM–Vit composites from thermogravimetric analysis.

Table A.6. Measured characteristic temperatures of LM–Vit composites

Material	$T_{5\%}$ (TGA) (°C)	T_o (TGA) (°C)	T_g (DMA) (°C)	T_v (Rheometer) (°C)
Vitrimer	364.2	378.2	32.7	126.8
10% LM–Vit	356.2	364.7	30.9	122.1
20% LM–Vit	367.6	364.2	31.4	120.5
30% LM–Vit	381.9	361.4	32.8	130.1
40% LM–Vit	392.8	361.6	33.8	128.4
50% LM–Vit	398.4	360.9	32.9	131.7

A.4.6 Scanning electron microscopy

SEM images show that LM particles merge and form a large droplet during synthesis because of weakened oxide layer and shear stress from mixing. This coalescence is more prevalent in high LM volume fractions (V_f of 40–50%) than low volume fractions (V_f of 10–30%). It is measured that 30% LM–Vit has a particle size of 4.26 ± 2.53 μm and 50% LM–Vit has a particle size of 6.73 ± 3.80 μm.

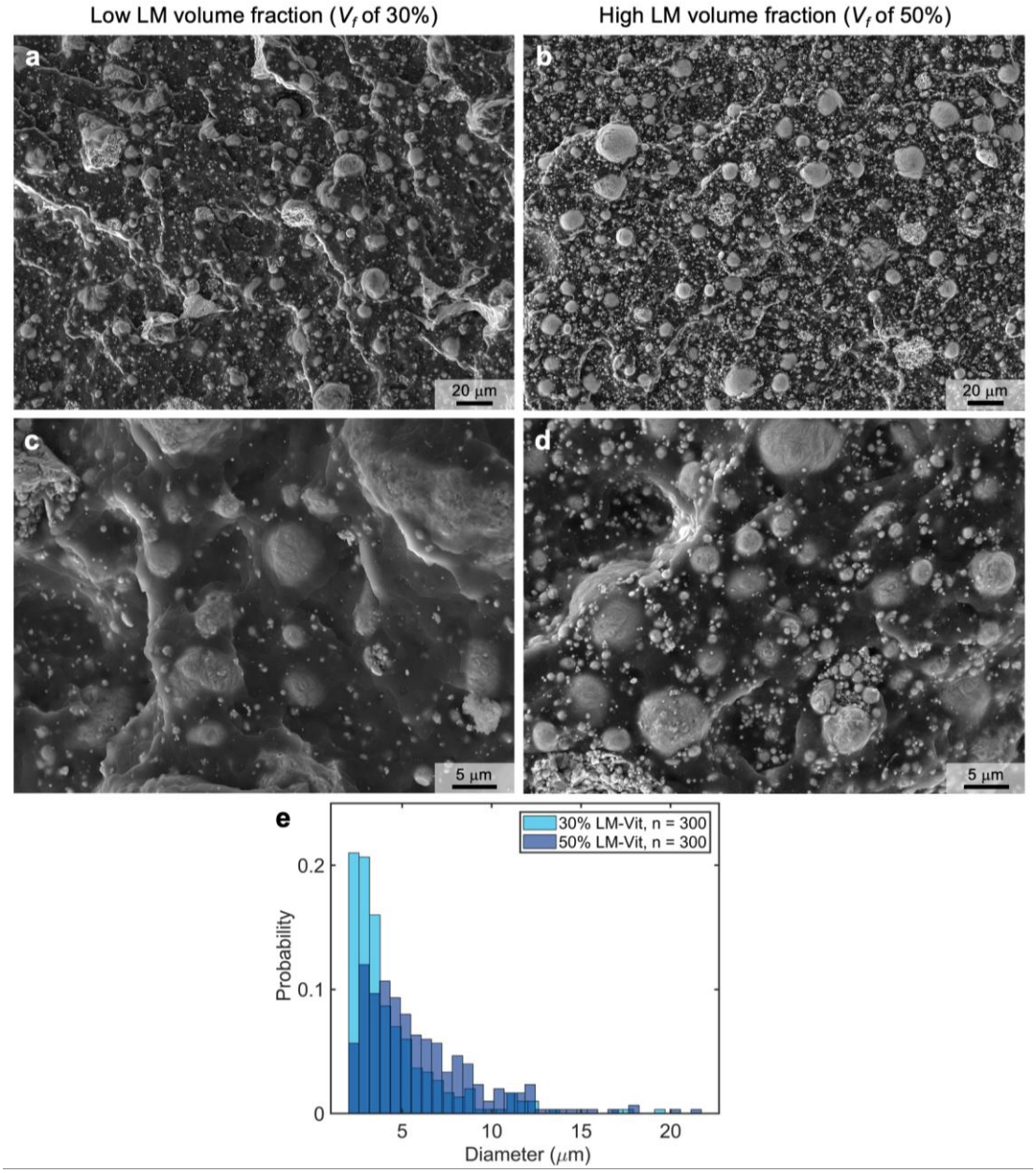

Figure A.23. SEM images of LM–Vit composites with Vf of (a and c) 30% LM and (b and d) 50% LM. (e) Particle size distributions of 30% and 50% LM–Vit (sample size of 300)

A.4.7 Dynamic mechanical analysis

Glass transition temperature (T_g) was evaluated from the composite's tan delta peak in the dynamic mechanical analysis (DMA) measurements. It is estimated that T_g was not affected by LM inclusions, staying consistently at around 32 °C. Additionally, DMA reveals that the non-polymeric filler influences the damping behavior of the composite. As shown by decreasing amplitude of tan delta peaks, higher filler dispersion restricts the mobility of polymer matrix and dissipates strain energy, causing stronger damping effect.

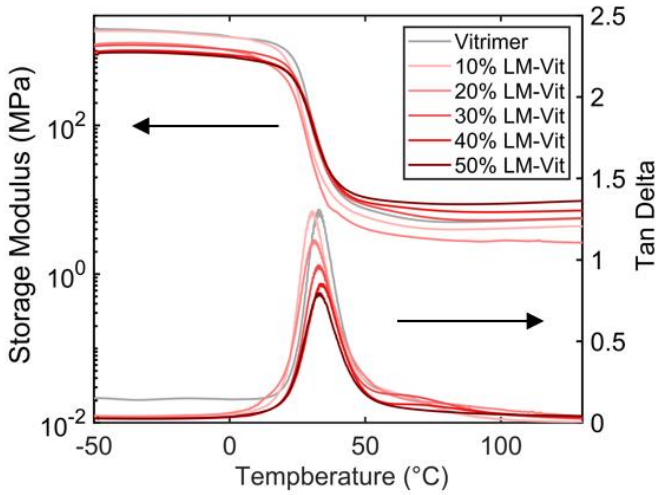

Figure A.24. Measured storage modulus and tan d of LM–Vit composites from dynamic mechanical analysis.

A.4.8 Stress relaxation measurement

At temperatures higher than T_v, vitrimer matrices can be considered as viscoelastic fluids and undergo stress relaxation. According to Maxwell's model for viscoelastic fluids as stated in Equation (A.5), polymers show both elastic deformation and plastic deformation, and the relaxation time (λ) is defined as a ratio of viscosity (η) over modulus (G). Stress relaxation follows a single exponential decay, where the material is considered fully relaxed when its shear modulus decreases to 1/e of its initial value, as shown in Figure A.25. LM–Vit composites show minimal stress relaxation like thermosets at a low temperature range, and stress relaxation is expected to take place after T_v. The temperature dependence of stress relaxation time (τ^*), a time required to reach 1/e, follows the Arrhenius model (Equation (A.6)), where λ_0 is pre-exponential factor, E_a is activation energy, R is gas constant, and T is absolute temperature. This can be linear fitted by taking natural log on both sides (Equation (A.7)), and the activation energy is calculated by extrapolating the slope of $\frac{1}{T}$, and dividing it by R. Topology freezing temperature (T_v) is a characteristic temperature where the vitrimer transitions from elastic behavior to viscoelastic behavior, as expressed in Equation (A.8). For the soft vitrimer systems, the viscosity of 10^{12} (Pa·s) and the modulus of 10^6 (Pa) are used to estimate T_v,[156,245] revealing activation energy values of 151–169 kJ mol^{-1} and a T_v in the range of 120 to 132 °C.

$$\lambda = \frac{\eta}{G} \tag{A.5}$$

$$\lambda = \lambda_0 * e^{E_a/RT} \tag{A.6}$$

$$\ln(\lambda) = \ln(\lambda_0) + \frac{E_a}{R}\frac{1}{T} \tag{A.7}$$

$$T_v = \frac{E_a}{R(\ln(\lambda_0) - \ln(\lambda))} \tag{A.8}$$

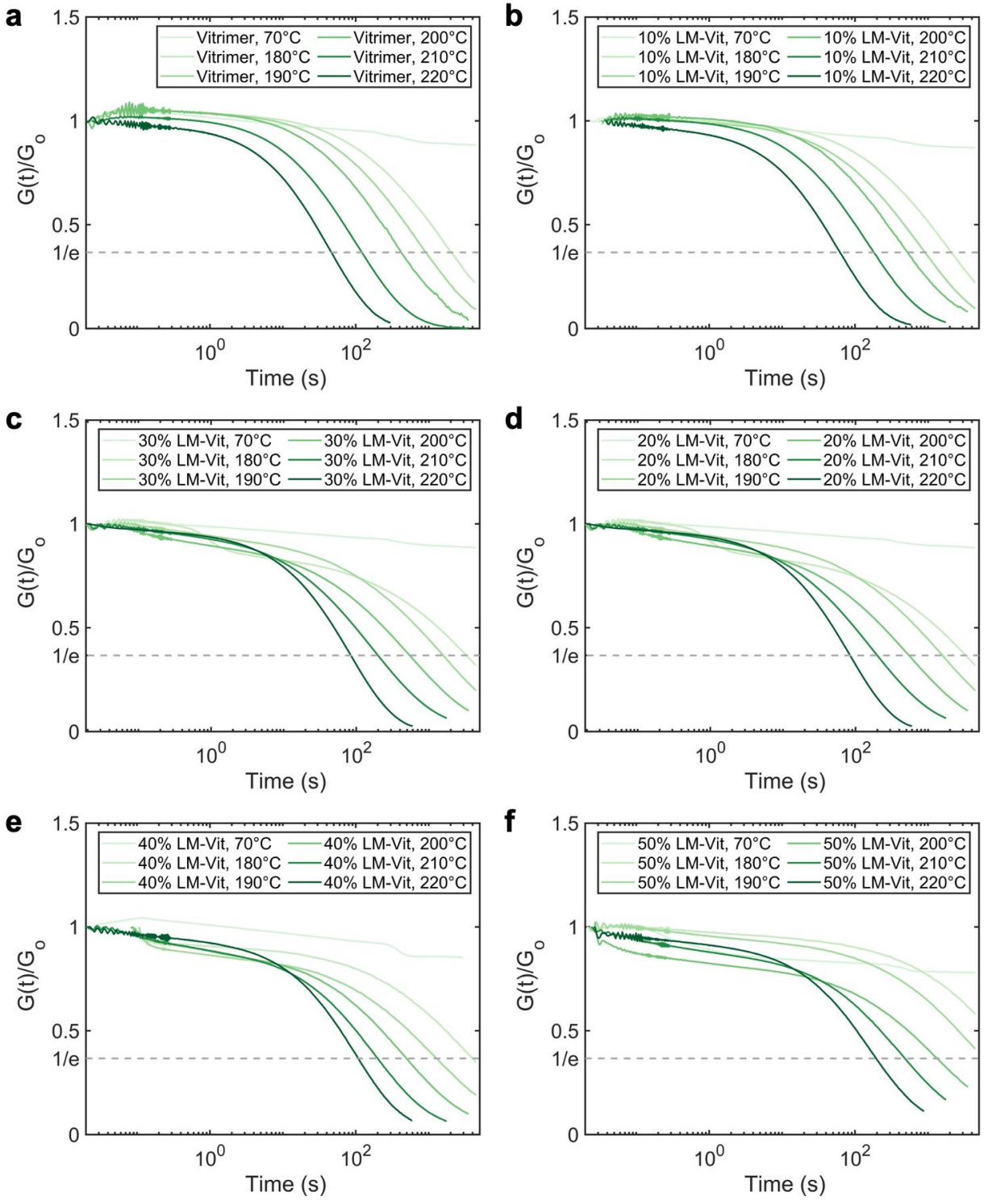

Figure A.25. Stress relaxation measurements of (a) neat vitrimer and liquid metal vitrimer composites with filler volume fractions of (b) 10%, (c) 20%, (d) 30%, (e) 40%, and (f) 50%.

A.4.9 Stress-strain behavior of LM–Vit

The increase in hysteresis by having higher LM volume fraction is attributed to the elevated internal friction within the composite caused by the reduced volume of polymer experiencing strain by having embedded LM particles. Furthermore, liquid-phase fillers do not store mechanical energy under strain like elastic polymers but deform along the applied strain direction instead. As a result, the composites show a reduction in strain energy during unloading.

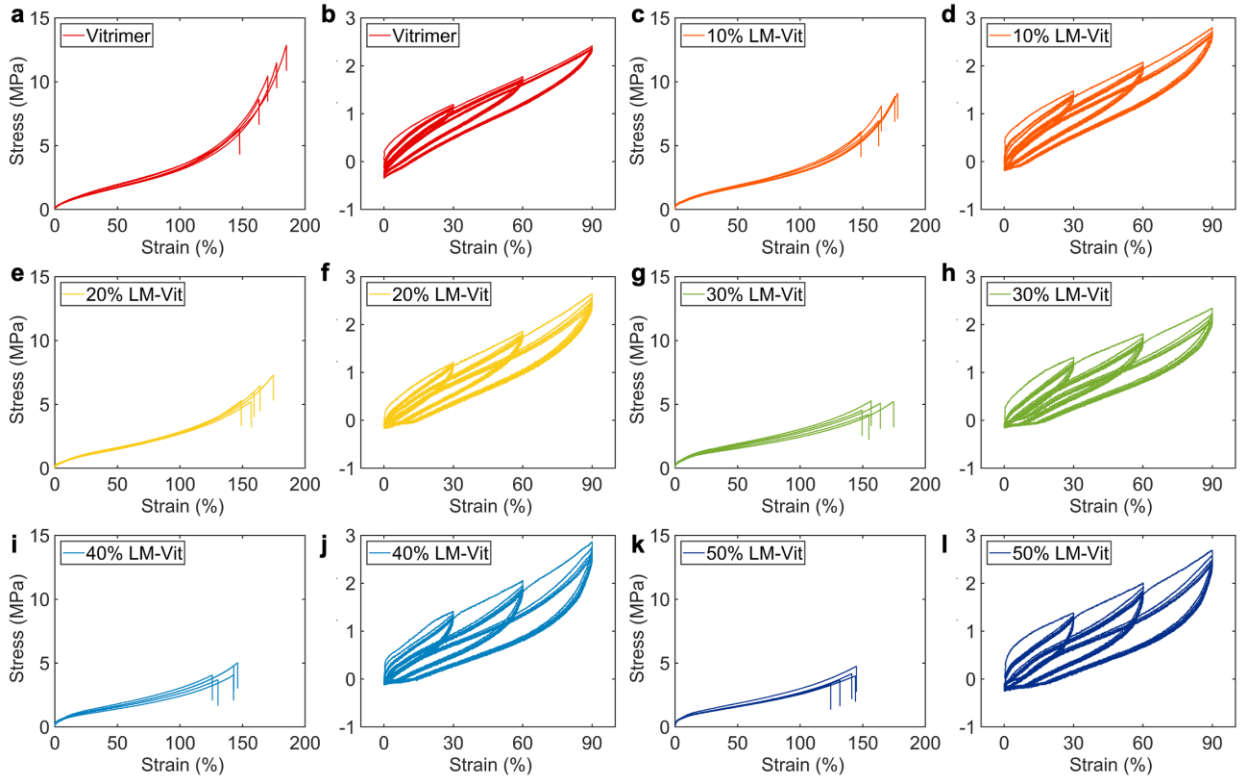

Figure A.26. Tensile test and cyclic loading tests of (a-b) neat vitrimer and liquid metal vitrimer composites with filler volume fractions of (c-d) 10%, (e-f) 20%, (g-h) 30%, (i-j) 40%, and (k-l) 50%.

A.4.10 LM–Vit thermomechanical reprocessing

LM–Vit composites were diced into approximately 3×3 mm^2 pieces and rinsed thoroughly using ethanol to cleanse any dust on the surface and dried before the thermomechanical reprocessing. For LM–Vit composites, cutting into smaller pieces caused LM to be dislodged at the open faces, unfavorably losing LM contents in the composite. Therefore, dicing is chosen over other disintegration methods (e.g., pulverizing) as LM fillers will be lost significantly when LM–Vit composite is shredded. The fragmented composites were put on a 2×200×200 mm^3 mold and hot-pressed at 220 °C and 5 tons for 2 hours. In this step, high pressure is required to heal the composite as the pieces must be well compacted into the mold. The reprocessed composite was cooled down at room temperature for an hour after the hot pressing.

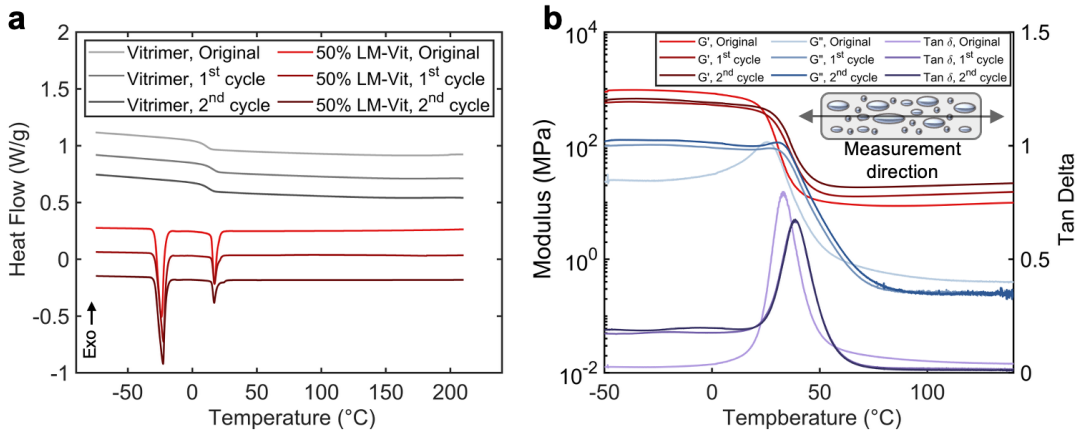

Figure A.27. Change in material properties due to elongated LM inclusions after thermomechanical reprocessing. (a) DSC results of successfully reprocessed vitrimer and 50% LM–Vit composite with elongated LM inclusions. (b) DMA result of 50% LM–Vit composite.

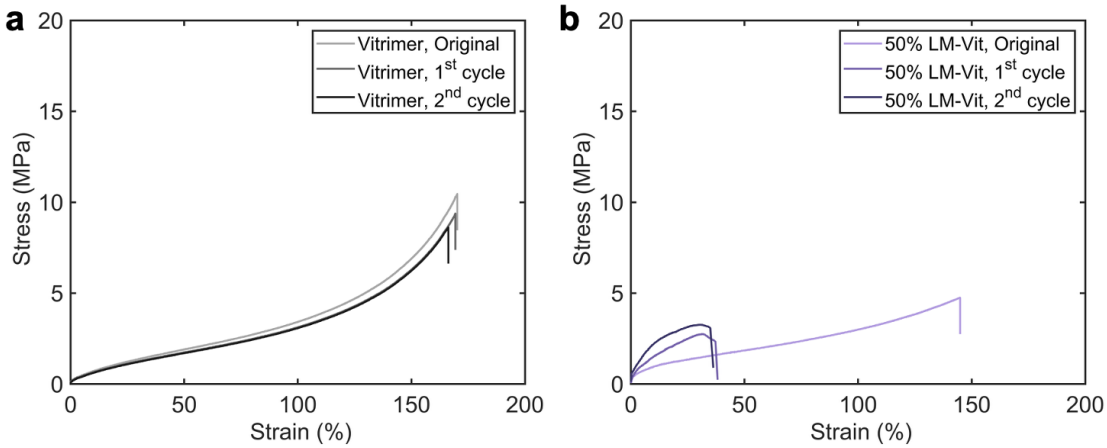

Figure A.28. Representative stress-strain behavior of (a) neat vitrimer and (b) 50% LM–Vit composite after first and second thermomechanical reprocessing cycles.

A.4.11 X-ray photoelectron spectroscopy (XPS)

Interfacial interactions between the liquid metal (EGaIn) particles and the vitrimer matrix were investigated using X-ray photoelectron spectroscopy (XPS). For gallium and indium-related ions (Ga 3d, In 4d, and O 1s), each core-level binding energy were deconvoluted into components corresponding to spin–orbit splitting and potential suboxide-related secondary peaks (e.g., Ga $3d_{5/2}$ and Ga $3d_{3/2}$ for Ga 3d). As shown in Figure 5.4b, the Ga 3d peaks in the 50% LM–Vit composite shift to higher binding energies compared to pure LM, suggesting reduced electron density around gallium due to chemical interaction with the matrix. Similarly, in the O 1s spectrum (Figure A.29), the Ga–O peak shifts by 0.19 eV, while polymer-derived oxygen peaks shift by 0.35 eV, further supporting electronic interaction at the interface. These shifts are consistent with coordination between electron-rich oxygen atoms in the vitrimer matrix and gallium ions on the oxide surface of EGaIn. While hydrogen bonding has been widely reported for LM–polymer systems,[49,50] the minimal shifts and negligible broadening in hydroxyl-related peaks in the XPS C 1s spectra (Figure 5.4c) and FTIR data (Figure A.21) suggest that hydrogen bonding is not a dominant role in this LM–vitrimer system. The binding energy changes collectively support a combination of partial coordination, reversible covalent bonding, and hydrogen bonding at the filler-matrix interface.

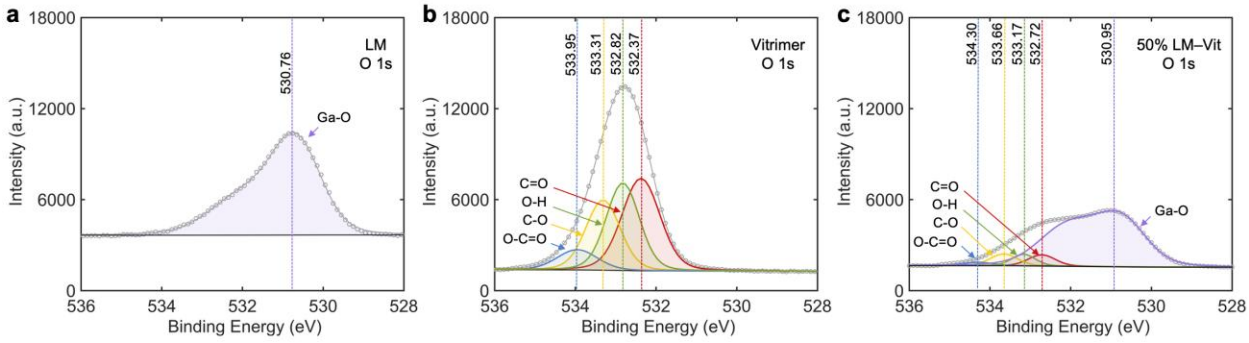

Figure A.29. XPS O 1s spectra of (a) LM, (b) neat vitrimer, and (c) 50% LM–Vit composite.

A.4.12 Chemical recycling process

LM–Vit composites were chemically recycled to retrieve LM filler and vitrimer matrix separately using EG and HCl solution, as shown in Figure A.30. LM–Vit was immersed in a beaker with an excessive amount of EG solution and sealed before being heated. The beaker was heated at 180 °C for 4 hours to fully dissolve the composite. The yellowish solution was decanted from the beaker and evaporated to reclaim the vitrimer. The remaining gray lump was centrifuged at 4000 RPM for 15 minutes (Sorvall ST 40, ThermoScientific) in another EG solution. The EG solution after the centrifugation can also be evaporated to obtain the vitrimer. However, because of the strong chemical interactions between the filler and the matrix, vitrimer could not be fully separated from the composite. The TGA result of the vitrimer, which is recycled through dissolving 50% LM–Vit with EG and the centrifuge, claims that approximately 17 wt% of vitrimer can be retrieved. A lump of dissolved 50% LM–Vit after centrifuging was composed of LM fillers and the majority of vitrimer. The centrifuged material was transferred to the beaker, and EG and HCl were added to the beaker. The weight ratio of solid material, EG, and HCl was 1:4:1. The beaker was sealed and heated at 130 °C for 30 minutes to break the filler–matrix interaction, resulting in the recovery of a single LM droplet. In EG-HCl solution at elevated temperature, gallium oxide undergoes acid-base reaction, which generates by-products and water, removing the passive oxide layer of EGaIn. The recycled LM was separated from the solution and washed with ethanol. From the 50% LM–Vit originally containing 6.42 g of LM, this process successfully recovered 6.05 g, demonstrating 94.2% recycling efficiency by weight. The unrecovered 0.37 g is mostly because of the dissolution of gallium oxide by HCl. Additional material loss likely occurred during solution transfer, as the dissolved composite adhered to the beaker surfaces. On the other hand, HCl can protonate hydroxy groups in dissolved vitrimer matrix, resulting in dehydration that substitutes the active groups in vitrimer which enabled bond exchange reaction. Consequently, the acidic solution degrades the dissolved vitrimer, diminishing the material properties of the thermoset network as demonstrated in the DSC results (Figure A.31). Drying the remaining solution in a vacuum oven yielded acid-treated vitrimer precursor.

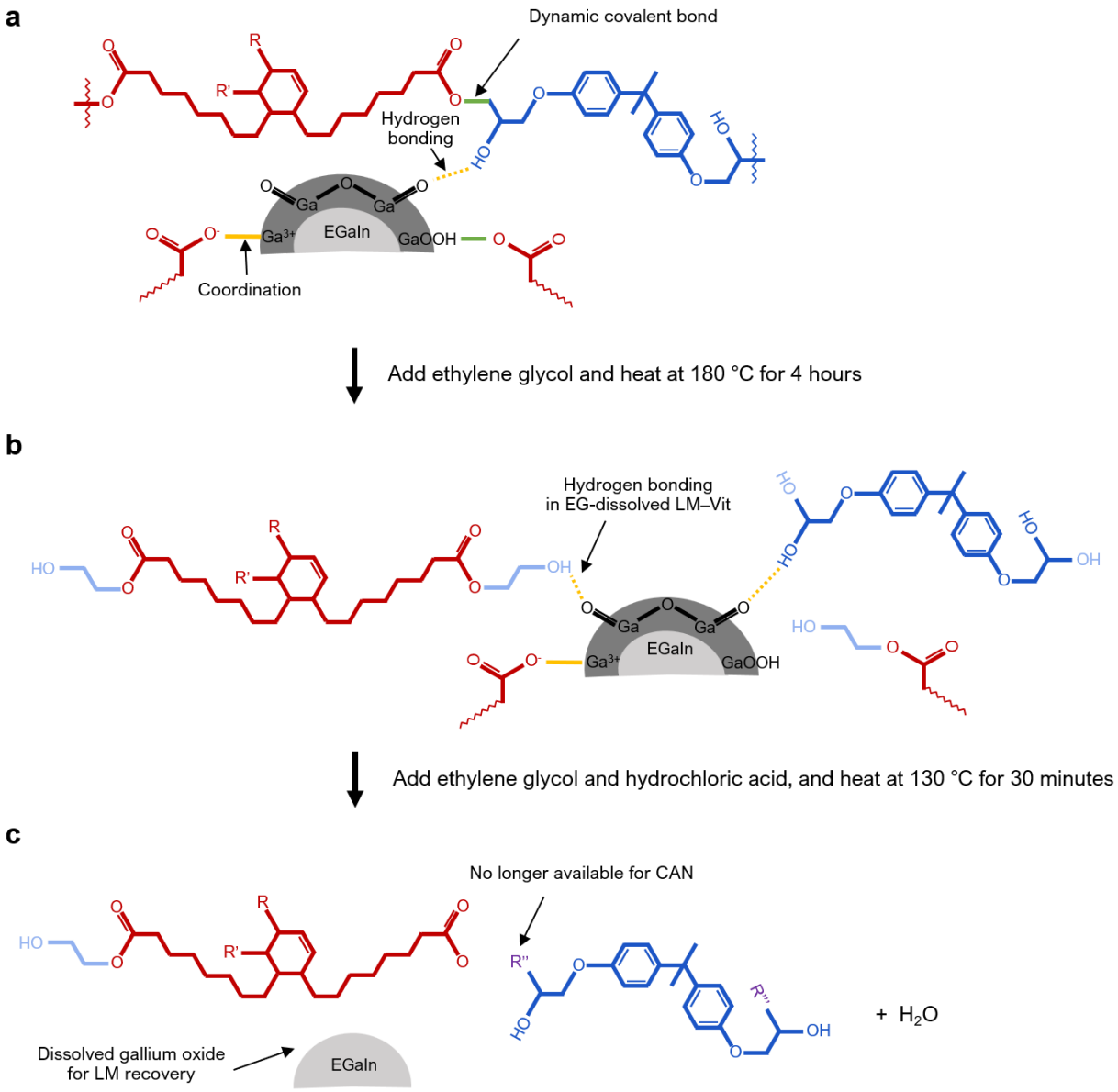

Figure A.30. Chemical recycling process of LM–Vit composites. (a) LM–Vit composite consists of a vitrimer matrix with dynamic covalent bonds, which form weak coordination, hydrogen bond, or dynamic covalent bond with the LM particle. (b) Dissolved vitrimer matrix in EG solution at elevated temperature and increased number of hydrogen bonds between gallium oxide and dissolved matrix. (c) Separated LM filler and vitrimer matrix in EG and HCl solution. Some hydroxyl groups in vitrimer matrix are substituted to different polymer structures that are no longer available for the covalent adaptable network.

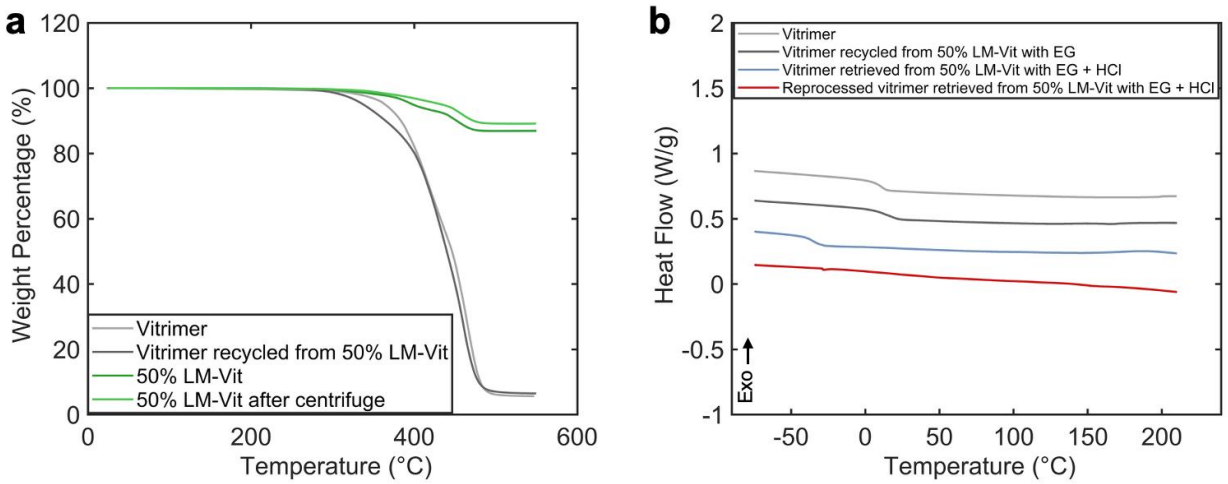

Figure A.31. Chemically recycled vitrimer matrix and degradation from acidic conditions. (a) TGA results of neat vitrimer, vitrimer recycled from 50% LM–Vit composite with EG, 50% LM–Vit composite, and 50% LM–Vit composite after centrifuge. (b) DSC results of neat vitrimer, vitrimer recycled from 50% LM–Vit with EG, vitrimer retrieved from 50% LM–Vit with EG and HCl, and reprocessed vitrimer retrieved from 50% LM–Vit with EG and HCl.

Table A.7. LM recovering comparison.

Reference	Polymer Matrix	Method	Efficiency (%)	Recycling Complexity
4th Study	Fatty acid vitrimer	Acid treatment	94.2	Simple
[42]	Thermoplastic (PMMA)	Acid treatment	Not reported	Simple
[150]	Thermoplastic (PVA)	Alkaline treatment	96	Intermediate
[151]	Thermoplastic (PVA)	Alkaline treatment	96.9	Simple
[152]	Block copolymer (SIS)	Acid treatment, alkaline treatment, leaching, and electrowinning	Not reported	Complicated
[154]	Diels–Alder bond polyurethane	Alkaline treatment	88	Simple
[170]	Lignin-based vitrimer	Centrifuge LM-vitrimer ink	98.7	Intermediate

References

1. Kim, C. Y. et al. Wireless Technologies for Wearable Electronics: A Review. *Adv. Electron. Mater*. 11, 2400884 (2025).
2. Ates, H. C. et al. End-to-end design of wearable sensors. *Nat. Rev. Mater*. 7, 887–907 (2022).
3. Divekar, N. V, Thomas, G. C., Yerva, A. R., Frame, H. B. & Gregg, R. D. A Versatile Knee Exoskeleton Mitigates Quadriceps Fatigue in Lifting, Lowering, and Carrying Tasks. *Sci. Robot.* 9, eadr8282 (2024).
4. Libanori, A., Chen, G., Zhao, X., Zhou, Y. & Chen, J. Smart textiles for personalized healthcare. *Nat. Electron*. 5, 142–156 (2022).
5. Shi, X. et al. Large-area display textiles integrated with functional systems. *Nature* 591, 240–245 (2021).
6. Zhao, C., Park, J., Root, S. E. & Bao, Z. Skin-inspired soft bioelectronic materials, devices and systems. *Nat. Rev. Bioeng*. 2, 671–690 (2024).
7. Kim, J. J. et al. Skin Electronics: Next-Generation Device Platform for Virtual and Augmented Reality. *Adv. Funct. Mater*. 31, 2009602 (2021).
8. Wu, M. et al. Self-powered skin electronics for energy harvesting and healthcare monitoring. *Mater. Today Energy* 21, 100786 (2021).
9. Tang, W., Sun, Q. & Wang, Z. L. Self-Powered Sensing in Wearable Electronics─A Paradigm Shift Technology. *Chem. Rev*. 123, 12105–12134 (2023).
10. Hou, S. et al. Stretchable Electronics with Strain-Resistive Performance. *Small* 20, 2306749 (2024).
11. Chen, S., Cui, Z., Wang, H., Wang, X. & Liu, J. Liquid metal flexible electronics: Past, present, and future. *Appl. Phys. Rev*. 10, 021308 (2023).
12. Chen, S. et al. Toxicity and Biocompatibility of Liquid Metals. *Adv. Healthc. Mater*. 12, 2201924 (2023).
13. Yan, J., Lu, Y., Chen, G., Yang, M. & Gu, Z. Advances in liquid metals for biomedical applications. *Chem. Soc. Rev*. 47, 2518–2533 (2018).
14. Niu, Y. et al. Thermal-Sinterable EGaIn Nanoparticle Inks for Highly Deformable Bioelectrode Arrays. *Adv. Healthc. Mater*. 12, 2202531 (2023).
15. Ye, X., Zheng, Z., Werner, J. G. & Boley, J. W. Mechanically Rupturing Liquid Metal Oxide Induces Electrochemical Energy. *Adv. Funct. Mater*. 34, 2309177 (2024).
16. Guymon, G. G. & Malakooti, M. H. Multifunctional liquid metal polymer composites. *J. Polym. Sci*. 60, 1300–1327 (2022).
17. Ji, Z., Liu, W., Ouyang, C. & Li, Y. High thermal conductivity thermoplastic polyurethane/boron nitride/liquid metal composites: The role of the liquid bridge at the filler/filler interface. *Mater. Adv*. 2, 5977–5985 (2021).
18. Bhanushali, S., Ghosh, P. C., Simon, G. P. & Cheng, W. Copper Nanowire-Filled Soft Elastomer Composites for Applications as Thermal Interface Materials. *Adv. Mater. Interfaces* 4, 1700387 (2017).
19. Zhou, L., Bustos-Nuño, S., Manohar, K. & Malakooti, M. H. Effective thermal conductivity and elastic modulus of elastomer composites with liquid metal and solid inclusions. *Compos. Sci. Technol*. 270, 111258 (2025).
20. Ralphs, M., Kong, W., Wang, R. Y. & Rykaczewski, K. Thermal Conductivity Enhancement of Soft Polymer Composites through Magnetically Induced Percolation and Particle–Particle Contact Engineering. *Adv. Mater. Interfaces* 6, 1801857 (2019).

21. Eristoff, S., Nasab, A. M., Huang, X. & Kramer-Bottiglio, R. Liquid Metal + x: A Review of Multiphase Composites Containing Liquid Metal and Other (x) Fillers. *Adv. Funct. Mater*. 34, 2309529 (2024).
22. Wang, Z. et al. A Roadmap Review of Thermally Conductive Polymer Composites: Critical Factors, Progress, and Prospects. *Adv. Funct. Mater*. 33, 2301549 (2023).
23. Bartlett, M. D. et al. High thermal conductivity in soft elastomers with elongated liquid metal inclusions. *Proc. Natl. Acad. Sci. U. S. A*. 114, 2143–2148 (2017).
24. Ma, J. et al. Shaping a Soft Future: Patterning Liquid Metals. *Adv. Mater.* 35, 220596 (2023).
25. Jia, L. C. et al. Highly thermally conductive liquid metal-based composites with superior thermostability for thermal management. *J. Mater. Chem. C Mater*. 9, 2904–2911 (2021).
26. Dickey, M. D. Stretchable and Soft Electronics using Liquid Metals. *Adv. Mater*. 29, 1606425 (2017).
27. Markvicka, E. J., Bartlett, M. D., Huang, X. & Majidi, C. An autonomously electrically self-healing liquid metal-elastomer composite for robust soft-matter robotics and electronics. *Nat. Mater*. 17, 618–624 (2018).
28. Chen, S., Wang, H. Z., Zhao, R. Q., Rao, W. & Liu, J. Liquid Metal Composites. *Matter* 2, 1446–1480 (2020).
29. Malakooti, M. H. et al. Liquid Metal Supercooling for Low-Temperature Thermoelectric Wearables. *Adv. Funct. Mater*. 29, 1906098 (2019).
30. Haque, A. B. M. T., Tutika, R., Byrum, R. L. & Bartlett, M. D. Programmable Liquid Metal Microstructures for Multifunctional Soft Thermal Composites. *Adv. Funct. Mater*. 30, 2000832 (2020).
31. Chiew, C. & Malakooti, M. H. A double inclusion model for liquid metal polymer composites. *Compos. Sci. Technol*. 208, 108752 (2021).
32. Hu, K. et al. Optimized thermal design for excellent wearable thermoelectric generator. *J. Mater. Chem. A,* 10, 24985-24994 (2022).
33. Lee, B. et al. High-performance compliant thermoelectric generators with magnetically self-assembled soft heat conductors for self-powered wearable electronics. *Nat. Commun*. 11, 5948 (2020).
34. Dickey, M. D. Emerging applications of liquid metals featuring surface oxides. *ACS Appl. Mater. Interfaces* 6, 18369–18379 (2014).
35. Farrell, Z. J. & Tabor, C. Control of Gallium Oxide Growth on Liquid Metal Eutectic Gallium/Indium Nanoparticles via Thiolation. *Langmuir* 34, 234–240 (2018).
36. Ford, M. J. et al. A multifunctional shape-morphing elastomer with liquid metal inclusions. *Proc. Natl. Acad. Sci. U. S. A*. 116, 21438–21444 (2019).
37. Krings, E. J. et al. Lightweight, Thermally Conductive Liquid Metal Elastomer Composite with Independently Controllable Thermal Conductivity and Density. *Small* 17, 2104762 (2021).
38. Bark, H., Tan, M. W. M., Thangavel, G. & Lee, P. S. Deformable High Loading Liquid Metal Nanoparticles Composites for Thermal Energy Management. *Adv. Energy Mater*. 11, 2170135 (2021).
39. Malakooti, M. H., Bockstaller, M. R., Matyjaszewski, K. & Majidi, C. Liquid metal nanocomposites. Nanoscale Adv. 2, 2668–2677 (2020).
40. Pan, C. et al. A Liquid-Metal–Elastomer Nanocomposite for Stretchable Dielectric Materials. *Adv. Mater*. 31, 1900663 (2019).

41. Lin, Y. et al. Sonication-enabled rapid production of stable liquid metal nanoparticles grafted with poly(1-octadecene-: Alt -maleic anhydride) in aqueous solutions. *Nanoscale* 10, 19871–19878 (2018).
42. Yan, J. et al. Solution processable liquid metal nanodroplets by surface-initiated atom transfer radical polymerization. *Nat. Nanotechnol*. 14, 684–690 (2019).
43. Chin, R. M., Han, Y. & Malakooti, M. H. Surface-Engineered Liquid Metal Particles for Printing Stretchable Conductive Composites with Enhanced Stability Under Different Strain Rates. *Adv. Mater. Technol*. 2301324 (2023).
44. Jung, J., Jeong, S. H., Hjort, K. & Ryu, S. Investigation of thermal conductivity for liquid metal composites using the micromechanics-based mean-field homogenization theory. *Soft Matter* 16, 5840–5847 (2020).
45. Han, Y., Tetik, H. & Malakooti, M. H. 3D Soft Architectures for Stretchable Thermoelectric Wearables with Electrical Self-Healing and Damage Tolerance. *Adv. Mater*. (2024).
46. Han, Y., Simonsen, L. E. & Malakooti, M. H. Printing Liquid Metal Elastomer Composites for High-Performance Stretchable Thermoelectric Generators. *Adv. Energy Mater*. 12, 2201413 (2022).
47. Jeong, S. H. et al. Mechanically Stretchable and Electrically Insulating Thermal Elastomer Composite by Liquid Alloy Droplet Embedment. *Sci. Rep*. 5, 18257 (2016).
48. Chin, R. M., Zhou, L. & Malakooti, M. H. Solution-Processable, Elongated Liquid Metal Particles for Composites with Enhanced Thermal Management. *ACS Appl. Mater. Interfaces* 17, 69908–69918 (2025).
49. Zhao, W. et al. Advanced Liquid Metal-Based Hydrogels for Flexible Electronics. *ACS Appl. Mater. Interfaces* 17, 27713–27739 (2025).
50. Qi, J. et al. Liquid Metal-Polymer Conductor-Based Conformal Cyborg Devices. *Chem. Rev*. 124, 2081–2137 (2024).
51. Kim, M., Lim, H. & Ko, S. H. Liquid Metal Patterning and Unique Properties for Next-Generation Soft Electronics. *Adv. Sci*. 10, 2205795 (2023).
52. Rao, A. S. et al. Concomitance of radio frequency energy harvesting and wearable devices: A review of rectenna designs. *Int. J. RF Microw. Comput. Aided Eng*. 32, e23536 (2022).
53. Vital, D., Bhardwaj, S. & Volakis, J. L. Textile-Based Large Area RF-Power Harvesting System for Wearable Applications. *IEEE Trans. Antennas Propag*. 68, 2323–2331 (2020).
54. Ali, I. et al. Advances in Smart Photovoltaic Textiles. *ACS Nano* 18, 3871–3915 (2024).
55. Chen, C. et al. A method for quantitatively separating the piezoelectric component from the as-received "Piezoelectric" signal. *Nat. Commun*. 13, 1391 (2022).
56. Jeong, S. Y. et al. Piezoelectric device operating as sensor and harvester to drive switching circuit in LED shoes. *Energy* 177, 87–93 (2019).
57. Kim, W. G. et al. Triboelectric Nanogenerator: Structure, Mechanism, and Applications. *ACS Nano* 15, 258–287 (2021).
58. Zhang, B. et al. Recent advances in stretchable hydrogel-based triboelectric nanogenerators for on-skin electronics. *Mater. Chem. Front*. 8, 4003–4028 (2024).
59. Liu, J., Zhang, L., Wang, N. & Li, C. Highly stretchable and transparent triboelectric nanogenerator based on multilayer structured stable electrode for self-powered wearable sensor. *Nano Energy* 78, 105385 (2020).
60. Zhang, Q., Deng, K., Wilkens, L., Reith, H. & Nielsch, K. Micro-thermoelectric devices. *Nat. Electron*. 5, 333–347 (2022).

61. G. Jeffrey Snyder & Eric S. Toberer. Complex thermoelectric materials. *Nat. Mater*. 7, 105–114 (2008).
62. He, T., Guo, X. & Lee, C. Flourishing energy harvesters for future body sensor network: from single to multiple energy sources. iScience 24, 101934 (2021).
63. Zadan, M. et al. Stretchable Thermoelectric Generators for Self-Powered Wearable Health Monitoring. *Adv. Funct. Mater*. 34, 2404861(2024).
64. Lee, J., Kim, D., Sul, H. & Ko, S. H. Thermo-Haptic Materials and Devices for Wearable Virtual and Augmented Reality. *Adv. Funct. Mater*. 31, 2007376 (2021).
65. Hong, S. et al. Wearable thermoelectrics for personalized thermoregulation. *Sci. Adv*. 5, eaaw0536 (2019).
66. Jung, Y., Jeong, S., Ahn, J., Lee, J. & Ko, S. H. High Efficiency Breathable Thermoelectric Skin Using Multimode Radiative Cooling/Solar Heating Assisted Large Thermal Gradient. *Small* 20, 2304338 (2024).
67. Zhou, W. et al. Seebeck-driven transverse thermoelectric generation. Nat. Mater. 20, 463–467 (2021).
68. Nozariasbmarz, A. et al. High Power Density Body Heat Energy Harvesting. *ACS Appl. Mater. Interfaces* 11, 40107–40113 (2019).
69. Snyder, G. J. & Snyder, A. H. Figure of merit ZT of a thermoelectric device defined from materials properties. *Energy Environ. Sci.* 10, 2280–2283 (2017).
70. Zadan, M., Malakooti, M. H. & Majidi, C. Soft and Stretchable Thermoelectric Generators Enabled by Liquid Metal Elastomer Composites. *ACS Appl. Mater. Interfaces* 12, 17921–17928 (2020).
71. Yu, Y. et al. Towards high integration and power density: Zigzag-type thin-film thermoelectric generator assisted by rapid pulse laser patterning technique. *Appl. Energy* 275, 115404 (2020).
72. Sun, T. et al. Stretchable fabric generates electric power from woven thermoelectric fibers. *Nat. Commun*. 11, 572 (2020).
73. Suarez, F., Nozariasbmarz, A., Vashaee, D. & Öztürk, M. C. Designing thermoelectric generators for self-powered wearable electronics. *Energy Environ. Sci*. 9, 2099–2113 (2016).
74. Zadan, M., Chiew, C., Majidi, C. & Malakooti, M. H. Liquid metal architectures for soft and wearable energy harvesting devices. *Multifunct. Mater*. 4, 012001 (2021).
75. Jia, Y. et al. Wearable Thermoelectric Materials and Devices for Self-Powered Electronic Systems. *Adv. Mater*. 33, 2102990 (2021).
76. Suarez, F. et al. Flexible thermoelectric generator using bulk legs and liquid metal interconnects for wearable electronics. *Appl. Energy* 202, 736–745 (2017).
77. Yang, Y. et al. Stretchable Nanolayered Thermoelectric Energy Harvester on Complex and Dynamic Surfaces. *Nano Lett*. 20, 4445–4453 (2020).
78. Kim, S. J., We, J. H. & Cho, B. J. A wearable thermoelectric generator fabricated on a glass fabric. *Energy Environ. Sci*. 7, 1959–1965 (2014).
79. Karthikeyan, V. et al. Wearable and flexible thin film thermoelectric module for multi-scale energy harvesting. *J. Power Sources* 455, 227983 (2020).
80. Wang, Y. et al. Flexible Thermoelectric Materials and Generators: Challenges and Innovations. *Adv. Mater*. 31, 1807916 (2019).
81. Zhang, L. et al. Fiber-Based Thermoelectric Generators: Materials, Device Structures, Fabrication, Characterization, and Applications. Adv. Energy Mater. 8, 1700524 (2018).

82. Hou, Y. et al. Whole Fabric-Assisted Thermoelectric Devices for Wearable Electronics. *Adv. Sci.* 9, 2103574 (2022).
83. Zhang, L., Han, X., Du, M., Shi, Y. & Zhang, K. Compliant three-dimensional thermoelectric generator filled with porous PDMS for power generation and solid-state cooling. *Compos. Commun*. 26, 100793 (2021).
84. Padmanabhan Ramesh, V. et al. Flexible thermoelectric generator with liquid metal interconnects and low thermal conductivity silicone filler. *npj Flex. Electron*. 5, 5 (2021).
85. Lee, Y. G. et al. Design and Experimental Investigation of Thermoelectric Generators for Wearable Applications. *Adv. Mater. Technol*. 2, 1600292 (2017).
86. Nozariasbmarz, A. et al. Thermoelectric generators for wearable body heat harvesting: Material and device concurrent optimization. *Nano Energy* 67, 104265 (2020).
87. Hyland, M., Hunter, H., Liu, J., Veety, E. & Vashaee, D. Wearable thermoelectric generators for human body heat harvesting. *Appl. Energy* 182, 518–524 (2016).
88. Sargolzaeiaval, Y. et al. Flexible thermoelectric generators for body heat harvesting – Enhanced device performance using high thermal conductivity elastomer encapsulation on liquid metal interconnects. *Appl. Energy* 262, 114370 (2020).
89. Jung, S. J. et al. Porous organic filler for high efficiency of flexible thermoelectric generator. *Nano Energy* 81, 105604 (2021).
90. Shi, X. L., Li, N. H., Li, M. & Chen, Z. G. Toward Efficient Thermoelectric Materials and Devices: Advances, Challenges, and Opportunities. *Chem. Rev*. 125, 7525–7724 (2025).
91. Pan, C., Liu, D., Ford, M. J. & Majidi, C. Ultrastretchable, Wearable Triboelectric Nanogenerator Based on Sedimented Liquid Metal Elastomer Composite. *Adv. Mater. Technol*. 5, 2000754 (2020).
92. Malakooti, M. H., Zadan, M., Kazem, N. & Majidi, C. Liquid metal composites for flexible thermoelectric energy harvesting. *Proc. SPIE* 11589, 115890D (2021).
93. Nan, K. et al. Compliant and stretchable thermoelectric coils for energy harvesting in miniature flexible devices. *Sci. Adv*. 4, eaau5849 (2018).
94. Wu, K., Ren, S., Ye, S., Wang, J. & Fang, J. 3D Helical Flexible Thermoelectric Film Generator Based on Bi2Te3/PEDOT: PSS/PU/MWCNT. *ACS Appl. Mater. Interfaces* 17, 23188–23196 (2025).
95. Ren, W. et al. High-performance wearable thermoelectric generator with self-healing, recycling, and Lego-like reconfiguring capabilities. *Sci. Adv*. 7, eabe0586 (2021).
96. Karthikeyan, V. et al. Three dimensional architected thermoelectric devices with high toughness and power conversion efficiency. *Nat. Commun*. 14, 2069 (2023).
97. Bikas, H., Stavropoulos, P. & Chryssolouris, G. Additive manufacturing methods and modeling approaches: A critical review. Int. J. Adv. Manuf. Technol. 83, 389–405 (2016).
98. Wang, Y., Li, L., Hofmann, D., Andrade, J. E. & Daraio, C. Structured fabrics with tunable mechanical properties. *Nature* 596, 238–243 (2021).
99. Katsantonis, S. N. & Tsamis, C. 3D-printed lattice structures for thermoelectric devices - a review. *J. Mater. Chem. A* 13, 27794–27806 (2025).
100. Blakey-Milner, B. et al. Metal additive manufacturing in aerospace: A review. *Mater. Des.* 209, 110008 (2021).
101. Ambulo, C. P., Ford, M. J., Searles, K., Majidi, C. & Ware, T. H. 4D-Printable Liquid Metal-Liquid Crystal Elastomer Composites. *ACS Appl. Mater. Interfaces* 13, 12805–12813 (2021).

102. Wang, J. et al. Printable Superelastic Conductors with Extreme Stretchability and Robust Cycling Endurance Enabled by Liquid-Metal Particles. *Adv. Mater*. 30, 1706157 (2018).
103. Won, P. et al. 3D Printing of Liquid Metal Embedded Elastomers for Soft Thermal and Electrical Materials. *ACS Appl. Mater. Interfaces* 14, 55028–55038 (2022).
104. Ge, W. et al. Recent progress in eutectic gallium indium (EGaIn): surface modification and applications. *J. Mater. Chem. A* 12, 657–689 (2023).
105. Park, Y.-G., An, H. S., Kim, J.-Y. & Park, J.-U. High-Resolution, Reconfigurable Printing of Liquid Metals with Three-Dimensional Structures. *Sci. Adv.* 5, eaaw2844 (2019).
106. Neumann, T. V. & Dickey, M. D. Liquid Metal Direct Write and 3D Printing: A Review. *Adv. Mater. Technol*. 5, 2000070 (2020).
107. Hur, O., Markvicka, E. J. & Bartlett, M. D. Anisotropic and Heterogeneous Thermal Conductivity in Programmed Liquid Metal Composites Through Direct Ink Writing. *Adv. Funct. Mater*. 35, 2417375 (2025).
108. Neumann, T. V., Facchine, E. G., Leonardo, B., Khan, S. & Dickey, M. D. Direct write printing of a self-encapsulating liquid metal-silicone composite. *Soft Matter* 16, 6608–6618 (2020).
109. Herbert, R. et al. Thermo-Mechanically Stable, Liquid Metal Embedded Soft Materials for High-Temperature Applications. *Adv. Funct. Mater*. 34, 2309725 (2024).
110. Cui, Z., Han, Y., Huang, Q., Dong, J. & Zhu, Y. Electrohydrodynamic printing of silver nanowires for flexible and stretchable electronics. *Nanoscale* 10, 6806–6811 (2018).
111. Ren, P., Song, R., Zhu, Y., O'Connor, B. & Dong, J. All Electrohydrodynamic Printed Flexible Organic Thin Film Transistors. *Adv. Mater. Technol*. 8, 2300410 (2023).
112. Dong, H. et al. Flexible pressure sensor with high sensitivity and fast response for electronic skin using near-field electrohydrodynamic direct writing. *Org. Electron*. 89, 106044 (2021).
113. Ma, J., Liu, Z. & Zhang, P. Precisely Patterning Liquid Metal Microfibers Through Electrohydrodynamic Printing for Soft Conductive Composites and Electronics. *Adv. Mater*. 37, 2507646 (2025).
114. Huang, Y., Li, Y., Zhang, Y., Yu, H. & Tan, Z. Near-field electrospinning for 2D and 3D structuring: Fundamentals, methods, and applications. *Mater. Today Adv*. 21, 100461 (2024).
115. Han, T., Yarin, A. L. & Reneker, D. H. Viscoelastic electrospun jets: Initial stresses and elongational rheometry. *Polymer (Guildf)*. 49, 1651–1658 (2008).
116. Lee, A., Jin, H., Dang, H. W., Choi, K. H. & Ahn, K. H. Optimization of experimental parameters to determine the jetting regimes in electrohydrodynamic printing. *Langmuir* 29, 13630–13639 (2013).
117. Rao, Z. et al. Soft Electronics for the Skin: From Health Monitors to Human–Machine Interfaces. *Adv. Mater. Technol*. 5, 2000233 (2020).
118. Lee, S. et al. Permeable Bioelectronics toward Biointegrated Systems. *Chem. Rev*. 124, 6543–6591 (2024).
119. Baker, L. B. Physiology of sweat gland function: The roles of sweating and sweat composition in human health. *Temperature* 6, 211–259 (2019).
120. Zhang, B. et al. A three-dimensional liquid diode for soft, integrated permeable electronics. *Nature* 628, 84–92 (2024).

121. Taylor, N. A. S. & Machado-Moreira, C. A. Regional variations in transepidermal water loss, eccrine sweat gland density, sweat secretion rates and electrolyte composition in resting and exercising humans. *Extrem. Physiol. Med*. 2, 4 (2013).
122. Ma, Z. et al. Permeable superelastic liquid-metal fibre mat enables biocompatible and monolithic stretchable electronics. *Nat. Mater*. 20, 859–868 (2021).
123. Ma, X. et al. Highly Permeable and Ultrastretchable Liquid Metal Micromesh for Skin-Attachable Electronics. *ACS Mater. Lett.* 4, 634–641 (2022).
124. Li, J. et al. Ultrathin, Soft, Radiative Cooling Interfaces for Advanced Thermal Management in Skin Electronics. *Sci. Adv.* 9, eadg1837 (2023).
125. Yoo, S. et al. Responsive materials and mechanisms as thermal safety systems for skin-interfaced electronic devices. *Nat. Commun*. 14, 1024 (2023).
126. Yang, J. et al. Toward a new generation of permeable skin electronics. *Nanoscale* 15, 3051–3078 (2023).
127. Hwang, J., Kim, Y., Yang, H. & Oh, J. H. Fabrication of hierarchically porous structured PDMS composites and their application as a flexible capacitive pressure sensor. *Compos. B Eng*. 211, 108607 (2021).
128. Wei, G. & Ma, P. X. Macroporous and nanofibrous polymer scaffolds and polymer/bone-like apatite composite scaffolds generated by sugar spheres. *J. Biomed. Mater. Res. A* 78, 306–315 (2006).
129. Li, Q., Duan, T., Shao, J. & Yu, H. Fabrication method for structured porous polydimethylsiloxane (PDMS). *J. Mater. Sci.* 53, 11873–11882 (2018).
130. Zhang, T., Sanguramath, R. A., Israel, S. & Silverstein, M. S. Emulsion Templating: Porous Polymers and beyond. *Macromolecules* 52, 5445–5479 (2019).
131. Lu, M. et al. Phase-Separation-Induced Porous Hydrogels from Amphiphilic Triblock Copolymer with High Permeability and Mechanical Strength. *Chemistry of Materials* 34, 10995–11006 (2022).
132. Kahrs, C. & Schwellenbach, J. Membrane formation via non-solvent induced phase separation using sustainable solvents: A comparative study. *Polymer (Guildf).* 186, 122071 (2020).
133. Liu, Q. et al. Porous polymers: structure, fabrication and application. *Mater. Horiz*. 12, 2436–2466 (2025).
134. Hołda, A. K. & Vankelecom, I. F. J. Understanding and guiding the phase inversion process for synthesis of solvent resistant nanofiltration membranes. *J. Appl. Polym. Sci.* 132, 42130 (2015).
135. Xu, Y. et al. Porous Liquid Metal-Elastomer Composites with High Leakage Resistance and Antimicrobial Property for Skin-Interfaced Bioelectronics. *Sci. Adv.* 9, eadf0575 (2023).
136. Xu, Y. et al. Phase-separated porous nanocomposite with ultralow percolation threshold for wireless bioelectronics. *Nat. Nanotechnol*. 19, 1158–1167 (2024).
137. Zhuang, Q. et al. Permeable, three-dimensional integrated electronic skins with stretchable hybrid liquid metal solders. *Nat. Electron*. 7, 598–609 (2024).
138. Keirouz, A. et al. The History of Electrospinning: Past, Present, and Future Developments. *Adv. Mater. Technol*. 8, 2201723 (2023).
139. Wang, H. et al. An electrospinning–electrospraying technique for connecting electrospun fibers to enhance the thermal conductivity of boron nitride/polymer composite films. *Compos. B Eng*. 230, 109505 (2022).

140. Zheng, S. et al. Pressure-stamped stretchable electronics using a nanofibre membrane containing semi-embedded liquid metal particles. *Nat. Electron*. 7, 576–585 (2024).
141. Liao, X. et al. Extremely Low Thermal Conductivity and High Electrical Conductivity of Sustainable Carbonceramic Electrospun Nonwoven Materials. *Sci. Adv.* 9, eade6066 (2023).
142. Min, H. et al. Highly Air/Water-Permeable Hierarchical Mesh Architectures for Stretchable Underwater Electronic Skin Patches. *ACS Appl. Mater. Interfaces* 12, 14425–14432 (2020).
143. Yeon, H. et al. Long-Term Reliable Physical Health Monitoring by Sweat Pore-Inspired Perforated Electronic Skins. *Sci. Adv.* 7, eabg8459 (2021).
144. Tian, L. et al. Large-area MRI-compatible epidermal electronic interfaces for prosthetic control and cognitive monitoring. *Nat. Biomed. Eng*. 3, 194–205 (2019).
145. Fang, Y. et al. Solution-Processed Submicron Free-Standing, Conformal, Transparent, Breathable Epidermal Electrodes. *ACS Appl. Mater. Interfaces* 12, 23689–23696 (2020).
146. Wang, Y. et al. Robust, self-adhesive, reinforced polymeric nanofilms enabling gas-permeable dry electrodes for long-term application. *Proc. Natl. Acad. Sci. U.S.A.* 118, e2111904118 (2021).
147. Awasthi, A. K., Li, J., Koh, L. & Ogunseitan, O. A. Circular economy and electronic waste. *Nat. Electron*. 2, 86–89 (2019).
148. Liu, K., Tan, Q., Yu, J. & Wang, M. A global perspective on e-waste recycling. *Circ. Econ*. 2, 100028 (2023).
149. Yao, D. R., Kim, I., Yin, S. & Gao, W. Multimodal Soft Robotic Actuation and Locomotion. *Adv. Mater*. 36, 2308829 (2024).
150. Teng, L. et al. Liquid Metal-Based Transient Circuits for Flexible and Recyclable Electronics. *Adv. Funct. Mater*. 29, 1808739 (2019).
151. Zheng, Y. et al. Lignin-Based Encapsulation of Liquid Metal Particles for Flexible and High-Efficiently Recyclable Electronics. *Adv. Funct. Mater*. 34, 2310653 (2024).
152. Tavakoli, M. et al. 3R Electronics: Scalable Fabrication of Resilient, Repairable, and Recyclable Soft-Matter Electronics. *Adv. Mater*. 34, 2203266 (2022).
153. Tutika, R., Haque, A. B. M. T. & Bartlett, M. D. Self-healing liquid metal composite for reconfigurable and recyclable soft electronics. *Commun. Mater*. 2, 64 (2021).
154. Chen, G. et al. Recyclable, weldable, mechanically durable, and programmable liquid metal-elastomer composites. *J. Mater. Chem. A Mater*. 9, 10953–10965 (2021).
155. Meng, F., Saed, M. O. & Terentjev, E. M. Rheology of vitrimers. *Nat. Commun*. 13, 5753 (2022).
156. Capelot, M., Unterlass, M. M., Tournilhac, F. & Leibler, L. Catalytic control of the vitrimer glass transition. *ACS Macro Lett*. 1, 789–792 (2012).
157. Montarnal, D., Capelot, M., Tournilhac, F. & Leibler, L. Silica-like malleable materials from permanent organic networks. *Science* 334, 965–968 (2011).
158. Zheng, J. et al. Vitrimers: Current research trends and their emerging applications. *Mater. Today* 51, 586–625 (2021).
159. Denissen, W., Winne, J. M. & Du Prez, F. E. Vitrimers: Permanent organic networks with glass-like fluidity. *Chem. Sci.* 7, 30–38 (2016).
160. Zhang, H., Cui, J., Hu, G. & Zhang, B. Recycling strategies for vitrimers. *Int. J. Smart Nano Mater*. 13, 367–390 (2022).

161. Yu, K., Taynton, P., Zhang, W., Dunn, M. L. & Qi, H. J. Reprocessing and recycling of thermosetting polymers based on bond exchange reactions. *RSC Adv.* 4, 10108–10117 (2014).
162. Yu, K., Shi, Q., Dunn, M. L., Wang, T. & Qi, H. J. Carbon Fiber Reinforced Thermoset Composite with Near 100% Recyclability. *Adv. Funct. Mater*. 26, 6098–6106 (2016).
163. Yang, Y. et al. Carbon nanotube-vitrimer composite for facile and efficient photo-welding of epoxy. *Chem. Sci*. 5, 3486–3492 (2014).
164. Schenk, V., Labastie, K., Destarac, M., Olivier, P. & Guerre, M. Vitrimer composites: current status and future challenges. *Mater. Adv.* 3, 8012–8029 (2022).
165. Shi, Q. et al. Recyclable 3D printing of vitrimer epoxy. *Mater. Horiz.* 4, 598–607 (2017).
166. Rohewal, S.S. et al. Flax fiber-reinforced fatty acid vitrimer biocomposite with enhanced chemical recyclability. *MRS Communications* 14, 534–542 (2024).
167. Seah, G. E. K. K. et al. Covalent Adaptable Networks for Sustainable Soft Electronic Sensors and Actuators. *Adv. Funct. Mater*. 35, 2421060 (2024).
168. Deng, J. et al. Vitrimer Elastomer-Based Jigsaw Puzzle-Like Healable Triboelectric Nanogenerator for Self-Powered Wearable Electronics. *Adv. Mater*. 30, 1705918 (2018).
169. Yang, S. et al. Sustainable epoxy composites with high thermal conductivity using poly(lipoic acid) modified liquid metal as crosslinkers. *Compos. Commun*. 44, 1705918 (2023).
170. Yang, Y., Yan, L., Zheng, Y., Dai, L. & Si, C. Lignin-Based Vitrimer for High-Resolution and Full-Component Rapidly Recycled Liquid Metal Printed Circuit. *Adv. Funct. Mater.* 35, 2425780 (2025).
171. Ralphs, M. I. et al. In Situ Alloying of Thermally Conductive Polymer Composites by Combining Liquid and Solid Metal Microadditives. *ACS Appl. Mater. Interfaces* 10, 2083–2092 (2018).
172. Kong, W. et al. Oxide-Mediated Formation of Chemically Stable Tungsten–Liquid Metal Mixtures for Enhanced Thermal Interfaces. *Adv. Mater*. 31, 1904309 (2019).
173. Wei, S., Yu, Z. F., Zhou, L. J. & Guo, J. D. Investigation on enhancing the thermal conductance of gallium-based thermal interface materials using chromium-coated diamond particles. *J. Mater. Sci.: Mater. Electron*. 30, 7194–7202 (2019).
174. Ford, M. J., Patel, D. K., Pan, C., Bergbreiter, S. & Majidi, C. Controlled Assembly of Liquid Metal Inclusions as a General Approach for Multifunctional Composites. *Adv. Mater*. 32, 2002929 (2020).
175. Zhu, L. et al. Anisotropic liquid metal-elastomer composites. *J. Mater. Chem. C Mater*. 7, 10166–10172 (2019).
176. Handschuh-Wang, S., Stadler, F. J. & Zhou, X. Critical Review on the Physical Properties of Gallium-Based Liquid Metals and Selected Pathways for Their Alteration. *J. Phys. Chem. C* 125, 20113–20142 (2021).
177. Haake, A., Tutika, R., Schloer, G. M., Bartlett, M. D. & Markvicka, E. J. On-Demand Programming of Liquid Metal-Composite Microstructures through Direct Ink Write 3D Printing. *Adv. Mater*. 34, 2200182 (2022).
178. Ladd, C., So, J. H., Muth, J. & Dickey, M. D. 3D printing of free standing liquid metal microstructures. *Adv. Mater*. 25, 5081–5085 (2013).
179. Shin, G., Jeon, B. & Park, Y. L. Direct printing of sub-30 μm liquid metal patterns on three-dimensional surfaces for stretchable electronics. *J. Micromech. Microeng*. 30, 034001 (2020).

180. Wang, L. & Liu, J. Advances in the Development of Liquid Metal-Based Printed Electronic Inks. *Front. Mater*. 6, 303 (2019).
181. Yu, S., Hing, P. & Hu, X. Thermal Conductivity of Polystyrene-aluminum Nitride Composite. 33, 289–292 (2002).
182. Witting, I. T. et al. The Thermoelectric Properties of Bismuth Telluride. *Adv. Electron. Mater*. 5, 1800904 (2019).
183. Saberi, Y. & Sajjadi, S. A. A comprehensive review on the effects of doping process on the thermoelectric properties of Bi2Te3 based alloys. *J. Alloys Compd*. 904, 163918 (2022).
184. Fassler, A. & Majidi, C. Liquid-Phase Metal Inclusions for a Conductive Polymer Composite. *Adv. Mater*. 27, 1928–1932 (2015).
185. Kim, C. S. et al. Structural design of a flexible thermoelectric power generator for wearable applications. *Appl. Energy* 214, 131–138 (2018).
186. Yuan, J. & Zhu, R. A fully self-powered wearable monitoring system with systematically optimized flexible thermoelectric generator. *Appl. Energy* 271, 115250 (2020).
187. Tavakoli, M. et al. EGaIn-Assisted Room-Temperature Sintering of Silver Nanoparticles for Stretchable, Inkjet-Printed, Thin-Film Electronics. *Adv. Mater*. 30, 1801852 (2018).
188. Lu, N., Lu, C., Yang, S. & Rogers, J. Highly sensitive skin-mountable strain gauges based entirely on elastomers. *Adv. Funct. Mater*. 22, 4044–4050 (2012).
189. Diani, J., Fayolle, B. & Gilormini, P. A review on the Mullins effect. *Eur. Polym. J*. 45, 601–612 (2009).
190. Lee, G. et al. Flexible heatsink based on a phase-change material for a wearable thermoelectric generator. *Energy* 179, 12–18 (2019).
191. Bang, K. M., Park, W., Ziolkowski, P. & Jin, H. Fabrication and Cooling Performance Optimization of Stretchable Thermoelectric Cooling Device. *ACS Appl. Electron. Mater.* 3, 5433–5442 (2021).
192. Lossec, M., Multon, B. & Ben Ahmed, H. Sizing optimization of a thermoelectric generator set with heatsink for harvesting human body heat. *Energy Convers. Manag*. 68, 260–265 (2013).
193. Zadan, M. et al. Liquid Crystal Elastomer with Integrated Soft Thermoelectrics for Shape Memory Actuation and Energy Harvesting. *Adv. Mater*. 34, 2200857 (2022).
194. Sato, Y., Terashima, S. & Iwase, E. Origami-Type Flexible Thermoelectric Generator Fabricated by Self-Folding. *Micromachines (Basel)*. 14, 218 (2023).
195. Jeong, S. H. et al. Stretchable Thermoelectric Generators Metallized with Liquid Alloy. *ACS Appl. Mater. Interfaces* 9, 15791–15797 (2017).
196. Shi, Y. et al. Stretchable thermoelectric generator for wearable power source and temperature detection applications. *Energy Convers. Manag*. 253, 115167 (2022).
197. Koshi, T. et al. High-performance stretchable thermoelectric generator using serpentine interconnects encapsulated in an ultrasoft silicone sponge. *Flex. Print. Electron.* 7, 025008 (2022).
198. Fukuie, K., Iwata, Y. & Iwase, E. Design of substrate stretchability using origami-like folding deformation for flexible thermoelectric generator. *Micromachines (Basel)*. 9, 315 (2018).
199. Jeong, M. H. et al. Increasing the thermoelectric power factor of solvent-treated PEDOT:PSS thin films on PDMS by stretching. *J. Mater. Chem. A Mater.* 6, 15621–15629 (2018).

200. Lee, T. S. et al. Highly surface-conformable thermoelectric patches for efficient thermal contact with arbitrary substrates. *Chem. Eng. J.* 455, 140925 (2023).
201. Wen, N. et al. High-performance stretchable thermoelectric fibers for wearable electronics. *Chem. Eng. J*. 426, 130816 (2021).
202. Wen, N. et al. Highly conductive, ultra-flexible and continuously processable PEDOT:PSS fibers with high thermoelectric properties for wearable energy harvesting. *Nano Energy* 78, 105361 (2020).
203. Zheng, Y. et al. Durable, stretchable and washable inorganic-based woven thermoelectric textiles for power generation and solid-state cooling. *Energy Environ. Sci*. 15, 2371–2385 (2022).
204. Wang, Y. et al. High-performance Stretchable Organic Thermoelectric Generator via Rational Thermal Interface Design for Wearable Electronics. *Adv. Energy Mater.* 12, 2102835 (2022).
205. Wu, B. et al. Stretchable thermoelectric generators with enhanced output by infrared reflection for wearable application. *Chem. Eng. J*. 453, 139749 (2023).
206. Won, P. et al. Controlling C2C12 Cytotoxicity on Liquid Metal Embedded Elastomer (LMEE). *Adv. Healthc. Mater.* 12, 2202430 (2023).
207. DiSalvo, F. J. Thermoelectric Cooling and Power Generation. *Science* 285, 703–706 (1999).
208. Lu, N., Lu, C., Yang, S. & Rogers, J. Highly sensitive skin-mountable strain gauges based entirely on elastomers. *Adv. Funct. Mater*. 22, 4044–4050 (2012).
209. Tutika, R., Haque, A. B. M. T. & Bartlett, M. D. Self-healing liquid metal composite for reconfigurable and recyclable soft electronics. *Commun. Mater.* 2, 64 (2021).
210. Zhao, Y. et al. A self-healing electrically conductive organogel composite. *Nat. Electron.* 6, 206–215 (2023).
211. Bartlett, M. D., Dickey, M. D. & Majidi, C. Self-healing materials for soft-matter machines and electronics. *NPG Asia Mater.* 11, 21 (2019).
212. Merlo, A., Mokkapati, V. R. S. S., Pandit, S. & Mijakovic, I. Boron nitride nanomaterials: Biocompatibility and bio-applications. *Biomater. Sci.* 6, 2298–2311 (2018).
213. Moon, S. et al. 3D Printable concentrated liquid metal composite with high thermal conductivity. *iScience* 24, 103183 (2021).
214. Zhu, Z. et al. Liquid Metal-Assisted High-Efficiency Exfoliation of Boron Nitride for Electrically Insulating Heat-Spreader Film. *ACS Appl. Mater. Interfaces* 14, 54256–54265 (2022).
215. Ji, Z., Liu, W., Ouyang, C. & Li, Y. High thermal conductivity thermoplastic polyurethane/boron nitride/liquid metal composites: The role of the liquid bridge at the filler/filler interface. *Mater. Adv.* 2, 5977–5985 (2021).
216. Li, J., Pan, K., Tian, H. & Yin, L. The Potential of Electrospinning/Electrospraying Technology in the Rational Design of Hydrogel Structures. *Macromol. Mater. Eng*. 305, 2000285 (2020).
217. Chen, K. et al. Mechanical-Thermal Co-Design of Flexible Thermoelectric Devices with Solid-Liquid Electrodes for Enhanced Stretchability and Power Generation. *Adv. Energy Mater.* 15, e03184 (2025).
218. Mao, J., Chen, G. & Ren, Z. Thermoelectric cooling materials. *Nat. Mater.* 20, 454–461 (2021).

219. Lee, J. et al. Stretchable Skin-Like Cooling/Heating Device for Reconstruction of Artificial Thermal Sensation in Virtual Reality. *Adv. Funct. Mater*. 30, 1909171 (2020).
220. Ding, J., Zhao, W., Jin, W., Di, C. an & Zhu, D. Advanced Thermoelectric Materials for Flexible Cooling Application. *Adv. Funct. Mater*. 31, 2010695 (2021).
221. Han, Y. et al. Conductive Liquid Metal Vitrimer Composites for Reconfigurable and Recyclable Flexible Electronics. *Adv. Funct. Mater*. 35, e11119 (2025).
222. Kim, D. et al. Recovery of nonwetting characteristics by surface modification of gallium-based liquid metal droplets using hydrochloric acid vapor. *ACS Appl. Mater. Interfaces* 5, 179–185 (2013).
223. Bilodeau, R. A., Zemlyanov, D. Y. & Kramer, R. K. Liquid Metal Switches for Environmentally Responsive Electronics. *Adv. Mater. Interfaces* 4, 1600913 (2017).
224. Zhang, X. D., Zhang, Z. T., Wang, H. Z. & Cao, B. Y. Thermal Interface Materials with High Thermal Conductivity and Low Young's Modulus Using a Solid-Liquid Metal Codoping Strategy. *ACS Appl. Mater. Interfaces* 15, 3534–3542 (2023).
225. Qi, D., Zhang, K., Tian, G., Jiang, B. & Huang, Y. Stretchable Electronics Based on PDMS Substrates. *Adv. Mater*. 33, 2003155 (2020).
226. Li, Y., Veronica, A., Ma, J. & Nyein, H. Y. Y. Materials, Structure, and Interface of Stretchable Interconnects for Wearable Bioelectronics. *Adv. Mater*. 37, 2408456 (2024).
227. Haake, A., Tutika, R., Schloer, G. M., Bartlett, M. D. & Markvicka, E. J. On-Demand Programming of Liquid Metal-Composite Microstructures through Direct Ink Write 3D Printing. *Adv. Mater*. 34, 2200182 (2022).
228. Morris, N. J., Farrell, Z. J. & Tabor, C. E. Chemically modifying the mechanical properties of core-shell liquid metal nanoparticles. *Nanoscale* 11, 17308–17318 (2019).
229. Rahim, M. A. et al. Polyphenol-Induced Adhesive Liquid Metal Inks for Substrate-Independent Direct Pen Writing. *Adv. Funct. Mater*. 31, 2007336 (2021).
230. Hafiz, S. S. et al. Surfaces and Interfaces of Liquid Metal Core–Shell Nanoparticles under the Microscope. *Part. Part. Syst. Charact*. 37, 1900469 (2020).
231. Zhang, Z., Chen, H., Diao, W., Zhou, C. & Liu, G. Simultaneous binding of carboxyl and amino groups to liquid metal surface for biosensing. *J. Mater. Chem. B* 12, 9703-9712 (2024).
232. Pérez, O., Odio, O. F. & Reguera, E. XPS as a probe for the bonding nature in metal acetates. *New J. Chem*. 46, 11255–11265 (2022).
233. Rohewal, S. S. et al. Hierarchically Structured Vitrimer Biocomposites for Sustainable Manufacturing. *Small* 21, 2500721 (2025).
234. Handschuh-Wang, S., Chen, Y., Zhu, L. & Zhou, X. Analysis and Transformations of Room-Temperature Liquid Metal Interfaces – A Closer Look through Interfacial Tension. *Chem. Phys. Chem*. 19, 1584–1592 (2018).
235. Zhou, L., Ohm, Y., Chin, R. M., Kerr, O., Manohar, K. & Malakooti, M. H. "Machine Learning-Assisted Inverse Design of Soft and Multifunctional Hybrid Liquid Metal Composites." *Adv. Funct. Mater.* e75719 (2026).
236. Jing, Y. et al. Scalable manufacturing of a durable, tailorable, and recyclable multifunctional woven thermoelectric textile system. *Energy Environ. Sci.* 16, 4334–4344 (2023).
237. Jang, D., Park, K. T., Lee, S. S. & Kim, H. Highly stretchable three-dimensional thermoelectric fabrics exploiting woven structure deformability and passivation-induced fiber elasticity. *Nano Energy* 97, 107143 (2022).

238. Liu, S., Zhang, M., Kong, J., Li, H. & He, C. Flexible, durable, green thermoelectric composite fabrics for textile-based wearable energy harvesting and self-powered sensing. *Compos. Sci. Technol.* 243, 110245 (2023).
239. He, X. *et al.* Three-dimensional flexible thermoelectric fabrics for smart wearables. *Nat. Commun.* 16, 2523 (2025).
240. He, X. *et al.* Highly stretchable, durable, and breathable thermoelectric fabrics for human body energy harvesting and sensing. *Carbon Energy* 4, 621–632 (2022).
241. Kwon, C. *et al.* Multi-Functional and Stretchable Thermoelectric Bi2Te3 Fabric for Strain, Pressure, and Temperature-Sensing. *Adv. Funct. Mater.* 33, 2300092 (2023).
242. Brondi, C. et al. Curing Behavior of Reprocessable Epoxy Vitrimers: Thermal Analysis and Kinetics Modeling. Macromol. *Chem. Phys*. 224, 2300273 (2023).
243. Xie, H. et al. Cure kinetic study of carbon nanofibers/epoxy composites by isothermal DSC. *J. Appl. Polym. Sci.* 96, 329–335 (2005).
244. Cheng, S. & Wu, Z. Microfluidic electronics. *Lab on a Chip* 12, 2782–2791 (2012).
245. Seo, J., Kearney, L. T., Toomey, M. D., Keum, J. K. & Naskar, A. K. Polyester-based epoxy vitrimer integrating spent coffee ground as a natural filler. *Compos. B Eng*. 260, 110756 (2023).